On Applications of Resonances, from One to Infinity

by

Mohammed Benzaouia

Dipl. Ing., École Polytechnique, France (2016)
M.S., Massachusetts Institute of Technology, USA (2018)

Submitted to the Department of Electrical Engineering
and Computer Science
in partial fulfillment of the requirements for the degree of

Doctor of Philosophy in Electrical Engineering and Computer Science

at the

MASSACHUSETTS INSTITUTE OF TECHNOLOGY

February 2022

Author ....
Department of Electrical Engineering
and Computer Science
October 20, 2021

Certified by ....
Steven G. Johnson
Professor of Applied Mathematics and Physics
Thesis Supervisor

Accepted by ....
Leslie A. Kolodziejski
Professor of Electrical Engineering and Computer Science
Chair, Department Committee on Graduate Students

On Applications of Resonances, from One to Infinity

by

Mohammed Benzaouia

Submitted to the Department of Electrical Engineering
and Computer Science
on October 20, 2021, in partial fulfillment of the
requirements for the degree of
Doctor of Philosophy in Electrical Engineering and Computer Science

Abstract

Resonances are everywhere. They have different manifestations and are used in many applications. In this work, we study multiple systems making use of resonances, with numbers ranging “from one to infinity.”

First, we derive single-frequency bounds for the surface-enhanced Raman scattering (SERS) where resonant nanostructures are used to enhance the Raman signal. These bounds are shape independent and only function of the material constants and the separation distance from the Raman molecule. They can be evaluated analytically or by simple numerical integration.

We then present analytical design criteria for multi-resonant filters in strongly coupled systems where standard approaches (such as coupled mode theory or network synthesis) are not adequate. For this, we develop a quasi-normal mode theory (QNMT) of the scattering matrix that enforces the fundamental constraints of energy conservation and reciprocity even for truncated sums. As an example of application, we design microwave metasurface filters with various orders, bandwidths and types (such elliptic or Chebyshev).

For systems making use of a large number of resonances over a large bandwidth (such as light trapping in solar cells), and in particular for metaparticle arrays, we present approximate frequency/angle-averaged absorption enhancement bounds in the radiative transfer regime and apply the results to ocean buoy energy extraction. Our results, which match full-wave simulations, enable us to propose and quantify approaches to increase performance through careful particle design and/or using external reflectors.

Finally, we study single-mode lasing stability in periodic systems where a full continuum of modes should be taken into account in the nonlinear regime above threshold. In particular, we show that, under the right conditions, single-mode lasing is still possible in an infinite periodic structure, with practical limitations arising from boundary effects and manufacturing inaccuracies. Examples of band-edge (1d) and bound-in-continuum (2d) mode lasing are presented.

Thesis Supervisor: Steven G. Johnson
Title: Professor of Applied Mathematics and Physics

إلى والديّ.

To my parents.

Acknowledgments

It is, without a doubt, impossible to thank all those who played a role in helping me reach this stage. Any effort to do so will simply be a mere approximation of the complex reality. I will then simply try to acknowledge the bare minimum here, asking forgiveness from all those who intersected with my path, but were not included in the next few lines.

I owe many debts of gratitude to Prof. Steven Johnson who supervised me in the last five years. No advisor is perfect, but Steven comes as close as possible to the best, given "fundamental constraints" due to the mere fact of being human. I keep getting amazed by his expertise, not only in mathematics and physics, but also in software engineering and numerical methods. (Yes, it is not very common to encounter a physicist who understands distributions!) He embodies the example of a top multi-disciplinary scientist whom I will keep looking up to. I learned many things from him, and I'm still looking to learn many more. Aside from research matters, he has also been a wonderful mentor who actually cares about his students, and I am very grateful to having worked with him. Steven, thank you.

Dr. Aristeidis Karalis deserves his own section. He has de facto been my second mentor, especially for the work on quasi-normal mode theory, and I owe him many thanks. We spent countless (and it is not an exaggeration at all) hours discussing coupled-mode theory and related subjects. I enjoyed the discussions we had and I learn many things from him, both in science and in life. I liked his meticulous approach in doing science, and it is something I will carry with me. Aristos, good luck for what is coming next for you.

Many others contributed to the work presented here. I thank them all for their discussions, contributions and trust: Prof. John Joannopoulos, Prof. Owen Miller, Prof. Dick Yue, Prof. Rasmus Christiansen, Prof. Douglas Stone, Dr. Alex Cerjan, Dr. Jérôme Michon, and Dr. Grgur Tokić. Thanks also go to other group members, Wenjie, Fan, and Raphael. I would also like to especially thank Prof. Rajeev Ram and Prof. Kevin O'Brien for accepting to being in my doctoral committee and evaluating my work.

My years at MIT would have been different without all the friends, with their smiles, discussions, meals, and others. They are simply too many to enumerate. From Houssam, the first Moroccan I met in Boston, to Mounir and all our shared meals, to many others: Bashir, Abdu-Razak, Abdallah, Sami, Amro, Harith, Abulaziz, Baraa, Ahmed, Amine and many many more. Also, ElMehdi and Soufiane for always keeping in touch in Morocco. Omar Saadi, for all the phone calls. And finally, Hamza, simply my friend. Thank you all.

Finally, I cannot thank my parents enough for all the love and support they showered me with, not asking for anything in return. Even though it is such a trivial statement (or tautology), it is always good to remember that I would not have been who I am without them. I hope that I will always be present for you, regardless of the challenges and difficulties that will face. Similar thanks go to my sisters and other family members, who simply loved me unconditionally. From the bottom of my heart, thank you.

Related publications

- **Benzaouia, M.**, Joannopoulos, J.D., Johnson, S.G. and Karalis, A., 2021. Analytical design criteria for ideal standard filters in strongly coupled resonant systems, with application to microwave metasurfaces. (Preprint, *arXiv:2103.08866*).
  [Chapter 4]
- **Benzaouia, M.**, Joannopoulos, J.D., Johnson, S.G. and Karalis, A., 2021. Quasi-normal mode theory of the scattering matrix, enforcing fundamental constraints for truncated expansions. *Physical Review Research, 3(3)*, p.033228.
  [Chapter 3]
- **Benzaouia, M.**, Cerjan, A. and Johnson, S.G., 2020. Is single-mode lasing possible in an infinite periodic system? *Applied Physics Letters, 117(5)*, p.051102.
  [Chapter 6]
- Christiansen, R.E., Michon, J., **Benzaouia, M.**, Sigmund, O. and Johnson, S.G., 2020. Inverse design of nanoparticles for enhanced Raman scattering. *Optics Express, 28(4)*, pp.4444-4462.
  [Chapter 2]
- Michon, J.,* **Benzaouia, M.**,* Yao, W., Miller, O.D. and Johnson, S.G., 2019. Limits to surface-enhanced Raman scattering near arbitrary-shape scatterers. *Optics Express, 27(24)*, pp.35189-35202.
  [Chapter 2]
- **Benzaouia, M.**, Tokić, G., Miller, O.D., Yue, D.K. and Johnson, S.G., 2019. From solar cells to ocean buoys: Wide-bandwidth limits to absorption by metaparticle arrays. *Physical Review Applied, 11(3),* p.034033.
  [Chapter 5]

THIS PAGE INTENTIONALLY LEFT BLANK

Contents

List of Figures **15**

1 Introduction **23**

1.1 Generalities 23

1.2 Overview 25

2 Loss in resonance: Bounding surfaced-enhanced Raman scattering **31**

2.1 On resonances 31

2.2 Surface-enhanced Raman scattering 34

2.3 Derivation of bounds 35

2.3.1 LDOS enhancement 36

2.3.2 Local field enhancement 36

2.3.3 Induced norm of the integral of the Green's function 40

2.3.4 Raman enhancement 41

2.3.5 Bound for a randomly oriented Raman molecule 43

2.4 Geometric results 44

2.4.1 Concentration enhancement for a plasmonic sphere 44

2.4.2 Isolated structures - Numerical simulation 45

2.4.3 Periodic structures - Numerical simulation 47

2.5 Topology optimization 49

2.5.1 Numerical results 49

2.5.2 Comparison with bounds 50

2.6 Conclusion 51

3 Few resonances 1: Quasi-normal mode theory (QNMT) **53**

3.1 On resonances 53

3.2 Overview 55

3.3 Quasi-Normal Mode Theory 57

3.3.1 Formulation 57
3.3.2 Physical constraints 62
3.3.3 Properties of 2-port systems 66
3.3.4 Absorption and gain 68
3.4 Examples in electromagnetism 68
3.4.1 Normal incidence on microwave metasurface 68
3.4.2 4-port metasurface via coupled polarizations 71
3.4.3 Oblique incidence on 2d photonic metasurface 72
3.5 Background scattering representation by low-Q modes 74
3.5.1 QNMT with background C matrix 74
3.5.2 C matrix due to $\Gamma \to \infty$ modes in 2-port systems 76
3.5.3 Choice of boundary for D calculation and C-matrix description of a port shift 78
3.5.4 Examples of Section 3.4 80
3.6 Conclusions 81

4 Few resonances 2: Filter design criteria with application to microwave metasurfaces 83

4.1 On resonances 83
4.2 Overview 84
4.3 S-matrix of lossless reciprocal 2-port systems 87
4.4 Filter Design 88
4.4.1 Conditions on C and σ_n 90
4.4.2 Types of Filters 92
4.4.3 Approximate solutions 94
4.4.4 Geometrical symmetry 95
4.4.5 Summary 95
4.5 Microwave metasurfaces 95
4.5.1 Second-order bandpass filter - Circuit model 96
4.5.2 Third-order bandpass filters 99
4.5.3 Third-order elliptic bandstop filter 101
4.5.4 Second-order elliptic bandpass and bandstop filters 102
4.5.5 Fabrication and tunability 104
4.6 Conclusions 104

5 Many resonances: From solar cells to ocean buoys 107
5.1 On resonances . . . 107
5.2 Overview . . . 108
5.3 Reciprocity . . . 110
5.3.1 Solar cells . . . 110
5.3.2 Ocean buoys . . . 113
5.4 Radiative transfer equation limits . . . 114
5.4.1 General limit . . . 115
5.4.2 Radiative-diffusion model . . . 117
5.5 Ocean-buoy arrays . . . 121
5.5.1 Example . . . 121
5.5.2 Larger interaction factor . . . 124
5.5.3 Surface membrane . . . 126
5.6 Conclusion . . . 129

6 Infinity of resonances: The periodic laser problem 131
6.1 On resonances . . . 131
6.2 Overview . . . 132
6.3 Stability of steady state solution Maxwell-Bloch . . . 133
6.4 Perturbation theory . . . 135
6.5 DFB laser: 1d example . . . 141
6.6 BiC lasing: 2d example . . . 145
6.7 Numerical validation of perturbation theory . . . 147
6.8 Conclusion . . . 151

7 Concluding remarks 153

8 Bibliography 157

A Elementary concepts 175
A.1 Planewave scattering . . . 175
A.2 Dipolar emission . . . 176

B QNM parameters for structures in Chapter 3 and Chapter 4 179
B.1 Structures of Chapter 3 . . . 179
B.2 Structures of Chapter 4 . . . 180

THIS PAGE INTENTIONALLY LEFT BLANK

List of Figures

1-1 Examples of a single resonance behaviour in many areas of physics. They all show the universal Lorentzian response $\propto 1/\left[(\omega-\Omega)^2+\Gamma^2\right]$. Left: Measurement of the Higgs boson mass based on the ATLAS experiment involving high-energy particles collisions at the CERN Large Hadron Collider [1]. Middle: Mechanical resonator using a single-walled carbon nanotube [2]. Right: Microwave resonator used to achieve highly sensitive electron spin resonance (ESR) spectroscopy [3]. 24

2-1 Schematics of the SERS configuration under study. The pump field is incident onto a scatterer, near which lies the Raman-active chemical. Upon interaction with the pump field, thus material behaves as a dipole emitting a Raman-shifted field. The Raman field interacts with the scatterer and is emitted to the far-field. 35

2-2 Comparison of the metric $(|\chi|^2/\mathrm{Im}\chi)^3$ for conventional metals used in SERS [4]. 43

2-3 Ratio of the analytical value of of $|\mathbf{E_{scat}}|^2$ given by Eq. (2.39) to the volume-scaling bound given by Eq. (2.14), for Ag spheres of different radii at the resonant frequency of Ag. Inset: Comparison of the analytical value (full lines) and the bound (dashed lines) for the same Ag spheres. 45

2-4 Simulation results and corresponding bounds for a Ag sphere of radius 10 nm and distance to emitter 20 nm. (a) Near-field enhancement with bound from main text. (b) LDOS with bound from [5]. 46

2-5 Raman enhancement bounds (dashed lines) and actual performances (full lines) for common SERS Ag structures. The distance to the emitter is $d = 20$ nm for all structures. The sphere has a radius of 10 nm. The triangles have a side of 160 nm, height of 30 nm, and tip curvature of 16 nm. The incident field's polarization is aligned with the sphere-emitter and triangle-emitter direction. 47

2-6 Near-field enhancement bounds for an isolated Ag sphere (bottom right schematics) and a square array of Ag spheres with varying period a (top right schematics). The region on top of the solid red and yellow lines indicates forbidden field-concentration values for the periodic case. The spheres have a radius $R = 12$ nm, and the emitter is located $d = 20$ nm away from their surface along the lattice axis. The incident field's polarization is aligned with the sphere-emitter direction and $\lambda = 350$ nm. In the large-enhancement limit, the area-scaling and volume-scaling bounds always intersect at a point, denoted P, where the period equals $\sqrt{k_p[V|\chi|^2/\left[\mathrm{Im}\chi\cos\theta\right]}$. Inset: map of the position of points P, Q, and Q' as a function of sphere radius and lattice period, for $d = 20$ nm. 48

2-7 (a) A sketch of the Raman scattering design problem where a Raman molecule (blue) in air background is surrounded by the design domain Ω_D (gray) and excited by an incident planewave (green). Optimization maximizes the total emitted power (red) through Γ_{out}. Distance separating the molecule and the structure is fixed at 10 nm. The outside radius of the optimization domain Ω_D is fixed at 100 nm. Results presented here assume a zero Raman frequency shift. (b) Raman enhancement as a function of wavelength, for a molecule placed at the center of different silver nanostructures (dark blue dot) relative to a molecule placed in free space. A topology-optimized structure (blue), a bowtie antenna (red) and coupled-cylinder antenna (black) are considered, all designed to maximize enhancement at 532 nm. 49

2-8 Left: Raman enhancement as a function of Ω_D area. Structures optimized for three different radii of Ω_D, equal to 50 nm, 75 nm, and 100 nm. Right: Raman enhancement as a function of $|\chi|^2/\mathrm{Im}\chi$ for different materials. . . . 51

3-1 A 2-port scattering system with important QNMT parameters. At excitation frequency ω, the coupling port-modes (CPMs) with transverse fields $\phi_p^\perp$ have input and output amplitudes respectively $s_{\pm p}$, related by the S-matrix through $s_- = Ss_+$. The open scattering system supports quasi-normal modes (QNMs) with complex frequencies ω_n and fields ψ_n, which have amplitudes a_n upon excitation. The CPM-to-QNM coupling coefficients are D_{pn}, with ratios $\sigma_n = D_{2n}/D_{1n}$. Imposing realness, unitarity, and symmetry constraints on S allows us to compute it as a function of only ω_n and σ_n [Eq. (3.10)]. Optionally, by separating low-Q modes ψ_n^C, we can also construct a slowly-varying background matrix C, which can give a physical intuition about the scattering response and help in specific scattering designs. 59

3-2 QNMT modeling scattering of a plane wave normally incident from the left on the microwave metasurface depicted in the inset of (a). Parameters are: $a = 15$mm, $h/a = 0.64$, $w_j/a = (0.05, 0.2, 0.1)$, $l_j/a = (0.62, 0.92, 0.82)$, metal (grey) layers' thickness $d_\mu = 18\mu$m, dielectric (green) layers' permittivities $\epsilon_i = (4, 6, 3, 10)$ and thicknesses $d_i/a = (0.1, 0.2, 0.3, 0.2)$. In the lossy simulation, we used copper and added loss $\tan\delta = 0.01$ to all dielectric layers [for simplicity, $-\tan\delta$ is assumed for $\mathrm{Re}(f) < 0$ to maintain realness of $\epsilon(f)$]. Curves: (a) magnitude and (b) group delay of the transmission coefficient (where a constant delay of $0.24 \times d/c$ was added to QNMT to match the exact simulation at low frequencies). (c) Lossless-system poles used in the QNM expansion (with their negative-frequency pairs used but not shown) and zeros of the resulting S coefficients, confirming unitarity and symmetry of S. The dotted arrows point at the 4 modes used to compute the slowly varying background C in the $S = \bar{S}C$ approximation. (d) Errors of asymmetric [Eq. (3.10) without Eq. (3.17), and approximate Eq. (3.23)] or non-unitary [Ref. 6] QNMT formulations. . 70

3-3 QNMT modeling of cross-polarization transmission of a normally incident plane wave from a metasurface with rotated apertures. The two planar metallic sheets are periodically patterned (period $a = 15mm$) with same cross-like apertures [with widths $(0.05a, 0.1a)$ and lengths $(0.5a, 0.3a)$ in two orthogonal directions], which are rotated by angles 30° and 60° with respect to the polarization of port 1. The three uniform dielectric layers have $\epsilon_i = (2, 3, 5)$ and thicknesses $d_i/a = (0.1, 0.05, 0.15)$. (b) Errors of asymmetric [Eq. (3.10) without Eq. (3.17)] or non-unitary [Ref. 6] QNMT formulations. 72

3-4 QNMT modeling of transmission of obliquely incident ($\theta = 30°$) TE plane wave from a dielectric ($\epsilon = 11$) grating with $w/a = 0.4$ and $d_i/a = (0.6, 0.4)$ so $d = d_1 + d_2 = a$. The lossy structure has $\epsilon = 11 + 0.77i$ (loss tangent $\tan\delta = 0.07$). 73

3-5 Normally incident plane wave transmission through slabs with indices $\tilde{n}_s = 3$, $\tilde{n} = 1.05$ and thickness d (black for exact result and red for QNMT prediction), and comparison to the limiting case of $\tilde{n} = 1$ (blue for exact result). (a) Geometry and poles, (b) amplitude and (c) group delay: the small shift is due to the extra propagation through the A–A′ slab, predicted by QNMT primarily via the contribution of the low-Q modes, as can be seen also from the $\bar{S}C$ approximation (green) where $S_{21} \approx \bar{S}_{21}C_{11}$ gives the correct delay $\tau_{21} \approx \tau_{21}[\bar{S}] + \tau_{11}[C]$. 79

4-1 A lossless reciprocal 2-port scattering system excited at frequency ω, with input and output amplitudes respectively $s_{\pm p}$, related by the S-matrix through $s_- = Ss_+$. The system supports high-Q quasi-normal modes (QNMs) with frequencies ω_n and port-coupling ratios σ_n, while low-Q resonances create an effective background response C. 87

93figure.4.2

4-3 (a) Symmetric metasurface for a second-order bandpass filter centered at 10 GHz with a single transmission-zero, designed for 0.25 dB passband ripple and 25 dB stopband attenuation (black dashed lines). (b) Equivalent circuit model. The coupling L_bC_b gives the transmission-zero. (c) Transmission spectrum of two optimized structures with a zero respectively on the left (L) and on the right (R) of their transmission peaks. Parameters for structure (L): a = 6mm, $w_1/a = w_2/a = 0.0479$, $l_1/a = l_2/a = 0.846$, $t_1/a = t_3/a = 0.493$, $t_2/a = 0.257$, $\epsilon_1 = \epsilon_3 = 1.43$, $\epsilon_2 = 14.51$. Parameters for structure (R): a = 9.34mm, $w_1/a = w_2/a = 0.00877$, $l_1/a = l_2/a = 0.905$, $t_1/a = t_3/a = 0.0237$, $t_2/a = 0.0966$, $\epsilon_1 = \epsilon_3 = 4.12$, $\epsilon_2 = 3.80$. 97

4-4 Optimized third-order bandpass filters (a) of different types with same bandwidth and (b) elliptic only for different bandwidths. We use the same structure as in Fig. 4-3 but with three metallic sheets and four dielectric layers. Physical parameters are provided in a table above. We notice good agreement of lossless structures (solid lines) with ideal filters (dashed lines), except for small deviations mainly due to effects from high-order modes. Copper losses (dotted line) reduce peak transmission while preserving the filter's shape. 100

4-5 (a) Third-order elliptic bandstop filter. The structure has three metallic-cross arrays and four dielectric layers with parameters: a = 16.99mm, $h/a = 0.03$, $d/a = 0.619$, $w/a = (1.53, 3.73, 1.61) \times 10^{-3}$, $l/a = (0.558, 0.589, 0.524)$, $t/a = (0.166, 0.358, 0.441, 0.183)$, $\epsilon = (4.76, 3.22, 4.05, 4.50)$. (b) Second-order elliptic bandpass filter. The structure has two metallic sheets and three dielectric layers with parameters: a = 17.571mm, $h/a = 0.456$, $w_1/a = w_2/a = 6.08 \times 10^{-3}$, $l_1/a = l_2/a =$

0.4355, $t_1/a = t_3/a = 0.3072$, $t_2/a = 0.3169$, $\epsilon_1 = \epsilon_3 = 3.82$, $\epsilon_2 = 1.893$. (c) Second-order elliptic bandstop filter. The structure has two metallic-cross arrays and three dielectric layers with parameters: $a = 18.70$mm, $h/a = 0.181$, $w_1/a = w_2/a = 2.74 \times 10^{-3}$, $l_1/a = l_2/a = 0.514$, $t_1/a = t_3/a = 0.204$, $t_2/a = 0.332$, $\epsilon_1 = \epsilon_3 = 1.60$, $\epsilon_2 = 3.10$. All filters satisfy quite well the marked requirements (black dashed lines) and agree with the ideal filters. 102

5-1 Figure taken from Ref. 7. (a) Solar-cell with a 2D grating on top and back reflector on the back. (b) Absorption spectrum of the cell for normally incident light. A large number of narrow resonances is present, which leads to an overall increase in absorption. The spectral-averaged absorption in presence of the grating and back reflector (red line) is 74.2 larger than the "single pass" absorption in their absence (blue line). 108

5-2 Left: We bound absorption for very general arrays of "particles", including arrays of buoys that extract energy from ocean waves. Left: Ocean surface displacement η for a cylindrical buoy array [8] where A is the amplitude of waves incident from left (arrow). 109

5-3 Sketch of RTE system. 115

5-4 Properties of a single truncated-cylinder wave energy converter (WEC) in heave (vertical) motion, with radius $a = 0.3h$ and draft $H = 0.2h$ where h is the ocean depth. The WEC has an isotropic response with respect to the direction of the incident field. Left: Scattering and absorption cross sections of a single buoy normalized to the cylinder diameter ($\sigma/2a$). The ocean spectral energy density (energy per horizontal surface) is chosen as Bretschneider [9] with resonant frequency matching that of the body and is shown in units of $\rho g H^2 T$ (ρ is the water density, g the acceleration of gravity, T the mean wave period and H the significant wave height). Right: Asymmetry factors, defined as the average of $\cos\phi$ and $\cos 2\phi$ for the two-dimensional differential scattering cross section. These parameters enter into the diffusion equation as $\mu = (\mu_1 - \mu_2)/(1 - \mu_2)$ and with σ_s replaced by $\sigma_s(1 - \mu_2)$ [10]. 122

5-5 Left: Frequency-averaged interaction factor q_s vs incident angle θ for $N_x \times N_y = 3 \times 30$ arrays of buoys from exact solution [8] (solid lines), compared to standard-diffusion (black dashed lines), corrected-diffusion (red dashed lines) and radiative-transfer (RTE with Monte Carlo simulation, dots) models. (q = array absorption / isolated-buoys absorption.) The average buoy spacings (randomly chosen via a Gamma distribution) are $d_x/h = 1.73$, $d_y/h = 3.63$, with h = ocean depth (the density is $\rho = 1/d_y d_x$). Numbers in legend are q_s averaged over θ for a typical ocean-wave directional spectrum $\cos^{2s}\theta$ with $s = 4$ [11]. Inset: q vs. wavelength at $\theta = 0$, where shaded regions is one standard deviation from mean value (blue line) for 100 random structures. Right: $\langle q \rangle$ for over isotropic incidence. Results compared to limit in Eq. (5.17). 123

5-6 Upper: Dependence of $q(0^\circ)$ on parameters in absence of reflecting boundaries. In the left plot, we take $\sigma_s/\sigma_a = 5$. In the right plot, we show the optimal $\rho d\sigma_s$ and q_{max} for different values of σ_s/σ_a and μ. Lower: Effect of a change in the index contrast and scattering cross section on the bandwidth-averaged factor q_s for the same array in Fig. 5-5. We tune the index n_1 along a strip surrounding the array, with n_0 being the index of the array's ambient medium. We suppose that the WEC has new scattering cross section $\tilde{\sigma}_s$, but keep the same absorption cross section. Left: q_s at normal incidence. Right: q_s averaged over θ with a directional spectrum of $\cos^{2s}\theta$ and s = 4. 125

5-7 Left: $\langle q_s \rangle$ with a directional spectrum of $\cos^{2s}\theta$ and s = 4 for different values of C_{b1} and C_{b2} corresponding to the front and back membranes respectively. Each point is obtained after optimizing over the membranes' thicknesses. Right: Frequency-averaged interaction factor q_s vs incident angle θ for the previously studied array using additional membranes with parameters $(C_{b1}, C_{b2}) = (0.048, 2)$ and $w_1 = w_2 = 1.6h$. 128

6-1 We study the stability of a single Bloch-periodic lasing mode under *aperiodic* perturbations. The stability eigenproblem can be solved using Bloch theorem by writing perturbations as a general Bloch wave. The lasing mode is stable when real parts of the eigenvalues $\sigma(q)$ are negative for all wavevectors q. 134

6-2 The cold cavity is 1D photonic crystal with uniform conductivity loss $\sigma_c = 0.001\omega_a$. The two-level gain medium is characterized by $\omega_a a/2\pi c = 0.31$ and $\gamma_\perp a/2\pi c = 0.008$. The frequency (dots) and pump (dashed lines) at the lasing threshold are computed for modes of the first band. The minimum pump at threshold is obtained at the band edge $ka = \pi$. In absence of gain, the decay rate for the band-edge mode is equal to $\kappa \approx 5.8 \times 10^{-5}(2\pi c/a)$. 142

6-3 Detailed stability map for $\gamma_{\|}a/2\pi c = 10^{-4}$ as a function of q. We compare results to FDTD simulations using a finite supercell with periodic boundary conditions (unstable in shaded regions), initialized with the SALT solution plus $\sim 1\%$ noise and checking stability after $\sim 10^5$ optical periods. Stars show the allowed q due to the finite supercell ($2\pi\ell/aN_{\text{cells}}$). (b) Modal intensity of lasing modes with FDTD ($N_{\text{cells}} = 50$) and multimode SALT (assuming second lasing mode at $q = 4\pi/50a$). 143

6-4 (a) Detailed stability map for $\gamma_{\|}a/2\pi c = 10^{-4}$ as a function of q. We compare results to FDTD simulations using a finite supercell with periodic boundary conditions (unstable in shaded regions), initialized with the SALT solution plus $\sim 1\%$ noise and checking stability after $\sim 10^5$ optical periods. Stars show the allowed q due to the finite supercell ($2\pi\ell/aN_{\text{cells}}$). (b) Modal intensity of lasing modes with FDTD ($N_{\text{cells}} = 50$) and multimode SALT (assuming second lasing mode at $q = 4\pi/50a$). 144

6-5 Inset shows a 2d array of cylindrical rods with diameter $= 0.7a$, $\epsilon_c = 2.58$, $\sigma_c = 0.001\omega_a$ and a separation $L = 1.078a$ to a perfect mirror. Gain inside the rods is characterized by $\omega_a a/2\pi c = 0.625$ and $\gamma_\perp a/2\pi c = 0.01$. Three BiCs are shown at $ka = 0, 0.4\pi, 0.8\pi$. The minimum pump at threshold D_t is obtained at $ka = 0.4\pi$ which is the first lasing mode. In absence of gain, the decay rate for this mode is equal to $\kappa \approx 8 \times 10^{-5}(2\pi c/a)$. Top inset shows a positive band curvature at threshold. 145

6-6 Result from stability eigenproblem. Shaded region indicates instability. Inset shows FDTD results using a supercell with 20 unit cells and periodic boundary conditions. Plots show the Fourier transform of the electric field at a point near a rod. Small insets show the eigenvectors obtained from (6.4) along with their frequencies $\omega a/2\pi c$. They do match modes obtained in the linear regime (below threshold) at $ka = 0.8\pi$ and $ka = \pi$. . 146

6-7 $\text{Re}(\sigma)$ as a function of q and D_0/D_t for different transition frequencies $\omega_a a/2\pi c$ $(= 0.625, 0.675)$. The threshold lasing frequency $\omega_t a/2\pi c$ is maintained at ≈ 0.65. The system is unstable near threshold when the laser detuning $(\omega_t - \omega_a)$ has opposite sign to the band curvature. Black solid line corresponds to $\text{Re}\,(\sigma) = 0$. 147

6-8 Same 1d structure in Sec. 6.5. Numerical simulation (stars and dashed contour lines) are in agreement with analytical results (solid lines). Since the lasing mode is at a bandedge, we have $\sigma_{10} = 0$. Black line corresponds to $\delta ka = \alpha_c d$ and represents the line of eigenvalue crossing (transition from two real to two complex conjugate eigenvalues). $\alpha_c \approx 0.018$ and $\alpha_s^2 \approx -4.2 \times 10^{-4}$. 148

6-9 Same 1d structure in Sec. 6.5 but with $\omega_a a/2\pi c = 0.306$ and $\gamma_\perp/2\pi c = 0.08$. The lasing mode is still at the band edge but the laser detuning $(\omega_t - \omega_a)$ is now positive. 149

6-10 Same 1d structure studied in Sec. 6.5 but with $\omega_a a/2\pi c = 0.306$ and $\gamma_\perp/2\pi c = 0.08$. Numerical simulation (stars and dashed contour lines) are in agreement with analytical results (solid lines). Black line corresponds to $\delta ka = \alpha_c d$ and represents the line of eigenvalue crossing (transition from two real to two complex conjugate eigenvalues). Magenta solid line corresponds to $\delta k = \alpha_s d$ from analytical perturbation results and matches $\mathrm{Re}\,(\sigma) = 0$ from numerical simulation. $\alpha_c \approx 0.022$ and $\alpha_s \approx 3 \times 10^{-3}$. . . . 149

6-11 Same 2d structure in Sec. 6.6 with $\omega_a a/2\pi c = 0.625$ and $\omega_t a/2\pi c \approx 0.65$. Left: $q_0 = 0$. Right: $q_0 = -2k$. Contour lines (dashed) are from numerical simulation. Black solid line corresponds to $\delta k = \alpha_c d$ from analytical perturbation results and represents the line of eigenvalue crossing (transition of $\sigma - \sigma_{10}\delta k$ from two real to two complex conjugate eigenvalues) when expanding around $q_0 = 0$. The analytical line matches results of numerical simulation. Expansion around $-2k$ does not show a critical line in agreement with perturbation theory (case $ka \neq \pi/2$). We have $\alpha_c \approx 0.05$, $\alpha_s^2 \approx -0.018$ and $\sigma_{10} \approx 0.59i$ when expanding around $q_0 = 0$ (opposite sign for $i\sigma_{10}$ when expanding around $q_0 = -2k$). 150

6-12 Same 2d structure in Sec. 6.6 with $\omega_a a/2\pi c = 0.675$. Left: $q_0 = 0$. Right: $q_0 = -2k$. The lasing mode is slightly shifted to $ka/2\pi \approx 0.1944$ but still with $\omega_t a/2\pi c \approx 0.65$. Contour lines (dashed) are from numerical simulation. Black solid line corresponds to $\delta k = \alpha_c d$ and magenta solid line corresponds to $\delta k = \alpha_s d$ from analytical perturbation results when expanding around $q_0 = 0$. Majenta line (analytical) matches $\mathrm{Re}\,(\sigma) = 0$ from numerical simulation. Expansion around $-2k$ does not show a critical line in agreement with perturbation theory (case $ka \neq \pi/2$). We have $\alpha_c \approx 0.21$, $\alpha_s \approx 0.088$ and $\sigma_{10} \approx 0.59i$ when expanding around $q_0 = 0$ (opposite sign for $i\sigma_{10}$ when expanding around $q_0 = -2k$). 151

Chapter 1

Introduction

1.1 Generalities

Resonances are everywhere. They appear in a vast number of natural phenomena and engineering problems. They are associated with a universal behaviour for any system that tends to "oscillate" at a given rate and for a given amount of time. These two properties give a universal description of the corresponding "resonance" in terms of a resonant frequency (oscillation rate) and a decay rate. Consider for example a simple playground swing (basically a pendulum) that is being pushed at a periodic rate. It should be obvious that in order to achieve a maximum swinging amplitude, you need to wait for the swing to a finish a full cycle before pushing it again, otherwise, if you do it too soon or too late, you will face resistance. The maximal response is then obtained when the "driving" frequency matches the "natural" frequency at which the system oscillates when left on its own. This is the resonant effect. If you neglect any friction in your swing, then every time you push the system, the oscillation amplitudes simply add up and you can obtain an infinite response. In practice, losses give the system its finite (but still enhanced) response.

While the swing system is a simple example, resonances have in fact a more general mathematical definition for an arbitrary operator and are an object of study in operator theory [12, 13]. The quantity that oscillates can be anything, which makes the resonant behaviour a universal phenomenon occurring in many areas of physics. First examples are usually encountered when studying a simple electrical resonator circuit (the oscillating quantity being the electric charge) or a mass-spring mechanical resonator (the oscillating quantity being the mass displacement). It is in general noted in undergraduate classes that these systems obey exactly the same mathematical equations, and particular emphasis is given to the equivalence between certain physical parameters describing the two systems. This equivalence in fact extends to many more systems which exhibit the same behaviour and can be practically described by similar equations. While the exact derivation of how to obtain the simplified resonant equations from a more complete ("microscopic") physical description may depend on the specific physics in play, it may not matter much since effective parameters can be directly extracted from the system's general response. Figure 1-1 shows multiple examples from modern physics with manifestations of the resonant effect. Regardless of the physics involved, all these systems exhibit the well-known Lorentzian-shaped resonant spectrum, with a maximum response at the resonant frequency, and a finite width associated with a loss factor.

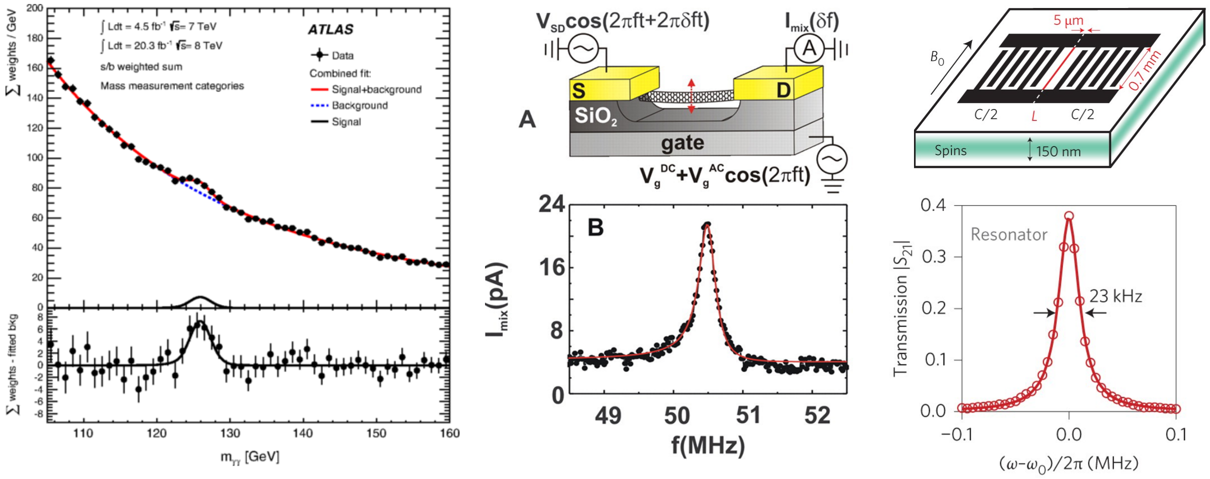

Figure 1-1: Examples of a single resonance behaviour in many areas of physics. They all show the universal Lorentzian response $\propto 1/\left[(\omega-\Omega)^2+\Gamma^2\right]$. Left: Measurement of the Higgs boson mass based on the ATLAS experiment involving high-energy particles collisions at the CERN Large Hadron Collider [1]. Middle: Mechanical resonator using a single-walled carbon nanotube [2]. Right: Microwave resonator used to achieve highly sensitive electron spin resonance (ESR) spectroscopy [3].

This universal response is actually a simple manifestation of the presence of a *single* resonance in the system. But this is only the tip of the iceberg, as resonances (yes, when you have many of them) can have a lot of other manifestations in different settings and configurations. In this work, we will explore resonances "from one to infinity", as demonstrated in several problems in physics and engineering.

While resonances appear in any wave scattering system, we will be mainly concerned with applications to modern electromagnetics and photonics (even though we also study an ocean wave energy problem in Chapter 5). In particular, there has been a recent increased interest in designing novel systems, in order to improve the electromagnetic response, which is greatly motivated by both recent micro- and nano-fabrication techniques allowing for a wider range of geometries to be fabricated, as well as modern computational techniques with the ability to analyze and numerically simulate increasingly complex systems. We will study four different problems, where the number of resonances involved progressively increases from one to infinity. The problems are relatively independent, but there are interesting interconnections that we highlight at multiple points. This means that the different chapters can, in principle, be read independently. Each chapter starts with a section "On resonances" that gives a high-level overview of the problem under consideration and the way in which resonances are involved. These sections can be read successively, without having to read the full chapter. As such, they can be seen as a storyline describing the flow of our work. In the next section, we give a brief overview of the different problems explored in this work. Most of the results have been published in journals as enumerated in the "Related publications" above.

1.2 Overview

◇ Loss in resonance: Bounding surfaced-enhanced Raman scattering (Chapter 2)

The large response of a system at resonance makes it particularly useful to enhance signals. However, the maximum response is fundamentally limited by absorption losses which are inherent to the materials used. In recent works, analytical bounds, based on optimization under energy-conservation constraints, were reported for various linear problems and quantify the fundamental limitations imposed by materials losses [5]. Here, we extend earlier bounds to a nonlinear process: Raman scattering.

Surface-enhanced Raman scattering (SERS) is a common method developed to overcome the low efficiency of conventional Raman spectroscopy. In SERS, the chemicals of interest are placed in the vicinity of a scatterer, typically a textured surface or collection of nanoparticles, which acts as an antenna that both concentrates the incoming pump field at the Raman material's location and enhances the radiated Stokes signal emitted by the Raman material, thereby increasing the collected signal.

Optimized structures with various shapes have been studied, but no study thus far has looked at the possibility of an upper limit to the enhancement achievable in SERS. In our work [14], we find fundamental upper bounds on the Raman enhancement for arbitrary-shaped scatterers, depending only on its material constants and the separation distance from the molecule. Our method is based on decomposing the process into two linear problems (concentration of the incident field on the molecule and a dipole emission at the Raman-shifted frequency) and then bounding each term separately. According to our metric, silver is optimal in visible wavelengths while aluminum is better in the near-UV region. Our general analytical bound scales as the volume of the scatterer and the inverse sixth power of the distance to the active molecule. Tighter bounds can be computed by simple numerical integration. We also compare the bounds to the actual performance of simple structures (spheres and bowties). Numerical computations show that such geometries fall short of the bounds, suggesting further design opportunities for future improvement. While the bounds can be reached in the quasistatic limit, both the bounds and the actual performance increase with the scatterer's volume and further shape optimization is required to get closer to the limits for large scatterers.

Motivated by the results from the bounds and in collaboration with others, we perform freeform shape optimization ("topology optimization", TO) of the total Raman enhancement and obtain surprising structures $\sim 60\times$ better than optimized coupled-sphere or bowtie [15]. Such results are a proof-of-concept of Raman TO in 2d systems, and the significant enhancements suggest promising results for future improvements in practical 3d Raman sensing.

◇ Few resonances: Quasi-normal mode theory for filter design (Chapters 3 and 4)

High-order (multi-resonance) filters are ubiquitous components in many wave physics systems. Typical design methods are based on independently tuning multiple distinct components, as in circuit theory where we can identify separate elements. Such standard methods are restricted to a specific wavelength regime (quasi-static for circuits [16]) or to systems with weakly coupled components (as in coupled mode theory [17]). Here we provide the missing universal methodology that is based on the final resonances of the global system.

It is known that the complex resonances of an open system are associated with the poles of its S-matrix, which describes the scattering response. A complete description of S requires the knowledge of additional coupling coefficients, which we do using a theory that is consistent with the physical constraints of energy conservation and reciprocity [18]. We then use this formulation to show that high-order filters with full transmission require couplings with specific unitary ratios [19]. While it is known that "peaks" of the scattering response correspond to resonant frequencies, we further show that its "zeros" are determined by the relative signs of the couplings. This gives direct criteria to design high-order filters with specific placement of transmission peaks and zeros.

As an example of application, we consider the problem of designing metasurface filters. Microwave frequency selective surfaces (FSS) are two-dimensional periodic metal-dielectric arrays exhibiting specific frequency-dependent transmission or reflection under planewave excitation [20]. Such FSSs are usually used to implement spatial (wave) filters for communication antennas, radars, radomes, lenses etc. An important design challenge in frequency-selective metasurfaces is the ability to obtain specific high-order filter responses using their strongly inter-coupled subwavelength resonances, attempted usually through multilayer FSSs. When the filter-design optimization problem is formulated directly in terms of matching a desired transmission spectrum, it can face severe numerical challenges such as poor local optima (due to the highly oscillatory transmission spectrum) and stringent constraints for stop- and pass-band transmission (leading to "stiff" optimization problems with slow convergence). It would be then advantageous to use the analytically-defined "optimal" (or ideal standard) filters already known in signal-processing theory, and characterized by various rational transfer functions with specified poles and zeros [16]. Our method, described earlier, gives a nice framework to design such standard filters using the resonant modes of the global system. We successfully apply our procedure to computationally design microwave metasurface filters precisely matching standard filters of various orders, bandwidths and types, especially optimal elliptic filters, which were demonstrated mostly approximately in the past.

◇ Many resonances: From solar cells to ocean buoys (Chapter 5)

In certain problems where a wide frequency bandwidth is considered, a large number of resonances is typically involved. This for example the case of light trapping in solar cells, where the use of surface texturing increases the efficiency of thin-film cells through total internal reflection. In this work, we are actually motivated by a different problem involving similar physics: arrays of buoys designed to extract energy from ocean waves [8]. In this case, wave energy converters (WEC) (or buoys) are designed to extract energy from ocean waves through a mechanical oscillating movement. When placing the buoys near each other in an array, the total energy extracted from the array may exceed the energy extracted from individual buoys due to multiple scattering effects. Previous numerical-optimization works showed promising results through the design of buoy positions [8, 21]. While most previous work focused on numerical optimization, the question we are trying to answer in this work is more general and concerns any array of scattering "metaparticles":

given the absorbing and scattering properties of an individual metaparticle, is there a limit on the total enhancement and how can it be reached?

One of the most influential theoretical results for solar-cell design has been the ray-optical Yablonovitch limit [22,23], which provides a bound to how much surface texturing can enhance the performance of an absorbing film averaged over a broad bandwidth and angular range. However, the Yablonovitch limit cannot be applied to all metaparticle arrays since it requires an effective-medium approximation, which is only accurate for either dilute weakly interacting dipolar particles or for strongly interacting particles with sufficiently subwavelength separation. Other known limits bound the absorption at every wavelength [24], but they tend to be loose when considering large bandwidths since coherent effects average out [25]. Here, we show that general limits, including the well-known Yablonovitch result in solar cells, arise from reciprocity conditions. The use of reciprocity for arrays of particles described by the radiative-transfer equation (RTE) leads us to a corrected diffusion model from which we derive our main result: an analytical prediction of optimal array absorption that closely matches exact simulations for both random and optimized arrays under angle and frequency averaging. This result also enables us to propose and quantify approaches to increase performance through careful particle design and/or using external reflectors. We show, in particular, that the use of membranes (which act as as external reflectors leading to total internal reflection, as in solar cells!) on the water's surface allows substantial enhancement.

◇ Infinity of resonances: The periodic laser problem (Chapter 6)

Since the first introduction of the distributed-feedback (DFB) laser, the use of the "distributed feedback" mechanism in periodic structures enabled novel lasers with enhanced functionality and improved performance. Applications range from the well-known photonic-crystal surface-emitting lasers (PCSELs) to more recent lasing action in plasmonic arrays or based on bound-in-continuum (BiC) states. While such lasers have attracted considerable attention due to their ability to maintain a stable single-mode over a large surface area, instabilities have been observed in large enough finite periodic lasers. Here, we address a fundamental question for periodic lasers: does stable single-mode lasing exist in an infinite periodic structure, or does it inherently require the boundaries of a finite structure to stabilize?

At first glance, it may seem that stability is unlikely: any resonance in a periodic system is in fact part of a *continuum* of resonances at different Bloch wavevectors with arbitrarily close lasing thresholds, and this seems to violate typical assumptions for stable lasing. However, we show that single-mode lasing is possible even in infinite periodic structures for range of powers above threshold, by applying a Bloch adaptation of linear-stability analysis to the full nonlinear Maxwell–Bloch equations [26]. Using perturbation theory, we also obtain a simple condition for stability near threshold of low-loss resonances: the sign of the laser detuning from the gain frequency should match the sign of the band curvature at threshold. Our result is particularly relevant to multiple recent studies of novel lasers.

THIS PAGE INTENTIONALLY LEFT BLANK

Chapter 2

Loss in resonance: Bounding surfaced-enhanced Raman scattering[1]

2.1 On resonances

Resonances are intuitively characterized by a substantial increase of the output in a given system, making it particularly useful for "enhancement" effects in many applications. This can be seen in the most simple, yet very useful, second-order linear differential system below, modelling for example the response $x(t)$ of a damped oscillator due to an external excitation $f(t)$:

$$\frac{d^2x}{dt^2} + 2\Gamma\frac{dx}{dt} + \Omega^2 x = f, \tag{2.1}$$

where Ω represents the natural frequency of the system and Γ represents a loss factor (damping). For a harmonic excitation $f = Fe^{-i\omega t}$, the response of the system is given by the transfer function:

$$H(\omega) = \frac{x}{f} = \frac{1}{-\omega^2 + \Omega^2 - 2i\omega\Gamma} = \frac{1}{2\Omega_0}\left[-\frac{1}{\omega - (\Omega_0 - i\Gamma)} + \frac{1}{\omega - (-\Omega_0 - i\Gamma)}\right], \tag{2.2}$$

where $\Omega_0^2 = \Omega^2 - \Gamma^2$. Note that $H(\omega)$ has poles at $\omega_0 = \Omega_0 - i\Gamma$ and $-\omega_0^*$. These correspond to the *complex* resonances of this system and will be discussed in more details in Chapter 3.

For a small enough loss factor Γ, $H(\omega)$ has a resonant behaviour and reaches a maxi-

---

[1] Our work on this topic was published in Ref. 14 and Ref. 15 and presented in Ref. 27.

mum amplitude at $\omega_m = \sqrt{\Omega^2 - 2\Gamma^2}$ where we have:

$$|H(\omega_m)|^2 = \frac{1}{4\Gamma^2\Omega_0^2}, \tag{2.3}$$

The maximal response of the system can then be made arbitrary large for arbitrary small loss factor Γ, highlighting the enhancement effect we mentioned earlier.

While this system is deceptively simple, it still captures the universal behaviour of resonant effects. It is not only that Eq. (2.1) describes simple systems in different physical settings (e.g. mechanical oscillator, RLC circuit...), but the results are, at least qualitatively, general for arbitrary operators. We can in fact substitute the simple second-order differential operator in Eq. (2.1) with an arbitrary operator and make a similar analysis. In this case, ω_0 represents the pole of the "inverse" of the new operator[2] and its value can usually be directly obtained by solving an adequate eigenproblem. This is expected to be true only locally (around the resonant frequency) as long as no other poles are present nearby in the complex ω-plane. In such case, Eq. (2.1) can be a good approximation describing the behaviour of the system. In a general scenario with multiple resonances, a higher-dimensional operator should rather be used in order to obtain an adequate simplified model including all the relevant poles of the system. This problem will be discussed in more details in Chapter 3.

In this chapter, we are concerned with the limitations imposed by losses on enhancement in electromagnetic and photonic systems. Such systems are described by Maxwell's equations which can be written in the operator form:

$$\frac{d\psi}{dt} = \Theta\psi + \phi, \;\; \psi = \begin{pmatrix} \mathbf{E} \\ \mathbf{H} \end{pmatrix}, \; \Theta = \begin{pmatrix} 0 & \frac{1}{\epsilon}\nabla\times \\ -\frac{1}{\mu}\nabla\times & 0 \end{pmatrix}, \; \phi = \begin{pmatrix} -\mathbf{j}/\epsilon \\ 0 \end{pmatrix}, \tag{2.4}$$

along with the conditions $\nabla \cdot \epsilon\mathbf{E} = 0$ and $\nabla \cdot \mu\mathbf{H} = 0$ for $\epsilon = \epsilon_0\epsilon_r$ and $\mu = \mu_0\mu_r$, where $\mathbf{E}$ (resp. $\mathbf{H}$) is the electric (resp. magnetic) field, $\mathbf{j}$ is the current density, ϵ_0 (resp. μ_0) is the dielectric constant (resp. magnetic permeability) of free space, and ϵ_r (resp. μ_r) is the dielectric constant (resp. permeability) of the medium. The speed of light c in free space is then given by $c^2 = 1/\epsilon_0\mu_0$. For nonmagnetic materials, which are mostly considered here, we have $\mu_r = 1$.

This equation describes the electromagnetic field response to external excitation (e.g., a dipole source or incident planewave). A very large number of applications are concerned

---

[2] Technically, it is a pole of a response function of the system, such as the Green's function or the scattering matrix. In operator theory, for a linear operator A, it is defined as the pole of the resolvent $R(\lambda) = (A - \lambda I)^{-1}$.

with designing structures or cavities, namely finding an appropriate $\epsilon(r)$ (by choosing the optimal geometry and materials) in order to optimize a given output (e.g. scattering, absorption or extinction cross section, or local density of states, see Appendix-A). Resonances are associated with self-sustained solutions of the problem ($\phi = 0$), therefore they correspond to complex eigenvalues of the operator ($-i\omega\psi = \Theta\psi$) with outgoing boundary conditions. In electromagnetic problems, $\Gamma = -\mathrm{Im}(\omega) = \Gamma_{\mathrm{r}} + \Gamma_{\mathrm{nr}}$ can be decomposed into a radiative part Γ_{r} (losses due to radiation outside the scattering structure) and non-radiative part Γ_{nr} (losses due to absorption inside the material). While we can easily design systems with small Γ_{r} [28], the total Γ and thus the maximal enhancement [e.g., Eq. (2.3)] is fundamentally limited by absorption losses.

Absorption losses are directly related to the imaginary part of materials' susceptibility χ ($= \epsilon - 1$). Previous work derived fundamental bounds on quantities of interest in scattering and emission problems (e.g. cross section or local density of states) for arbitrary shapes, given only the materials [5,29,30]. These bounds depend on a material figure given by $|\chi|^2/\mathrm{Im}\chi$, thus *quantifying* the limits imposed by absorption in the material (i.e., $\mathrm{Im}\chi$). In this chapter, we derive upper limits to surface-enhanced Raman scattering (SERS) [described in the next section] for arbitrary periodic and aperiodic shapes, extending these earlier bounds on linear light emission to a nonlinear process (Fig. 2-1). We also show that existing designs such as bowtie antennas are typically far from the theoretical optimum.

Earlier work indeed showed that the efficiency of a single light emitter scales as $|\chi|^2/\mathrm{Im}\chi$ for a material with susceptibility χ [5], but we find that the Raman bounds scale as the *cube* of this [Eq. (2.31)] because they result from nonlinear composition of a light *concentration* bound (in which an incident planewave is concentrated on the Raman molecule) and a light *emission* bound similar to the previous local densoty of states (LDOS) bounds. The concentration part of our bound [$\sim |\chi|^4/\left(\mathrm{Im}\chi\right)^2$] may also be applicable to many other problems involving light focusing [31, 32]. For periodic surfaces, one can gain an additional enhancement to concentration from the contribution of other periods, but we show that there is a trade-off and that the largest benefits (for a single Raman molecule) seem to arise from optimizing individual scatterers. We obtain both analytical formulas within general design regions as well as semi-analytical bounds involving numerical integration for more specific spatial configurations, and we compare typical structures to these bounds. For structures constrained to lie within a subwavelength spherical volume, we show that spherical particles are nearly optimal in the quasistatic regime. For structures that are allowed to extend into larger volumes, we find that simple geometries such as bowtie antennas [33–35] are far from our upper limits, suggesting exciting opportunities for improvement in future designs. In particular, using topology optimization based inverse design, we obtain surprising structures maximizing the Raman enhancement. These optimization results shed light to what extent our bounds are achievable.

2.2 Surface-enhanced Raman scattering

Surface-enhanced Raman scattering (SERS) [36–42] was developed to overcome the low efficiency of conventional Raman spectroscopy, as the very small Raman cross-section of most chemicals results in Raman radiation typically on the order of 0.001% of the power of the pump signal [36]. In SERS, the chemicals of interest are placed in the vicinity of a scatterer, typically a surface or collection of nanoparticles, which acts as an antenna that both concentrates the incoming pump field at the Raman material's location and enhances the radiated Stokes signal emitted by the Raman material [43, 44], thereby increasing the collected signal. Charge-transfer mechanisms also lead to a chemical enhancement, although their contribution is smaller than the electromagnetic enhancement effect [45, 46]. Many different materials and antenna geometries have been used for SERS measurements: metals such as silver, gold, or copper, and dielectrics such as silicon carbide or indium tin oxide, were implemented in various shapes such as spheres, triangular prisms, or disks. Several studies have optimized SERS substrates over one or two parameters [47–51]. Others have used topology optimization yet only to optimize the concentration of the incident field [52, 53]. Efficiencies up to 12 orders of magnitude larger than that of traditional Raman spectroscopy have been demonstrated, allowing for detection levels down to the single molecule [39, 40] and opening up applications in the fields of biochemistry, forensics, food safety, threat detection, and medical diagnostics.

However, to the best of our knowledge, no study thus far has looked at the possibility of an upper limit to the enhancement achievable in SERS, and it is therefore not known whether current SERS substrates possess much room for improvement. To investigate the existence of such a bound, a key point is to notice that the process can be decomposed into two linear problems [54]: concentration of the incident field on the molecule and a dipole emission at the Raman-shifted frequency, as is described in more details below. Upper bounds on the power radiated by a dipole near a scatterer of arbitrary shape were already obtained in Ref. 5. Given only the material susceptibility χ, this is an upper limit for the LDOS for any possible geometric shape in a given region of space near the emitter. The bounding method is based on optimizing the quantity of interest under energy-conservation constraints, using the fact that extinction (linear in the induced fields) is larger than absorption (quadratic in the induced fields). This method has been successfully applied to various other problems [29, 30]. Here, we apply this method to obtain a bound on local field concentration enhancement, again for any possible shape given only the material and the bounding volume. Combined with the LDOS limit, we then obtain a bound on the Raman enhancement. We also obtain a *second* bound for the concentration problem using reciprocity in the case of a periodic structure (we use a similar approach in Chapter 5 to relate the Yablonovitch limit for solar cells to the LDOS enhancement). By comparing the two concentration bounds as a function of the period, we obtain a tighter bound for periodic structures.

2.3 Derivation of bounds

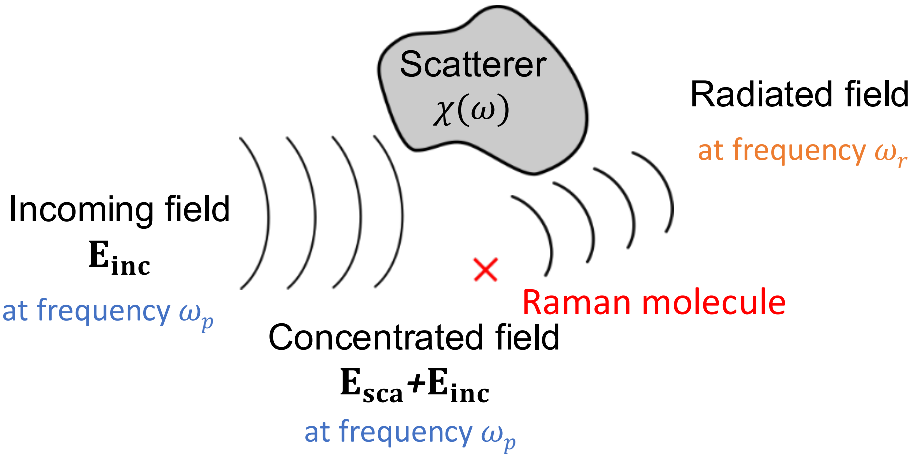

Figure 2-1: Schematics of the SERS configuration under study. The pump field is incident onto a scatterer, near which lies the Raman-active chemical. Upon interaction with the pump field, thus material behaves as a dipole emitting a Raman-shifted field. The Raman field interacts with the scatterer and is emitted to the far-field.

In order to derive a bound on the Raman enhancement, we consider the configuration represented in Fig. 2-1. An incident "pump" planewave $\mathbf{E_{inc}}$ is scattered by the nanostructure, leading to a near-field enhancement. A Raman-active molecule close to the structure then acquires a dipole moment proportional to the enhanced field, $\mathbf{p} = \alpha_{\mathrm{R}}\mathbf{E}$ where α_{R} is the Hermitian (usually real-symmetric) Raman polarizability tensor [54]. The power radiated by the dipole in the far field at the Raman frequency is our quantity of interest and is given by $P = |\alpha_{\mathrm{R}}\mathbf{E}|^2 P_{\mathbf{p}}$ where $P_{\mathbf{p}}$ is the power radiated by a unit-vector dipole $\hat{\mathbf{p}} = \alpha_{\mathrm{R}}\mathbf{E}/|\alpha_{\mathrm{R}}\mathbf{E}|$. $P_{\mathbf{p}}$ can be related to the (electric) LDOS through $\rho_{\mathbf{p}} = \frac{2\epsilon_0 n_b^2}{\pi\omega^2} P_{\mathbf{p}}$ where n_b

is the index of the background medium [55, 56]. We note that typically LDOS is defined as the sum of $\rho_{\mathbf{p}}$ over three orthogonal directions, so that in our notation, the background LDOS is equal to $\rho_b = n_b^3\omega^2/6\pi^2c^3$ (see Appendix A). The Raman enhancement (compared to the background) is then equal to:

$$q = \frac{|\alpha_{\mathrm{R}}\mathbf{E}|^2\rho_{\mathbf{p}}}{\|\alpha_{\mathrm{R}}\|^2|\mathbf{E_{inc}}|^2\rho_b}\,, \tag{2.5}$$

where $\|.\|$ is the induced norm (which gives an upper bound on the magnitude of $\hat{\mathbf{p}}$ for any $\mathbf{E}$ orientation [57]). We see that the enhancement comes from two parts: LDOS enhancement ($q_{\mathrm{rad}} = \rho_{\mathbf{p}}/\rho_b$) and local field enhancement ($q_{\mathrm{loc}} = |\alpha_{\mathrm{R}}\mathbf{E}|^2/\|\alpha_{\mathrm{R}}\|^2|\mathbf{E_{inc}}|^2$). To bound the total efficiency, we need to bound both contributions.

2.3.1 LDOS enhancement

A bound on LDOS enhancement due to scattering by lossy structures can be obtained starting from a result of Ref. 5: the maximum LDOS enhancement near a scatterer with susceptibility χ, in a background with Green's function $\mathbf{G}$, is given by:

$$q_{\mathrm{rad}} = \frac{\rho_{\mathbf{p}}}{\rho_b} \leq 1 + \frac{3\pi n_b^2}{2k^3}\frac{|\chi|^2}{\mathrm{Im}\chi}\int_V |\mathbf{G}\hat{\mathbf{p}}|^2\,, \tag{2.6}$$

where the integration is carried over the volume of the scatterer and k the wavenumber in the background medium. Since the direction of $\mathbf{p} = \alpha_{\mathrm{R}}\mathbf{E}$ is also to be optimized, we can then obtain a bound using:

$$\int_V |\mathbf{G}\hat{\mathbf{p}}|^2 = \frac{(\alpha_{\mathrm{R}}\mathbf{E})^\dagger}{|\alpha_{\mathrm{R}}\mathbf{E}|}\left(\int_V \mathbf{G}^\dagger\mathbf{G}\right)\frac{\alpha_{\mathrm{R}}\mathbf{E}}{|\alpha_{\mathrm{R}}\mathbf{E}|} \leq |||\mathbf{G}\mathbf{U}_{\mathrm{R}}|||^2 := \left\|\int_V \mathbf{U}_{\mathrm{R}}{}^\dagger\mathbf{G}^\dagger\mathbf{G}\mathbf{U}_{\mathrm{R}}\right\|, \tag{2.7}$$

where the columns of $\mathbf{U}_{\mathrm{R}}$ – a $3 \times \mathrm{rank}(\alpha_{\mathrm{R}})$ matrix – are the orthonormal principle axes of α_{R} with non-zero Raman polarizability. If α_{R} is invertible we simply obtain $|||\mathbf{G}|||^2$. On the other hand, if the Raman polarization is along a fixed axis $\hat{\mathbf{p}}$ we obtain $|||\mathbf{G}\hat{\mathbf{p}}|||^2$. Details for the computation of the induced norm are given in subsection 2.3.3.

2.3.2 Local field enhancement

We now obtain a bound on local field concentration by using the same method as in Ref. 5 while working with a suitable figure of merit. This bound applies to scatterers of *any* shape and scales with the volume of the scatterer. (The focusing of thin parabolic mirrors and lenses provides an example of concentration scaling with volume.) For periodic structures, since there is finite power incident on each unit cell (and a periodic set of foci), we obtain a second bound that scales as the unit-cell area.

Single-point focusing (volume-scaling bound)

Let $\mathbf{x_0}$ be the position of the Raman-active molecule and $\mathbf{E_{sca}}$ be the scattered field. For Eq. (2.5), we want to bound $|\alpha_\mathrm{R}\mathbf{E}(\mathbf{x_0})|^2$ where $\mathbf{E} = \mathbf{E_{sca}} + \mathbf{E_{inc}}$ is the total field. Recall that the scattered field is given by $\mathbf{E_{sca}}(\mathbf{x_0}) = \int_V \mathbf{G}(\mathbf{x_0}, \mathbf{x})\mathbf{P}$ where $\mathbf{P} = \chi\mathbf{E}$ is the polarization current (Appendix-A, Ref. 58). As explained in Ref. 5, the fields are subject to:

$$\mathrm{Im}\int_V \mathbf{E}^\dagger\mathbf{P} \leq \mathrm{Im}\int_V \mathbf{E}^\dagger_{\mathbf{inc}}\mathbf{P}\,, \tag{2.8}$$

which simply states that absorption is smaller than extinction. For a given unit vector $\hat{\mathbf{e}}$, maximizing $|\hat{\mathbf{e}}^\dagger\alpha_\mathrm{R}\mathbf{E_{sca}}(\mathbf{x_0})|^2$ under the constraint (2.8) is equivalent to:

$$\max_{\mathbf{P}}\, \langle\mathbf{P}, \mathbf{A}\mathbf{P}\rangle \;\text{ subject to } \langle\mathbf{P}, \mathbf{P}\rangle \leq \alpha\mathrm{Re}\langle\mathbf{b}, \mathbf{P}\rangle\,, \tag{2.9}$$

where $\alpha = |\chi|^2/\mathrm{Im}\chi$, $\mathbf{A}\mathbf{P} = \langle\mathbf{a}, \mathbf{P}\rangle\mathbf{a}$, $\mathbf{a} = \mathbf{G}^*\alpha_\mathrm{R}\hat{\mathbf{e}}$, $\mathbf{b} = i\mathbf{E_{inc}}$ and $\langle\mathbf{X}, \mathbf{Y}\rangle = \int_V \mathbf{X}^\dagger\mathbf{Y}$. The optimum of Eq. (2.8) must satisfy the KKT conditions [59, 60]:

$$\mathbf{A}\mathbf{P} + \lambda(\mathbf{P} - \frac{\alpha}{2}\mathbf{b}) = 0\,,\;\; \langle\mathbf{P}, \mathbf{P}\rangle - \alpha\mathrm{Re}\langle\mathbf{b}, \mathbf{P}\rangle = 0\,, \tag{2.10}$$

where $\lambda = -\frac{\langle\mathbf{a},\mathbf{P}\rangle}{\beta}$. The first equation can be written as $\mathbf{P} = \frac{\alpha}{2}\mathbf{b} - \frac{1}{\lambda}\langle\mathbf{a}, \mathbf{P}\rangle\mathbf{a} = \frac{\alpha}{2}\mathbf{b} + \frac{\beta}{2}\mathbf{a}$. The second equation then leads to $|\beta||\mathbf{a}| = \alpha|\mathbf{b}|$. Since $\lambda \in \mathbb{R}$, then $\frac{\langle\mathbf{a},\mathbf{b}\rangle}{\beta} \in \mathbb{R}$. From this we have $\beta = \pm\alpha\frac{|\mathbf{b}|\langle\mathbf{a},\mathbf{b}\rangle}{|\mathbf{a}||\langle\mathbf{a},\mathbf{b}\rangle|}$. We finally conclude that the optimal value of $\langle\mathbf{P}, \mathbf{A}\mathbf{P}\rangle$ is equal to:

$$\frac{\alpha^2}{4}\left(|\langle\mathbf{a}, \mathbf{b}\rangle| + |\mathbf{a}||\mathbf{b}|\right)^2 \leq \alpha^2|\mathbf{a}|^2|\mathbf{b}|^2\,. \tag{2.11}$$

If we plug in the physical quantities, we get:

$$|\hat{\mathbf{e}}^\dagger\alpha_\mathrm{R}\mathbf{E_{sca}}(\mathbf{x_0})|^2 \leq \left(\frac{|\chi|^2}{\mathrm{Im}\chi}\right)^2 \int_V |\mathbf{E_{inc}}|^2 \int_V |\mathbf{G}^*\alpha_\mathrm{R}\hat{\mathbf{e}}|^2\,. \tag{2.12}$$

A bound on the norm of $\alpha_\mathrm{R}\mathbf{E_{sca}}$ is then obtained similarly to the LDOS result in subsection 2.3.1 using $|||.|||$. A simpler bound can be obtained using a spectral decomposition $\alpha_\mathrm{R} = \mathbf{U}_\mathrm{R}\mathbf{d}_\mathrm{R}\mathbf{U}_\mathrm{R}{}^\dagger$ where $\mathbf{d}_\mathrm{R}$ is a $\mathrm{rank}(\alpha_\mathrm{R}) \times \mathrm{rank}(\alpha_\mathrm{R})$ diagonal matrix with entries equal to the nonzero eigenvalues of α_R. In particular, for $\hat{\mathbf{e}}$ in the column space of α_R, we have:

$$\int_V |\mathbf{G}^* \alpha_\mathrm{R} \hat{\mathbf{e}}|^2 \leq |||\mathbf{G}^* \alpha_\mathrm{R} \mathbf{U}_\mathrm{R}|||^2 = |||\mathbf{G}^* \mathbf{U}_\mathrm{R} \mathbf{d}_\mathrm{R}|||^2 \leq |||\mathbf{G}^* \mathbf{U}_\mathrm{R}|||^2 \|\mathbf{d}_\mathrm{R}\|^2 = |||\mathbf{G}\mathbf{U}_\mathrm{R}^*|||^2 \|\alpha_\mathrm{R}\|^2 \,. \tag{2.13}$$

We then conclude by the triangle inequality [57]:

$$q_\mathrm{loc} \leq \left(1 + \frac{|\chi|^2}{\mathrm{Im}\chi} |||\mathbf{G}\mathbf{U}_\mathrm{R}^*||| \sqrt{V}\right)^2 \,. \tag{2.14}$$

For large enhancement ($q_\mathrm{loc} \gg 1$), the bound is simply given by the second term squared and the material's figure of merit for the concentration bound is the *square* of the usual factor $|\chi|^2/\mathrm{Im}\chi$ from previous works [5]. Essentially, this arises because concentration involves coupling to two electromagnetic waves: the incoming planewave and the dipole field. The usual material's metric thus comes into play two times. This also explains the presence of the volume of the scatterer (from the coupling with the planewave) and of the integral of the Green's function (from the coupling with the dipole). Identical scalings are also found in the exact results for a quasistatic plasmonic sphere as we show later in subsection 2.4.1.

Periodic-array focusing (area-scaling bound)

In practice, wafer-scale microfabrication techniques favor the manufacturing of repeating patterns over large areas rather than single, isolated structures. Moreover, periodic structures may offer increased SERS performances thanks to interference effects. While the previous bound is still valid for periodic structures by using the *periodic* Green's function, we can also use reciprocity to relate the local field enhancement to LDOS enhancement and obtain a bound that scales as the surface area of the unit cell. For this, we study a 2d-periodic structure with unit-cell surface area S and $(\mathbf{b_1}, \mathbf{b_2})$ the reciprocal lattice vectors orthogonal to $\hat{\mathbf{z}}$ [61]. We consider the scattering (resp. emission) problem with $\mathbf{E^s_{inc}} = e^{i\mathbf{k}\cdot\mathbf{x}}\mathbf{E_{inc}}$ (resp. $\mathbf{j} = -i\omega\delta_{\mathbf{x_0}}\hat{\mathbf{e}}$, with $-\mathbf{k}_\parallel$ Bloch boundary-conditions, where the subscript $\parallel$ refers to the component perpendicular to $\hat{\mathbf{z}}$). We can write the outgoing fields in the far field as:

$$\mathbf{E^{e,s}_{out}} = \sum_{n,m} T^{e,s}_\mathrm{nm} e^{i\mathbf{x}\cdot\mathbf{k}^\mathrm{e,s}_\mathrm{nm}} \hat{\mathbf{e}}^\mathrm{e,s}_\mathrm{nm}, \quad \mathbf{H^{e,s}_{out}} = -\sum_{n,m} T^{e,s}_\mathrm{nm} e^{i\mathbf{x}\cdot\mathbf{k}^\mathrm{e,s}_\mathrm{nm}} \frac{\mathbf{k}^\mathrm{e,s}_\mathrm{nm} \times \hat{\mathbf{e}}^\mathrm{e,s}_\mathrm{nm}}{\omega\mu_0} \,, \tag{2.15}$$

where $|\mathbf{k}^{\mathrm{e,s}}_{\mathrm{nm}}| = k$, $\mathbf{k}^{\mathrm{s,e}}_{\parallel} = \pm(\mathbf{k}_{\parallel} + n\mathbf{b_1} + m\mathbf{b_2})$ and $\hat{\mathbf{e}}^{\mathrm{e,s}}_{\mathrm{nm}} \cdot \mathbf{k}^{\mathrm{e,s}}_{\mathrm{nm}} = 0$. We take $k_z \geq 0$ (with $k_{\mathrm{nm},z} \geq 0$ for $z > 0$ and $k_{\mathrm{nm},z} \leq 0$ for $z < 0$).

From reciprocity [62], we have:

$$\int_S (\mathbf{E}^{\mathrm{s}} \times \mathbf{H}^{\mathrm{s}} - \mathbf{E}^{\mathrm{e}} \times \mathbf{H}^{\mathrm{s}}) \cdot \hat{\mathbf{n}} dS = i\omega\, \hat{\mathbf{e}} \cdot \mathbf{E}^{\mathrm{s}}(\mathbf{x_0})\,, \tag{2.16}$$

where $\mathbf{E}^{\mathrm{s}}$ and $\mathbf{E}^{\mathrm{e}}$ are the total fields ($\mathbf{E}^{\mathrm{s}} = \mathbf{E}^{\mathbf{s}}_{\mathbf{out}} + \mathbf{E}^{\mathbf{e}}_{\mathbf{inc}}$ and $\mathbf{E}^{\mathrm{e}} = \mathbf{E}^{\mathbf{e}}_{\mathbf{out}}$).

The integration around the lateral boundary is cancelled due to boundary conditions. We only need to compute the surface integral in the far-field. For $|z|$ large enough, we integrate over the cross section S_z:

$$\begin{aligned}
\omega\mu_0 \int_{S_z} \mathbf{E}^{\mathbf{e}}_{\mathbf{out}} \times \mathbf{H}^{\mathbf{s}}_{\mathbf{out}} \cdot \hat{\mathbf{s}} dS &= -\sum_{n,m,k,l} \int_{S_z} T^{e}_{n,m} T^{s}_{k,l} e^{i\mathbf{x}\cdot(\mathbf{k}^{\mathbf{e}}_{\mathrm{nm}} + \mathbf{k}^{\mathbf{s}}_{\mathrm{kl}})}\, \hat{\mathbf{e}}^{\mathbf{e}}_{\mathrm{nm}} \times (\mathbf{k}^{\mathbf{s}}_{\mathrm{kl}} \times \hat{\mathbf{e}}^{\mathbf{s}}_{\mathrm{kl}}) \cdot \hat{\mathbf{z}}\, dS \\
&= S \sum_{nm} T^{e}_{n,m} T^{s}_{n,m} e^{-2ik_{\mathrm{nm},z} z} \left[(\hat{\mathbf{e}}^{\mathbf{e}}_{\mathrm{nm}} \cdot \hat{\mathbf{e}}^{\mathbf{s}}_{\mathrm{nm}}) \mathbf{k}^{\mathbf{s}}_{\mathrm{nm}} - (\hat{\mathbf{e}}^{\mathbf{e}}_{\mathrm{nm}} \cdot \mathbf{k}^{\mathbf{s}}_{\mathrm{nm}}) \hat{\mathbf{e}}^{\mathbf{s}}_{\mathrm{nm}}\right] \cdot \hat{\mathbf{z}} \\
&= S \sum_{nm} T^{e}_{n,m} T^{s}_{n,m} k_{\mathrm{nm},z} e^{-2ik_{\mathrm{nm},z} z} \left[(\hat{\mathbf{e}}^{\mathbf{e}}_{\mathrm{nm}} \cdot \hat{\mathbf{e}}^{\mathbf{s}}_{\mathrm{nm}}) - 2(\hat{\mathbf{e}}^{\mathbf{s}}_{\mathrm{nm}} \cdot \hat{\mathbf{z}})(\hat{\mathbf{e}}^{\mathbf{e}}_{\mathrm{nm}} \cdot \hat{\mathbf{z}})\right] \\
&= \omega\mu_0 \int_{S_z} \mathbf{E}^{\mathbf{e}}_{\mathbf{out}} \times \mathbf{H}^{\mathbf{e}}_{\mathbf{out}} \cdot \hat{\mathbf{s}}\, dS\,.
\end{aligned} \tag{2.17}$$

The last equality comes from the symmetry of the equation with respect to e/s, and the second to last comes from $\mathbf{k}^{\mathbf{s}}_{\mathrm{nm}} = k_{\mathrm{nm},z}\hat{\mathbf{z}} - (\mathbf{k}^{\mathbf{e}}_{\mathrm{nm}} - k_{\mathrm{nm},z}\hat{\mathbf{z}})$.

For $z < 0$, we also have:

$$\omega\mu_0 \int_{S_z} \mathbf{E}^{\mathbf{e}}_{\mathbf{out}} \times \mathbf{H}^{\mathbf{s}}_{\mathbf{inc}} \cdot \hat{\mathbf{z}}\, dS = S T^{e}_{00} [k_z \hat{\mathbf{e}}^{\mathbf{e}}_{00} \cdot \mathbf{E}_{\mathbf{inc}} - \cancel{(\hat{\mathbf{e}}^{\mathbf{e}}_{00} \cdot \mathbf{k})} (\mathbf{E}_{\mathbf{inc}} \cdot \hat{\mathbf{z}})] = S T^{e}_{00} k_z \hat{\mathbf{e}}^{\mathbf{e}}_{00} \mathbf{E}_{\mathbf{inc}}\,. \tag{2.18}$$

Similarly, we find $\int_{S_z} \mathbf{E}^{\mathbf{s}}_{\mathbf{inc}} \times \mathbf{H}^{\mathbf{e}}_{\mathbf{out}} \cdot \hat{\mathbf{z}} = -\int_{S_z} \mathbf{E}^{\mathbf{e}}_{\mathbf{out}} \times \mathbf{H}^{\mathbf{s}}_{\mathbf{inc}} \cdot \hat{\mathbf{z}}$. On the other hand,

$$\int_{S_{-z}} \mathbf{E}^{\mathbf{s}}_{\mathbf{inc}} \times \mathbf{H}^{\mathbf{e}}_{\mathbf{out}} \cdot \hat{\mathbf{z}} = \int_{S_{-z}} \mathbf{E}^{\mathbf{e}}_{\mathbf{out}} \times \mathbf{H}^{\mathbf{s}}_{\mathbf{inc}} \cdot \hat{\mathbf{z}} = S T^{e}_{00} k_z \hat{\mathbf{e}}^{\mathbf{e}}_{\mathbf{00}} \cdot [\mathbf{E}_{\mathbf{inc}} - 2(\mathbf{E}_{\mathbf{inc}} \cdot \hat{\mathbf{z}})\hat{\mathbf{z}}] e^{2ik_z z}\,. \tag{2.19}$$

By replacing all integrals in Eq. (2.16), we conclude:

$$\hat{\mathbf{e}} \cdot \mathbf{E}^{\mathrm{s}}(\mathbf{x_0}) = \frac{2iS\epsilon}{k} \mathbf{T}^{\mathbf{e}}_{00} \cdot \mathbf{E}_{\mathbf{inc}} \cos\theta \tag{2.20}$$

where we noted $\mathbf{T}^{\mathbf{e}}_{00} = T^{e}_{00} \hat{\mathbf{e}}^{\mathbf{e}}_{00}$ and θ the incidence angle with respect to $\hat{\mathbf{z}}$. This equation simply relates the field's component $\hat{\mathbf{e}} \cdot \mathbf{E}^{\mathrm{s}}(\mathbf{x_0})$ due to an incident plane wave $e^{i\mathbf{k}\cdot\mathbf{x}}\mathbf{E}_{\mathbf{inc}}$ to the far-field component along $-\mathbf{k}$ of the field created by a unit vector dipole $\hat{\mathbf{e}}$ placed at

$\mathbf{x_0}$ (where the problem in the unit-cell is $-\mathbf{k}_\parallel$ Bloch-periodic).

Using this relation, we can now bound the amplitude of $\alpha_\mathrm{R}\mathbf{E}$ using:

$$\frac{|\hat{\mathbf{e}}^\dagger \alpha_\mathrm{R} \mathbf{E}(\mathbf{x_0})|^2}{\|\alpha_\mathrm{R}\|^2 |\mathbf{E_{inc}}|^2} \leq \frac{4S^2\epsilon^2\cos^2\theta}{k^2}|\mathbf{T}^{\mathbf{p}}_{00}|^2 \leq \frac{4S^2\epsilon^2\cos\theta}{k^2}\sum_{nm}|\mathbf{T}^{\mathbf{p}}_{\mathrm{nm}}|^2\frac{k_{nm,z}}{\omega\mu_0}\frac{\omega\mu_0}{k}$$
$$= \frac{4S\epsilon^2\cos\theta}{k^2}\frac{\omega\mu_0}{k}\,\mathrm{Re}\int_{S_{+\infty}}\mathbf{E}^{\mathbf{p}}\times\mathbf{H}^{\mathbf{p}*}\cdot\hat{\mathbf{z}}\,dS \leq 8S\epsilon^2\cos\theta\frac{\omega\mu_0}{k^3}P_{\mathbf{p}}\,, \qquad (2.21)$$

where we recall that $P_{\mathbf{p}}$ is the total power radiated by the dipole $\hat{\mathbf{p}}$. The first inequality is based on Cauchy-Schwartz [57] while the second one states that the power emitted along $-\mathbf{k}$ ($\propto |\mathbf{T}^{\mathbf{p}}_{00}|^2$) is smaller than the total power emitted in the $+\hat{\mathbf{z}}$ direction, which is then smaller than the total radiated power $P_{\mathbf{p}}$. The inequalities used in Eq. (2.21) will be tight (equalities) if ω is smaller than the first-order diffraction frequency (so that all the power is in $\mathbf{T}^{\mathbf{p}}_{00}$ [61]) and in the absence of radiated field in the opposite direction (the structure should completely "block" the unit-cell's surface). Now using the previous LDOS bound [Eqs. (2.6–2.7)], we conclude:

$$q_\mathrm{loc} \leq \frac{2Sk^2\cos\theta}{3\pi}\left[\frac{\rho^{\mathrm{per}}_{b,\mathbf{p}}}{\rho_b} + \frac{3\pi n_b^2}{2k^3}\frac{|\chi|^2}{\mathrm{Im}\chi}|||\mathbf{G^{per}}\mathbf{U}^*_\mathrm{R}|||^2\right]\,, \qquad (2.22)$$

where $\rho^{\mathrm{per}}_{b,\mathbf{p}}$ is the polarized periodic LDOS related to the power radiated by a dipole $\mathbf{p}$ and $\mathbf{G^{per}}$ is the free-space *Bloch-periodic* Green's function. If only one diffraction channel is supported (for example, when the period a is smaller than $\lambda/2$), we have:

$$\rho^{\mathrm{per}}_{b,\mathbf{p}} = \frac{\rho^{\mathrm{per}}_b}{2}\left(1 - \frac{|\hat{\mathbf{p}}^\dagger\hat{\mathbf{k}}_+|^2 + |\hat{\mathbf{p}}^\dagger\hat{\mathbf{k}}_-|^2}{2}\right) \leq \frac{\rho^{\mathrm{per}}_b}{2} = \frac{n_b}{2\pi c S\cos\theta} \qquad (2.23)$$

where ρ^{per}_b is the total periodic LDOS (sum of $\rho^{\mathrm{per}}_{b,\mathbf{p}}$ over three orthogonal directions) and $\mathbf{k}_\pm = -\mathbf{k_0}_\parallel \pm k_{0z}\hat{\mathbf{z}}$ (directions of far-field emission). In this case, Eq. (2.22) becomes:

$$q_\mathrm{loc} \leq 2 + \frac{Sn_b^2\cos\theta}{k}\frac{|\chi|^2}{\mathrm{Im}\chi}|||\mathbf{G^{per}}\mathbf{U}^*_\mathrm{R}|||^2\,. \qquad (2.24)$$

The constant factor of 2 simply reflects the enhancement in the case of a perfect back-reflector and in absence of any resonant structure.

2.3.3 Induced norm of the integral of the Green's function

Before combining the previous results to obtain final Raman bounds, we show how to compute the induced norm of the integral of the Green's function. Recall that [58] (with

k_0 being the free-space wavenumber):

$$\mathbf{G} = \frac{k_0^2 e^{ikr}}{4\pi r}\left[\left(1+\frac{i}{kr}-\frac{1}{(kr)^2}\right)\mathbf{1}+\left(-1-\frac{3i}{kr}+\frac{3}{(kr)^2}\right)\hat{\mathbf{r}}\hat{\mathbf{r}}^+\right], \tag{2.25}$$

so that:

$$\mathbf{G}^\dagger\mathbf{G} = \frac{k_0^4}{16\pi^2 r^2}\left[\left(1-\frac{1}{(kr)^2}+\frac{1}{(kr)^4}\right)\mathbf{1}+\left(-1+\frac{5}{(kr)^2}+\frac{3}{(kr)^4}\right)\hat{\mathbf{r}}\hat{\mathbf{r}}^\dagger\right] = a(r)\mathbf{1}+b(r)\hat{\mathbf{r}}\hat{\mathbf{r}}^\dagger. \tag{2.26}$$

If the structure has two mirror symmetry planes orthogonal to $\hat{\mathbf{x}}$, $\hat{\mathbf{y}}$ or $\hat{\mathbf{z}}$, the non-diagonal terms of $\int_V \mathbf{G}^\dagger\mathbf{G}$ are zero, and we obtain:

$$|||\mathbf{G}|||^2 = \|\int_V \mathbf{G}^\dagger\mathbf{G}\| = \int_V a(r) + \max_j \int_V b(r)\frac{x_j^2}{r^2}. \tag{2.27}$$

We can obtain finite analytical expression by integrating over simple geometries and only considering the near-field terms ($\propto 1/r^6$). For spherical shell of polar angle θ separated from the Raman molecule by a small distance d, we have:

$$\int_V \frac{dV}{r^6} = \frac{2\pi(1-\cos\theta)}{3d^3},\ \int_V \frac{dV}{r^6}\frac{z^2}{r^2} = \frac{2\pi(1-\cos^3\theta)}{9d^3},\ \int_V \frac{dV}{r^6}\frac{x^2}{r^2} = \frac{\pi(8-9\cos\theta+\cos 3\theta)}{36d^3}. \tag{2.28}$$

So $|||\mathbf{G}|||^2 n_b^4$ is equal to:

$$\frac{1}{24\pi d^3}\left(2-\cos\theta-\cos^3\theta\right)\left[0\le\theta\le\frac{\pi}{2}\right],\quad \frac{1}{192\pi d^3}(16-17\cos\theta+\cos 3\theta)\left[\frac{\pi}{2}\le\theta\le\pi\right]. \tag{2.29}$$

For a half-plane, we have:

$$\int_V \frac{dV}{r^6} = \frac{\pi}{6d^3},\ \int_V \frac{dV}{r^6}\frac{z^2}{r^2} = \frac{\pi}{9d^3},\ \int_V \frac{dV}{r^6}\frac{x^2}{r^2} = \frac{\pi}{36d^3}, \tag{2.30}$$

so that $|||\mathbf{G}|||^2 n_b^4 = 1/32\pi d^3$.

2.3.4 Raman enhancement

The bound for the Raman enhancement $q = q_{\text{loc}}(\omega_P)q_{\text{rad}}(\omega_R)$ is now simply obtained by multiplying the previous bounds [Eqs. (2.6–2.7) and Eq. (2.14)]:

$$\begin{aligned} q &\leq \left(1 + \frac{|\chi_p|^2}{\mathrm{Im}\chi_p} |||\mathbf{G}_p \mathbf{U}_{\mathrm{R}}^*||| \sqrt{V}\right)^2 \left(1 + \frac{3\pi n_b^2}{2k_r^3} \frac{|\chi_r|^2}{\mathrm{Im}\chi_r} |||\mathbf{G}_r \mathbf{U}_{\mathrm{R}}|||^2\right) \\ &\approx \frac{3\pi n_b^2}{2k_r^3} \frac{|\chi_r|^2}{\mathrm{Im}\chi_r} \left(\frac{|\chi_p|^2}{\mathrm{Im}\chi_p}\right)^2 V |||\mathbf{G}_r \mathbf{U}_{\mathrm{R}}|||^2 |||\mathbf{G}_p \mathbf{U}_{\mathrm{R}}^*|||^2 , \end{aligned} \tag{2.31}$$

where the subscripts p and r denote the pump and Raman frequencies at which the variables are evaluated. The second line is obtained in the case of large enhancement.

If we now assume that the tensor α_{R} is isotropic and consider simple structures enclosing the scatterer and separated from the Raman-active molecule by a *small* distance d, we obtain analytical bounds by considering the lowest order term in d and neglecting far-field terms:

$$q \lesssim \frac{3\pi}{2n_b^6} \beta^2 \frac{V}{k_r^3 d^6} \frac{|\chi_r|^2}{\mathrm{Im}\chi_r} \left(\frac{|\chi_p|^2}{\mathrm{Im}\chi_p}\right)^2 , \tag{2.32}$$

where β is a geometrical factor equal to $1/6\pi$ for a full sphere, $1/12\pi$ for a half-sphere, and $1/32\pi$ for a half-plane (see subsection 2.3.3). This fundamental limit scales as V/d^6 (compared to $1/d^3$ for LDOS). $1/d^6$ is related to both the radiation of the dipole and the coupling to it, while V is due to the planewave coupling. In practice, the Raman frequency shift is small enough so that the bounds do not change much when the expressions are simply evaluated at the same (pump or Raman) frequency. In this case, the bound is simply proportional to $\left(|\chi|^2/\mathrm{Im}\chi\right)^3$. This material figure of merit can be used to compare the optimal performance of different materials and is shown in Fig. 2-2. We note that silver (Ag) has the highest bound at visible wavelengths but is outperformed by aluminum (Al) in the near-UV region.

The bound of Eq. (2.31) is also valid for a periodic structure after substituting the appropriate periodic Green's function, which can be integrated numerically, for the concentration enhancement term (Raman molecules emit incoherently, so the radiation enhancement is not periodic). Near-field coupling from adjacent unit cells causes the periodic Green's function to increase as the period shrinks so that the maximal bound is obtained for the smallest possible period. However, comparison with the area-scaling bound obtained using Eq. (2.24) shows that this bound isn't tight for small periods. For strong scattering and emission, this area-scaling bound is given by:

$$q \lesssim \frac{3\pi S \cos\theta}{2k_p k_r^3} \frac{|\chi_p|^2}{\mathrm{Im}\chi_p} \frac{|\chi_r|^2}{\mathrm{Im}\chi_r} \left|\left|\left|\mathbf{G}_p^{\mathbf{per}} \mathbf{U}_{\mathrm{R}}^*\right|\right|\right|^2 |||\mathbf{G}_r \mathbf{U}_{\mathrm{R}}|||^2 . \tag{2.33}$$

By neglecting the Raman frequency shift, this new bound is now proportional to

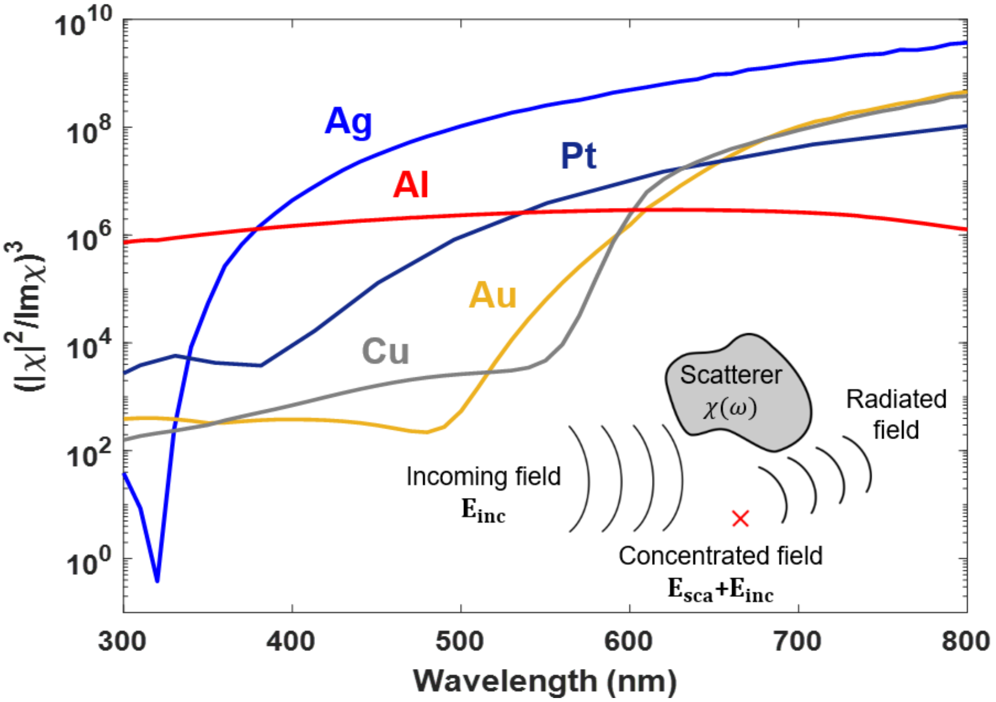

Figure 2-2: Comparison of the metric $(|\chi|^2/\mathrm{Im}\chi)^3$ for conventional metals used in SERS [4].

$(|\chi|^2/\mathrm{Im}\chi)^2$ and scales as the surface area of the unit cell instead of the volume of the scatterer. We can actually see that this area-scaling limit is the same as the volume-scaling one [Eq. (2.31)] when using an effective volume equal to:

$$V_{\text{eff}} = \frac{S\cos\theta}{k_p n_b^2}\frac{\mathrm{Im}\chi_p}{|\chi_p|^2}\,. \tag{2.34}$$

This area-scaling bound highlights the fact that for a periodic structure, only a fraction of the actual volume of the scatterer (proportional to the projected unit-cell area) is effectively "used" in the scattering. As explained in more detail below, combining the volume-scaling and area-scaling bounds leads to a tighter bound with different behavior as a function of the period.

2.3.5 Bound for a randomly oriented Raman molecule

We can also obtain a bound assuming a randomly oriented Raman molecule. We use $\langle.\rangle$ to denote the average over the random orientation of the molecule. We can then obtain a bound using:

$$
\begin{aligned}
\langle q\rangle &\leq \left(1+\frac{3\pi n_b^2}{2k_r^3}\frac{|\chi_r|^2}{\mathrm{Im}\chi_r}|||\mathbf{G}_r|||^2\right)\langle q_{loc}\rangle = \left(1+\frac{3\pi n_b^2}{2k_r^3}\frac{|\chi_r|^2}{\mathrm{Im}\chi_r}|||\mathbf{G}_r|||^2\right)\frac{\mathrm{tr}(\alpha_R^\dagger\alpha_R)|\mathbf{E}|^2/3}{\|\alpha_R\|^2|\mathbf{E_{inc}}|^2}\\
&\leq \frac{\mathrm{tr}(\alpha_R^\dagger\alpha_R)}{3\|\alpha_R\|^2}\left(1+\frac{3\pi n_b^2}{2k_r^3}\frac{|\chi_r|^2}{\mathrm{Im}\chi_r}|||\mathbf{G}_r|||^2\right)\left(1+\frac{|\chi_p|^2}{\mathrm{Im}\chi_p}|||\mathbf{G}_p|||\sqrt{V}\right)^2
\end{aligned}
\tag{2.35}
$$

2.4 Geometric results

2.4.1 Concentration enhancement for a plasmonic sphere

We start by computing the concentration enhancement for a plasmonic sphere in the quasistatic limit and comparing it to our bound. In this regime, a plane wave with amplitude $\mathbf{E_{inc}}$ incident upon a sphere excites a dipole moment $\mathbf{p} = \alpha V \mathbf{E_{inc}}$, where the polarizability α is given by:

$$
\alpha = \frac{3(\epsilon-1)}{\epsilon+2} = \frac{1}{1/3+\chi^{-1}}\,. \tag{2.36}
$$

On resonance $\mathrm{Re}\chi^{-1} = -\frac{1}{3}$, such that $\alpha_{max} = 1/\mathrm{Im}\chi^{-1} = |\chi|^2/\mathrm{Im}\chi$. The field at a distance d from the sphere of radius R is given by:

$$
\mathbf{E_{sca}} = \frac{1}{4\pi}\left[\frac{3\hat{\mathbf{n}}(\hat{\mathbf{n}}\cdot\mathbf{p})-\mathbf{p}}{(d+R)^3}\right], \tag{2.37}
$$

where $\hat{\mathbf{n}}$ is the unit vector along the line from the dipole to the measurement point. The amplitude of the field is maximum when $\hat{\mathbf{n}}$ is along $\mathbf{p}$ giving:

$$
\mathbf{E_{sca}} = \frac{\mathbf{p}}{2\pi(d+R)^3}\,. \tag{2.38}
$$

Putting all this together, the maximum field concentration outside the sphere at the plasmon frequency is given by:

$$
|\mathbf{E_{sca}}|^2 = \frac{1}{4\pi^2}\frac{1}{(d+R)^6}\left(\frac{|\chi|^2}{\mathrm{Im}\chi}\right)^2 V^2|\mathbf{E_{inc}}|^2\,. \tag{2.39}
$$

This analytical expression includes all the same factors as our bound on the concentrated field, with $|||\mathbf{G}_r|||^2$ to be compared to the factor $V/4\pi^2(d+R)^6$.

We can easily check that the performance of the sphere reaches the bound in the limit

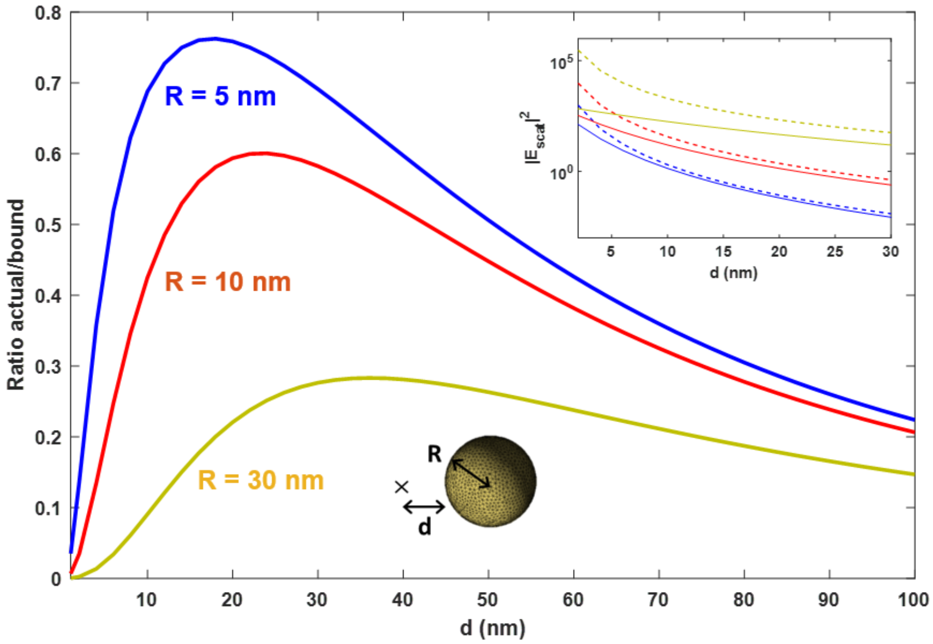

Figure 2-3: Ratio of the analytical value of of $|\mathbf{E}_{\mathbf{scat}}|^2$ given by Eq. (2.39) to the volume-scaling bound given by Eq. (2.14), for Ag spheres of different radii at the resonant frequency of Ag. Inset: Comparison of the analytical value (full lines) and the bound (dashed lines) for the same Ag spheres.

of small radius, in particular we can use:

$$\frac{1}{(d+R)^6} \leq \frac{1}{r^6} \leq \frac{1}{(d-R)^6}, \quad \frac{x^2}{r^2} \leq \frac{R^2}{(d-R)^2}, \quad \frac{y^2}{r^2} \leq \frac{R^2}{(d-R)^2}, \quad \frac{(d-R)^2}{(d+R)^2} \leq \frac{z^2}{r^2} \leq 1\,, \tag{2.40}$$

where z is the coordinate along the axis relating the sphere's center and the molecule. We then obtain:

$$\frac{1}{V}\int_V \frac{dV}{r^6} \xrightarrow[R\to 0]{} \frac{1}{d^6}, \quad \frac{1}{V}\int_V \frac{x^2 dV}{r^8} \xrightarrow[R\to 0]{} 0, \quad \frac{1}{V}\int_V \frac{y^2 dV}{r^8} \xrightarrow[R\to 0]{} 0, \quad \frac{1}{V}\int_V \frac{z^2 dV}{r^8} \xrightarrow[R\to 0]{} \frac{1}{d^6}\,. \tag{2.41}$$

We then conclude that $|||\mathbf{G}_r|||^2 \approx V/4\pi^2 d^6$ for $R \ll d$ and that the dipole-sphere performance reaches the upper bound in this limit.

2.4.2 Isolated structures - Numerical simulation

We now compare our bounds to exact numerical simulations. For this, the performance of specific structures, assuming an isotropic Raman tensor α_{R} and a background medium of air, was evaluated using SCUFF-EM, an open-source implementation of the boundary-element method [63,64]. Two simulations were performed for each structure: a scattering simulation to evaluate the field concentration at the Raman material's location, and an emission simulation to evaluate the radiative LDOS (example in Fig. 2-4). The actual performance of each structure can then be compared to its volume-specific bound by carrying the integration over the volume of the structure [in the expression of $|||\mathbf{G}_r|||^2$ in Eq. (2.31)], and to a shape-independent bound by carrying the integration over simple geometric structures encompassing the structure [Eq. (2.32)].

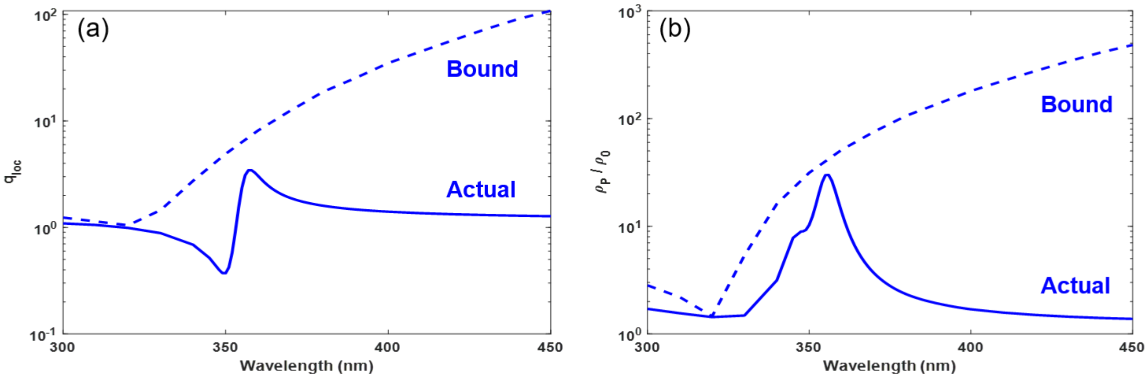

Figure 2-4: Simulation results and corresponding bounds for a Ag sphere of radius 10 nm and distance to emitter 20 nm. (a) Near-field enhancement with bound from main text. (b) LDOS with bound from [5].

We simulated two of the most common nanostructures used in SERS: triangular prisms used in a bowtie configuration, and a sphere. In subsection 2.4.1, we saw that the sphere's enhancement reaches the bound in the limit $R \ll d \ll \lambda$, so we selected here a radius of 10 nm and a distance of 20 nm. While in practice molecules are located at various distances from the scatterer, with smaller separation distances yielding a higher absolute enhancement, 20 nm corresponds to the maximum performance-to-bound ratio for the selected sphere radius (Fig. 2-3). All simulated structures were made of silver, which is the best-performing Raman material at visible frequencies (Fig. 2-2) and also satisfies the resonance condition for χ, unlike e.g. gold. The geometry of the triangles was taken from [65], with a gap set at 40 nm to readily compare with the sphere results. We included a shape-independent bound by considering the exterior of a spherical shell (entire space minus a sphere of radius d), and using the largest volume of all structures, that of the 4-triangle bowtie. The results in Fig. 2-5 show that all structures fall short of the shape-independent bound by several orders of magnitude. The performances of bowties also lie far from their shape-specific limits. Only the sphere approaches its bound, at frequencies greater than the plasma frequency of silver.

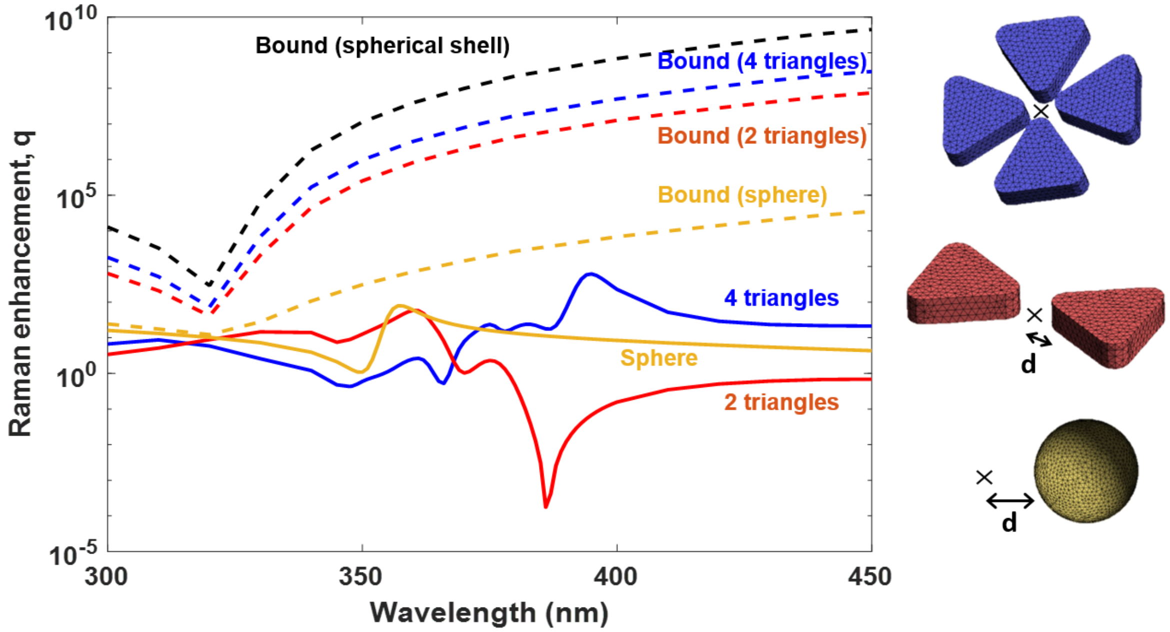

Figure 2-5: Raman enhancement bounds (dashed lines) and actual performances (full lines) for common SERS Ag structures. The distance to the emitter is $d = 20$ nm for all structures. The sphere has a radius of 10 nm. The triangles have a side of 160 nm, height of 30 nm, and tip curvature of 16 nm. The incident field's polarization is aligned with the sphere-emitter and triangle-emitter direction.

Finally, it is worth noting that smaller structures get easily closer to the bound compared to larger structures. As we saw in the example of the electrostatic sphere (subsection 2.4.1), the ratio between the actual performance and the bound goes to zero as the radius R increases for a fixed d. While both the bound and the actual performance increase with the volume, further shape optimization is required to get closer to the limits for large structures.

2.4.3 Periodic structures - Numerical simulation

To investigate the potential enhancement due to periodicity, we compared the bounds for a single sphere and for a square lattice of similar spheres. We have seen that our Raman limit can be applied to periodic structures by using either of our two bounds on the near-field enhancement: Eq. (2.14) with the corresponding periodic Green's function, or Eq. (2.24). We thus only needed to compare the near-field enhancement bounds (Fig. 2-6). The two approaches for the periodic bound yield different geometrical dependencies. The limit of Eq. (2.14) scales with the volume of the scatterer, kept constant here, and the integral of the periodic Green's function, which decreases towards the non-periodic value as the period increases. The integral of the periodic Green's function also appears in the limit of Eq. (2.24), yet alongside a factor scaling as the area of the unit cell which reduces the bound for small periods. These behaviors, expected to hold for any scatterer, are indeed observed in Fig. 2-6 for arrays of spheres. The actual limit is given by the smaller of the two bounds resulting in different regions in the graph as the period is varied. For periods larger than that of point P (given by Eq. (2.34) for large enhancement), the volume-scaling bound is limiting because of the reduced interactions between the scatterers of the array. For smaller periods, the performance of the array is limited by the area-scaling bound since the intensity received by each sphere is reduced. Between points Q and Q', this causes the periodic limit to be smaller than the single-sphere limit. Maximum enhancement due to periodicity is still to be found at the smallest possible period, where increased interactions between the scatterers dominate the decrease in incident intensity received by each unit cell.

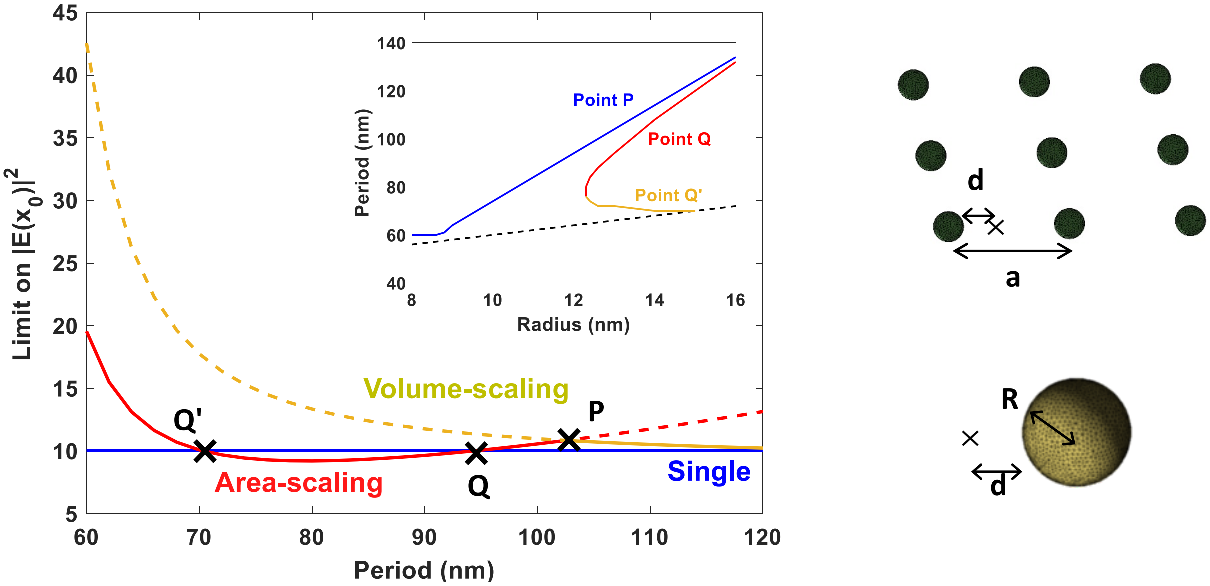

Figure 2-6: Near-field enhancement bounds for an isolated Ag sphere (bottom right schematics) and a square array of Ag spheres with varying period a (top right schematics). The region on top of the solid red and yellow lines indicates forbidden field-concentration values for the periodic case. The spheres have a radius $R = 12$ nm, and the emitter is located $d = 20$ nm away from their surface along the lattice axis. The incident field's polarization is aligned with the sphere-emitter direction and $\lambda = 350$ nm. In the large-enhancement limit, the area-scaling and volume-scaling bounds always intersect at a point, denoted P, where the period equals $\sqrt{k_p[V|\chi|^2/[\text{Im}\chi \cos\theta]}$. Inset: map of the position of points P, Q, and Q' as a function of sphere radius and lattice period, for $d = 20$ nm.

2.5 Topology optimization

2.5.1 Numerical results

Encouraged by results from bounds, we also performed freeform shape optimization ("topology optimization", TO) to maximize Raman enhancement as discussed in details in Ref. 15. The Raman scattering process is modeled as described in the previous section using two sequentially-coupled frequency-domain electromagnetic simulations. In particular, the system is first excited by an incident planewave at the pump frequency. Afterwards, the Raman molecule is modeled as a dipole source at the Raman-shifted frequency (with dipole moment given by the polarizability tensor α_R multiplied by the electric field obtained in the first simulation) which then allows to compute the total emitted power. Simulations are for two-dimensional (2d) structures with in-plane polarization [Fig. 2-7(a)].

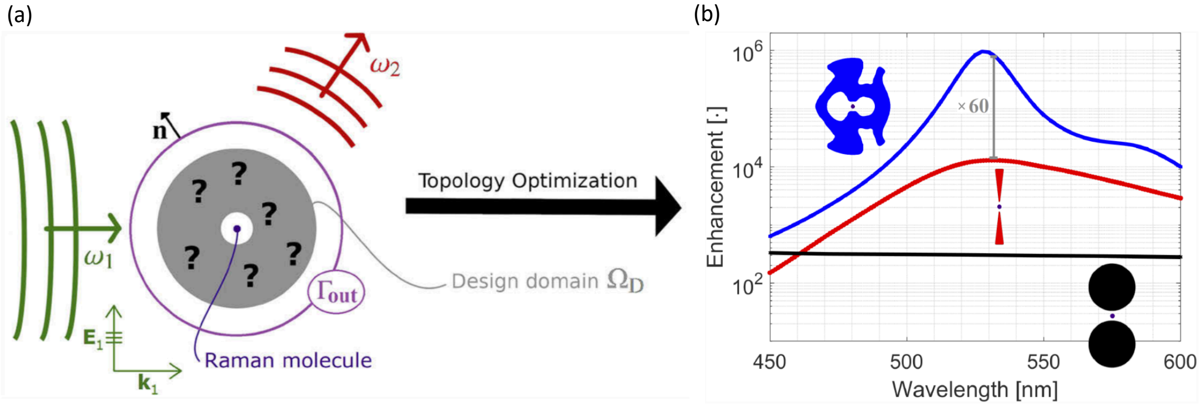

Figure 2-7: (a) A sketch of the Raman scattering design problem where a Raman molecule (blue) in air background is surrounded by the design domain Ω_D (gray) and excited by an incident planewave (green). Optimization maximizes the total emitted power (red) through Γ_{out}. Distance separating the molecule and the structure is fixed at 10 nm. The outside radius of the optimization domain Ω_D is fixed at 100 nm. Results presented here assume a zero Raman frequency shift. (b) Raman enhancement as a function of wavelength, for a molecule placed at the center of different silver nanostructures (dark blue dot) relative to a molecule placed in free space. A topology-optimized structure (blue), a bowtie antenna (red) and coupled-cylinder antenna (black) are considered, all designed to maximize enhancement at 532 nm.

The use of density-based topology optimization operates by introducing a continuous design field to control the physical material distribution, enabling the use of adjoint sensitivity analysis and gradient-based optimization algorithms to efficiently solve design problems with potentially billions of design degrees of freedom. Hence, the approach provides near-unlimited design freedom, with a computational complexity dominated by the solution of the Maxwell equations, utilizing mature finite-element techniques [15].

Solutions are presented in Fig 2-7-b, where topology optimization results are also compared to reference geometries (coupled triangles and discs). Reference structures are parameter-optimized (through the radius of the discs and through the tip-angle and the side length of the triangles) to maximize performance at the targeted wavelength (532 nm). We see that topology optimization leads to a surprising structure that fully encloses the molecule and that, in some sense, is a fusion of different features tailored to enhance either focusing or emission [15]. The TO structure has a maximum enhancement of $\approx 8 \cdot 10^5$, which is $60\times$ larger than bowtie-antenna enhancement ($\approx 1.3 \cdot 10^5$) and $2.6 \cdot 10^3\times$ larger than coupled-discs enhancement ($\approx 3 \cdot 10^2$). These extreme enhancement results, serve as a proof-of-concept suggesting promising improvements for practical 3d structures. Topology optimization has also been used to optimize focusing and radiation enhancements separately, showing the need to optimize both processes simultaneously [15].

2.5.2 Comparison with bounds

When compared to the fundamental upper bounds presented in Sec. 2.3, we find that the TO structure optimized for radiation comes to within a factor of 4 of the radiation bound. This is a reasonable difference that can be attributed to the length-scale imposed during optimization as well as simplifications leading to the bound. On the other hand, the TO structure optimized for focusing is ~ 600 smaller than the bound. This suggests that the upper limit may not be tight, in the sense that it may be difficult to achieve optimal coupling to both far-field and near-field, as is required by the focusing bound. The discrepancy may also be due to the fact that the outside radius of the domain Ω_D was kept fixed in the optimization. In fact, the focusing bound rather suggests the need of a large volume for a good coupling to the planewave. This can for example be seen in the area-scaling bound for periodic structures where we obtained a $\left(|\chi|^2/\mathrm{Im}\chi\right)^2$ dependence due to the *finite* incident power per unit cell. A similar dependence on the material metric has indeed been noticed in optimized (non-periodic) structures where the outside radius of Ω_D was fixed (Fig. 2-8-right). In general, it remains an open problem, for future theoretical and numerical investigations, to understand practical limitations related to the near-field focusing problem.

Finally, we note that the optimized structures follow the 'volume-scaling' (i.e., area-scaling for this 2d problem) predicted from the bounds (Fig. 2-8-left).

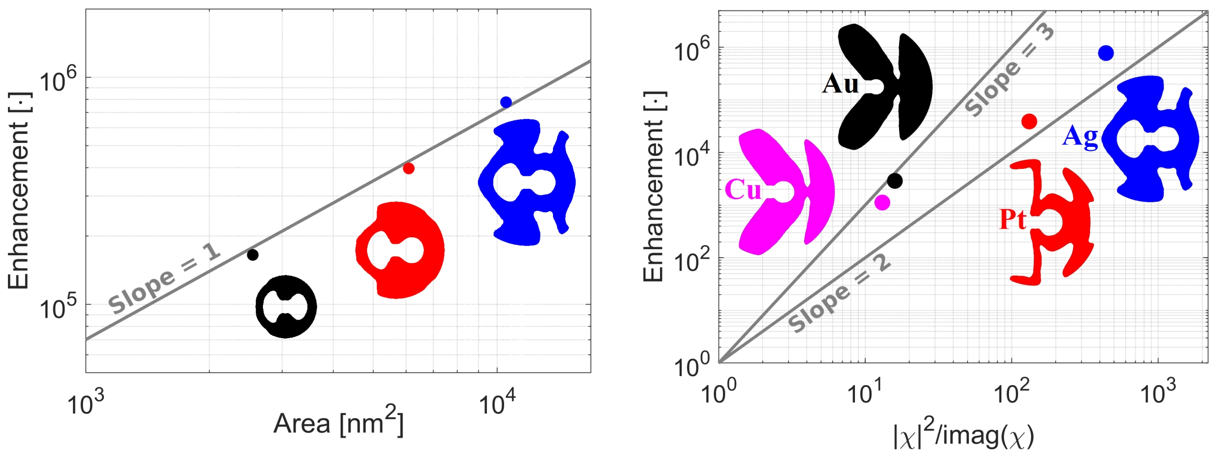

Figure 2-8: Left: Raman enhancement as a function of Ω_D area. Structures optimized for three different radii of Ω_D, equal to 50 nm, 75 nm, and 100 nm. Right: Raman enhancement as a function of $|\chi|^2/\text{Im}\chi$ for different materials.

2.6 Conclusion

The upper bounds presented in this chapter allow a simple estimate of optimal Raman enhancement for arbitrary scatterers. Such bounds include all electromagnetic effects and depend only on the material susceptibility and the separation distance from the molecule. Our analysis of periodic bounds shows the presence of different optimality regions as function of periodicity. While the use of an array can lead to a worse performance for intermediate values of the period, improvement may be still expected for very small periods. In general, the results show that there is still much room for improvement for large scatterers through further shape optimization. In particular, very promising results using topology optimization of 2d structures with substantial enhancement compared to simple structures have been obtained.

THIS PAGE INTENTIONALLY LEFT BLANK

Chapter 3

Few resonances 1: Quasi-normal mode theory (QNMT)[1]

3.1 On resonances

As briefly discussed in Sec. 2.1, resonances can give a lot of information about the behaviour of a given a system. But how are they defined in general? And what information can we extract from them?

A resonance corresponds to a sustained response of the system. It is a solution that does not, in principle, require an external excitation. Defined this way, a resonance corresponds to a solution of the eigenproblem $-i\omega\psi = \Theta\psi$ [from Eq. 2.4][2] with an *outgoing* boundary condition. Such boundary condition can be implemented either directly, for example using the Sommerfield radiation condition $r\left(\partial_r - ik\right)\psi \to 0$ for $r \to \infty$ (k is the wavenumber in surrounding medium), or using a perfectly matched layer (PML) [66, 67] that acts as an absorbing layer leading to an attenuated field, which can then be terminated by a simple boundary condition such as Dirichlet (field is zero at the outside boundary). The PML is equivalent to a complex coordinate stretching, also called spectral deformation [12].

The rigorous relation between the operator and the corresponding eigenvalues requires a spectral theory analysis [12, 13]. The spectrum of an operator corresponds to the set of *complex* numbers s for which $\Theta - s$ is not invertible. For finite dimensional operators, this can only happen if Θ has an eigenvalue [$\ker\left(\Theta - s\right) \neq \{0\}$]. For infinite dimensional

---

[1] Our work on this topic was published in Ref. 18.

[2] Note that this can also be written using only the electric field [$\nabla \times \frac{1}{\mu}\nabla \times \mathbf{E} = (\omega/c)^2\epsilon\mathbf{E}$] or magnetic field [$\nabla \times \frac{1}{\epsilon}\nabla \times \mathbf{H} = (\omega/c)^2\mu\mathbf{H}$] [61]. An appropriate scalar product should to be used.

operators, this is not always true. In such case, the spectrum can be decomposed into a discrete (the set of eigenvalues) and essential (the rest) spectrum [12]. In physics, the essential spectrum is usually called the "continuum" and matches the real axis (for Maxwell's equations) or the positive real axis (for the Schrödinger equation). One of the most important results of spectral theory is the spectral theorem, mostly known in the finite dimensional case allowing to diagonalize the operator using an appropriate basis, and generalized for bounded self-adjoint operators [68].

The resonances of open systems, as defined above, are actually *not* part of the spectrum. In fact, since the eigenvalues are complex, the corresponding "eigenvectors" describe fields that exponentially diverge outside the scatterer[3] and cannot be normalized, so they are not part of the Hilbert space. This why resonant modes in open systems are called "quasi-normal modes" (QNMs) [69]. Resonances can instead be rigorously defined using the Aguilar-Balslev-Combes-Simon theory [12]. In particular, we need to define new spectrally-deformed operators, obtained by applying a spectral deformation (aka PML) to the original operator. The essential spectrum of these new operators, originally on the real axis, is then rotated inside the complex plane, unveiling complex eigenvalues (where the corresponding eigenvectors now describe fields that *decay* outside the scatterer due to the absorbing PML layer). These eigenvalues are part of the spectrum of the deformed operators and define the resonances (or QNMs) of the original operator (for example, see Ref. 70 and Chapter 16 of Ref. 12 for more details). Of course, it is expected that these resonances do not depend on the details of the spectral deformation. Later on, and even though it is a clear abuse of notation, we will equivalently use the words "resonances", "quasi-normal modes" or "eigenfrequencies"/"eigenfields" to refer to such solutions, since all these terms are used in the literature.

While the previous discussion gives some background and definitions related to resonances, we still need to know how we can benefit from the knowledge of resonances in practice. At the most simple level, we can assume that we only have a small number of *effective* degrees of freedom, each one related to a resonance ω_n of the system and described by a scalar amplitude a_n representing the modal contribution of the corresponding eigenfield. We would then like to be able to write simple equations [as in Eq. (2.1)] to describe the evolution of the system (i.e., evolution of the coefficients a_n as well as their relation to observable physical quantities). In photonics, a very well-known such set of

---

[3] For example, in a one dimensional problem, an outgoing planewave $e^{i\omega|x|/c}$ exponentially diverges for complex $\omega = is$, as causality and passivity require ω to be in the lower complex half plane. Physically, the divergence is due to that fact that, upon excitation of the system, the energy ends up leaking far from the scatterer, so the corresponding field has an increasing-amplitude profile.

equations is based on the coupled mode theory (CMT) [17,71], or equivalently the state-space representation in diagonal canonical form in circuit theory [72]. As expected, such equations not only require the knowledge of the resonances ω_n (QNM eigenfrequencies), but are also based on other coupling coefficients that need to be estimated. In this chapter, we present a systematic procedure to compute the coupling coefficients and extract the scattering matrix of a given system based on the sole knowledge of the QNMs (eigenfrequencies and eigenfields). Our method is based on imposing physical constraints on the final scattering matrix, thus further reducing the degrees of freedom of CMT-like equations. This approach is reminiscent of Heisenberg's program, that never quite materialized, and that aimed to determine the scattering matrix for quantum field interactions by imposing general constraints on S such as unitarity, causality and analyticity [73–75]. In the next section, we give a brief overview on the scattering problem and the different QNM-based models present in the literature and summarize our novel results presented in this chapter.

3.2 Overview

Scattering phenomena in all areas of wave physics are well described by the universal S-matrix operator, which relates ingoing and outgoing modes amplitudes. As the resonant (quasi-normal) modes of a system heavily determine its scattering response and coincide with the poles of S, numerous works [6,76–79] have focused on expressing S as an expansion over QNMs, calculated via eigensolvers. In this chapter, we present the first such QNM theory (QNMT) for multiport lossless scatterers that *simultaneously* satisfies all fundamental physical constraints of reciprocity, energy conservation and time-domain realness even for the practical case of a *small truncated* QNM set (in contrast to previous formulations [6,78]) and without the need for the intricate normalization of the divergent QNMs [78,79]. Weak absorption or gain can then be easily incorporated as a perturbation. Furthermore, by explicitly separating a slowly varying effective-background response C, we provide a novel additional formula for S, approximate but very convenient to design Fano-scattering systems [80] such as even-order elliptic filters (see Chapter 4). This C is calculated without resorting to any type of fitting [17,78,81] and without having to choose a specific background scattering medium [79]: we simply use a subset of low-Q modes of the entire system. We then build useful intuition for how various low-Q-mode configurations shape the background C. We demonstrate the accuracy of our QNMT for plane-wave incidence on several electromagnetic (microwave and photonic, 2-port and 4-port) metasurfaces. In particular, we solve a nonlinear eigenproblem with a complex

Bloch wavevector to calculate S with QNMT for a fixed *angle* of incidence (instead of a fixed transverse wavevector [78]).

As explained earlier, the resonant modes of open physical systems are often called quasi-normal modes (QNM) as they are not square-integrable and exponentially diverge outside the resonator. They can allow a fast approximate solution for scattering and emission problems [69, 82–84] while providing physical understanding and good spectral accuracy around sharp resonances, in contrast to direct numerical methods using frequency/time discretization. The system S-matrix quantifies such problems and its poles coincide with the QNM eigenvalues. For lossless 1-port systems, the numerator of the scalar S is trivial, since its zeros simply coincide with the conjugates of the poles [73], while loss can be simply treated either by perturbation or by directly computing the zeros [76, 85]. In the general multiport case, based on a pole expansion of S, QNMT is usually concerned with identifying the pole residues/coefficients and any additional background. One approach computes frequency-dependent expansion coefficients from the exact field equations via volume integrals involving the QNMs and the excitation field to achieve good accuracy [79, 82]. Other QNMT formulations identify frequency-independent residues to obtain a reduced-order model, with the advantage of simplicity and easier interpretation [77, 78]. Most of these approaches require normalization of the QNMs, which, due to their far-field divergence, can be accomplished only by intricate techniques with increased computational complexity [86]. To avoid normalization, a new phenomenological approach was proposed in Ref. 6, starting from the coupled mode theory (CMT) equations [17, 71] and changing basis to the QNMs (a rather confusing approach, as the uncoupled orthonormalized modes required by CMT are ambiguous for arbitrary scatterers). However, for lossless reciprocal systems, these existing formulations do not guarantee energy conservation for a small truncated expansion, but presumably only in the infinite limit. While QNMTs with frequency-dependent expansion coefficients are expected to converge faster towards satisfying this important physical constraint, those with constant residues exhibit large errors for a practical small number of QNMs (Ref. 78 mentions that they violate energy conservation visibly even with 301 modes and we show examples where Ref. 6 violates it by 50% with few modes). In this chapter, we consider an S-matrix expansion over the QNMs and directly derive conditions for it to satisfy the necessary physical constraints. We calculate the QNM-to-ports coupling matrix D from simple surface integrals of the fields without need for QNM-normalization, and then fine-tune D to prioritize and impose these conditions. In this way, rather than being fixed from the field equations, the expansion parameters are adjusted as more modes are included in order to enforce reciprocity and energy conservation for any finite sum. The final result is a simple equation for S [Eq. (3.10)] using only the eigenfrequencies and the fine-tuned D [Eq. (3.17)] (Sec. 3.3). We confirm the improved accuracy of our QNMT using 2-port and 4-port electromagnetic metasurface examples, and with excitation of both normally and obliquely incident plane waves. For the latter, most previous approaches [78] imposed a fixed incidence transverse wavevector ($k^{\perp} = \omega \sin\theta / c$), so that the angle θ changed with frequency ω (given the constant wave speed c). Instead, QNMT can be used to compute $S(\omega)$ for fixed θ by evaluating the relevant QNMs involving eigenfrequency-dependent complex Bloch wavevectors, formulated as a generalized linear eigenproblem in Ref. 87 (Sec. 3.4).

In addition to providing a fast computational tool, QNMT (like CMT) has the advantage of offering a simple analytical model for gaining physical insight into resonant systems and for designing practical resonant devices. One interesting example is the case of Fano resonant shapes [80] emerging from the interplay between a high-Q resonance and a slowly varying background response, useful for sensors and filters. This background scattering is usually described by a separate matrix C, which previous works have almost always estimated only by fitting it *a posteriori* to the total S, either with a polynomial approximation [78] or an effective averaged structure [17, 81]. Recently, an exact volume-integral formula was alternatively derived by factoring out a choice of physical background [79] (but may require further development to handle certain boundary conditions, such as perfect electric conductors in electromagnetism). While it is understood that this background is related to the low-Q modes of the actual structure, a detailed systematic prescription to compute it directly from them and its relation to the final S are lacking. In Sec. 3.5, we extend our QNMT to non-trivial direct-scattering pathways, by showing that a slowly varying C can be calculated with our general recipe using only the system low-Q modes and by placing the high-Q modes into a different matrix $\bar{S}$, in order to then obtain a good approximation $S = \bar{S}C$ [Eq. (3.23)]. We then analyze simple low-Q pole configurations corresponding to different physical interpretations of C, such as a desired background transmission or group delay. Finally, we demonstrate this additional formulation for the electromagnetic-metasurface examples mentioned above.

3.3 Quasi-Normal Mode Theory

3.3.1 Formulation

We consider a general scattering problem of an arbitrary linear time-independent scatterer, coupled to incoming (excited) and outgoing (scattered) radiation via several physical linear ports. At the frequency ω of excitation, the scatterer has a total of P "coupling port-modes" (CPM) of radiation, which can be either single propagating modes of P different physical ports or several propagating modes of fewer ports (while all other port-modes are either evanescent, or of incompatible symmetry, or their coupling is simply too small at ω). Let CPM p propagate with wavevector $\mathbf{k}_p(\omega)$ and field $\boldsymbol{\phi}_p(\omega,\mathbf{r}) = \boldsymbol{\phi}_p^{\perp}(\omega,\mathbf{r}_p^{\perp})e^{ik_p r_p^{\parallel}}$, separable in the propagation ($r_p^{\parallel}$) and transverse ($\mathbf{r}_p^{\perp} \perp \mathbf{k}_p$) coordinates. In the most common case of reciprocal lossless physical ports, the CPMs at ω are orthogonal under the standard (conjugated) "power" inner product (a cross-sectional overlap surface integral) and can be normalized to carry unit power $\left\langle \boldsymbol{\phi}_p^{\perp} | \boldsymbol{\phi}_q^{\perp} \right\rangle = \delta_{pq}$ [71]. Then, for the P pairs of incident and scattered CPM waves, if the vectors $\mathbf{s}_+$ and $\mathbf{s}_-$ denote respectively their amplitudes at specific reference cross-sections $r_p^{\parallel} = z_p$ of their physical ports, $|s_{\pm p}|^2$ equals the power carried by the $\pm p$ wave, $\mathbf{s}_{\pm}^{\dagger}\mathbf{s}_{\pm}$ is the net incident/scattered power, and the system scattering matrix S at these reference cross-sections is defined by $\mathbf{s}_- = S\,\mathbf{s}_+$.

Since the scattering system is open (coupled to radiation), its Hamiltonian H is non-Hermitian, so it supports a set of resonant modes [with resonant frequencies ω_n and fields $\boldsymbol{\psi}_n(\mathbf{r})$ namely $H(i\omega_n)\boldsymbol{\psi}_n = i\omega_n\boldsymbol{\psi}_n$]. Causality and stability [88] imply that the system response is analytic in the upper half of the complex ω-plane, namely ω_n must lie in the lower half plane. $\boldsymbol{\psi}_n$ are linearly independent but quasi-normal and non-orthogonal under the standard (conjugated) "energy" inner product (a volume integral). However, when the system is reciprocal, H is complex-symmetric, so its QNMs are orthogonal under the non-conjugated inner product $\{\boldsymbol{\psi}_n|\boldsymbol{\psi}_l\} = 0$ for $n \neq l$ [82, 89]. We consider N such modes, whose normalization we leave *unspecified*, and denote by the *diagonal* matrix Ω their complex frequencies and by the vector $\mathbf{a}$ their amplitudes upon excitation. Moreover, it is usually assumed there are also pathways other than the resonant QNMs for direct scattering of input to output CPM waves, through the background medium without the scatterer, quantified by a separate scattering matrix C [17, 71].

The part of the scattered field *not* due to direct pathways ($\mathbf{s}_-^{\mathrm{Q}} = \mathbf{s}_- - C\mathbf{s}_+$) can be written outside the scatterer as an expansion over the complete set of port modes (propagating CPMs and evanescent). QNMT makes the approximation that it can be written also within the volume V of the scatterer as a linear combination of the N QNMs (an assumption also used in CMT [17]):

$$\mathbf{F}_{\mathrm{scat}}^{\mathrm{Q}} = \begin{cases} \sum\limits_{p=1}^{P} s_{-p}^{\mathrm{Q}}(\omega)\boldsymbol{\phi}_p^{\perp}(\omega,\mathbf{r}_p^{\perp})e^{ik_p(r_p^{\parallel}-z_p)} + \text{evan.};\ \mathbf{r} \notin V \\ \sum\limits_{n=1}^{N} a_n(\omega)\boldsymbol{\psi}_n(\mathbf{r});\ \mathbf{r} \in V. \end{cases} \tag{3.1}$$

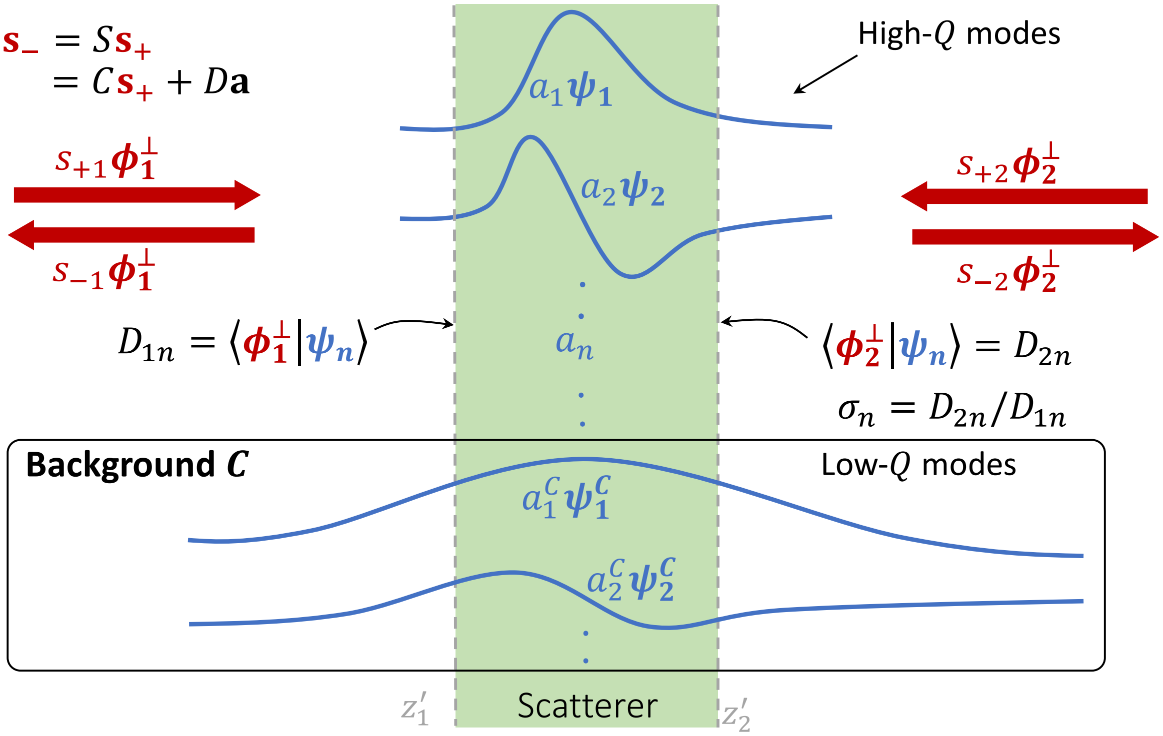

Figure 3-1: A 2-port scattering system with important QNMT parameters. At excitation frequency ω, the coupling port-modes (CPMs) with transverse fields $\phi_p^\perp$ have input and output amplitudes respectively $s_{\pm p}$, related by the S-matrix through $s_- = Ss_+$. The open scattering system supports quasi-normal modes (QNMs) with complex frequencies ω_n and fields ψ_n, which have amplitudes a_n upon excitation. The CPM-to-QNM coupling coefficients are D_{pn}, with ratios $\sigma_n = D_{2n}/D_{1n}$. Imposing realness, unitarity, and symmetry constraints on S allows us to compute it as a function of only ω_n and σ_n [Eq. (3.10)]. Optionally, by separating low-Q modes ψ_n^C, we can also construct a slowly-varying background matrix C, which can give a physical intuition about the scattering response and help in specific scattering designs.

By inserting the second line into the exact equation for the field inside the scatterer and by mode-matching the two lines on the cross-section z_p' where the p-port meets the scatterer boundary, one respectively gets the final two QNMT equations, which, with $\exp(-i\omega t)$ notation, takes the form (for a rigorous derivation see, e.g., Ref. 79):

$$\begin{gathered} -i\left(\omega - \Omega\right)\mathbf{a} = K^t\mathbf{s}_+ \\ \mathbf{s}_- - C\mathbf{s}_+ = D\mathbf{a}, \end{gathered} \tag{3.2}$$

where

$$D_{pn}(\omega) = e^{ik_p(z_p - z_p')}\left\langle \boldsymbol{\phi}_p^\perp(\omega, \mathbf{r}_p^\perp) | \boldsymbol{\psi}_n(\mathbf{r}_p^\perp) \right\rangle_{z_p'} \tag{3.3}$$

and $z_p - z_p'$ is the distance of the p-port reference cross-section from the boundary of the scatterer. This z'_p cross-section choice for the calculation of the D overlaps is further justified in the subsection 3.5.3. The $P \times N$ matrices K and D quantify the couplings of the QNMs to the input and output CPM waves respectively, and they are generally frequency dependent. Eqs. (3.2) with Ω diagonal (also known as state-space representation in diagonal canonical form in circuit theory [72]) constitute the basis of QNMT and their solution for the scattering matrix S is given by

$$S = C - D(i\omega - i\Omega)^{-1}K^t. \tag{3.4}$$

Although a general $C(\omega)$ was included in Eqs. (3.2,3.4) to align with literature, we rely on the presumed completeness of the resonant QNMs to stipulate that each incident CPM wave is scattered to other CPMs only due to resonances. Therefore, for now, we take C as a diagonal phase matrix. Later, we will show that, indeed, low-Q QNMs can be combined to write a general effective background $C(\omega)$; in particular, a fully-transmissive C comes from a zero-frequency mode with an infinite radiative rate (Sec. 3.5.2).

Shifts of ports' reference cross-sections

When $S(\omega)$ is a meromorphic function, it is useful to employ the Weierstrass factorization theorem and arguments from causality to write S using a "proper" rational function. The Weierstrass factorization theorem [90] in fact states that a "meromorphic" function (analytic except for poles) can be factorized into a non-zero analytic function (an exponential) and a rational function (zeros and poles). If $S(\omega)$ is meromorphic, an exponential phase factor can then be factored out of each term as $S_{pq}(\omega) = e^{i\varphi_{pq}(\omega)}S'_{pq}(\omega)$, with S'_{pq} a "proper" rational function (degree of numerator polynomial not larger than degree of denominator, so finite as $\omega \to \infty$) and φ_{pq} an analytic function that we assume corresponds to a real phase shift for real frequencies. Similarly to the approach in Ref. 73, the combination of Phragmén-Lindelöf theorem (giving $|e^{i\varphi_{pq}(\omega)}| \leq 1$ in the upper-half complex plane) and Čebotarev theorem shows that φ_{pq} has to be a linear ($= \tau_{pq}\omega$ with $\tau_{pq} \geq 0$, since the constant term can be added to S'_{pq}).

When the system is lossless and reciprocal, unitarity and symmetry of S combine to $S^*(\omega)S(\omega) = I$. The off-diagonal pq term can be expanded as $\sum_r S^*_{pr}S_{rq} = \sum_r e^{-i(\tau_{pr}-\tau_{rq})\omega}S'^*_{pr}S'_{rq} = 0$. Since this has to be true for all real ω, all the phase terms in the sum must be the same, namely $\tau_{pr} - \tau_{rq} = \theta_{pq}$ for each r. Specifically, for $r = p$ and $r = q$, we get $\tau_{pp} - \tau_{pq} = \tau_{pq} - \tau_{qq} \Leftrightarrow \tau_{pq} = (\tau_{pp} + \tau_{qq})/2$. Therefore, the S matrix can be written as $S = e^{i\tau\omega}S'e^{i\tau\omega}$ with a *diagonal* τ matrix with real positive elements.

Eq. (3.4) then implies that $C(\omega) = e^{i2\tau\omega}C'$, $D(\omega) = e^{i\tau\omega}D'$ and $K(\omega) = e^{i\tau\omega}K'$, where

C' is a diagonal constant phase matrix that can be taken equal to $-I$ (as we justify later and is often used in CMT [71]) without loss of generality, and D', K' are now *constant* matrices.

This is the case for CPMs with fields transverse to their direction of propagation ($\boldsymbol{\phi}_p \cdot \mathbf{k}_p = 0$), such as plane waves or dual-conductor TEM microwave modes, which will be the focus of our work. They have $k_p = \omega / c_p$ (where c_p the wave velocity) and $\boldsymbol{\phi}_p^{\perp}(\mathbf{r}_p^{\perp})$ independent of ω, so Eq. (3.3) suggests that $D_{pn}(\omega) = D'_{pn} e^{i\omega(z_p - z'_p)/c_p}$ with D'_{pn} in fact constant. Thus, in all structures simulated in this work, we remove this linear phase to compute S', referenced at the new port cross-sections z'_p on the scatterer boundary. In practice, τ_{pp} may be slightly larger from $(z_p - z'_p)/c_p$, adding a small constant group delay just to the phases of S, so it is of no concern for applications dependent only on their amplitudes, such as amplitude filters.

Therefore, hereafter we drop the $'$ and consider S to be such a proper rational function that can be decomposed as

$$S = -[I + D(i\omega - i\Omega)^{-1} K^t] \Leftrightarrow S_{pq} = -\delta_{pq} - \sum_{n=1}^{N} \frac{D_{pn} K_{qn}}{i\omega - i\omega_n}. \tag{3.5}$$

For other types of CPMs, $S(\omega)$ may not be meromorphic, for example when higher-order CPMs have a cutoff frequency, which appears as a branch-point [and frequency dependent $D'(\omega)$, $K'(\omega)$]. Similarly to previous QNMT formulations with constant coefficients, such systems are not investigated in this work.

Normalization independence

Recall that measurable physical quantities (such as the S-matrix) do not depend on the choice of normalization for the QNM amplitudes $\mathbf{a}$. For example, it is easily seen from the QNMT Eqs. (3.2) that, for the fixed normalization of $\mathbf{s}_{\pm}$, two different sets (a_n, K_{qn}, D_{pn}) and $\left(a'_n, K'_{qn}, D'_{pn}\right)$ scale as $a'_n / a_n = K'_{qn} / K_{qn} = D_{pn} / D'_{pn}$, hence S_{pq} in Eq. (3.5) is unchanged. Thus an overall scaling factor can be chosen arbitrarily for each QNM.

For some physical quantities analytically computed via the QNM fields (such as the Green's function), this normalization independence is typically ensured by dividing with the volume-integral norm $\{\boldsymbol{\psi}_n | \boldsymbol{\psi}_n\}$ of these fields. However, since they are non-integrable, regularizing this norm is a procedure that adds complexity (e.g. choice of method and dependence on outgoing boundary condition) [86] to the QNMT formulations based only on calculations from the field equations [77–79]. In contrast, as highlighted in Ref. 6 and we show also later, this phenomenological (relying on physical constraints) QNMT formulation does not require such norm evaluation, so it is much simpler.

3.3.2 Physical constraints

We now proceed by imposing constraints on S, based on the physical properties of the system.

Realness

For many physical systems, real input fields lead to real output fields so that the system response $S(t)$ must also be real. In frequency domain, this realness of S is stated as $S^*(i\omega) = S(-i\omega^*)$. For such systems, the same relation holds for their Hamiltonian H satisfying $H\left(i\omega\right)\boldsymbol{\psi} = i\omega\boldsymbol{\psi}$, so every QNM solution $(\omega_n,\, \boldsymbol{\psi}_n)$ is paired with another QNM $(\omega_{n'},\, \boldsymbol{\psi}_{n'}) = (-\omega_n^*,\, \boldsymbol{\psi}_n^*)$. Similarly, the CPMs satisfy $\boldsymbol{\phi}_p^*(\omega) = \boldsymbol{\phi}_p(-\omega^*) \Rightarrow \boldsymbol{\phi}_p^{\perp *} = \boldsymbol{\phi}_p^{\perp}$. Eq. (3.3) thus shows that $D_{pn'} = D_{pn}^*$. Then, to satisfy $S^*(i\omega) = S(-i\omega^*)$, Eq. (3.5) requires also $K_{pn'} = K_{pn}^*$. Note, S realness implies that not only poles but also zeros of any S_{pq} appear in pairs $(\omega_o, -\omega_o^*)$, and that S_{pq} is a rational function of $i\omega$ with real coefficients. Note that our QNMT is still applicable to systems that do not satisfy realness[4], where simply the QNMs included in the S-expansion do not appear in pairs.

Energy conservation

In absence of absorption or gain, energy conservation implies that the S matrix is unitary $(\mathbf{s}_+^\dagger \mathbf{s}_+ = \mathbf{s}_-^\dagger \mathbf{s}_- \Leftrightarrow S^\dagger S = I)$ [71]. We can use this to find a relation between K and D.

From Eq. (3.5), namely $S = -I - DdK^t$, where $d = (i\omega - i\Omega)^{-1}$:

$$S^\dagger S = I + K^* d^\dagger D^\dagger + DdK^t + K^* d^\dagger D^\dagger DdK^t. \tag{3.6}$$

We compute the coefficient (p, q) of this matrix. The second and third terms are equal to:

$$\sum_n \frac{K_{pn}^* D_{qn}^*}{i(\omega - \omega_n^*)} - \sum_n \frac{D_{pn} K_{qn}}{i(\omega - \omega_n)}. \tag{3.7}$$

The final term, after decomposing into simple elements through $\frac{1}{i(\omega - \omega_n) i(\omega - \omega_l^*)} = \frac{1}{i(\omega_n - \omega_l^*)}\left[\frac{1}{i(\omega - \omega_n)} - \frac{1}{i(\omega - \omega_l^*)}\right]$ and relabelling indices (n and l), becomes:

$$\sum_{r,n,l} \frac{K_{pl}^* D_{rl}^* D_{rn} K_{qn}}{i(\omega - \omega_l^*) i(\omega - \omega_n)} =$$

---

[4] The resonances of the Schrödinger equation do not appear in pairs in the $\omega = E/\hbar$ plane.

$$= \sum_n \frac{K_{qn}}{i(\omega - \omega_n)} \sum_l K^*_{pl} \frac{\sum_r D_{rn} D^*_{rl}}{i(\omega_n - \omega^*_l)} - \sum_n \frac{K^*_{pn}}{i(\omega - \omega^*_n)} \sum_l K_{ql} \frac{\sum_r D_{rl} D^*_{rn}}{i(\omega_l - \omega^*_n)}. \tag{3.8}$$

In order to impose $S^\dagger S = I$ for every ω, necessary and sufficient conditions are given by $K^* M = D$ and $K M^t = D^*$, with $M_{nl} = \frac{\sum_p D_{pl} D^*_{pn}}{i(\omega_l - \omega^*_n)}$. The two relations are actually equivalent, since $M = M^\dagger$, and can be rewritten as $K^t = M^{-1} D^\dagger$.

From this, we conclude that a *necessary and sufficient* condition for unitarity is given by

$$K = D^* \left(M^t\right)^{-1}, \text{ with } M_{nl} = \frac{\sum_{p=1}^P D_{pl} D^*_{pn}}{i\omega_l - i\omega^*_n} = M^*_{ln}, \tag{3.9}$$

thus S can be written as

$$S = -\left[I + D(i\omega - i\Omega)^{-1} M^{-1} D^\dagger\right]. \tag{3.10}$$

— **Realness** — We now show that this Eq. (3.9) choice of K satisfies the realness requirement. Including negative-frequency modes with $D_{pn'} = D^*_{pn}$, we can write $M = \begin{pmatrix} A & B \\ B^* & A^* \end{pmatrix}$ (where $A = A^\dagger$ and $B = B^t$, so that $M = M^\dagger$). Now, consider matrices $\tilde{A}$, $\tilde{B}$ such that $\begin{pmatrix} \tilde{A} & \tilde{B} \end{pmatrix} M = \begin{pmatrix} I & 0 \end{pmatrix}$; then, by directly substituting M, we can immediately show that we also have $\begin{pmatrix} \tilde{B}^* & \tilde{A}^* \end{pmatrix} M = \begin{pmatrix} 0 & I \end{pmatrix}$, so $M^{-1} = \begin{pmatrix} \tilde{A} & \tilde{B} \\ \tilde{B}^* & \tilde{A}^* \end{pmatrix}$. Finally, from $K = D^* \left(M^t\right)^{-1}$, we conclude that $K_{pn'} = K^*_{pn}$.

— **Normalization independence** — Next, we rearrange Eq. (3.10) to show that S is fully and uniquely determined by the resonant frequencies ω_n and the ratios $\sigma_{r,pn} = D_{pn}/D_{r_n n}$, for some chosen port r_n for each mode n (for example, we can simply take $r_n = 1$). Let D_r be a $N \times N$ diagonal matrix, with elements $D_{r,nn} = D_{r_n n}$. Then, denote by $\sigma_r = D D_r^{-1}$ the r-scaled $P \times N$ coupling matrix (naturally, $\sigma_{r,r_n n} = 1$ for all n). Now, by inserting I twice in Eq. (3.10), the scattering matrix S from can be rewritten as

$$\begin{aligned} S &= -I - D(i\omega - i\Omega)^{-1} M^{-1} D^\dagger \\ &= -I - D\left(D_r^{-1} D_r\right)(i\omega - i\Omega)^{-1} M^{-1} \left[D_r^\dagger \left(D_r^{-1}\right)^\dagger\right] D^\dagger \\ &= -I - \sigma_r (i\omega - i\Omega)^{-1} M_r^{-1} \sigma_r^\dagger, \end{aligned} \tag{3.11}$$

where

$$M_r = \left(D_r^{-1}\right)^\dagger M D_r^{-1} \Leftrightarrow M_{r,nl} = \frac{1}{D^*_{r_n n}} \frac{\sum_p D_{pl} D^*_{pn}}{i\omega_l - i\omega^*_n} \frac{1}{D_{r_l l}} = \frac{1 + \sum_{p \neq r_n} \sigma_{r,pl} \sigma^*_{r,pn}}{i\omega_l - i\omega^*_n}. \tag{3.12}$$

These two equations show that, for a lossless system, S in Eq. (3.10) can be fully computed using only the resonant frequencies Ω and the ratios σ_r of modal coupling among different ports, independently of the overall scaling factors in D.

Reversely, we also show that S uniquely determines Ω and σ_r. In particular, for two different sets $\{\Omega, \sigma_r\}$, $\{\Omega', \sigma'_r\}$ such that $S_{\{\Omega,\sigma_r\}} = S_{\{\Omega',\sigma'_r\}}$, we see from Eq. (3.11) that $\Omega = \Omega'$ and

$$\sigma_{r,pn} \left[\sigma_r M_r^{-1}\right]^*_{qn} = \sigma'_{r,pn} \left[\sigma'_r M'^{-1}_r\right]^*_{qn}. \tag{3.13}$$

For $p = r_n$, we have $[\sigma_r M_r^{-1}]_{qn} = [\sigma'_r M'^{-1}_r]_{qn}$. Then, for any p, Eq. (3.13) again gives $\sigma_{r,pn} = \sigma'_{r,pn}$.

This proves that S is fully and uniquely determined by the resonant frequencies ω_n and the ratios $\sigma_{r,pn} = D_{pn}/D_{r_n n}$. These quantities can be readily calculated using any appropriate eigenmode solver, where D_{pn} is determined by the surface integral in Eq. (3.3) and the ratios $\sigma_{r,pn}$ remove the $\boldsymbol{\psi}_n$-normalization-dependent scaling-factor. Therefore, as promised, S in Eq. (3.10) does not require computing the volume-integral norms of the QNMs. Note also that, as more modes are included, the residue coefficients automatically update themselves through M in order to satisfy energy conservation for the entire set, in contrast to other formulations based on the exact field equations, where these residues are cosntant [78, 79]. Finally, Eq. (3.9) is different from the usual CMT expression of energy conservation $D^\dagger D = 2\left|\mathrm{Im}\left\{\Omega\right\}\right|$, associated with modes orthonormal under the standard "energy" inner product, which does not hold for QNMs.

Reciprocity

Reciprocity implies that the S matrix is symmetric ($S = S^t$) [71]. From Eq. (3.5), we can see that this is equivalent to having

$$\frac{K_{pn}}{D_{pn}} = \frac{K_{qn}}{D_{qn}} \Leftrightarrow K = D\Lambda, \tag{3.14}$$

and therefore

$$S = -\left[I + D(i\omega - i\Omega)^{-1} \Lambda D^t\right], \tag{3.15}$$

for some *arbitrary* diagonal matrix Λ with entries λ_n [with the only restriction that $\lambda_{n'} = \lambda^*_n \neq 0$, so that Eq. (3.14) is compatible with realness], where a specific choice of λ_n fixes the $\boldsymbol{\psi}_n$-normalization-dependent scaling-factor. For any such choice, as mentioned earlier, the numerator of pole n for S_{pq} in Eq. (3.15) stays the same, however, its calculation requires evaluation/regularization of divergent volume integrals involving the QNM fields (including their norm $\{\boldsymbol{\psi}_n|\boldsymbol{\psi}_n\}$), which we try to avoid here. Note also that, since Λ can be arbitrary, the usually assumed condition of reciprocity $K = D$ (corresponding to the specific normalization choice $\Lambda = I$) is *not necessarily* true.

D-optimization

In order to satisfy both energy conservation and reciprocity (unitarity and symmetry of S), the input coupling coefficients K must satisfy both Eq. (3.9) and (3.14) simultaneously, namely the output coupling coefficients D must satisfy

$$D_{qn} \sum_{l} M^{-1}_{nl} D^*_{pl} = D_{pn} \sum_{l} M^{-1}_{nl} D^*_{ql} \Leftrightarrow D^* = D\Lambda M^t. \tag{3.16}$$

Here again, for each resonance n, either $D_{r_n n}$ (for one port r_n) or λ_n can be chosen arbitrarily. In practice, this reciprocity condition Eq. (3.16) is a set of PN equations. Let D^c be the coupling coefficients computed from the eigenmode solver. In most cases, as we see in numerical examples, it turns out that D^c are very close to satisfying this required condition, but they don't satisfy it perfectly, since the finite set of chosen resonances is not truly complete. This is why in Ref. 6, Eq. (3.16) was not enforced exactly, rather the N coefficients of Λ were chosen as $\lambda_j = [X^\dagger X]_{jj}/[X^\dagger D]_{jj}$ with $X = D^*(M^t)^{-1}$ as one way to minimize its error (note [5]), and their final S-matrix, which was formulated as in Eq. (3.15), was reciprocal but not necessarily unitary. Instead, here, we give priority to exactly satisfying these physical properties of the actual system, if we want our model to be a physically realistic and thus, as we will show, a more accurate description. Therefore, we fine-tune the PN coefficients D by using a constrained optimization procedure, with the goal of exactly satisfying Eq. (3.16) while staying as close as possible to the computed system performance:

$$D = \underset{D^* = D\Lambda M^t}{\arg\min}\, f\left(D, D^c\right) \tag{3.17}$$

where $f(D, D^c)$ is some penalty function to ensure that D stays close to D^c (note [6]). An obvious choice is $f(D, D^c) = \|D - D^c\|^2$. Another option is $f(D, D^c) = \sum_{\{p,q\}} \|R_{pq}(D) - R_{pq}(D^c)\|^2$, where $R(D)$ represents the residues of the scattering ma-

---

[5] $f(\Lambda) = |X\Lambda^{-1} - D|^2$ was minimized, however, different results would have been obtained for other choices, e.g. $f(\Lambda) = |X - D\Lambda|^2$ leads to $\lambda_j = [D^\dagger X]_{jj}/[D^\dagger D]_{jj}$.

[6] The optimization can for example be done using an augmented Lagrangian method [91]. Gradients can also be effectively computed using automatic differentiation [92] or even analytically, when $\Lambda = I$.

trix expansion given in Eq. (3.10) and $\{p, q\}$ is a chosen subset of indices. When summing over $p \neq q$, the global optimum is reached for D satisfying $R_{pq}(D) = R_{qp}(D) = [R_{pq}(D^c) + R_{qp}(D^c)]/2$, but such a set of D is not guaranteed to exist. When it does exist, directly solving this system of equations has given the best results in our experience with actual 2-port systems.

3.3.3 Properties of 2-port systems

Since many common applications of scattering theory involve lossless reciprocal 2-port systems, we discuss some properties of their S matrix.

Energy conservation leads to the unitary S-matrix of Eq. (3.10), which was recast in a normalization-independent form [Eq. (3.12)]. We can then simply choose $r_n = 1$, skip the r-subscript and denote $\sigma_n = D_{2n}/D_{1n}$. The S-matrix then becomes $(p, q = 1, 2)$

$$S_{pq} = -\delta_{pq} - \sum_{n=1}^{N} \frac{\sigma_{pn} \sum_{l=1}^{N} M_{nl}^{-1} \sigma_{ql}^*}{i\omega - i\omega_n}; \;\; M_{nl} = \frac{1 + \sigma_l \sigma_n^*}{i\omega_l - i\omega_n^*}; \;\sigma_{1n} = 1, \sigma_{2n} = \sigma_n. \tag{3.18}$$

When the system has mirror symmetry, these ratios can only take the values $\sigma_n = \pm 1$, so they act like eigenvalues of the symmetry operator.

Realness requires also that, for each mode (ω_n, σ_n), the mode $(-\omega_n^*, \sigma_n^*)$ is also included. Then, the dependence of S on σ_n can be easily checked to satisfy, for $\gamma = \pm 1$,

$$\begin{aligned} S_{11\{\omega_n, \gamma\sigma_n\}} &= S_{11\{\omega_n, \sigma_n\}}, \;\; S_{12\{\omega_n, \gamma\sigma_n\}} = \gamma^* S_{12\{\omega_n, \sigma_n\}} \\ S_{21\{\omega_n, \gamma\sigma_n\}} &= \gamma S_{21\{\omega_n, \sigma_n\}}, \;\; S_{22\{\omega_n, \gamma\sigma_n\}} = S_{22\{\omega_n, \sigma_n\}}. \end{aligned} \tag{3.19}$$

[If only positive-frequency modes are considered and thus the realness requirement is relaxed—commonly known as a rotating-wave approximation (RWA)—Eq. (3.19) holds for any phase factor $\gamma = e^{i\varphi}$.] Moreover, swapping ports $1 \leftrightarrow 2$ corresponds simply to replacing $\sigma_n \leftrightarrow 1/\sigma_n$:

$$S_{11\{\omega_n, \sigma_n\}} = S_{22\{\omega_n, 1/\sigma_n\}}, \;\; S_{21\{\omega_n, \sigma_n\}} = S_{12\{\omega_n, 1/\sigma_n\}}. \tag{3.20}$$

As a consequence, when all σ_n are ± 1 (as for a symmetric structure, whose modes must be even or odd [61]), $S_{11} = S_{22}$ and $S_{21} = S_{12}$, so the 2-port system is immediately reciprocal. (Obviously, $\sigma_n = \pm 1$ is not *necessary* for the reciprocity condition Eq. (3.16) to hold.) Note that energy conservation alone implies that $|S_{12}| = |S_{21}|$, so reciprocity in lossless 2-ports is mostly a statement on the transmission phase responses.

— **Properties of zeros** — Combining realness $S^*(\omega) = S(-\omega)$, unitarity $S^\dagger(\omega)S(\omega) = I$ and symmetry $S^t(\omega) = S(\omega)$ on the real-ω axis, gives $S(-\omega)S(\omega) = I$, which can then be analytically continued in the entire complex-ω plane. Expanding this equation for a 2-port, we get

$$S_{11}(-\omega)\,S_{11}(\omega) + S_{21}(-\omega)\,S_{21}(\omega) = 1 \tag{3.21a}$$

$$S_{11}(-\omega)\,S_{11}(\omega) = S_{22}(-\omega)\,S_{22}(\omega) \tag{3.21b}$$

$$S_{11}(-\omega)\,S_{21}(\omega) = -S_{21}(-\omega)\,S_{22}(\omega)\,. \tag{3.21c}$$

We can use these equations to derive some useful properties of the zeros of S-coefficients. As a reminder, realness requires all poles and zeros to be symmetric across the imaginary ω-axis.

Let's first assume that $-\omega_o$ is *not* a system pole [so $S(-\omega_\mathrm{o})$ is finite]. Eq. (3.21a) then prevents S_{11} and $S_{21} = S_{12}$ from having simultaneous zeros at ω_o, and using also Eq. (3.21b) the same holds for S_{22} and S_{21}. Therefore, Eq. (3.21c) mandates that (i) the zeros of S_{21} can only appear as complex quadruplets $(\omega_o, \omega_o^*, -\omega_o, -\omega_o^*)$, real or imaginary pairs $(\omega_o, -\omega_o)$, or at $\omega_o = 0$ and that (ii), for each zero-pair $(\omega_o, -\omega_o^*)$ of S_{11}, $(-\omega_o, \omega_o^*)$ is a zero-pair of S_{22}.

If now $-\omega_o$ is a system pole (so at least one S-element diverges there), the same rules (i) and (ii) still apply, as long as zero-pole cancellations that occur at $(-\omega_o, \omega_o^*)$ are taken into account. All possible scenarios are: (I) If $S_{11}(\omega_o) = 0 \neq S_{22}(\omega_o)$, Eq. (3.21b) forces $S_{22}(-\omega_o)$ to be finite, thus S_{22} must exhibit a zero at $-\omega_o$ that cancels the pole there (and similarly when switching S_{11} and S_{22}). Moreover, if simultaneously $S_{21}(\omega_o) = 0$, Eq. (3.21c) mandates a pole-zero cancellation also for S_{21} at $-\omega_o$. (II) If $S_{11}(\omega_o) = S_{22}(\omega_o) = 0$, Eq. (3.21c) implies that also $S_{21}(\omega_o) = 0$, namely the entire matrix $S(\omega_\mathrm{o}) = 0$. In this case, we can consider that all S-coefficients also have another zero at $-\omega_o$ that cancels a degenerate pole, which usually do appear when the physical system is perturbed. (III) If $S_{11}(\omega_o) \neq 0 \neq S_{22}(\omega_o)$, Eq. (3.21a,3.21c) dictate also that $S_{21}(\omega_o) \neq 0$. In the cases above, for any coefficient with $S_{pq}(\omega_\mathrm{o}) = 0$, then $S_{pq}(\omega) \propto e^{i\varphi(\omega)} = (\omega - \omega_o)(\omega + \omega_o^*)\,/\,(\omega + \omega_o)(\omega - \omega_o^*)$, a behavior known as an "all-pass" phase filter. Moreover, when $S(\omega_\mathrm{o})$ is singular, ω_o is called an "S-matrix zero" (for example generalized in Ref. 85).

The restrictions (i) on the S_{21} zeros imply that its numerator is a polynomial of ω^2 with real coefficients, optionally with multiplicative $i\omega$ factors. We emphasize that, for any lossless system with more than one port, the zeros of the S coefficients are different from the "S-matrix zeros", where $\det(S) = 0$ and which always coincide with the conjugates of the poles [85].

3.3.4 Absorption and gain

In presence of small absorption loss, S is no longer unitary, but it can be calculated perturbatively when all relevant modes have high Q. In particular, the denominators of Eq. (3.10) must obviously use the poles $\tilde{\Omega}$ of the actual absorptive system, however, if the QNM loss rates are split into radiative (Γ_{r}) and non-radiative (Γ_{nr}) parts, the numerators of Eq. (3.10) scale as $DM^{-1}D \sim \Gamma_{\mathrm{r}}(1 + \mathrm{const} \cdot \Gamma_{\mathrm{nr}})$ [no scattering when $\Gamma_{\mathrm{r}} \to 0$]. We then see that, for high-Q modes (where both Γ_{r} and Γ_{nr} are much smaller than the frequencies), these numerators are equal to those of the lossless case to first order in $\Gamma_{\mathrm{r}}, \Gamma_{\mathrm{nr}}$, namely absorption only affects the poles. (A similar argument is often implicitly used in CMT, where it is typically assumed that $\Gamma = D^{\dagger}D + \Gamma_{\mathrm{nr}}$ with D not changing in the presence of Γ_{nr} because Γ itself is small [6], or is explicitly used to argue that the coupling coefficients to different CMT channels can be determined independently [28].) Therefore, in practice, to compute S for absorptive or active scatterers, we first calculate the QNMs (ω_n, D_{pn}) of the lossless (radiative only) structure and use them to evaluate the numerators of Eq. (3.10). Then, we turn on absorption or gain mechanisms (adiabatically if needed for QNM-tracking purposes) to get the exact denominator poles ($\tilde{\omega}_n$). Since the lossless-case D was fine-tuned for reciprocity, the non-unitary S will still be symmetric. The perturbation argument assumes high-Q modes but does not restrict the relative strength between radiation and absorption/gain rates. Indeed, as we see in the next examples, our QNMT gives quite accurate predictions even in the presence of modes with $\Gamma_{\mathrm{nr}} \gg \Gamma_{\mathrm{r}}$ and, in fact, even when relatively low-Q modes are present.

3.4 Examples in electromagnetism

Our QNMT for the S matrix is applicable to all kinds of wave physics, such as acoustics [93–95], electromagnetics [6, 78, 79], and quantum mechanics [77, 96]. Therefore, in our derivation, we used general physics-agnostic notation to render our results usable for any wave-scattering problem. In this section, to examine the accuracy of our QNMT, we study multiple examples in electromagnetism.

3.4.1 Normal incidence on microwave metasurface

We now study scattering of an electromagnetic plane wave with frequency $f = \omega/2\pi$ normally incident on the metasurface depicted in the inset of Fig. 3-2(a). It consists of alternating dielectric (green) and metallic (grey) layers, where the latter have been etched out to form two-dimensional square periodic lattices (of period a) of thin metallic crosses, whose centers are the same for all patterned layers. A square air-hole has also been etched throughout the entire thickness d of the metasurface in the region between the crosses. The metal thickness is 18μm (corresponding to 0.5oz copper). We study for frequencies below the first diffraction cutoff ($f_{\text{cut}} = c/a$ at normal incidence), so only transmission and reflection need to be considered. Moreover, there is C_{2v} symmetry, so the response for normal incidence is independent of the polarization $\hat{e}$ and only 2 ports are needed. Numerical computation of the "exact" frequency response (S-matrix) for plane-wave excitation as well as of the eigenmodes for use in our QNMT is carried out using COMSOL Multiphysics [97]. Complex eigenfrequencies ω_n are immediately obtained from the eigensolver, while the coupling coefficients D_{1n}, D_{2n} are computed from Eq. (3.3) as "power" inner-product surface integrals

$$D_{pn} \propto \int_{z'_p} \left(\mathbf{E}_p^* \times \mathbf{H}_n + \mathbf{E}_n \times \mathbf{H}_p^*\right) \cdot d\mathbf{S} \tag{3.22}$$

at the two (left/right for $p = 1, 2$) external boundaries of the metasurface between the QNM field $\boldsymbol{\psi}_n = (\mathbf{E}_n, \mathbf{H}_n)$ and the coupling port-modes $\boldsymbol{\phi}_p^{\perp} = (\mathbf{E}_p, \mathbf{H}_p)$ [plane waves in this case, so $D_{pn} \propto \int_{z'_p} (\hat{e} \cdot \mathbf{E}_n)\ dS$], where, as emphasized earlier, only their ratio σ_n is needed. In Appendix-B, we provide further details and guidelines for the numerical simulations (mainly how to avoid spurious modes [67, 70, 98, 99]), as well as tables with the calculated QNMs (ω_n, σ_n) for every structure presented in the article.

For the asymmetric structure of Fig. 3-2, the parameters were chosen arbitrarily to test a very general response, with σ_n departing substantially from ± 1. Even so, we see a very good match between the exact numerical computation (black lines) and the QNM expansion of Eq. (3.10) (red lines), for both the amplitude of $S_{21} = |S_{21}|e^{i\phi_{21}}$ (a) and its time delay $\tau_{21} = d\phi_{21}/d\omega \times c/d$ (b), in both cases of lossless (solid lines) and lossy (dashed lines) structures. In the lossless case, we emphasize again that, due to our symmetrization procedure of Eq. (3.17), the QNM expansion we obtained is both unitary and symmetric. This is why the zeros of $S_{21} = S_{12}$ are either real or complex conjugate pairs, and the zeros of S_{11}, S_{22} complex conjugates of each other, as they should [Fig. 3-2(c)]. The response with copper and dielectric losses mostly maintains the same overall features, and merely exhibits reduced transmission at high frequencies and "superluminal" ($0 \leq \tau_{21} < 1$) or negative group delay ($\tau_{21} < 0$) around transmission zeros. The latter does not violate causality [100], instead it has been shown to necessarily occur at peaks of absorption [101], and thus is indeed typically associated with lossy bandstop ("notch")

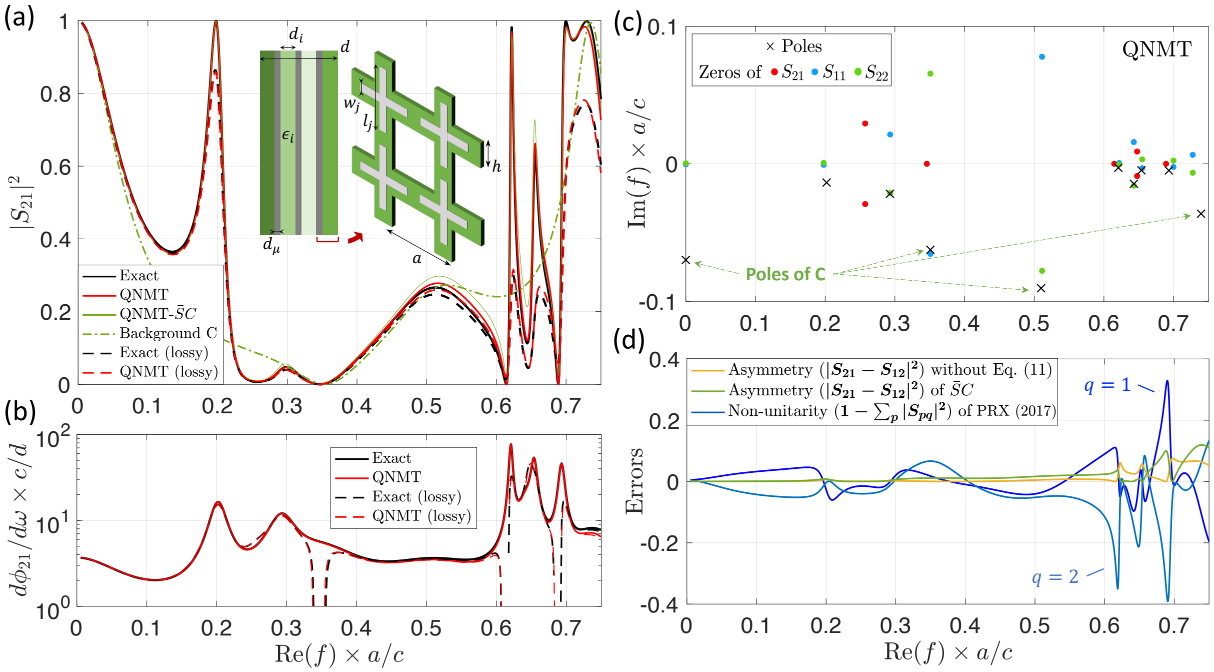

Figure 3-2: QNMT modeling scattering of a plane wave normally incident from the left on the microwave metasurface depicted in the inset of (a). Parameters are: $a = 15\text{mm}$, $h/a = 0.64$, $w_j/a = (0.05, 0.2, 0.1)$, $l_j/a = (0.62, 0.92, 0.82)$, metal (grey) layers' thickness $d_\mu = 18\mu\text{m}$, dielectric (green) layers' permittivities $\epsilon_i = (4, 6, 3, 10)$ and thicknesses $d_i/a = (0.1, 0.2, 0.3, 0.2)$. In the lossy simulation, we used copper and added loss $\tan\delta = 0.01$ to all dielectric layers [for simplicity, $-\tan\delta$ is assumed for $\mathrm{Re}(f) < 0$ to maintain realness of $\epsilon(f)$]. Curves: (a) magnitude and (b) group delay of the transmission coefficient (where a constant delay of $0.24 \times d/c$ was added to QNMT to match the exact simulation at low frequencies). (c) Lossless-system poles used in the QNM expansion (with their negative-frequency pairs used but not shown) and zeros of the resulting S coefficients, confirming unitarity and symmetry of S. The dotted arrows point at the 4 modes used to compute the slowly varying background C in the $S = \bar{S}C$ approximation. (d) Errors of asymmetric [Eq. (3.10) without Eq. (3.17), and approximate Eq. (3.23)] or non-unitary [Ref. 6] QNMT formulations.

transmission responses (such as zeros) [102]. Our QNMT correctly predicts even these unusual phenomena.

To quantify the benefits of our QNMT, we calculate the errors associated with not exactly enforcing reciprocity or energy conservation, for the same QNMs of the lossless structure. If the D coefficients are not fine-tuned with Eq. (3.17), S from Eq. (3.10) is not exactly symmetric, so Fig. 3-2(d) shows the resulting error in $|S_{21} - S_{12}|^2$ (orange curve). It is relatively small (although increasing at higher frequencies), indicating that Eq. (3.10) is already a good approximation. In contrast, the QNMT of Ref. 6 [analogous to our Eq. (3.15)] is reciprocal but violates energy conservation by large amounts, leading to non-physical “absorption/gain”. As indeed shown in Fig. 3-2(d), for this lossless 2-port, the sum of transmission and reflection $|S_{pp}|^2 + |S_{21}|^2$ $(p = 1, 2)$ deviates from 1 by almost ± 0.4 at some frequencies (blue curves)! It turns out that these large errors exhibit themselves mostly in the reflection coefficients. Additionally, in both cases, the violation of a physical constraint leads to errors also in the group-delay prediction (such as negative group delay, which is impossible for a *lossless* 2-port). However, these errors are of less importance, since they usually appear around transmission zeros and they are mitigated when a finite-bandwidth pulse is considered [103].

One key advantage of the QNMT method is that it resolves spectra around very-high-Q modes with perfect detail, while a frequency simulation requires a very dense uniform frequency-grid to resolve them, being ignorant of their location. This, in turn, leads to a stark benefit in speed for QNMT. For this example, on the same machine and finite-element mesh, the QNMT calculation took an average of ~ 60 secs per mode ($\times 10$ modes in Fig. 3-2), while the frequency-domain calculation an average of ~ 100 secs per point ($\times 600$ points in Fig. 3-2).

3.4.2 4-port metasurface via coupled polarizations

We now consider the 4-port system described in Fig. 3-3 which consists of a microwave metasurface with three dielectric layers sandwiching two metallic sheets, with patterned arrays of *rotated* cross-like apertures. The ports correspond to the two polarizations on the left (1,2) and right (3,4) sides of the structure. This system does not have the required symmetry for the normally incident plane-wave polarization to be conserved, instead the two orthogonal polarizations on each side cross-couple in both reflection and transmission, so a 4-port system is needed.

In Fig. 3-3(a), we plot the cross-polarization transmission $|S_{41}|^2$ and again find a good agreement with our QNMT. In Fig. 3-3(b), we again show for comparison the errors of QNMT without symmetry or unitarity. For the non-unitary QNMT of Ref. 6, the quantity $1 - \sum_p |S_{p1}|^2$ reaches values as low as -0.5 (blue curve), in stark contradiction with energy conservation. The asymmetric QNMT using Eq. (3.10) without the D correction of Eq. (3.17) has errors in $|S_{pq} - S_{qp}|^2$ as large as 0.3 (orange curves). Moreover, in this example, it also has nonzero $|S_{pq}|^2 - |S_{qp}|^2$ with an error up to ~ 0.015. This happens, because, for P-port systems with $P > 2$, unitarity alone does not guarantee $|S_{pq}| = |S_{qp}|$ anymore, so our method of fine-tuning D to also enforce symmetry [Eq. (3.17)] corrects errors not just in the scattering phase, but in the amplitudes too.

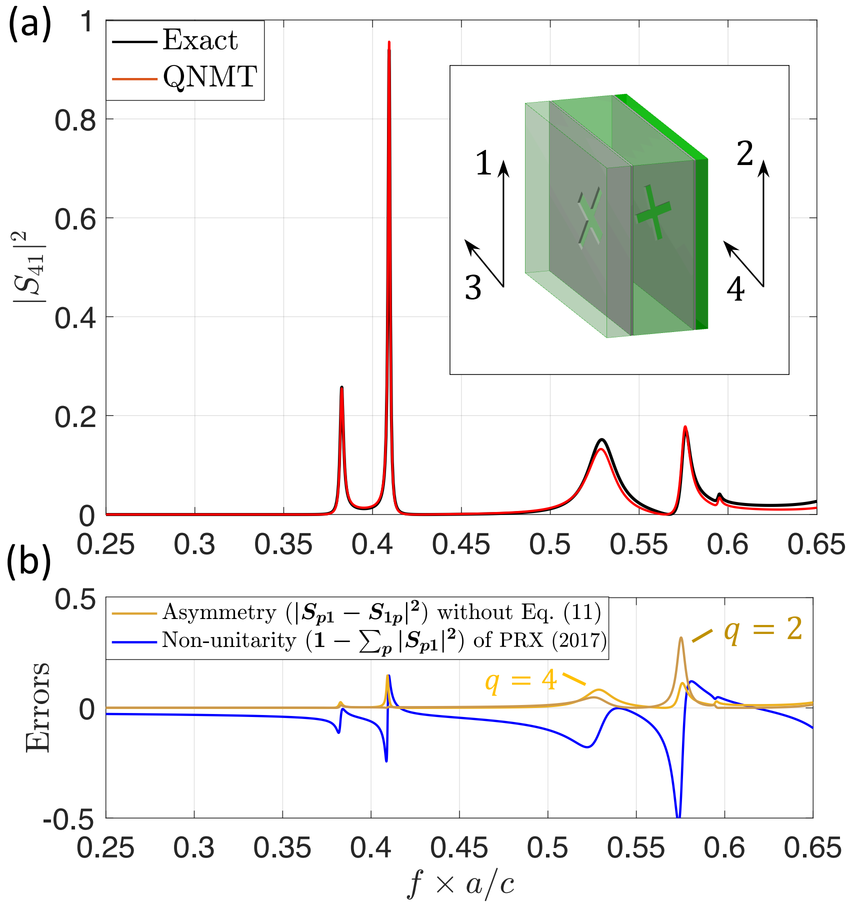

Figure 3-3: QNMT modeling of cross-polarization transmission of a normally incident plane wave from a metasurface with rotated apertures. The two planar metallic sheets are periodically patterned (period $a = 15mm$) with same cross-like apertures [with widths $(0.05a, 0.1a)$ and lengths $(0.5a, 0.3a)$ in two orthogonal directions], which are rotated by angles 30° and 60° with respect to the polarization of port 1. The three uniform dielectric layers have $\epsilon_i = (2, 3, 5)$ and thicknesses $d_i/a = (0.1, 0.05, 0.15)$. (b) Errors of asymmetric [Eq. (3.10) without Eq. (3.17)] or non-unitary [Ref. 6] QNMT formulations.

3.4.3 Oblique incidence on 2d photonic metasurface

When a plane wave is incident on a metasurface at an angle θ, its transverse wavevector component at frequency ω is $k^{\perp} = \omega \sin\theta/c$. Phase matching then imposes that this must also be the Bloch wavevector within the metasurface. QNMT modeling with such excitation may seem intractable at first glance, if one tries to obtain a full band diagram to apply QNMT at each fixed real $k^{\perp}$. However, we calculate the relevant QNMs are those calculated from a *nonlinear* eigenproblem, where the phase matching condition is imposed at the complex eigenfrequency by analytic continuation (thus giving a complex Bloch wavevector $k_n^{\perp} = \omega_n \sin\theta/c$). To find such unusual resonances, we developed software for two-dimensional (2d) dielectric structures, whose geometry can be split into uniform layered sections: at any complex ω, these complex Bloch modes are calculated within each section with a T-matrix formulation, then matched at interfaces between sections, and finally radiation conditions are applied to find the resonances (similar to CAMFR [104] and other interface mode-matching analyses [105, 106]).

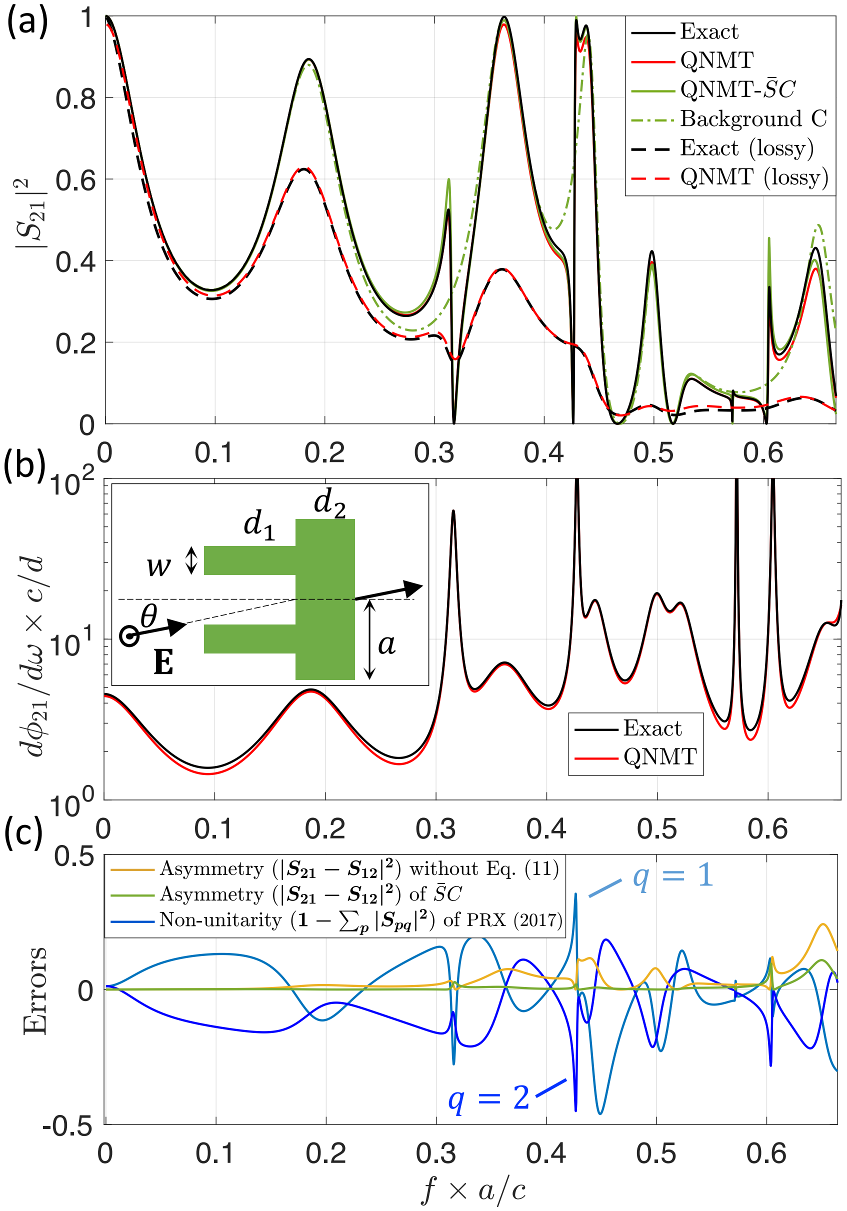

Figure 3-4: QNMT modeling of transmission of obliquely incident ($\theta = 30°$) TE plane wave from a dielectric ($\epsilon = 11$) grating with $w/a = 0.4$ and $d_i/a = (0.6, 0.4)$ so $d = d_1 + d_2 = a$. The lossy structure has $\epsilon = 11 + 0.77i$ (loss tangent $\tan\delta = 0.07$).

We then study scattering of a plane wave incident at a 30° angle on a 2d photonic grating with its **E**-field transverse to the plane [inset of Fig. 3-4(a)]. For frequencies below the first diffraction cutoff $f_{\text{cut}} = c/a(1+\sin\theta)$, the system again has only 2 ports. In Fig. 3-4(a,b), we show transmission, calculated both exactly (black curves) and with our QNMT (red curves). The agreement is indeed very good all throughout the range. The QNMTs without unitarity or symmetry reach errors ~ 0.5 and ~ 0.25 respectively [Fig. 3-4(c)]. We highlight that QNMTs are expected to improve as more (higher-frequency) modes are included, however, the non-unitary formulation [6] exhibits large errors even down to very low frequencies. Transmission is also plotted in the case of strong dielectric losses and it highlights that our perturbative approach works very well, even though now (due to absorption) several modes have decay rates $\tilde{\Gamma}_n$ more than an order of magnitude larger than their rates Γ_n for the lossless structure (see QNMs in Appendix-B).

3.5 Background scattering representation by low-Q modes

In some design situations, as we will see in Chapter 4, one needs an effective slowly-varying background response, which has to be designed collectively and in conjunction with the high-Q modes. This background response (responsible also for the concept of Fano resonances [80]) is usually modeled in standard CMT via the direct-coupling matrix C in Eq. (3.2). In most cases, researchers have approximated C by simulating an effective background structure derived by some type of topology averaging which removes the high-Q resonances, with parameters chosen *a posteriori* for a best fit [17,78,81]. Here, we show how C can be calculated using the actual structure under study by appropriately combining its low-Q modes, providing also intuition for this dependency and its physical interpretation. Given the background C, we also derive how the total S can be computed and we test it for the electromagnetic examples of section 3.4.

3.5.1 QNMT with background C matrix

Consider a lossless system supporting some high-Q resonant modes ($\omega_n = \Omega_n - i\Gamma_n,\ D_n$), while the rest ($\omega_n^C = \Omega_n^C - i\Gamma_n^C,\ D_n^C$) have much smaller Q (Fig. 3-1). Starting from Eq. (3.5), we combine these low-Q-mode terms within the sum to define $C(\omega) \equiv S_{\{\omega_n^C, D_n^C\}}(\omega)$, so that S takes the form of Eq. (3.4), with Ω including only the high-Q modes. In the limit $\Gamma^C \to \infty$, C becomes a frequency-independent matrix, which is unitary, since $S(\omega \to \infty) = C$. Therefore, we can use Eqs. (3.10) to calculate C and Eq. (3.17) to guarantee its symmetry. In this process, $M_{nl}^C \approx \sum_{p=1}^{P} D_{pl}^C D_{qn}^{C*} / \left(\Gamma_l^C + \Gamma_n^C\right)$, so the $\Gamma_n^C \to \infty$ cancel out between M^C and the C-denominator poles, leading to a constant C not necessarily equal to $-I$. In the next subsection, we calculate this limiting C for some simple but useful pole configurations. Now, for the total S-matrix of Eq. (3.4), following the same procedure for energy conservation in the subsection 3.3.2 but with $-I$ replaced by a unitary symmetric constant C, one can easily see that $S^\dagger S = I$ is now equivalent to $K^t = -M^{-1}D^\dagger C$. Therefore, the background C can be factored out of Eq. (3.4) to write:

$$\begin{aligned} S = \bar{S}C &= \left[I + D(i\omega - i\Omega)^{-1}M^{-1}D^\dagger\right] C \\ \Leftrightarrow S_{pq} &= C_{pq} + \sum_n \frac{D_{pn}\sum_l M_{nl}^{-1}\sum_r D_{rl}^* C_{rq}}{i\omega - i\omega_n}. \end{aligned} \tag{3.23}$$

Here, $\bar{S}$ has the form of a separate scattering matrix, which itself also satisfies realness, unitarity and the properties of Eqs. (3.19, 3.20). The condition of Eq. (3.16), to additionally impose exact symmetry on S, is modified to

$$D_{qn}\sum_l M_{nl}^{-1}\sum_r D_{rl}^* C_{rp} = D_{pn}\sum_l M_{nl}^{-1}\sum_r D_{rl}^* C_{rq} \Leftrightarrow CD^* = -D\Lambda M^t, \tag{3.24}$$

through which a fine-tuned D can be evaluated by an optimization procedure, as before, to obtain the final S.

Such extremely-low Q modes are very difficult to locate numerically. Thankfully, in practice, real systems usually have modes with reasonably low Q, which are easier to find. However, the problem then is that their associated $C(\omega)$ is slowly varying instead of constant and is *not* necessarily unitary (as it does not describe a physical system by itself). Nevertheless, we can still use Eq. (3.10) for those low-Q modes to obtain a unitary (thus approximate) C, symmetrize it with Eq. (3.17), and then use Eq. (3.23) with the high-Q modes inside $\bar{S}$ to get S simply as a best-effort *approximation* to the actual system response. This $\bar{S}C$ construction still guarantees that S will also satisfy realness $[S^*(\omega) = \bar{S}^*(\omega)C^*(\omega) = \bar{S}(-\omega^*)C(-\omega^*) = S(-\omega^*)]$ and unitarity ($S^\dagger S = C^\dagger \bar{S}^\dagger \bar{S} C = I$), but does *not* guarantee reciprocity ($S^t = C^t \bar{S}^t \neq \bar{S}C = S$) even though $C^t = C$ [at least, unitarity implies $|S_{12}| = |S_{21}|$ for a 2-port]. Attempts to symmetrize S (for example, [7]) are not expected to have much success: if it were possible to exactly satisfy also reciprocity for a varying $C(\omega)$, one would then be able to build a unitary and symmetric S by multiplying

---

[7] One could, for example, use the approximation that, within the bandwidth of each high-Q resonance in Eq. (3.23), $C(\omega) \approx C(\omega_n)$, which translates to substituting $C_{pq} \to C_{pq,n}$ in the symmetrization condition Eq. (3.24). However, this only gives an approximate condition that does not improve much on the original result.

unitary and symmetric C matrices formed by individual modes, which obviously is not possible. Regardless, as we show later in examples, for many physical systems, $S = \bar{S}C$ is a good enough approximation, which we use in separate Chapter 4 to design accurate metasurface standard (e.g. elliptic) filters with a non-trivial background. In such design situations where a specific background is desired, $C = \bar{S}^{-1}S$ can alternatively be used to estimate and then design $C(\omega_c)$ at the target frequencies ω_c without having to calculate any low-Q modes, rather by using $S(\omega_c)$ from a direct simulation and $\bar{S}(\omega_c)$ from QNMT using only the high-Q modes.

3.5.2 C matrix due to $\Gamma \to \infty$ modes in 2-port systems

In this subsection, we study some very basic configurations of high-Γ modes (ω_n^C, σ_n^C) in 2-port systems to build intuition on their influence in shaping the background scattering. (For notational simplicity, here we drop the superscript "^{C}".)

Single zero-frequency mode $(-i\Gamma_\mathrm{o}, \sigma_\mathrm{o})$

Consider a 2-port system supporting a zero-frequency mode $\omega_\mathrm{o} = -i\Gamma_\mathrm{o}$. As explained above, when $\Gamma_\mathrm{o} \to \infty$, this mode can be factored out of S into a unitary symmetric background response C. The symmetry of C dictates that the modal ports-coupling ratio σ_o is *real*. Using Eq. (3.18) for just this mode, we find $M = (1+\sigma_\mathrm{o}^2)/2\Gamma_\mathrm{o}$ and then

$$\begin{aligned} C_{pq} = -\delta_{pq} - \frac{\sigma_{p\mathrm{o}} M^{-1} \sigma_{q\mathrm{o}}}{i\omega - \Gamma_\mathrm{o}} &\xrightarrow{\Gamma_\mathrm{o} \gg |\omega|} -\delta_{pq} + \frac{2\sigma_{p\mathrm{o}}\sigma_{q\mathrm{o}}}{1+\sigma_\mathrm{o}^2} \\ \Leftrightarrow\ C = \begin{pmatrix} r & t \\ t & -r \end{pmatrix};\ r &= \frac{1-\sigma_\mathrm{o}^2}{1+\sigma_\mathrm{o}^2},\ t = \frac{2\sigma_\mathrm{o}}{1+\sigma_\mathrm{o}^2}, \end{aligned} \tag{3.25}$$

which can give any "reflection matrix" in the orthogonal group $O(2)$. A given transmission t is achieved for

$$\sigma_\mathrm{o} = \frac{1}{t} \pm \sqrt{\frac{1}{t^2} - 1}. \tag{3.26}$$

In particular, we obtain $r = 1$ for $\sigma_\mathrm{o} = 0$, while $r = -1$ for $\sigma_\mathrm{o} \to \infty$. On the other hand, $\sigma_\mathrm{o} = \pm 1$ gives a fully-transmissive background with $t = \pm 1$.

A concrete example which confirms this last result comes from considering a uniform material slab with thickness d and refractive index $\tilde{n}$. Its "Fabry–Perot" modes are an equi-spaced spectrum given by [82]

$$\omega_n = \frac{2c}{\tilde{n}d}\left(\frac{n\pi}{2} - i \cdot \mathrm{atanh}\frac{1}{\tilde{n}}\right),\ \sigma_n = (-1)^n. \tag{3.27}$$

Consider now appropriately large $\tilde{n}$, so that $\operatorname{atanh}(1/\tilde{n}) \ll \pi/2 \Leftrightarrow \Gamma_\mathrm{o} \ll \Omega_1$. Then, at frequencies of interest $0 < \omega \ll \Omega_1$, the modal contribution ($\sim \Gamma_\mathrm{o}/\Omega_n$) is negligible for all $n \neq 0$. In the limit $d \to 0$, indicating the absence of slab, the only relevant $n = 0$ system mode has $\Gamma_\mathrm{o} \to \infty$. Therefore, perhaps counter-intuitively, full transmission can be seen as equivalent to such a mode at $0 - i\infty$ with $\sigma_0 = 1$.

This result of $t = 1$ for a zero-thickness slab is a consequence our initial phase choice $C' = -I$ in Eq. (3.5). If we had instead chosen $C' = +I$, we would have obtained $t = -1$ for zero thickness, which would be a valid but awkward phase convention.

Conjugate-modes pair $[(\omega_\mathrm{o}, \sigma_\mathrm{o}), (-\omega_\mathrm{o}^*, \sigma_\mathrm{o}^*)]$

Let us now consider a single mode $\omega_\mathrm{o} = \Omega_\mathrm{o} - i\Gamma_\mathrm{o}$ with $\Omega_\mathrm{o} \neq 0$, together with its negative (paired) mode at $-\omega_\mathrm{o}^*$. The symmetry of the associated background matrix C again requires a real σ_o, and Eq. (3.18) gives

$$\begin{aligned} C_{pq} =& -\delta_{pq} - \frac{2\sigma_{p\mathrm{o}}\sigma_{q\mathrm{o}}}{1+\sigma_\mathrm{o}^2} \frac{i2\Gamma_\mathrm{o}\omega}{[i(\omega - \Omega_\mathrm{o}) - \Gamma_\mathrm{o}][i(\omega + \Omega_\mathrm{o}) - \Gamma_\mathrm{o}]} \\ \Rightarrow\ & C_{pq}(\Omega_\mathrm{o}) = -\delta_{pq} + \frac{2\sigma_{p\mathrm{o}}\sigma_{q\mathrm{o}}}{1+\sigma_\mathrm{o}^2} \frac{1}{1 + i\Gamma_\mathrm{o}/2\Omega_\mathrm{o}}. \end{aligned} \tag{3.28}$$

When $|\omega - \Omega_\mathrm{o}| \ll \Gamma_\mathrm{o} \ll 2\Omega_\mathrm{o}$ (so that RWA holds), $C(\omega \sim \Omega_\mathrm{o})$ again takes the single-mode value of Eq. (3.25) independent of Ω_o. Instead, when $\Gamma_\mathrm{o} \gg 2\Omega_\mathrm{o}$, the two broad resonances effectively cancel each other and $C \approx -I$.

Two uncoupled modes $[(\omega_1, \sigma_1), (\omega_2, \sigma_2)]$

Two modes with $\Omega_{1,2} \neq 0$ and $\sigma_1\sigma_2^* = -1$ do not couple [$M_{12} = 0$ in Eq. (3.18)] and their pole contributions add up independently in $C(\omega)$. Symmetry of their C again forces $\sigma_1 = -1/\sigma_2$ to be real. [This is the case of an even ($\sigma_1 = 1$) and an odd ($\sigma_2 = -1$) mode. Another example with $\sigma_1 \to 0^\pm$ and $\sigma_2 \to \mp\infty$ can occur for a strongly reflecting mirror, where each mode is localized on one of the two asymmetric sides and couples mainly to one port, thus defining two essentially disjoint 1-port systems.] Under the RWA $|\omega - \Omega_{1,2}| \ll \Gamma_{1,2} \ll 2\Omega_{1,2}$, the pole contribution of each mode is like the one in Eq. (3.25) and then $C(\omega \sim \Omega_{1,2}) \approx I$. However, in the limit $\Gamma_{1,2} \gg 2\Omega_{1,2}$, their negative poles cannot be ignored, the contributions are as in Eq. (3.28), and the result is instead $C \approx -I$.

Equi-spaced (Fabry–Perot) modes $[n\omega_\mathrm{o} - i\Gamma_\mathrm{o}, (-1)^n]$

When the structure has localized resonant elements but does not exhibit very strong overall reflection, the background response is commonly assumed to arise from the averaged geometry. When this is a simple uniform material slab, it corresponds to a Fabry–Perot system with the infinite set of equi-spaced alternating-symmetry modes given in Eq. (3.27) and a "comb" transmission response (see e.g. Fig. 3-5 blue circles and dashed lines). In the limit $\tilde{n} \to 1$, the system approaches a slab of free space of thickness d and its array of modes (equi-spaced by $\pi c/d$) is shifted down towards $-i\infty$. The corresponding limiting value of C is simply the scattering matrix for propagation through d, namely $|C_{21}| \to 1$ and $d\phi_{21}^C/d\omega \to d/c$.

One-sided equi-spaced modes $[n\omega_\mathrm{o} - i\Gamma_\mathrm{o}, 0 \textit{ or } \infty]$

When instead the structure has strongly reflective components separating the two ports, the background response will comprise low-Q modes with fields mostly localized on either of the two port sides, thus having $|\sigma_n| \ll 1$ or $|\sigma_n| \gg 1$ respectively, adding up to $|C_{11}|, |C_{22}| \approx 1$. If the average geometry on one side is a uniform material slab of thickness $d/2$ on a perfect mirror, its modes will again be Eq. (3.27) but for only odd or only even n. As $\tilde{n} \to 1$ and $\Gamma_\mathrm{o} \to \infty$, its round-trip reflection phase approaches $d\phi_{11}^C/d\omega \to d/c$.

From the last two examples, note that, although a conjugate-mode pair gives $C \approx -I$ in the large-Γ limit, when considering many such modes, their small pole contributions (deviations from $-I$), $\propto i2\omega/\Gamma_\mathrm{o}$ from Eq. (3.28), add up to give a non-trivial phase term (in transmission or reflection).

3.5.3 Choice of boundary for D calculation and C-matrix description of a port shift

In our QNMT formulation, we suggest calculating the coupling coefficient D_{pn} as an overlap between the QNM n and the CPM p at the latter's cross-section z'_p which first touches the scatterer boundary [Eq. (3.3)]. A reasonable question is whether such a choice is always appropriate, especially in unusual geometries where a thin "needle" sticks out from the scatterer or when very-low-index materials surround the scatterer. In such scenarios, the QNMs are expected to be localized close to the center of the scatterer and likely are already exponentially increasing inside the suggested outermost boundary. Here, we study a simple such photonic structure to explain the physics that come into play to

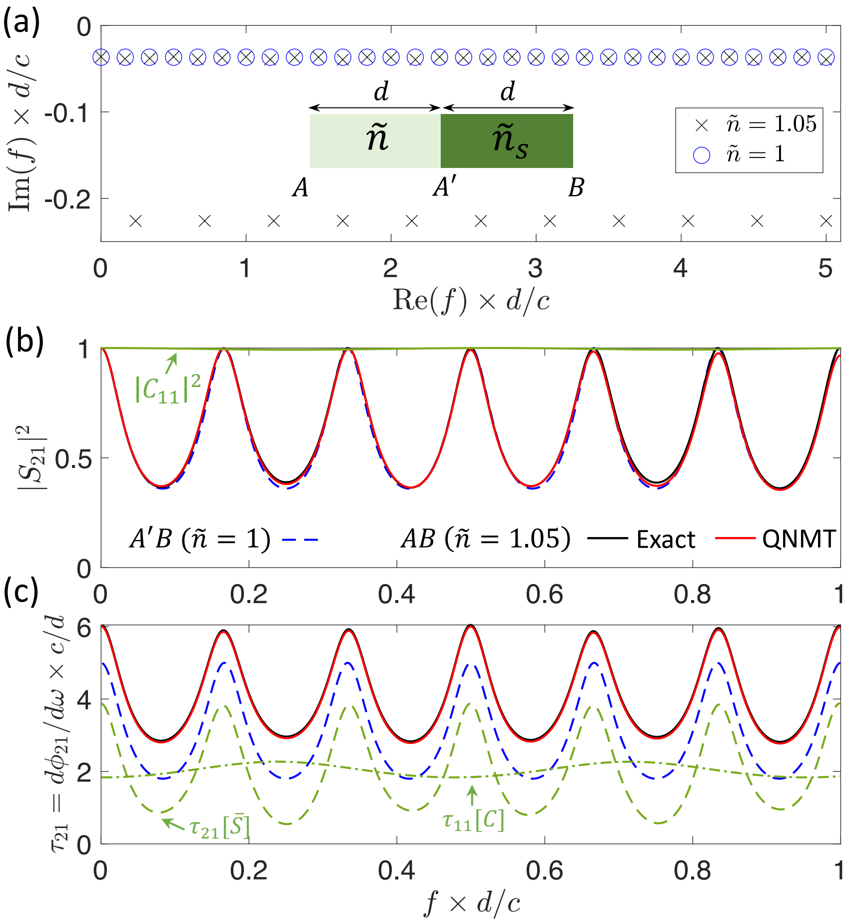

Figure 3-5: Normally incident plane wave transmission through slabs with indices $\tilde{n}_s = 3$, $\tilde{n} = 1.05$ and thickness d (black for exact result and red for QNMT prediction), and comparison to the limiting case of $\tilde{n} = 1$ (blue for exact result). (a) Geometry and poles, (b) amplitude and (c) group delay: the small shift is due to the extra propagation through the A–A′ slab, predicted by QNMT primarily via the contribution of the low-Q modes, as can be seen also from the $\bar{S}C$ approximation (green) where $S_{21} \approx \bar{S}_{21}C_{11}$ gives the correct delay $\tau_{21} \approx \tau_{21}[\bar{S}] + \tau_{11}[C]$.

render our boundary choice indeed suitable and we show how the $S = \bar{S}C$ formulation can give an interesting physical interpretation.

A plane wave at frequency $f = \omega/2\pi$ is normally incident on a uniform material slab of refractive index $\tilde{n}_s = 3$ and thickness d that is attached to another slab of the same thickness but with $\tilde{n} = 1.05$ (Fig. 3-5 inset). As a reference, the limiting symmetric system with $\tilde{n} = 1$ and ports' cross-sections A′, B on the boundaries of the $\tilde{n}_s$ slab has the response shown in Fig. 3-5 for (a) the poles (blue circles) with $\sigma_n = \pm 1$, (b) transmission amplitude and (c) phase delay (blue dashed lines). The response of the actual test system (shown with black 'x' and lines) obviously approaches that of the limiting case in amplitude and has an additional phase delay due to the propagation through the $\tilde{n}$ slab A–A′ [Fig. 3-5 (b,c)]. It may be tempting to think that the two systems should have the same QNMT parameters (ω_n, σ_n). However, its high-Q modes now have σ_n different from ± 1 (e.g. $\omega_n d/2\pi c = 0.165 - 0.039i$ has $\sigma_n = -0.45 + 0.68i$), exactly because they are calculated on our suggested boundary $z'_p = \mathrm{A}$ and the structure between A–B is asymmetric. How can we then expect QNMT to give an accurate prediction? The key lies in a set of very-low-Q modes ω_n^C that are supported mainly by the weakly scattering $\tilde{n}$ slab [Fig. 3-5(a) below the inset] and have highly asymmetric $|\sigma_n^C| \ll 1$ [e.g. $\omega_n^C d/2\pi c = 0.24 - 0.23i$ has $\sigma_n^C \sim 10^{-3}(1 + 1i)$]. As $\tilde{n} \to 1$, their $\Gamma_n^C \to \infty$ and, when taken into account, the QNMT prediction of S gives the correct result with the additional expected group delay through A–A′.

To clearly understand the effect of the low-Q modes, we separate them into a background response C, shown in green lines in Fig. 3-5. We see that C is almost a diagonal matrix [$|C_{11}|^2 \approx 1$ in Fig. 3-5(b)] and that C_{11} represents a group delay equal to $2d/c$ [Fig. 3-5(c)]. Indeed, this spectrum of low-Q-modes matches the "one-sided equi-spaced modes" of the previous subsection: due to $n_s \gg n$, A' acts as a highly reflective boundary, so τ_{11}^C models the roundtrip phase propagation through $A \to A' \to A$. The group delay of $\bar{S}_{21}$ through A–B is surprisingly reduced (and not increased!) by d/c compared to the A′–B S_{21}, and that is because the high-Q modes have modified σ_n values. In this way, $S_{21} \approx \bar{S}_{21} C_{11}$ works out correctly to give the required additional group delay d/c. It is worth reminding that $\bar{S}$ does not have to be symmetric. In fact, oppositely to $\bar{S}_{21}$, the A–B $\bar{S}_{12}$ has group delay *increased* by d/c compared to the A′–B transmission, so that, combined with $C_{22} \approx -1 \neq -e^{i\omega 2d/c} \approx C_{11}$, we get the correct $\bar{S}_{12} C_{22} \approx S_{12} = S_{21} \approx \bar{S}_{21} C_{11}$.

We conclude that all structural features contribute to scattering, which may be expressed via low-Q modes that need to be included in the QNM expansion. This justifies our choice of surface for the calculation of D in Eq. (3.3) to be the closest port cross-section that encloses the entire scatterer z'_p. For a different port choice z_p, additional (practically impossible to locate) infinite-Γ modes would need to be accounted for to express the extra phase shift through $z_p - z'_p$.

3.5.4 Examples of Section 3.4

We finally test this formulation on the 2-port electromagnetic structures of Figs. 3-2 & 3-4 by using the modes with lowest Qs (much lower than the other modes) to construct the C matrix [see modes in Fig. 3-2(c)]. C_{21} indeed yields a slowly-varying transmission background, as shown in Figs. 3-2(a) & 3-4(a) (green dash-dotted lines). Sharp features in

S_{21} are then obtained by the high-Q modes within the $\bar{S}C$ formulation (green solid lines), which actually gives a very good approximation of the overall transmission amplitude spectrum. Due to the remaining asymmetry of $\bar{S}C$, we find that there are some errors in the group-delay prediction close to transmission zeros, but these errors are reduced when considering realistic finite-bandwidth pulses.

The 4-port structure of Fig. 3-3 has large connected metallic sheets, so it exhibits some very-low-Q “one-sided equi-spaced modes" (Sec. 3.5.2) due to the outermost dielectric layers that only couple ports on the same side (namely they have $\sigma_{r,pq} \to 0$ or ∞ for p, q in opposite sides, so that $|C_{pq}| \to 0$). This explains the sharp features observed in S_{41}, as only high-Q modes contribute to it. Moreover, the layers in this example are very thin, so these low-Q modes are located very far from the frequencies of interest anyway.

3.6 Conclusions

In this chapter, we have presented an expansion of the system scattering matrix S over non-normalized QNMs, formulated to satisfy the fundamental physical conditions of realness, energy conservation and reciprocity even for a small truncated number of terms. Resonant QNMs with frequencies ω_n are computed with a numerical eigensolver. Coupling coefficients D_{pn} are evaluated as surface overlap integrals between normalized-CPM and non-normalized-QNM fields (as only ratios $\sigma_{r,pn} = D_{pn}/D_{rn}$ are needed). Negative-frequency modes $(-\omega_n^*, D_{pn}^*)$ are included. The D matrix is then adjusted through Eq. (3.17) and S is finally calculated via Eq. (3.10). For applications where it is convenient to separate an effective background response from the high-Q resonances, C can be determined by the same procedure using only the low-Q resonances, with $\bar{S}$ from the high-Q modes, and then $S \approx \bar{S}C$. In Sec. 3.5.2, we discussed several limiting cases, and showed that a nearly frequency-independent C with nonzero transmission can be produced by a very-low-Q mode on the imaginary-frequency axis, while a propagation phase is modeled by a set of several low-Q modes. The agreement of our QNMT with exact simulations gives us confidence that it can be successfully employed for rapid device design. In the next chapter, we indeed use this formulation to design precise standard (especially elliptic) high-order filters.

Our QNMT was mainly developed for linear ports with frequency-independent transverse mode profiles, such as plane waves. However, it could also be extended to finite arbitrary-shape scatterers using a spherical CPM basis. (Note that systems with spherical symmetry studied in previous QNMT formulations [6, 79] can be modeled merely as multiple 1-ports, so QNMT was not really needed, as explained in the overview.) Difficulties arise with other types of ports, such as when QNM-to-CPM coupling coefficients $D(\omega)$ are frequency dependent, and specifically when the S matrix has branch points due to CPM cutoff frequencies. While a rigorous extension of the theory to such systems may require a different approach, our model may still provide good approximate results for slowly varying coupling coefficients (such as for dielectric waveguides with low waveguide dispersion).

Chapter 4

Few resonances 2: Filter design criteria with application to microwave metasurfaces[1]

4.1 On resonances

In the previous chapter, we derived a general expansion for the scattering matrix based on enforcing fundamental physical constraints. As highlighted there, such formalism is general and does not necessarily depend on a specific physics. The most simple example corresponds to transfer functions of electronic circuits, which are equal to rational functions determined by their poles, zeros, and an overall constant factor. In signal processing, such rational transfer functions are used to obtain standard approximations to ideal peacewise constant filters [16]. A corresponding physical electronic circuit can then be designed using network synthesis [16]. This filter design approach is usually restricted to systems with distinct components (e.g. electronic circuits) where the elements (e.g. capacitors and inductors) can be independently tuned to achieve the desired response. As we describe later, for certain applications and wavelength regimes, the different "componants" of the system (e.g. individual resonators) cannot be designed independently as they are strongly coupled and affect each others properties (e.g. resonance frequency) when they are "put together". In this case, the system should be considered as a whole in the design. Since our QNMT theory in Chapter 3 allows us to compute a rational function approximation of the scattering matrix directly using the quasi-normal modes of the full system, we can use it to derive universal analytical criteria for standard-filter de-

---

[1] Our work on this topic was published in Ref. 19.

sign. These can in principle be used in all areas of wave physics to design general devices, which can be seen as a black boxes, as long as we can compute their quasi-normal modes. In this chapter, we derive such universal filter design criteria and apply our method to design microwave metasurfaces implementing standard amplitude filters of various types, orders and bandwidths. In the next section, we first give a brief overview on filters and design methods and describe the structure of the rest of the chapter.

4.2 Overview

High-order (multi-resonance) filters—especially ideal standard filters (ISFs), such as Butterworth or elliptic [16]—have been designed for many types of wave physics (electromagnetic [20, 107–116], mechanical [117–121], etc.) by a variety of techniques, including brute-force optimization of the transmission/scattering spectrum [122–125], circuit theory in the microwave regime [126–135], and coupled-mode theory (CMT) [17, 71, 136] for cascaded optical resonators [107–113]. Circuit theory and CMT provide attractive semi-analytical frameworks for filter design, but are restricted to systems composed of spatially separable components (either discrete circuit elements or weakly coupled resonances, respectively), while brute-force spectrum optimization faces several numerical challenges. To design ultra-compact filters, involving strongly coupled elements and spatially overlapping resonances, a precise, systematic and computationally tractable methodology is missing. In this chapter, we develop a new such filter-design approach by deriving a minimal set of explicit *analytical* criteria on the system resonances, applicable to all symmetric and “antimetric” [137] filters, including ISFs. To derive these conditions, we use the unitary and symmetric quasi-normal-mode (QNM) expansion of the scattering matrix S from Chapter 3 to derive the required coupling coefficients of the resonances (QNMs) to the input and output ports in conjunction with the net background response, in order to achieve multiple configurations for the zeros of the S coefficients (generalizing previous work [138, 139]) and thus realize any desired ISF. We apply our procedure to computationally design microwave metasurface filters that precisely match ISFs of various orders, bandwidths, and types—especially optimal elliptic filters, which were demonstrated only approximately in the past [125–129].

Large-scale optimization (including a variety of inverse-design and machine-learning algorithms) is a powerful approach to design complex structures by optimizing thousands of degrees of freedom [140, 141]. However, if the optimization problem is formulated directly in terms of matching a desired transmission spectrum, it can face severe numerical challenges: the highly oscillatory nature of the transmission spectrum can trap optimizers in poor local optima, and stringent constraints (e.g. on stop- and pass-band transmission) can lead to very "stiff" optimization problems with slow convergence. One proposed solution was to restrict the designs to spatially distinct resonators as in CMT [142]. However, when analytical solutions to *parts* of the problem exist, the numerical side of the optimization can be rendered simpler and more robust. For filter design in particular, signal-processing theory analytically defines many such "optimal" filters (ISFs), characterized by various rational transfer functions with specified poles and zeros, the latter necessary to achieve a steep transition between the "pass" and "stop" frequency bands. Therefore, when designing physical filters, it is advantageous to exploit these analytical solutions. An exact methodology, called network synthesis, was developed to implement these ISFs in the extreme quasi-static (subwavelength) limit, where structures can be modeled precisely by networks of discrete elements, as in electronic circuits [16]. In the other limit of structures spanning multiple wavelengths, the simple mapping between coupled resonators and transfer-function poles has made temporal coupled-mode theory (CMT) [17, 71, 136] a popular design tool, especially for (high-order) optical add-drop filters [107–112], most of which are only Chebyshev or Butterworth filters with no transmission-zeros, using a symmetric topology. However, in the intermediate limit of physical structures with size on the order of the wavelength or only a few times smaller (metamaterials), no complete filter-design methodology exists. Discrete-element equivalent networks must often become overly complicated to model the full-wave physics accurately and they change for each different structural topology [133] or, worse, they fail to provide any adequate model (as is typically the case in dielectric photonic structures). Therefore, network synthesis may be useful for the intuitive choice of an appropriate system topology but not for the calculation of its exact parameters. CMT, on the other hand, is typically based on weakly coupled resonators and the knowledge of the "uncoupled" modes of the system [17], but neither of these conditions usually hold for wavelength-scale structures with multiple strongly inter-coupled/overlapping resonances [143]. Still missing has been a unified, physics-independent, set of exact conditions for the precise design of filters with multiple zeros that can be fed as a smooth objective to optimization algorithms. Using our QNM theory (QNMT) from Chapter 3, in Sec. 4.4 we derive such simple and general rules to design ISFs using eigenmode solvers. In particular, we show that the resonant QNM fields of *all* lossless reciprocal 2-port systems with symmetric ($S_{22} = S_{11}$) or "antimetric" ($S_{22} = -S_{11}$) [137] response couple to the input and output ports with specific unitary ratios, whose relative signs determine the position of the scattering zeros. Thus, for filter design, apart from the obvious matching of system resonant frequencies to the desired filter's complex poles, we explain that, to also obtain the desired-filter zeros, these ratios must be enforced for the critical filter resonances and the remaining QNMs must add up to a required overall background response.

As an application of our theory, we design microwave frequency selective surfaces (FSS), which are usually used to implement spatial (wave) filters for communication antennas, radars, radomes [20,115,116], lenses [144,145] etc. FSSs typically take the form of two-dimensional periodic metal-dielectric arrays exhibiting specific frequency-dependent transmission or reflection under planewave excitation. While older designs were based on wavelength-sized unit cells (as in typical antenna design), the use of subwavelength dimensions to form metasurfaces has attracted much attention in the past decade due to multiple advantages, such as higher unit-cells density and smaller angular sensitivity [130,131,146]. An important design challenge in frequency-selective metasurfaces is the ability to obtain specific high-order frequency responses using their strongly inter-coupled subwavelength resonances, attempted usually through multilayer FSSs. Most previous efforts have been based on effective-circuit models [130–135]. The basic FSS building blocks are metallic patches with gaps (effective capacitors C) and apertures/loops (effective inductors L) that can be combined to make effective LC resonators. Then, the shape, size and arrangement of patches and apertures in the FSS dielectric and metallic sheets are designed to accomplish the necessary circuit topology and element-values for the transmission desired. While such circuit models can give a good physical intuition about the expected response of a FSS, they are too approximate and less flexible for a precise design method (as explained above). This is why, although particular attention has been given to the design of elliptic filters, most of previous efforts have only achieved an approximate "quasi-elliptic" response [125–129]. In Sec. 4.5, we discuss the relation between QNMT and effective-circuit models to motivate appropriate structural-topology choices for different filters and scattering-zero placements. However, following our systematic filter-design procedure, we then implement microwave metasurfaces that exhibit, for a normally incident plane wave, transmission spectra matching ISF responses of various orders, bandwidths and types. Notably, we demonstrate second- and third-order elliptic filters for both bandpass and bandstop behaviors. We show that, in some cases, even though symmetric performance is desired, structural asymmetry should be used, while conversely, in cases where the ideal performance is antimetric, we also present approximate symmetric solutions. The designed metasurfaces are compatible with fabrication by printed-circuit board technology, and also offer potential electrical tunability.

4.3 S-matrix of lossless reciprocal 2-port systems

We consider a linear time-independent reciprocal system, without material absorption or gain (although these could easily be included perturbatively as described in subsection 3.3.4), coupled to radiation only via two ports. These are used as channels for an incoming excitation at frequency ω and outgoing scattered waves, described by a 2×2 scattering matrix S (Fig. 4-1). Here, we summarize some key properties of S and its QNMT model, derived in Chapter 3, which we will need in this chapter.

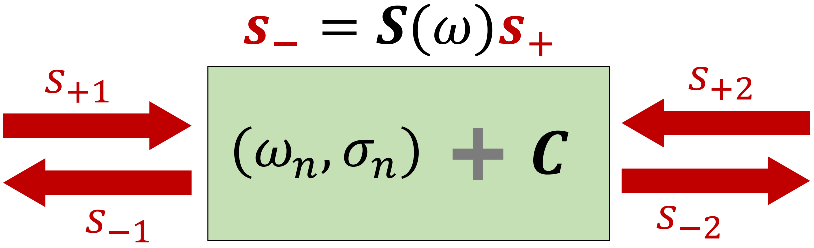

Figure 4-1: A lossless reciprocal 2-port scattering system excited at frequency ω, with input and output amplitudes respectively $s_{\pm p}$, related by the S-matrix through $s_- = S s_+$. The system supports high-Q quasi-normal modes (QNMs) with frequencies ω_n and port-coupling ratios σ_n, while low-Q resonances create an effective background response C.

To begin with, recall from subsection 3.3.3 that (i) the poles of S appear in pairs $(\omega_n, -\omega_n^*)$ due to realness $[S^*(i\omega) = S(-i\omega^*)]$; (ii) the zeros of $S_{21} = S_{12}$ can only appear as complex quadruplets $(\omega_o, \omega_o^*, -\omega_o, -\omega_o^*)$, real or imaginary pairs $(\omega_o, -\omega_o)$, or at $\omega_o = 0$; and (iii), for each zero-pair $(\omega_o, -\omega_o^*)$ of S_{11}, $(-\omega_o, \omega_o^*)$ is a zero-pair of S_{22}. These restrictions imply that S_{pq} is a rational function of $i\omega$ with real coefficients and, in particular, that the numerator of S_{21} is a polynomial of ω^2 with real coefficients, optionally with multiplicative $i\omega$ factors.

We consider the high-Q modes of the system with frequencies ω_n and coupling coefficients to the ports $p = 1, 2$ equal to D_{pn}, which can be computed as an overlap surface integral between the n-QNM field and the p-port mode at the boundary of the scatterer [e.g. Eq. (3.22)]. Their ratios $\sigma_n = D_{2n}/D_{1n}$ do not depend on the normalization of the QNMs. Moreover, any system low-Q resonances ω_n^C can admit a simplified description in terms of an effective "background" response between the two ports, quantified by a background scattering matrix C. When these background QNMs have $Q \to 0$, they give a frequency-independent unitary symmetric C. In this case, our QNMT formulation shows that, when the ports are referenced at the boundary of the scatterer, enforcing energy conservation (unitary S) gives:

$$\begin{gathered} S = \bar{S}C, \quad \bar{S} = I + \sum_{n=1}^{N} \frac{\bar{S}^{(n)}}{i\omega - i\omega_n}, \\ \bar{S}^{(n)}_{pq} = \sigma_{pn} \sum_{l=1}^{N} M^{-1}_{nl} \sigma^*_{ql}, \quad M_{nl} = \frac{1 + \sigma_l \sigma^*_n}{i\omega_l - i\omega^*_n}, \quad \sigma_{1n} = 1,\ \sigma_{2n} = \sigma_n, \end{gathered} \tag{4.1}$$

where σ_n are further fine-tuned from the computed values in order to satisfy also reciprocity (symmetric S via $[\bar{S}^{(n)}C]_{21} = [\bar{S}^{(n)}C]_{12}$), using a simple constrained optimization. C itself can be computed as $C = -\bar{S}_{\{\omega_n^C\}}$. In practice, the background Qs are small but nonzero, so C is slowly varying but not constant; nevertheless, Eq. (4.1) provides a good approximation for S. The distinction between high- and low-Q modes is, in fact, somewhat arbitrary and based mainly on computational convenience. In the limit where one includes all modes in $\bar{S}$, then $C = -I$.

$\bar{S}$ in Eq. (4.1) is *uniquely* determined by the values $\{\omega_n, \sigma_n\}$ and can be easily shown [18] to satisfy, for $\gamma = \pm 1$ (extended to complex γ in Sec. 4.4),

$$\begin{aligned} \bar{S}_{11\{\omega_n,\gamma\sigma_n\}} &= \bar{S}_{11\{\omega_n,\sigma_n\}},\ \bar{S}_{12\{\omega_n,\gamma\sigma_n\}} = \gamma^* \bar{S}_{12\{\omega_n,\sigma_n\}} \\ \bar{S}_{21\{\omega_n,\gamma\sigma_n\}} &= \gamma \bar{S}_{21\{\omega_n,\sigma_n\}},\ \bar{S}_{22\{\omega_n,\gamma\sigma_n\}} = \bar{S}_{22\{\omega_n,\sigma_n\}}. \end{aligned} \tag{4.2}$$

and, by swapping ports 1 ↔ 2,

$$\bar{S}_{11\{\omega_n,\sigma_n\}} = \bar{S}_{22\{\omega_n,1/\sigma_n\}},\ \bar{S}_{21\{\omega_n,\sigma_n\}} = \bar{S}_{12\{\omega_n,1/\sigma_n\}}. \tag{4.3}$$

4.4 Filter Design

Our goal is to design physical 2-port systems with standard network-synthesis filter responses, specifically N^{th}-order band-pass and band-stop filters of a finite bandwidth, which are given as rational functions of frequency $H(\omega)$ with specified $2N$ complex poles [appearing as N pairs $(\omega_n, -\omega_n^*)$], $2N$ zeros (abiding by the restrictions detailed in subsection 3.3.3) and an overall constant. Attempting this design by optimizing over structural parameters to find a scattering-matrix that matches specific values of the desired $H(\omega)$ at a finite set of key frequencies can be very difficult in practice, as this highly-resonant problem can present a vast number of local extrema and lead to "stiff" constraints [142]. Instead, the eigenmode-solver-derived components of a QNMT expansion have a much slower dependence on the physical structural parameters, so they yield a more tractable optimization formulation.

It is obvious that the complex resonant frequencies ω_n of the physical system must match the complex poles of the desired filter. In this work, we show how to also enforce the desired zeros in the system response, by deriving the corresponding σ_n coefficients and the matrix C. Specifically, $|C_{21}|$ must match the desired filter background transmission and then, for exact ISFs, we find that the ratios of couplings of the QNMs' fields to the two ports must be $\sigma_n = \pm 1$ for N odd or $\sigma_n = \pm i$ for N even, with alternating signs for consecutive modes. Enforcing $|C_{21}|$ and the N complex ω_n, σ_n results in a minimal set of $4N + 1$ real equations. We also explain that good approximate solutions can be obtained, if an overall common phase for all σ_n is allowed, according to Eqs. (4.12–4.15).

— **Symmetric and antimetric filters** — We explained in subsection 3.3.3 that, for a general lossless reciprocal 2-port system, the zeros of S_{11} and S_{22} are conjugates of each other, but they do not necessarily coincide. In this work, we are interested in the special cases of filters where they do coincide, so that these zeros can only appear as complex quadruplets $(\omega_o, \omega_o^*, -\omega_o, -\omega_o^*)$, real or imaginary pairs $(\omega_o, -\omega_o)$, or at $\omega_o = 0$. Their numerator is then also (as is always true for S_{21}) a polynomial of ω^2 with real coefficients, optionally with multiplicative $i\omega$ factors. These cases include, in particular, common practical amplitude filters, for which all zeros of reflection (S_{11} and S_{22}), corresponding to full transmission, lie on the real frequency axis or at infinity. To satisfy realness, this class of filters is collectively described by the condition $S_{22} = \pm S_{11}$, namely they are either symmetric or "antimetric" [137] (note [2]). Energy conservation and reciprocity then force $\sqrt{\gamma} S_{11} S_{21}^*$ to be purely imaginary for $\gamma \equiv S_{22}/S_{11} = \pm 1$, corresponding to (+) odd or (-) even number of $i\omega$ factors in the numerator of S_{11} or S_{21}.

The most important subclass comprises the ideal standard filter (ISF) approximations [16]: Butterworth (flat passband and stopband), Chebyshev (equiripple passband, flat stopband), inverse Chebyshev (equiripple stopband, flat passband) and elliptic (equiripple passband and stopband) (see Fig. 4-4). For a N^{th}-order Butterworth or Chebyshev transmission bandpass filter, S_{21} has N zeros at $\omega = 0$ (N $i\omega$-factors in numerator) and N zeros at $\omega \to \infty$ ($2N$ zeros total). For N^{th}-order inverse Chebyshev or elliptic filters, which have zeros at finite real frequencies, S_{21} still has one zero at $\omega = 0$ and one at $\omega \to \infty$ for N odd, while all $2N$ zeros are finite for N even (no $i\omega$ factors). For a transmission bandstop filter, the same observations hold instead for S_{11}. In all ISF cases, we conclude that $S_{11} S_{21}^*$ is purely imaginary ($\gamma = 1$), if N is odd, and purely real ($\gamma = -1$), if N is even.

---

[2] This should not be confused with a symmetric S matrix, which holds for a *reciprocal* system.

4.4.1 Conditions on C and σ_n

A partial-fraction expansion of the desired network-synthesis expresses $H(\omega)$ in terms of the complex poles, their residues, and a direct term t (which gives the limiting response at high frequencies according to the filter's type). Using the $S = \bar{S}C$ formulation of Eq. (4.1) for an actual physical system, we assume that C can be designed as approximately constant over the finite bandwidth of interest, where it can generally be complex. Far from the high-Q resonances ($\omega \gg |\omega_n|$), Eq. (4.1) dictates $\bar{S} \to I$ and thus $S \to C$. Therefore, for a transmission filter, one must design $|C_{21}| = t$. This provides design intuition for the topology of the structure, where appropriate low-Q modes are utilized to get the desired C, as we will see in practical examples later. During structural optimization, it may be difficult to find the low-Q modes contributing to C, in which case it can also be calculated efficiently as $C = \bar{S}^{-1}S$, where S is obtained via direct simulation of the structure (with the ports referenced at the scatterer boundary) and the filter-relevant high-Q modes are used to get a QNMT evaluation of $\bar{S}$.

For the class of filters of interest with $S_{22} = \gamma S_{11}$ ($\gamma = \pm 1$), $S \to C$ means that the unitary symmetric C also satisfies $C_{22} = \gamma C_{11}$ and that $\sqrt{\gamma} C_{11} C_{21}^*$ is purely imaginary. Now, since $\bar{S} = SC^{-1}$, we can write:

$$\bar{S} = \frac{1}{|C|} \begin{pmatrix} S_{11}\gamma C_{11} - S_{21}C_{21} & -S_{11}C_{21} + S_{21}C_{11} \\ S_{21}\gamma C_{11} - \gamma S_{11}C_{21} & -S_{21}C_{21} + \gamma S_{11}C_{11} \end{pmatrix} \tag{4.4}$$

so that $\bar{S}_{11} = \bar{S}_{22}$ and $\bar{S}_{21} = \gamma \bar{S}_{12}$. Further, using Eqs. (4.2, 4.3) for the dependence of $\bar{S}$ on σ_n:

$$\begin{aligned} \bar{S}_{11\{\omega_n,\frac{1}{\sigma_n}\}} &= \bar{S}_{22\{\omega_n,\sigma_n\}} = \bar{S}_{11\{\omega_n,\sigma_n\}} = \bar{S}_{11\{\omega_n,\frac{\sigma_n}{\gamma}\}} \\ \bar{S}_{21\{\omega_n,\frac{1}{\sigma_n}\}} &= \bar{S}_{12\{\omega_n,\sigma_n\}} = \tfrac{1}{\gamma}\bar{S}_{21\{\omega_n,\sigma_n\}} = \bar{S}_{21\{\omega_n,\frac{\sigma_n}{\gamma}\}}. \end{aligned} \tag{4.5}$$

The same result applies to $\bar{S}_{22}$ and $\bar{S}_{21}$, so we obtain $\bar{S}_{\{\omega_n,1/\sigma_n\}} = \bar{S}_{\{\omega_n,\sigma_n/\gamma\}}$. From the uniqueness property mentioned earlier, we conclude that $1/\sigma_n = \sigma_n/\gamma$. Therefore, for a lossless reciprocal 2-port system:

$$S_{22} = \gamma S_{11} \Leftrightarrow \sigma_n = \pm\sqrt{\gamma}, \tag{4.6}$$

so that all modes have $\sigma_n = \pm 1$ for a symmetric filter ($\gamma = 1$), while $\sigma_n = \pm i$ for an antimetric ($\gamma = -1$). (This generalizes the well-known CMT result for a single resonance, where transmission reaches 1 only for equal decay rates into the two ports [28].) Moreover, with this σ_n choice, $i\sigma_n C_{11} C_{21}^*$ is purely real.

In the particular case of ISFs, C is constant over all frequencies, so it must be real, to satisfy the realness condition. Consistently with $i\sigma_n C_{11} C_{21}^*$ real, odd-order ISFs have $\sigma_n = \pm 1$ and $C_{11} C_{21} = 0$, while $\sigma_n = \pm i$ for even order.

— **Transfer-matrix method** — Eq. (4.6) can be also derived using general arguments based on the transfer matrix as we show here. For a 2-ports system as in Fig. 4-1, the (forward) transfer matrix is defined as:

$$\begin{pmatrix} s_{+1} \\ s_{-1} \end{pmatrix} = \begin{pmatrix} T_{11} & T_{12} \\ T_{21} & T_{22} \end{pmatrix} \begin{pmatrix} s_{-2} \\ s_{+2} \end{pmatrix} \tag{4.7}$$

and is related to the scattering matrix via the transformation:

$$T = \frac{1}{S_{21}} \begin{pmatrix} 1 & -S_{22} \\ S_{11} & -\det(S) \end{pmatrix}. \tag{4.8}$$

In terms of the T matrix, on the real-ω axis, realness is expressed as $T^*(i\omega) = T(-i\omega)$ and energy conservation as $|T_{11}|^2 - |T_{21}|^2 = |T_{22}|^2 - |T_{12}|^2 = 1$, $T_{11}^* T_{12} = T_{21}^* T_{22}$, while reciprocity holds anywhere on the complex-ω plane and is written as $\det(T) = 1$.

At a system complex pole ω_n, there are non-zero outgoing fields ($s_{-1}, s_{-2} \neq 0$) without an input ($s_{+1} = s_{+2} = 0$), so $T_{11}(\omega_n) = 0$. Since then $D_{1n} \propto s_{-1}$ and $D_{2n} \propto s_{-2}$, the ports-coupling ratio of the mode is $\sigma_n = 1/T_{21}(\omega_n)$ and reciprocity further mandates $T_{12}(\omega_n) = -1/T_{21}(\omega_n) = -\sigma_n$.

The types of filters we are interested in satisfy $S_{22} = \gamma S_{11}$, namely $T_{12} = -\gamma T_{21}$. Therefore, for reciprocal such filters, we get $\sigma_n^2 = -T_{12}(\omega_n)/T_{21}(\omega_n) = \gamma$, as in Eq. (4.6) of the main text. (Reminder that, if realness must hold, then $\gamma = \pm 1$.)

Inversely, consider a unitary reciprocal system where all the modes verify $\sigma_n^2 = \gamma$. We write $S_{pq}(\omega) = A_{pq}(\omega)/P(\omega)$, where $P(\omega) = \prod_n (\omega - \omega_n)$ includes all the $2N$ poles ω_n and $A_{pq}(\omega)$ is a polynomial of degree at most $2N$, so Eq. (4.8) implies that $T_{12}(\omega) = -A_{22}(\omega)/A_{21}(\omega)$ and $T_{21}(\omega) = A_{11}(\omega)/A_{21}(\omega)$. At a pole, we have $T_{12}(\omega_n) = -\sigma_n^2 T_{21}(\omega_n) = -\gamma T_{21}(\omega_n)$, thus $A_{22}(\omega_n) - \gamma A_{11}(\omega_n) = 0$ [because $A_{21}(\omega_n) \neq 0$]. Since the degree of $A_{22} - \gamma A_{11}$ is at most $2N$, we then have $A_{22}(\omega) - \gamma A_{11}(\omega) = \alpha P(\omega) \Leftrightarrow S_{22} = \gamma S_{11} + \alpha$, where α is a constant. Now, assuming a unitary system, we have $|S_{22}|^2 = |\gamma S_{11} + \alpha|^2 = |S_{11}|^2 \Leftrightarrow |\alpha|^2 + 2\mathrm{Re}[\alpha^* \gamma S_{11}(\omega)] = 0$ at *all* real frequencies ω, leading to $\alpha = 0$ and thus $S_{22} = \gamma S_{11}$.

In the remainder of this section, we use the scattering-matrix QNMT to further specify the choice of σ-signs in order to enforce the desired positions of S-coefficients zeros.

4.4.2 Types of Filters

For each mode n, the appropriate choice of sign for σ_n in Eq. (4.6) depends on the specific filter type that is being designed. We find the adequate choice analytically in the limit of large Qs, or more specifically when $\Gamma_{n,l} \ll |\Omega_n - \Omega_l|$ for $\omega_n = \Omega_n - i\Gamma_n$. Under such condition, the matrix M is dominated by its diagonal terms $M_{nn} = \left(1 + |\sigma_n|^2\right)/2\Gamma_n$, so Eq. (4.1) becomes:

$$\bar{S}_{pq} \approx \delta_{pq} + \sum_n \frac{\Gamma_n}{i(\omega - \Omega_n) - \Gamma_n} \frac{2\sigma_{pn}\sigma_{qn}^*}{1 + |\sigma_n|^2}, \tag{4.9}$$

with $\sigma_{1n} = 1$, $\sigma_{2n} = \sigma_n$. Then, away from the resonances ($\Gamma_n \ll |\omega - \Omega_n|$) and to lowest order in Γ_n, further using $|\sigma_n| = 1$ from Eq. (4.6), transmission is

$$S_{21} \approx C_{21} - i\sum_n \frac{\Gamma_n}{\omega - \Omega_n}\left(\sigma_n C_{11} + C_{21}\right). \tag{4.10}$$

As the overall background transmission $C_{21} \approx S_{21}(\omega \gg \Omega_n)$ determines the filter type, we will study its different cases separately.

Case (a) $C_{21} = 0 \Leftrightarrow |C_{11}| = 1$**:** This is a band-pass filter with zero transmission at $\omega \to \infty$. From Eq. (4.10), we have $S_{21} \propto \sum_n \Gamma_n\sigma_n/(\omega - \Omega_n)$, which, under condition Eq. (4.6), is proportional to a real function that can be easily used to determine the placement of its zeros. As an example, we look at the simple scenario of two modes with $\Omega_1 < \Omega_2$ and calculate the zero at

$$\omega_o \approx \frac{\Omega_2\Gamma_1\sigma_1 + \Omega_1\Gamma_2\sigma_2}{\Gamma_1\sigma_1 + \Gamma_2\sigma_2}. \tag{4.11}$$

One can easily confirm that, when $\sigma_1 = \sigma_2$, the zero appears between the modes ($\Omega_1 < \omega_o < \Omega_2$), a feature often observed in interference phenomena, such as electromagnetically induced transparency (EIT) [138,147]. When $\sigma_1 = -\sigma_2$, it appears on the side of the mode with the smallest loss rate ($\omega_o < \Omega_1$ if $\Gamma_1 < \Gamma_2$ and $\omega_o > \Omega_2$ if $\Gamma_2 < \Gamma_1$), while there is no zero if $\Gamma_2 = \Gamma_1$ (explaining the lack of transmission zeros predicted by traditional CMT for two equal-loss coupled resonances [17] and in symmetric "Fabry-Perot" systems where all Γ's are the same [71]). These points are illustrated in Figure 4-2(a).

These conclusions can be extended to the scenario of multiple high-Q modes: a real zero always occurs between two consecutive modes of same σ_n, there can only be an even (or zero) number of real zeros between two consecutive modes of opposite σ_n and, below the lowest mode or above the highest mode, a zero can exist only if there is at least one change in σ-sign.

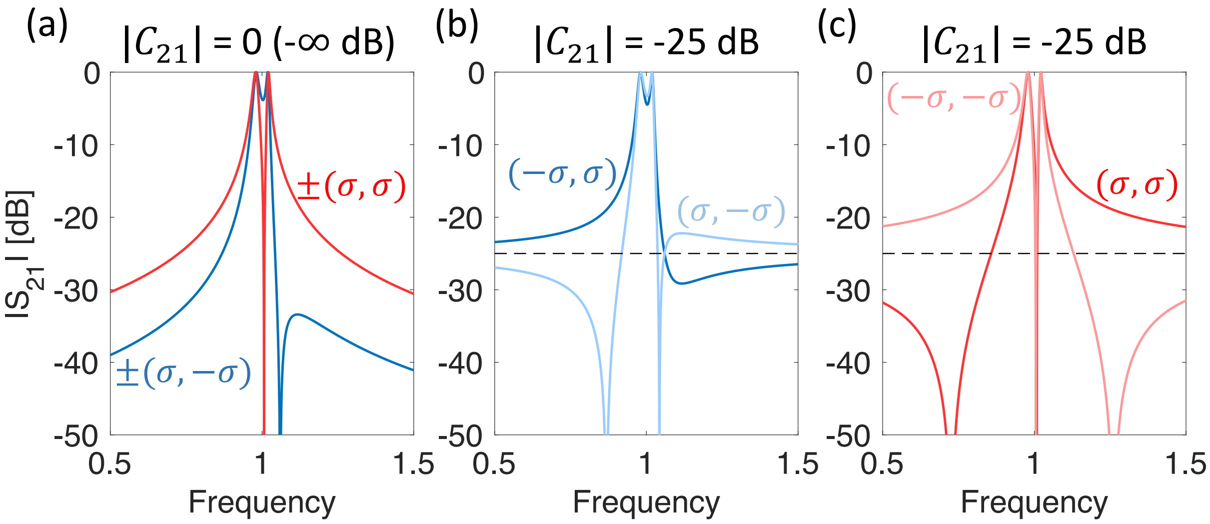

Figure 4-2: Second-order filter responses, using QNM expansions of the form $S = \bar{S}C$, with two modes of frequencies $\Omega = (0.98{-}0.01i, 1.02{-}0.005i)$ and coupling ratios $(\pm\sigma, \pm\sigma)$ in $\bar{S}$, and with unitary reciprocal $C = \begin{pmatrix} i\sigma^* r & t \\ t & i\sigma r \end{pmatrix}$ where $r = \sqrt{1-t^2}$ and such that $\beta = i\sigma^*$ and $C_{22} = \sigma^2 C_{11}$ ($\Leftrightarrow S_{22} = \sigma^2 S_{11}$), for different values of real background transmission t indicated in the plots. We use the RWA of ignoring negative-frequency poles, so the amplitudes of S-matrix coefficients are exactly the same for any complex $\sigma = \sqrt{\gamma} = e^{i\varphi/2}$. A zero always occurs between modes of same coupling ratio (red), so filters with no zeros between the poles require opposite signs of the ratios (blue). Including negative-frequency poles would result to the same qualitative behavior and only slightly change the response away from the resonances.

For the ISFs with no transmission at infinity, such as a Butterworth, Chebyshev, odd-order inverse Chebyshev or odd-order elliptic, where the transmission zeros are always outside the passband, it is necessary to design σ_n with alternating signs, namely

$$\sigma_n = \pm\sqrt{\gamma}\,(1, -1, 1, -1, ...) = \pm\sqrt{\gamma}\,(-1)^{n-1}\,. \tag{4.12}$$

Case (b) $0 < |C_{21}| \ll |C_{11}| < 1$: This is a band-pass filter with finite small transmission at $\omega \to \infty$. From Eq. (4.10), we have $S_{21} \approx C_{21} - iC_{11}\sum_n \Gamma_n\sigma_n/(\omega - \Omega_n)$. If we denote $\beta = C_{11}C_{21}^*/|C_{11}C_{21}|$, then, from the previous discussion, $i\sigma_n\beta = \pm i\sqrt{\gamma}\beta = \pm 1$. Therefore, S_{21} is proportional to a real expression whose zeros can be easily predicted, as in the previous case. In particular, a real zero always occurs between two consecutive modes of same σ_n. Moreover, there is an odd number of real zeros below the lowest mode, when $i\sigma_1\beta = -1$, and an even (or zero) number when $i\sigma_1\beta = 1$, with a similar result above the highest mode but for opposite signs of $i\sigma_N\beta$. This is simply illustrated in Figs. 4-2(b,c).

For ISFs ($\beta = \pm 1$), in this case inverse Chebyshev or elliptic of even order N ($\gamma = -1$), with a total of $N/2$ positive-frequency transmission zeros on each side of the passband, it is necessary to have

$$\sigma_n = \frac{1}{\beta} (-1)^{n-1} i^{N-1};\ \beta = \frac{C_{11} C_{21}^*}{|C_{11} C_{21}|}. \tag{4.13}$$

Case (c) $0 < |C_{11}| \ll |C_{21}| < 1$**:** This is a band-stop filter with finite small reflection at $\omega \to \infty$. Similar analysis by considering S_{11} dictates, for even-order inverse Chebyshev or elliptic ISFs,

$$\sigma_n = \frac{1}{\beta} (-1)^{n-1} i^{N+1};\ \beta = \frac{C_{11} C_{21}^*}{|C_{11} C_{21}|}. \tag{4.14}$$

Case (d) $C_{11} = 0 \Leftrightarrow |C_{21}| = 1$**:** This is a band-stop filter with zero reflection at $\omega \to \infty$ and a ISF implementation requires again simply

$$\sigma_n = \pm\sqrt{\gamma} (-1)^{n-1}. \tag{4.15}$$

By designing σ_n to satisfy the appropriate condition from Eqs. (4.12–4.15) according to the filter type, the pole residues in the partial-fraction expansion of $H(\omega)$ are also matched and thus the filter design is complete.

4.4.3 Approximate solutions

Negative-frequency modes are necessary to exactly satisfy realness. However, for filters with high-Q modes, the response can be well approximated (at positive frequencies ω) by the well-known rotating-wave approximation (RWA) of including only positive-frequency modes in QNMT. In this case, the previous results hold for any complex phase factor $\gamma = e^{i\varphi}$. Therefore, in filter design, Eqs. (4.12–4.15) permit σ_n to be tuned to the desired values up to an overall common phase factor (expressed via γ or $\beta = \pm i/\sqrt{\gamma}$). Then, the resulting filters, even after including also negative modes with their corresponding σ_n^* to satisfy realness, will be good approximations of ISFs within the bandwidth of interest.

As seen from Eq. (4.3), for $\sigma = \pm 1$ ($\gamma = 1$), $\bar{S}$ is symmetric, so $S = \bar{S}C$ is also symmetric if $C_{22} = C_{11}$. Similarly, for $\sigma = \pm i$ ($\gamma = -1$), S is symmetric with $C_{22} = -C_{11}$. However, when γ is complex, reciprocity and realness of $S = \bar{S}C$ cannot be satisfied with a constant C. Since an actual physical system is obviously reciprocal, even when designed for complex γ, this means that C is necessarily non-constant, but rather slowly varying due to other modes, in a way that guarantees reciprocity. In other words, it is not possible to obtain high-Q modes verifying Eq. (4.6) with complex γ without additional modes proximal enough to form a frequency-dependent C.

4.4.4 Geometrical symmetry

$\sigma_n = \pm 1$ means that the radiative part of the modes is even or odd, which can be easily obtained using a structure with geometrical (e.g. mirror) symmetry between the two ports [28]. This can explain the increase in transmission previously observed in symmetric structures [148]. However, we will later see filter designs where it is preferable for the structure to *not* be symmetric, so the modes themselves are not even or odd, even though their radiative far fields may in fact be (satisfying $\sigma_n = \pm 1$).

On the other hand, for $\gamma \neq 1$, the mode and structure have to be asymmetric anyway. In particular, even-order antimetric ISFs ($\gamma = -1$) can be made only from asymmetric structures, as confirmed for example by their known corresponding electric-circuit topologies [16]. However, we explained that good approximate filters can be obtained with γ deviating from its optimal value by a phase factor (as long as the background C is slowly varying, in contrast to being constant for ISFs). Therefore, approximate even-order ISFs can be designed also with $\gamma = 1$. To highlight this point, we later show implementations of such filters, using *symmetric* structures.

4.4.5 Summary

A N-order 2-port filter, whose reflection is zero at N real frequencies, obeys $S_{22} = \gamma S_{11}$ ($\gamma = \pm 1$) and consists only of modes whose radiation couples to the two ports with the ratios $\sigma_n = \pm\sqrt{\gamma}$. To design standard filters, these ratios must alternate sign among consecutive modes, and a background scattering C, appropriate for the desired filter type, must be established [Eqs. (4.12–4.15)]. Approximate filters can also be designed with complex unitary γ. Once the QNMT design objectives (background transmission $|C_{21}|$, eigenfrequencies ω_n and port-coupling ratios σ_n) have been determined for the desired filter profile, the physical metasurface parameters can be identified using adequate optimization/nonlinear-solver tools.

4.5 Microwave metasurfaces

The analytical criteria we have presented in this chapter give a direct pathway to precisely design high-order microwave metasurface filters. In this section, we obtain all types of bandpass and bandstop ISFs with different orders and bandwidths. For each desired filter, we choose a fixed topology, based on circuit-theory principles and also on intuition from QNMT itself (for the background scattering C), with few unknown physical parameters. These are then optimally identified by simply applying a multivariable solver of nonlinear systems of equations on the filter conditions derived in section 4.4. This rather "traditional" approach leads to very rapid computational design, as physics and analytics have already been used to facilitate the job of the optimizer.

Unless otherwise stated, in all microwave metasurfaces studied in this chapter: (i) We use perfect metal with thickness 18μm (corresponding to 0.5oz copper). (ii) The square-lattice period a and the centers of the crosses are the same for all patterned layers. (iii) We study for frequencies below the first diffraction cutoff ($f_{\text{cut}} = c/a$ at normal incidence), so only transmission and reflection need to be considered. (iv) There is C_{2v} symmetry, so the response for normal incidence is independent of the polarization $\hat{e}$ and indeed only 2 ports are needed. (v) Numerical computation of the "exact" frequency response $S(\omega)$ for plane-wave excitation as well as of the eigenmodes (ω_n, σ_n) for use in our QNMT is carried out using COMSOL Multiphysics [97]. In the Supplemental Material [149], we provide tables with the calculated QNMs for every metasurface presented.

4.5.1 Second-order bandpass filter - Circuit model

We start by studying a simple *symmetric* second-order metasurface, in order to build some physical intuition on how a particular structural topology can be modeled by an effective circuit, to relate this circuit to the QNMT, and to derive design guidelines for transmission-zero placement. The metasurface, shown in Fig. 4-3(a), is formed by two planar metallic sheets sandwiched between three uniform dielectric layers. A square array (with period a) of narrow cross-like apertures in each metallic sheet creates a resonance, which can be modeled in the subwavelength limit ($a \ll \lambda$) as an effective shunt parallel $L_a C_a$ ($\equiv 1/\omega_a^2$) to a plane wave incoming from free space with impedance Z. The inductance L_a originates from the current flowing around the edge of the aperture, while the capacitance C_a comes from the opposite-charge accumulation across facing sides of this narrow gap [see Fig. 4-3(a)]. The connected topology of the metallic sheets represents a short-circuit to an incident plane wave at long wavelengths (shunt L_a), leading to no transmission at zero frequency. Moreover, a longitudinal inductance L_b couples the apertures on the two metallic sheets, corresponding both to first-order transmission-line effects of the thin dielectric layer and to the direct mutual inductance between the apertures. Finally, capacitance C_b builds up between the two metallic sheets [see Fig. 4-3(a)], which is an interesting feature that has an important consequence: it leads to the emergence, in series with the path of incident-wave propagation (longitudinally), of a parallel-resonant L_bC_b, which becomes an open circuit at the frequency $\omega_b = 1/\sqrt{L_bC_b}$, thus leading to a zero in the transmission function. The final equivalent-circuit model is given in Fig. 4-3(b), corresponding to a passband filter with a finite-frequency zero.

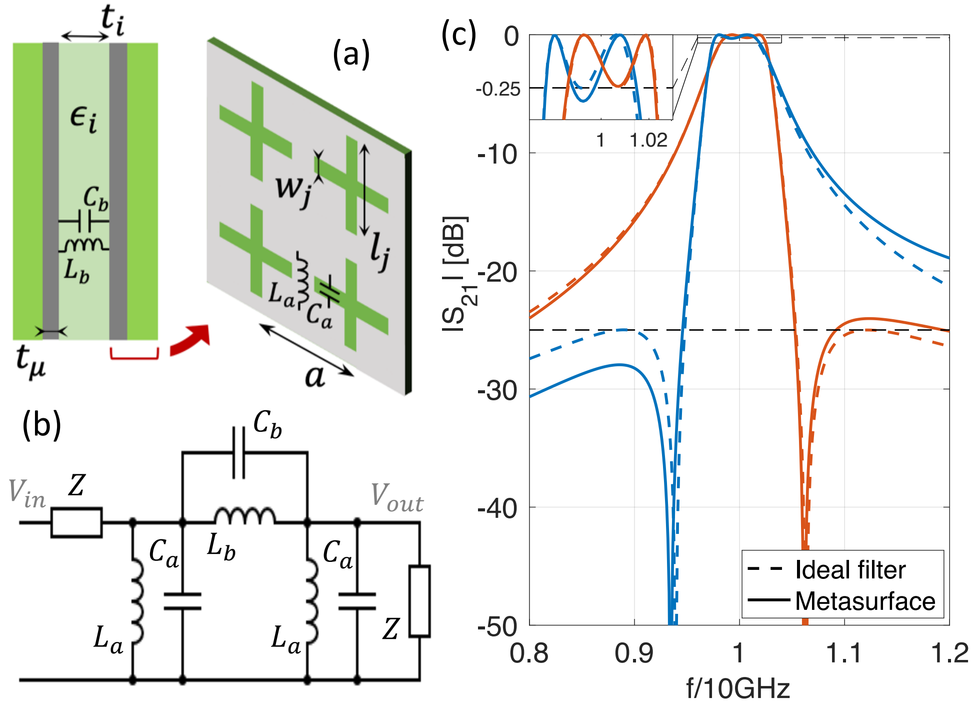

Figure 4-3: (a) Symmetric metasurface for a second-order bandpass filter centered at 10 GHz with a single transmission-zero, designed for 0.25 dB passband ripple and 25 dB stopband attenuation (black dashed lines). (b) Equivalent circuit model. The coupling L_bC_b gives the transmission-zero. (c) Transmission spectrum of two optimized structures with a zero respectively on the left (L) and on the right (R) of their transmission peaks. Parameters for structure (L): a = 6mm, $w_1/a = w_2/a = 0.0479$, $l_1/a = l_2/a = 0.846$, $t_1/a = t_3/a = 0.493$, $t_2/a = 0.257$, $\epsilon_1 = \epsilon_3 = 1.43$, $\epsilon_2 = 14.51$. Parameters for structure (R): a = 9.34mm, $w_1/a = w_2/a = 0.00877$, $l_1/a = l_2/a = 0.905$, $t_1/a = t_3/a = 0.0237$, $t_2/a = 0.0966$, $\epsilon_1 = \epsilon_3 = 4.12$, $\epsilon_2 = 3.80$.

The transmission spectrum can be computed through $S_{21} = 2V_{out}/V_{in}$ [16], and with $y_j = Z\left(1/\omega L_j - \omega C_j\right)$ for $j = a, b$ we obtain:

$$S_{21}(\omega) = \frac{2iy_b}{(1+iy_a)(1+i(y_a+2y_b))}. \tag{4.16}$$

This clearly shows transmission zeros at $\pm\omega_b$, and also at $\omega = 0$, $\omega \to \infty$ (bandpass behavior). Denoting the loss rates $\Gamma_j = 1/(2ZC_j)$, the denominator shows the system poles at $\pm\Omega_1 - i\Gamma_1$ and $\pm\Omega_2 - i\Gamma_2$, where $\Gamma_1 = \Gamma_a$, $\Omega_1 \approx \omega_a$, $\Gamma_2 = 1/\left(1/\Gamma_a + 2/\Gamma_b\right)$, $\Omega_2 \approx$

$\Gamma_2(\omega_a/\Gamma_a + 2\omega_b/\Gamma_b)$. One system resonance is identical to the single-sheet resonance, while the second is affected also by the inter-sheet couplings: it is always narrower ($\Gamma_2 < \Gamma_1$) and $\Omega_2 \gtrless \Omega_1$ if $\omega_b \gtrless \omega_a$.

When ω is close to the positive resonances, the RWA $y_j \approx (\omega_j - \omega)/\Gamma_j$ effectively drops the negative resonances. Then, a partial-fraction expansion of Eq. (4.16) can be obtained:

$$S_{21}(\omega) \approx \frac{i\Gamma_1}{\omega - (\Omega_1 - i\Gamma_1)} - \frac{i\Gamma_2}{\omega - (\Omega_2 - i\Gamma_2)}, \tag{4.17}$$

This is identical to the QNMT result in Eq. (4.1) with $\sigma = (-1, 1)$ and $C = I$. As mentioned earlier, the two *different* values for the decay rate Γ lead to a transmission zero, which is not usually described in typical CMT models that assume equal Γ for the two resonances.

We saw from Eq. (4.11) that this zero ω_b appears on the side of the resonance with the smallest loss rate, which is Γ_2 in this case, so $\omega_b < \Omega_2 < \Omega_1 = \omega_a \Leftrightarrow L_aC_a < L_bC_b$ or the opposite order. Therefore, we have a recipe to design the zero for this metasurface, based on the equivalent circuit elements. To translate those to physical structural parameters, we observe that, in the quasi-static limit, $L_b \propto t_2$ and $C_b \propto \epsilon_2/t_2$, where t_2 is the small separation between the two metallic sheets and ϵ_2 is the dielectric constant of the separating layer. This means that $L_bC_b \propto \epsilon_2$ and does not depend on t_2 to first order. On the other hand, L_aC_a also does not depend on t_2, but it has a weighted dependence on ϵ_1 and ϵ_2. The location of the transmission zero relative to the poles then mainly depends on the ratio of permittivities of the two dielectric materials. In particular, a zero at a frequency below the poles is obtained using a large $\epsilon_2/\epsilon_1 > 1$.

We can also use Eq. (4.17) to compute the full-transmission frequencies ($|S_{21}(\omega_t)| = 1$):

$$\omega_t = \frac{\Omega_1 + \Omega_2}{2} \pm \sqrt{\left(\frac{\Omega_1 - \Omega_2}{2}\right)^2 - \Gamma_1\Gamma_2}. \tag{4.18}$$

We see that there are two full-transmission maxima between Ω_1 and Ω_2, as long as the eigenfrequencies are well separated ($|\Omega_1 - \Omega_2| > 2\sqrt{\Gamma_1\Gamma_2}$).

We can now use the QNMT to design second-order bandpass filters with a transmission-zero either on the right or on the left of the transmission peaks. In both cases, we choose the two complex eigenfrequencies, for which Eq. (4.17) gives a transmission peak-to-peak passband ripple of 0.25 dB, a stopband attenuation of at least 25 dB and a 3dB-bandwidth of 5% around the center frequency $f_c = \omega_c/2\pi = 10$ GHz. (For comparison, we will target these passband/stopband limits and center frequency for all filters designed in this chapter.) Then, we use the multivariable nonlinear-equation solver to find the structural parameters that will make the eigenmodes of the metasurface of Fig. 4-3(a) match those desired eigenfrequencies and with port-coupling ratios $\sigma = \pm(1, -1)$. Results for optimized structures are shown in Fig. 4-3(c). We note that, as expected, the structure with a transmission-zero at smaller frequencies has a larger dielectric constant for the inside layer. We also see that the shapes of the transmission spectra deviate somewhat from the ideal filters. This is mainly due to higher-frequency resonances that affect the scattering matrix (acting as a background C) and make it different from the two-poles approximation of Eq. (4.17), leading to slight reduction of transmission at low frequencies and increase at higher ones. As commonly known for metasurfaces, higher-order diffraction modes can be pushed away by looking, if possible, for solutions with reduced periodicity a and higher permittivities ϵ_j.

4.5.2 Third-order bandpass filters

Using the QNMT design method, as well as guidance from the previous two-pole bandpass structure, we now design all four standard types mentioned in section 4.4 for third-order bandpass filters. The three poles necessary for each wanted filter are given by standard analytical expressions or software tools [16]. Since all filter types are of third order with $C_{21} = 0$ [case (a)], we see from Eq. (4.12) that we trivially need port-coupling coefficients with ratios $\sigma \propto (1, -1, 1)$ for the three modes.

To implement these filters, we use a structure with the same unit-cell topology as in Fig. 4-3(a), but with three metallic sheets and four dielectric layers. Based on the insight gained in section 4.5.1 from the effective circuit model, we realize that each of the inside layers will create a longitudinal parallel $L_jC_j \propto \epsilon_j$ resonance, which will cause a transmission zero $\propto 1/\sqrt{\epsilon_j}$. For the inverse Chebyshev and elliptic filters, two *distinct* zeros are required. Therefore, we need different dielectric constants ϵ_j for the inside layers. This means that the physical structure for these filter types must *not* be symmetric, so their modes are not even or odd, even if their radiative tails are [$\sigma = (1, -1, 1)$]. On the other hand, Butterworth and Chebyshev filters do not have real zeros, so there we can choose a symmetric structure, which simplifies the optimization problem, as only eigenfrequencies need to be matched (in the correct order of modal symmetry). However, for these "zeroless" ISFs, the challenge with the chosen metasurface topology is to push away from our bandwidth the unavoidable zero that will arise from the inside layers. The simplest way to accomplish this, is to look for solutions where these layers are thick enough that the second-order dependence of the longitudinal parallel L_jC_j on t_j moves the zero to sufficiently high frequencies. Different topologies could also be devised that eliminate either the mutual inductance or capacitance between sheets.

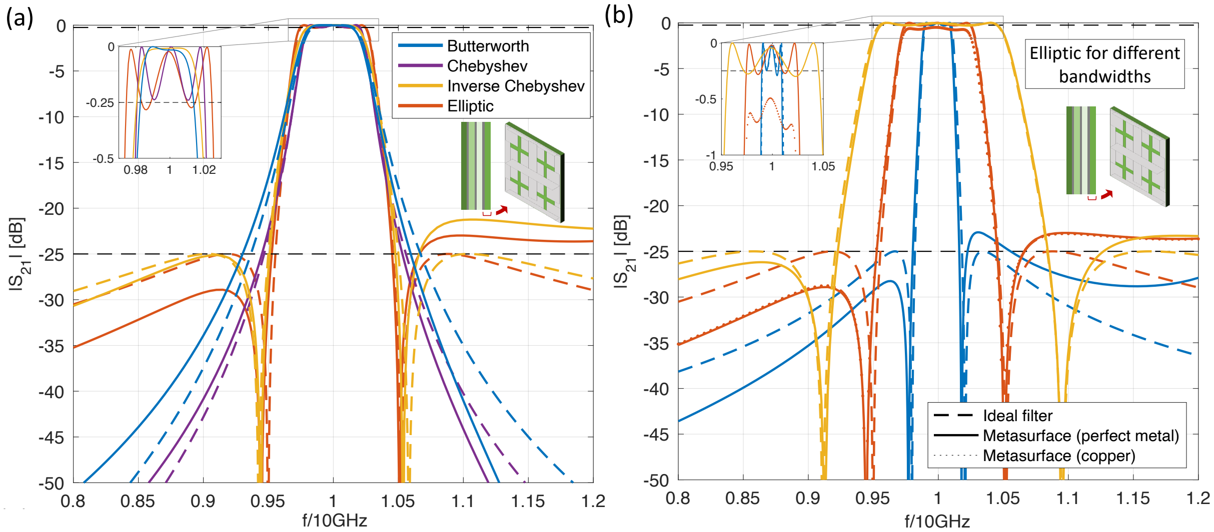

Figure 4-4: Optimized third-order bandpass filters (a) of different types with same bandwidth and (b) elliptic only for different bandwidths. We use the same structure as in Fig. 4-3 but with three metallic sheets and four dielectric layers. Physical parameters are provided in a table above. We notice good agreement of lossless structures (solid lines) with ideal filters (dashed lines), except for small deviations mainly due to effects from high-order modes. Copper losses (dotted line) reduce peak transmission while preserving the filter's shape.

Again by optimizing the structural topology, for each filter, we get the desired three complex resonant frequencies ω_n and their corresponding σ_n. The optimized structural parameters are summarized here:

Type	a (mm)	w_1/a	w_2/a	w_3/a	l_1/a	l_2/a	l_3/a
Butterworth	13.49	0.024	0.003	0.024	0.805	0.709	0.805
Chebyshev	12.02	0.0099	0.0027	0.0099	0.7896	0.6639	0.7896
Inverse Chebyshev	9.83	0.221	0.050	0.055	0.772	0.645	0.944
Elliptic 1	10.00	0.28	0.034	0.009	0.501	0.535	0.849
Elliptic 2	9.175	0.222	0.068	0.022	0.692	0.607	0.908
Elliptic 3	10.45	0.207	0.012	0.071	0.806	0.710	0.992

Type	t_1/a	t_2/a	t_3/a	t_4/a	ϵ_1	ϵ_2	ϵ_3	ϵ_4
Butterworth	–	0.445	0.445	–	1	2.41	2.41	1
Chebyshev	–	0.483	0.483	–	1	3.45	3.45	1
Inverse Chebyshev	–	0.278	0.096	0.018	1	6.72	3.64	2.73
Elliptic 1	–	0.451	0.026	0.020	1	8.21	3.95	3.00
Elliptic 2	–	0.343	0.071	0.021	1	8.58	4.42	3.19
Elliptic 3	–	0.187	0.066	0.014	1	5.72	2.61	3.41

Transmissions of the optimized metasurfaces that implement the four filter types with ~5-6% 3dB-bandwidth are shown in Fig. 4-4(a), while in Fig. 4-4(b) only for elliptic filters with varying bandwidth (~2-10%). We note a good agreement with the ideal filters, except for small discrepancies again due to effects from higher-order modes and to small errors in the values of optimized resonances. Notice that, indeed, Butterworth and Chebyshev filters require thick inside dielectric layers to move the zero away and that smaller bandwidths need higher ϵ_j to increase the modal Qs. Moreover, we test the effect of metal (here, copper) losses on an elliptic filter and find that it mainly just reduces the values of the transmission peaks (only by ~ 0.5 dB at 10 GHz operation).

4.5.3 Third-order elliptic bandstop filter

In order to design a third-order *bandstop* filter, we now need to achieve a full-transmission background $|C_{21}| = 1$ [case (d)], and then Eq. (4.15) dictates again three QNMs with $\sigma \propto (1, -1, 1)$. As saw in Sec. 3.5.2, the background-C design can generally be understood using the system low-Q modes and, in particular, a fully-transmissive C can be achieved by a mode with infinite radiative rate, which effectively models free space (see Sec. 3.5.2). Thus, as expected, we need a physical structure with a very small effective index (~ 1), while still able to support the required high-Q resonances. Moreover, since we want full transmission at zero frequency, the metallic components now should not have a fully-connected topology. Therefore, relying on the principle of duality, we choose, in place of each metallic sheet with cross apertures, an array of non-connected thin metallic crosses. These are supported by dielectric crosses, also non-connected to minimize the total effective index. The structure is shown as an inset in Fig. 4-5(a). Its effective circuit model now sees each array of crosses as a shunt series-LC resonance, where L is the inductance of the cross wires and C is the capacitance across adjacent crosses within each array [see Fig. 4-5(a)], and then the couplings between arrays are effectively longitudinal parallel-LC, where C is the capacitance across facing (cocentric) crosses and L is the first-

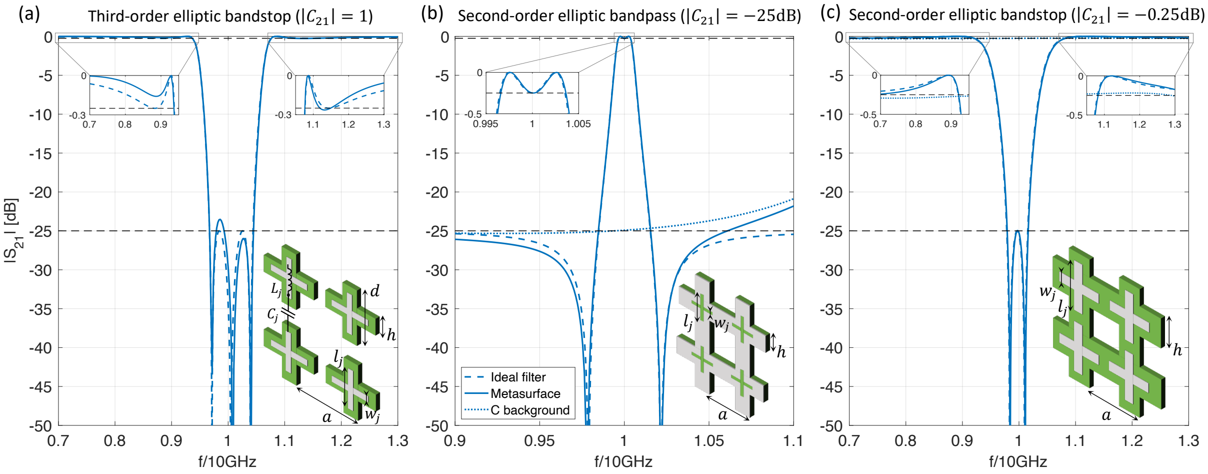

Figure 4-5: (a) Third-order elliptic bandstop filter. The structure has three metallic-cross arrays and four dielectric layers with parameters: $a = 16.99$mm, $h/a = 0.03$, $d/a = 0.619$, $w/a = (1.53, 3.73, 1.61) \times 10^{-3}$, $l/a = (0.558, 0.589, 0.524)$, $t/a = (0.166, 0.358, 0.441, 0.183)$, $\epsilon = (4.76, 3.22, 4.05, 4.50)$. (b) Second-order elliptic bandpass filter. The structure has two metallic sheets and three dielectric layers with parameters: $a = 17.571$mm, $h/a = 0.456$, $w_1/a = w_2/a = 6.08 \times 10^{-3}$, $l_1/a = l_2/a = 0.4355$, $t_1/a = t_3/a = 0.3072$, $t_2/a = 0.3169$, $\epsilon_1 = \epsilon_3 = 3.82$, $\epsilon_2 = 1.893$. (c) Second-order elliptic bandstop filter. The structure has two metallic-cross arrays and three dielectric layers with parameters: $a = 18.70$mm, $h/a = 0.181$, $w_1/a = w_2/a = 2.74 \times 10^{-3}$, $l_1/a = l_2/a = 0.514$, $t_1/a = t_3/a = 0.204$, $t_2/a = 0.332$, $\epsilon_1 = \epsilon_3 = 1.60$, $\epsilon_2 = 3.10$. All filters satisfy quite well the marked requirements (black dashed lines) and agree with the ideal filters.

order transmission-line model of propagation through the free space, but also includes the small contribution (a large in-parallel value) of the mutual inductance between facing crosses. This circuit can implement the desired ISF, where each shunt series-LC or longitudinal parallel-LC can directly impose one of the required three distinct transmission zeros.

An example of an optimized structure with a third-order elliptic bandstop response of 12% 3dB-bandwidth is shown in Fig. 4-5(a). We note again the very good agreement compared to the ideal filter. Notice that, in duality to the passband filter, the permittivity of one inside dielectric turns out to be *smaller* than the outside layers.

4.5.4 Second-order elliptic bandpass and bandstop filters

To complete our set of design examples, we now demonstrate second-order elliptic bandpass and bandstop metasurface filters. In this case, we need to design a specific non-trivial background C, in particular, C_{21} must be roughly constant within the bandwidth of interest and its amplitude set respectively to the desired stopband minimum attenuation value (-25 dB) [case (b)] or passband maximum ripple value (-0.25 dB) [case (c)]. Furthermore, the coefficients σ_n should respectively satisfy Eq. (4.13) or Eq. (4.14). As discussed in section 4.4, for even-order ISFs, $\gamma = -1$ and C is a real constant matrix, so $\beta \equiv C_{11}C_{21}^{*}/\left|C_{11}C_{21}\right| = \pm 1$ and $\sigma_n = \pm i$, which corresponds to asymmetric structures, such as the standard circuit topologies of even-order ISFs. However, we explained that approximate solutions with a different unitary γ are possible (using the RWA) and here we present *symmetric* structures ($\gamma = 1$) exhibiting a second-order elliptic filter response within the bandwidth of interest. Since symmetry guarantees $\sigma_n = \pm 1$, Eqs. (4.13,4.14) become design objectives for β, which must respectively match $\pm i/\sigma_1$.

For the bandpass filter (with two transmission zeros), we use as starting point for the structural topology that from Fig. 4-3(a) corresponding to a second-order bandpass filter with only one zero. There, the large metallic sheets led to $C_{21} = 0$. In order to increase $\left|C_{21}\right|$ to the small required -25 dB around the filter center-frequency ω_c, we open holes through the entire metasurface, as shown in Fig. 4-5(b), so that some of the incident wave will directly go through without coupling to the high-Q resonances of the crosses. Excluding those two high-Q modes, using QNMT we calculate $C = \bar{S}_{\{\omega_n^C\}}$, and it turns out that even-odd pairs of *almost* degenerate low-Q modes below ω_c together with higher-order modes lead to a background with a flat small $\left|C_{21}\right|$ and constant β over a fairly large frequency range (see modes in Supplemental Material [149]). [Traditionally, one would approximate C by simulating an effective background structure (e.g. where the cross apertures which cause the high-Q resonances are closed), but the result is inaccurate (-19 dB instead of -25 dB).] The optimization then consists of enforcing the values of the two complex eigenfrequencies, $\left|C_{21}\left(\omega_c\right)\right| = -25$ dB and, from Eq. (4.13), $\beta\left(\omega_c\right) = i/\sigma_1$. The transmission of the designed structure is shown in Fig. 4-5(b) and agrees very well with the 1%-bandwidth ISF spectrum. It turns out that the modal symmetry is $\sigma = (-1, 1)$, so $\beta\left(\omega_c\right) = -i$. Note that, since each metallic sheet is still connected (in a topological sense), the transmission at very long wavelengths will still go to zero.

For the second-order bandstop elliptic filter, we use as starting point the structural topology from Fig. 4-5(a) for the third-order bandstop filter, but with two metallic-cross arrays sandwiched between three dielectric layers. There, the effective refractive index of the entire metasurface was designed small to get $\left|C_{21}\left(\omega_c\right)\right| \approx 1$. In order to decrease $\left|C_{21}\right|$ to the required -0.25 dB, we connect the dielectric crosses, as shown in Fig. 4-5(c), to reflect back some of the incident wave. In QNMT terms, an averaging over the metasurface leads to an effective slab of low refractive index, which supports equispaced "Fabry-Perot" low-Q modes $\omega_n^C = n\Omega^C - i\Gamma^C$ [71]; the "Fabry-Perot" transmission hits $\left|C_{21}\right| = 1$ at Ω_n^C, but is less than 1 and flat between modes $[n\Omega^C, (n+1)\Omega^C]$, with roughly constant $\beta \approx i$ if n even (and $\beta \approx -i$ if n odd). For this structure, it turns out that these modes ω_n^C have such a small Q (see modes in Supplemental Material [149]) that it is difficult to accurately find all of those contributing to $C(\omega_c)$. Therefore, we instead calculate it indirectly from $C(\omega_c) = \bar{S}^{-1}(\omega_c)S(\omega_c)$, as explained earlier. [Again, the traditional method of an effective background structure (removing the metallic crosses) gives a noticeably less accurate estimate of C (-0.11 dB instead of -0.25 dB).] The two high-Q modes have symmetry $\sigma = (-1, 1)$, consistent with $\beta(\omega_c) = i$ from Eq. (4.14), and the optimized final structure has transmission shown in Fig. 4-5(c), matching precisely an elliptic bandstop ISF of 10% bandwidth.

4.5.5 Fabrication and tunability

All the metasurface filters that we presented were based on a layered topology with metallic sheets sandwiched between dielectric layers. This layered form was chosen, because it has the great advantage of allowing easy fabrication. Especially in the cases where patterning is only on the metallic sheets, these metasurfaces can be manufactured even with widespread printed-circuit board (pcb) techniques. In fact, all designed ISFs presented in this work used dielectrics with permittivities less than 11.2, which is roughly the upper limit for (typically Al_2O_3-based) low-loss materials compatible with pcbs. Furthermore, the clear separation between metallic sheets allows them to be connected to separate electrodes, where voltage can be applied to potentially tune the permittivity of the intermediate dielectrics, if those are chosen to be tunable materials (liquid crystals, ferro-electrics etc.) [150]. Previous attempts at elliptic filters have usually employed topologies with shunt metal paths connecting different metal sections within the metasurface, which hinders both these benefits [126–128].

4.6 Conclusions

In this chapter, we presented a systematic method using eigensolvers for designing standard filters or other useful transmission/reflection spectra, especially ones with multiple finite real zeros, allowing ultra-compact devices with spatially overlapping resonances (unlike previous circuit-theory or CMT approaches). It is based on a non-normalized QNM expansion of the system scattering matrix S and entails identifying the necessary background response C, the exact complex eigenfrequencies ω_n of these modes, and the values of the ratios σ_n with which these modes must couple to the system coupling ports, to achieve the desired scattering frequency profile. An efficient optimization procedure is then applied to determine the structural parameters (geometry and materials) that meet these criteria. We have demonstrated the method for microwave planar metasurface filters, for all standard amplitude-filter types (especially the most challenging, elliptic), for both bandpass and bandstop behaviors, and for a variety of frequency bandwidths.

In our examples, we used fixed topologies, guided by general physical intuition from circuit models, and then applied a simple multi-variable equation solver to obtain a small set of structural parameters. In principle, our conditions can also be combined with various large-scale topology-optimization algorithms and solver methods [140]. While we focused on amplitude standard filters, our design process can be used for any desired scattering spectrum, by fitting it to QNMT to extract the corresponding eigenmode optimization objectives (ω_n, σ_n). Moreover, it should be clear that the accurate QNMT prediction of the time delay in Chapter 3 also makes the theory applicable to design phase filters, such as all-pass delay filters [151] (useful also for metalenses [152]). Our design method was demonstrated for microwave metasurfaces, but it can also be used for resonant systems with any qualitatively similar physics, such as mechanical, acoustic, photonic, or quantum-electronic filters.

THIS PAGE INTENTIONALLY LEFT BLANK

Chapter 5

Many resonances: From solar cells to ocean buoys[1]

5.1 On resonances

In Chapter 4, we saw how we can use few resonances to design high-order filters and demonstrated it by designing a variety of microwave metasurfaces. In certain applications concerned with a large frequency bandwidth, a considerable number of resonances is involved. For example, Figure 5.1(b) shows the absorption spectrum for a solar cell with a patterned surface [Figure 5.1(a)]. The spectrum includes a very large number of sharp peaks, associated with resonances, due to the use of a top grating. These resonances lead to a significant enhancement of the solar-cell absorption compared to the bare slab in absence of a top grating and back mirror. The detailed spectral-resolved shape of the spectrum hardly matters, as we are mainly concerned with the *spectral-averaged* absorption (weighted with the wide-bandwidth solar spectrum). In general, we want our solar-cell to also perform well for different angles of incidence (to avoid mechanical tracking of the sun throughout the day), so our final quantity of interest involve both spectral and angle averaging. From the spectrum in Figure 5.1(b), it may seem that the details of the resonances distribution would not matter after averaging, and that the result would only depend on some global property of the structure. This is indeed (mostly) the case! In fact, using ray optics, Yablonovitch [22] found an upperlimit to the enhancement that simply depends on the refractive index n of the cell, and that is equal to $4n^2$ (in 3D, for isotropic incidence and small absorption). This limit turned out to be hard to beat (after averaging) even using more complex nanopatterns to scatter light [154, 155].

---

[1] Our work on this topic was published in Ref. 153.

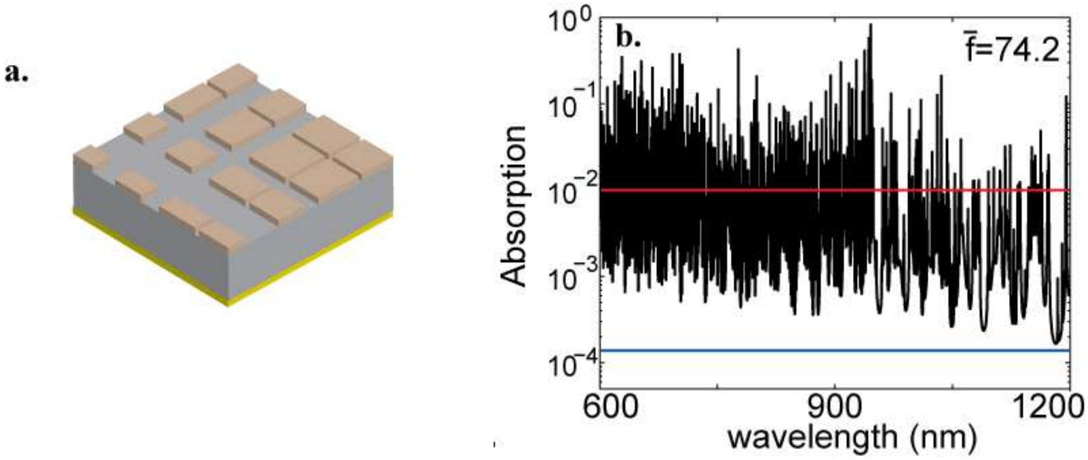

Figure 5-1: Figure taken from Ref. 7. (a) Solar-cell with a 2D grating on top and back reflector on the back. (b) Absorption spectrum of the cell for normally incident light. A large number of narrow resonances is present, which leads to an overall increase in absorption. The spectral-averaged absorption in presence of the grating and back reflector (red line) is 74.2 larger than the "single pass" absorption in their absence (blue line).

Absorption enhancement due to scattering can happen in all areas of wave physics, and does not only apply to solar cells. In this chapter, we will be mostly concerned with an application to ocean wave energy extraction [156]. Multiple scattering between ocean buoys (mechanical oscillators used to absorb ocean wave power) in an array can in fact increase the total absorption [8, 21]. Since an effective uniform slab is not an appropriate model in this case, Yablonovitch limit cannot directly be applied to this problem. In this chapter, we develop approximate bounds on the spectral/angle-averaged absorption enhancement for an array of "metaparticles" and successfully apply it to the ocean buoy problem. In the next section, we give a general overview and describe the layout of the chapter.

5.2 Overview

One of the most influential theoretical results for solar-cell design has been the ray-optical Yablonovitch limit [22, 23, 25, 154, 155, 157–159], which provides a bound to how much surface texturing can enhance the performance of an absorbing film averaged over a broad bandwidth and angular range. In this chapter, we obtain approximate broad-band/angle absorption limits for a case in which the traditional Yablonovitch result is not useful: dilute arrays of "metaparticles"(synthetic absorbers/scatterers). Known limits bound the absorption at every wavelength [24, 160], but they tend to be loose when considering

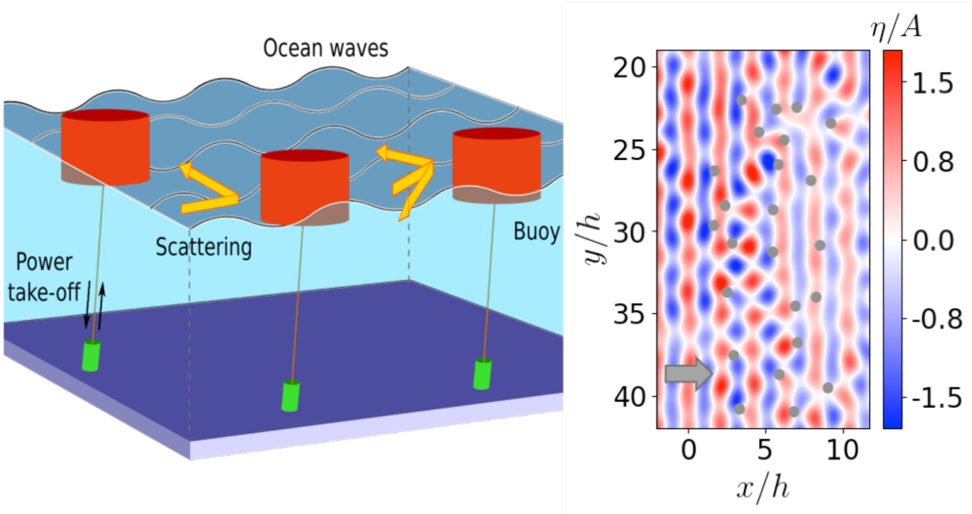

Figure 5-2: Left: We bound absorption for very general arrays of "particles", including arrays of buoys that extract energy from ocean waves. Left: Ocean surface displacement η for a cylindrical buoy array [8] where A is the amplitude of waves incident from left (arrow).

large bandwidths since coherent effects average out [7, 25]. Here, we find limits on the absorption for arrays of particles that can be described by the radiative-transfer equation (RTE) [62, 161]. In particular, we show that an isotropic diffusive regime is *optimal* for maximizing absorption. This allows us both to obtain analytical upper bounds (Eqs. 5.17, 5.26) and identify the ideal operating regime of absorbing metaparticle arrays.

In optics contexts, scattering particles can be used to enhance absorption in thin-film or dye-sensitized solar cells [162–165]. Most previous work focused on numerical optimization using the full-wave equations [162, 163] or, in the case of dye-sensitized solar cells, RTE for random arrays [164, 165]. In Ref. 166, approximate analytical estimations of absorption enhancement were given in cases of optically-thin/thick layers under assumptions of weak absorption, normal incidence and isotropic differential cross section. In this work, we were actually motivated by arrays of buoys designed to extract energy from *ocean* waves [156, 167–169] depicted in Fig. 5-2. Previous numerical-optimization work [8, 21, 170, 171], in particular a recent extensive computational study on large arrays [8, 21], showed promising results through the design of buoy positions. The question we are trying to answer in this work is more general: given the absorbing/scattering properties of an individual metaparticle, is there a limit on the total enhancement and how can it be reached? The Yablonovitch limit cannot be applied to all metaparticle arrays since it requires an effective-medium approximation, which is only accurate for either dilute weakly interacting dipolar particles [172] or for strongly interacting particles with sufficiently subwavelength separation [173], neither of which is true of the ocean-power problem. Moreover, the Yablonovitch limit is independent of the precise nature of the scattering texture, whereas in our case the whole point is to extrapolate the array properties from the individual-scatterer properties.

In this chapter, we define the *interaction factor* $q(\theta)$ [174,175] as the ratio of the power extracted by the array to that of the equivalent number of isolated particles for a given incident angle θ. We first point out that previously known limits in both solar cells and ocean buoys arise from reciprocity constraints on the full-wave equations (Sec. 5.3). The use of reciprocity in the radiative-transfer equation leads to a general limit (Eq. 5.17), valid for any geometrical configuration in RTE regime, that is reached through an isotropic distribution of intensity in the ideal case of small absorption (Sec. 5.4). This optimal solution justifies the use of a *corrected* radiative-diffusion model (Eq. 5.26) that predicts the frequency-averaged performance of random arrays, but also the angle/frequency-averaged performance of the optimized *periodic* array with better than 5% accuracy. This corrected model can be used to estimate the upper bound on q (which is proportional to the spatially-averaged intensity in RTE framework) even in regimes where the standard diffusion model is not expected to be accurate. This result allows us to quickly evaluate the performance benefits of different metaparticle designs and array configurations, and we show that substantial improvement is possible if the scattering cross-section is increased (relative to the absorption cross-section) and/or if partially reflecting strips are placed on either side of the array (Sec. 5.5). More specifically, we show that the use of bending membranes on the water's surface around the buoys significantly increases the interaction factor. We finally use the corrected radiative-diffusion model to find optimal parameters that maximize q.

5.3 Reciprocity

5.3.1 Solar cells

The original intuition behind the ray-optical Yablonovitch limit is that the optimal enhancement is achieved through an *isotropic* distribution of light inside the device [22,157]. This can be thought of as a reciprocity condition. Reciprocity [62] implies that rays at a given position cannot emerge in the same direction from two different paths. In consequence, if a given point in the absorber is to be reached from as many ray bounces as possible, the rays must be entering/exiting that point from all angles. More formally, we show here that reciprocity can be applied to the *full* Maxwell's equations in order to relate the enhancement to the density of states. Although the end result is not new, we wish to emphasize that the underlying ideas of the Yablonovitch and LDOS limits are closely tied to reciprocity. This is an alternative to the derivation in Ref. 160, which differs in that it directly uses the reciprocity (or generalized reciprocity) from Maxwell's equations. As was also emphasized in Ref. 160, the result also applies to linear *nonreciprocal* systems, since the density of states of transposed-related materials is the same ($G_\epsilon(r,r) = G^t_{\epsilon^t}(r,r)$ [62]).

Here for simplicity, we consider a reciprocal system in the derivation. We have then:

$$\int_{S_\infty} [\mathbf{E}_a \times \mathbf{H}_b - \mathbf{E}_b \times \mathbf{H}_a] \cdot \hat{\mathbf{k}}\, dS = \int_V [\mathbf{E}_a \cdot \mathbf{J}_b - \mathbf{E}_a \cdot \mathbf{J}_a] dV \tag{5.1}$$

If we choose ($\mathbf{J}_a = \frac{1}{i\mu\omega}\hat{\mathbf{e}}_s \delta_{\mathbf{r_0}}$, $\mathbf{E}_a^{inc} = \mathbf{0}$) and ($\mathbf{J}_b = \mathbf{0}$, $\mathbf{E}_b^{inc} = e^{ik\hat{\mathbf{k}}_0\cdot\mathbf{r}}\hat{\mathbf{e}}_b$), then $\mathbf{E}_a = \bar{\bar{\mathbf{G}}}_E(\mathbf{r_0},\mathbf{r_0})\hat{\mathbf{e}}_s$.

The far field term can be written as $\mathbf{E}_a^s = e^{ikr} f_s(\hat{\mathbf{k}})\hat{\mathbf{e}}_a/r$, $\mathbf{H}_a^s = \left(\hat{\mathbf{k}} \times \mathbf{E}_a^s\right)/\eta$ with $\eta = \sqrt{\mu_0/\epsilon_0}$, and similarly for the far-field of the scattered field "b", so that: $\int_{S_\infty} [\mathbf{E}_a^s \times \mathbf{H}_b^s - \mathbf{E}_b^s \times \mathbf{H}_a^s] \cdot \hat{\mathbf{k}}\, dS = 0$. We then expand the integrand of the left term in Eq. (5.1) to obtain:

$$\begin{aligned}\int_{S_\infty} [\mathbf{E}_a^s \times \mathbf{H}_b^{inc} - \mathbf{E}_b^{inc} \times \mathbf{H}_a^s]\, dS = -\frac{1}{\eta}\int f_s(\hat{\mathbf{k}}) e^{ikr(1+\hat{\mathbf{k}}\cdot\hat{\mathbf{k}}_0)} \times \\ [(\hat{\mathbf{e}}_a \cdot \hat{\mathbf{e}}_b)(1 - \hat{\mathbf{k}}\cdot\hat{\mathbf{k}}_0) + (\hat{\mathbf{e}}_a \cdot \hat{\mathbf{k}}_0)(\hat{\mathbf{e}}_b \cdot \hat{\mathbf{k}})] r\, d\hat{\mathbf{k}} = -\frac{1}{\eta} e^{ikrg(\theta,\phi)} h(\theta,\phi) d\theta d\phi\end{aligned} \tag{5.2}$$

The integral can be evaluated using the method of stationary phase [176]. The function $g(\theta,\phi) = 1 + \hat{\mathbf{k}}\cdot\hat{\mathbf{k}}_0 = 1 + \cos\theta\cos\theta_0 + \sin\theta\sin\theta_0\cos(\phi-\phi_0)$ has two extrema at $\pm\hat{\mathbf{k}}_0$. The integrand is null at the first, so only the second matters. The Hessian matrix at $-\hat{\mathbf{k}}_0$ is given by: $\begin{pmatrix} 1 & 0 \\ 0 & \sin\theta_0^2 \end{pmatrix}$. We then conclude that the integral we want to evaluate is equal to:

$$\frac{-1}{\eta} i \frac{1}{\sin\theta_0/2\pi} \frac{1}{kr} h(-\hat{\mathbf{k}}_0) = \frac{i}{\eta}\frac{4\pi}{k}(\hat{\mathbf{e}}_a \cdot \hat{\mathbf{e}}_b) f_s(-\hat{\mathbf{k}}_0) \tag{5.3}$$

where $\hat{\mathbf{e}}_a$ is evaluated at $-\hat{\mathbf{k}}_0$.

We finally conclude from Eq. (5.1) that:

$$-\hat{\mathbf{e}}_s \cdot \mathbf{E}_b(\mathbf{r_0}) = 4\pi(\hat{\mathbf{e}}_a \cdot \hat{\mathbf{e}}_b) f_s(-\hat{\mathbf{k}}_0) \tag{5.4}$$

which is the reciprocity relation relating the far field of a point source at $\mathbf{r_0}$ in the direction $-\hat{\mathbf{k}}_0$ to the field at $\mathbf{r_0}$ due to an incoming plane wave from the same direction.

Now, we use the Poynting theorem to compute the far field of the point source:

$$\frac{1}{\eta}\int |f_s(\hat{\mathbf{k}})|^2 d\mathbf{k} = \int \mathrm{Re}[\mathbf{E}_a \times \mathbf{H}_a^*]\cdot \hat{\mathbf{k}}\, dS \leq -\int \mathrm{Re}[\mathbf{J}_a^* \cdot \mathbf{E}_a] = \frac{1}{\omega\mu}\mathrm{Im}[\mathbf{E}_a(\mathbf{r_0})\cdot \hat{\mathbf{e}}_\mathbf{s}] \quad (5.5)$$

At this point we are able to combine Eq. (5.4) and Eq. (5.5) to find our main result about the enhancement. We consider an incoming angular distribution $f(\hat{\mathbf{k}}_0)$ with a normalized flux ($\int_{4\pi}|\cos\theta| f(\hat{\mathbf{k}}_0)d\hat{\mathbf{k}}_0 = 1$). By integrating over all coming angles and polarizations of the "b" field, we have:

$$\begin{aligned}\int \sum_{\hat{\mathbf{e}}_b} |\mathbf{E}_b|^2 f(\hat{\mathbf{k}}_0)\, d\hat{\mathbf{k}}_0 &= \int \sum_{\hat{\mathbf{e}}_b,\hat{\mathbf{e}}_s} |\mathbf{E}_b\cdot\hat{\mathbf{e}}_s|^2 f(\hat{\mathbf{k}}_0)\, d\hat{\mathbf{k}}_0 \\ &= (4\pi)^2 \int \sum_{\hat{\mathbf{e}}_b,\hat{\mathbf{e}}_s} |\hat{\mathbf{e}}_a\cdot\hat{\mathbf{e}}_b|^2 |f_s(-\hat{\mathbf{k}}_0)|^2 f(\hat{\mathbf{k}}_0)\, d\hat{\mathbf{k}}_0 \\ &= (4\pi)^2 \int \sum_{\hat{\mathbf{e}}_s} |f_s(-\hat{\mathbf{k}}_0)|^2 f(\hat{\mathbf{k}}_0)\, d\hat{\mathbf{k}}_0 \leq (4\pi)^2 \frac{\max f}{k}\sum_{\hat{\mathbf{e}}_s}\mathrm{Im}[\mathbf{E}_a(\mathbf{r_0})\cdot\hat{\mathbf{e}}_s] \\ &= (4\pi)^2\frac{\max f}{k}\mathrm{Tr}[\mathrm{Im}\bar{\bar{\mathbf{G}}}_E(\mathbf{r_0},\mathbf{r_0})] = (4\pi)^2\frac{\max f}{k}\frac{\pi c^2}{\omega n^2}\rho_d(\mathbf{r_0})\end{aligned} \quad (5.6)$$

which relates rigorously the enhancement and the local density of states.

We can use this result to compute the absorbed power and deduce the enhancement compared to the single pass for a cell of surface S and effective thickness d. We have:

$$\langle P_{abs}\rangle = \frac{1}{2}\omega\epsilon_r''\epsilon_0 \int_V \int \sum_{\hat{\mathbf{e}}_b} |\mathbf{E}_b|^2 f(\hat{\mathbf{k}}_0)\, d\hat{\mathbf{k}}_0 \leq \frac{1}{2}\epsilon_r''\epsilon_0 (4\pi)^2 \frac{\pi c^3}{\omega n^2}\max f \int_V \rho_d \quad (5.7)$$

The total incident power, taking into account the two polarizations, is given by $\frac{1}{2\eta}\int f(\hat{\mathbf{k}}_\mathbf{0})|\cos\theta| d\hat{\mathbf{k}}_\mathbf{0} \times 2 \times S = S/\eta$, and the normalized single pass absorption is $\alpha d = \frac{\epsilon_r''}{n}\frac{\omega}{c}d$. The enhancement is then given by:

$$\langle q\rangle = \frac{\langle P_{abs}\rangle}{P_{inc}\alpha d} \leq \frac{4\pi}{n}\frac{\langle\rho_d\rangle}{\rho_v}\max f \quad (5.8)$$

where $\rho_v = \omega^2/2\pi^2c^3$ is the free space density of states. We remind that $\langle q\rangle$ refers to the absorption enhancement compared to the single pass, averaged over both polarizations and over a directional spectrum $f(\theta)$ with normalized flux ($\int_{4\pi}|\cos\theta| f(\theta)d\Omega = 1$), and $\langle\rho_d\rangle$ is the average density of states in the device. This inequality becomes an *equality* in the case of negligible absorption and isotropic incidence ($f = \frac{1}{2\pi}$).

For a bulk dielectric, we have $\rho_d = n^3\rho_v$ so that $\langle q\rangle \leq 2n^2$ for isotropic incident light which is the standard limit in the absence of a back reflector.

5.3.2 Ocean buoys

A similar procedure can be followed in the ocean-buoy problem. Here, we review the result in Ref. 24 and emphasize that it is also a consequence of reciprocity, which shows the similarity with the LDOS limit in solar cells.

The problem of ocean wave energy extraction using oscillating bodies is formally equivalent to the problem where there are discrete sources of which the amplitude can in principle be controlled externally (velocity of the body that can be controlled through an external mechanical mechanism). Considering the effect of the incoming wave and interaction between bodies, the total absorption can be written as a quadratic function in terms of the amplitudes of the different sources as in [174] for example. Maximizing the absorption allows to find the optimal amplitudes as a function of the scattered field and the radiated fields from the sources. This gives [174]:

$$P_{max} = \frac{1}{8}\mathbf{F_e}^*(\theta)R^{-1}\mathbf{F_e}(\theta) \tag{5.9}$$

where $\mathbf{F_e}(\theta)$ is the force applied on the bodies for an incident wave from the direction θ and R is the *resistance* matrix (radiation damping matrix).

One would try to see the effect of the reciprocity relations discussed before on the maximum absorption in this context. The exact equivalent of Eq. (5.4) is already known in the ocean waves problem as the Haskind-Hanaoka formula that relates the force applied on a body due to an incident wave to the radiated field when the the body acts as a source [177]. It leads to:

$$F_{e,i}(\theta) = -\frac{4}{k}\rho_o g A c_g A_i(\theta + \pi) \tag{5.10}$$

where A is the amplitude of the incident wave, A_i is the far-field amplitude of the radiation mode i, k is the wavenumber, c_g is the group velocity, ρ_o is the water density, and g is the gravity of Earth.

The use of this formula on the maximum absorbed power by an array of oscillating bodies leads to the bound on the power absorbed by the array. For a given incident angular distribution $f(\theta)$ normalized so that $\int_{2\pi} f(\theta)d\theta = 1$:

$$\langle P_{max}\rangle = \int f(\theta)P_{max}(\theta)\mathrm{d}\theta \leq \max f \int P_{max}(\theta)\mathrm{d}\theta = \max f \frac{1}{8}\sum_{i,j}[R^{-1}]_{i,j}\int_{2\pi} F^*_{e,i}F_{e,j}\mathrm{d}\theta \tag{5.11}$$

Using Eq. (5.10) and the fact that $R_{i,j} = \frac{2}{\pi k}\rho_o g c_g \operatorname{Re}(\int_{2\pi} A_i^* A_j)$ [174], we conclude that:

$$\langle \sigma_{a,max}^N \rangle = \int_{2\pi} \sigma_{a,max}^N(\theta) f(\theta) d\theta \leq \frac{NM}{k} 2\pi \max f \tag{5.12}$$

where $\sigma_{a,max}^N = P_{max}/(\frac{1}{2}\rho_o g |A|^2 c_g)$ is the *maximum* absorption cross section of the array, N is the number of buoys and M is the number of degrees of freedom for the buoy motion (1–6 [174], e.g. 1 for only heave motion).

This result is general and does not depend on assumptions on the scatterers. It means that the interaction factor $q = \langle \sigma_{a,max}^N \rangle / N \langle \sigma_a^1 \rangle$ is bounded by $M/(k\langle \sigma_a^1 \rangle)$ for isotropic incidence. For buoys in heave motion which are studied in this chapter, we have $M = 1$ and $\langle \sigma_a^1 \rangle = \sigma_a^1$ (the absorption cross section of the single buoy does not depend on the incident angle).

Note that Eq. (5.12) is also valid for a single buoy. Depending on the symmetries of the buoy, the actual absorption may be smaller (for an axisymmetric buoy, we always have $k\sigma_a^1 \leq 3$ [177]).

It is important to realize that for *isotropic incidence*, we have $\langle q \rangle \leq 1$ at the resonance frequency [the k where $\langle \sigma_a^1 \rangle$ reaches the maximum M/k from Eq. (5.12)], while it can in principle be larger at other frequencies. Although this sets a general limit valid at any frequency for any structure, we show in the following that it is not tight when considering the frequency-averaged performance.

5.4 Radiative transfer equation limits

We consider a two-dimensional array of scattering/absorbing particles distributed inside a *region* S bounded with a curve C (Fig. 5-3).

In the case of dilute and non-structured arrays, coherent scattering effects average out. This allows one to use the radiative-transfer equation (RTE) that only involves specific intensity $I(\mathbf{r}, \theta)$, and that is applicable to ensemble averages of random arrays at a single frequency [62, 161]:

$$\mathbf{e}_\theta \cdot \nabla_r I = -\rho \sigma_e I + \rho \sigma_s \int d\theta' p(\theta, \theta') I + \epsilon \tag{5.13}$$

where σ_s, σ_a and σ_e denote respectively the scattering, absorbtion and extinction cross sections of the individual particles ($\sigma_e = \sigma_s + \sigma_a$), p the normalized differential cross section, ρ the particles' density, $\mathbf{e}_\theta$ the unit vector with direction θ and ϵ internal sources.

We conjecture that a similar averaging of coherent effects arises from averaging over frequency and/or angle, and below we demonstrate numerically that this allows RTE to

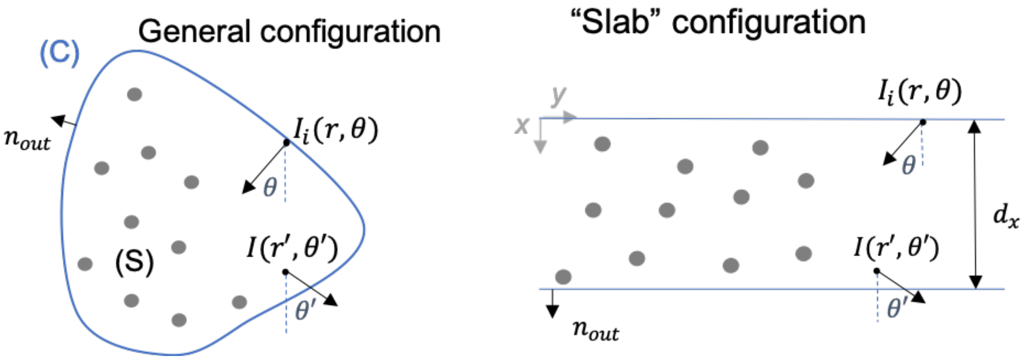

Figure 5-3: Sketch of RTE system.

make accurate predictions even for a small number of random samples or for optimized periodic arrays. This is similar to optical light trapping where Yablonovitch model can predict the frequency/angle-average performance of textured solar cells even though it cannot reproduce the exact spectral or angular response [7, 25].

5.4.1 General limit

Similarly to our previous discussion of reciprocity-based limits from the wave equation, we now use reciprocity constraints on RTE to obtain general limits on the interaction factor q.

One can first define a surface Green's function $G_s(\mathbf{r},\theta;\mathbf{r}',\theta')$ [178] giving $I(\mathbf{r},\theta)$ for an incident field $I_i(\mathbf{r_i},\theta_i) = \delta(\theta_i-\theta')\delta(\mathbf{r_i}-\mathbf{r}')$ and no internal sources $\epsilon = 0$. Similarly, a volume Green's function $G_p(\mathbf{r},\theta;\mathbf{r}',\theta')$ can be defined as the intensity $I(\mathbf{r},\theta)$ obtained with no incident field $I_i = 0$ and a point source $\epsilon(\mathbf{r_i},\theta_i) = \delta(\theta_i-\theta')\delta(\mathbf{r_i}-\mathbf{r}')$.

We recall that the flux density $\mathbf{F}$ is defined as $\int_{2\pi} I\mathbf{e}_\theta d\theta$. Conservation of energy [161] then leads to $\int_C \mathbf{F}\cdot\mathbf{n}_{out}d\mathbf{r} = P_e - P_a$ where P_e and P_a are the generated and absorbed power respectively. For a unit source, we have $P_e = \int_S \epsilon(\mathbf{r},\theta)d\mathbf{r}d\theta = 1$ so that:

$$\int_C \int_{\mathbf{e}_\theta\cdot\mathbf{n}_{out}>0} G_p(\mathbf{r},\theta;\mathbf{r}',\theta')(\mathbf{e}_\theta\cdot\mathbf{n}_{out})d\mathbf{r}d\theta = 1 - P_a \tag{5.14}$$

To bound this last expression, we need a *lower*-bound for P_a. By noting that the intensity at any point is larger than the *single pass* value (obtained after extinction without multiple scattering), we have:

$$\begin{aligned} P_a &= \rho\sigma_a \int_S \int_{2\pi} G_p(\mathbf{r},\theta;\mathbf{r}',\theta') d\mathbf{r} d\theta \\ &\geq \rho\sigma_a \int_S \frac{e^{-\rho\sigma_e|\mathbf{r}-\mathbf{r}'|}}{|\mathbf{r}-\mathbf{r}'|} \delta[angle(\mathbf{r}-\mathbf{r}') - \theta'] d\mathbf{r} = \frac{\sigma_a}{\sigma_e} H_{\rho\sigma_e}(\mathbf{r}',\theta') \end{aligned} \tag{5.15}$$

where $H_{\rho\sigma_e}(\mathbf{r}',\theta')$ defined in the previous equation can be interpreted as the power absorbed by a medium *without* scattering and with an absorption coefficient $\rho\sigma_e$ in the presence of a unit source at the point $\mathbf{r}'$ emitting in direction θ'.

Finally, we relate G_s to G_p through reciprocity using $G_p(\mathbf{r},\theta;\mathbf{r}',\theta')|\mathbf{e}_\theta \cdot \mathbf{n}_{out}| = G_s(\mathbf{r}',\pi-\theta';\mathbf{r},\pi-\theta)$ [178]. We conclude from Eq. (5.14) and Eq. (5.15) after a simple change of variable that:

$$\int_C \int_{\mathbf{e}_\theta \cdot \mathbf{n}_{out}<0} G_s(\mathbf{r}',\theta';\mathbf{r},\theta) d\mathbf{r} d\theta \leq 1 - \frac{\sigma_a}{\sigma_e} H_{\rho\sigma_e}(\mathbf{r}',\pi-\theta') \tag{5.16}$$

with equality *always* realized in the absence of absorption.

Since the interaction factor in RTE is given by $q = \langle \int_0^{2\pi} I(\mathbf{r}',\theta') d\theta' \rangle_{\mathbf{r}'} / I_i$ where I_i is the incident intensity and $\langle . \rangle_{\mathbf{r}'}$ is the average over $\mathbf{r}'$ in S, we can therefore bound the interaction factor q for a given directional spectrum $f(\theta)$ [fraction of power incident from angle θ]:

$$\langle q \rangle = \int_C \int_{2\pi} \int_{\mathbf{e}_\theta \cdot \mathbf{n}_{out}<0} f(\theta) \langle G_s(\mathbf{r}',\theta';\mathbf{r},\theta) \rangle_{\mathbf{r}'} d\mathbf{r} d\theta' d\theta \leq 2\pi \left[1 - \frac{\sigma_a}{\sigma_e} h(\rho\sigma_e) \right] \max_\theta f \tag{5.17}$$

where $h(\rho\sigma_e) = \langle H_{\rho\sigma_e}(\mathbf{r}',\theta') \rangle_{\mathbf{r}',\theta'} \geq 0$.

We can compute the function h in Eq. (5.17) for a "slab" of thickness d (with perfectly transmitting boundaries). We assume that the slab is normal to the x-axis. We first write the integral H using polar coordinates (r,θ):

$$H_\alpha(x',\theta') = \int_{-\pi/2}^{\pi/2} \int_0^{\frac{x'}{\cos\theta}} \alpha e^{-\alpha r} \delta(\theta-\theta') d\theta dr + \int_{-\pi/2}^{\pi/2} \int_0^{\frac{d-x'}{\cos\theta}} \alpha e^{-\alpha r} \delta(\theta-\theta') d\theta dr \tag{5.18}$$

After simplification, we have then:

$$h(\alpha) = \frac{1}{2\pi d} \int_0^{2\pi} \int_0^d H_\alpha(x',\theta') dx' d\theta' = 1 - \frac{2}{\pi} \frac{1-e_1(\alpha d)}{\alpha d},\ e_i(x) = \int_0^{\pi/2} e^{-x\sec\alpha} \cos^i \alpha d\alpha. \tag{5.19}$$

Note that the bound in Eq. (5.17) reaches its maximal value $2\pi \max f$ in the limit of small absorption. This maximal value, which does not assume optimal single-buoy absorption, generalizes then the previous ocean-buoy bound, giving $\langle q \rangle \leq 1$ for isotropic incidence $f = 1/2\pi$ at any wavelength in RTE regime. In addition, $\langle q \rangle = 1$ is always realized in the small absorption limit. This special case is sometimes referred to as Aronson's theorem [179].

The equality in Eq. (5.17) is reached for:

$$\int\limits_{C_{\{\mathbf{e}_\theta \cdot \mathbf{n}_{out} < 0\}}} G_s(\mathbf{r}', \theta'; \mathbf{r}, \theta) d\mathbf{r} = \left[1 - \frac{\sigma_a}{\sigma_e} H_{\rho\sigma_e}(\mathbf{r}', \theta')\right] \delta(\theta - \theta_m) \tag{5.20}$$

where $\theta_m = \arg\max f$. This means that the interaction factor should be equal to zero for any incident angle different from θ_m. In the ideal case of small absorption, the optimal G_s becomes independent of θ', which corresponds to *isotropic* interior intensity, similar to the Yablonovitch model. Therefore, in order to explore *optimal* solutions of RTE, we solve it under the assumption of nearly isotropic intensity, which is well known to lead to a diffusion model [62,161,178]. We emphasize that not all RTE systems are diffusive, but our result above shows that the optimal $\langle q \rangle$ is attained in an isotropic diffusive regime.

5.4.2 Radiative-diffusion model

Unless otherwise stated, we restrict ourselves to scatterers distributed inside a slab of thickness d (Fig. 5-3).

Diffusion equation

We start by reproducing the diffusion equation as in Ref. 62, 161 but adjusting the numerical coefficients for a two-dimensional medium. In addition to RTE parameters and reflection coefficients at the boundaries (R_i), the radiative-diffusion solution uses an asymmetry factor (μ) [see below] of the single particle (Fig. 5-4).

We first separate the intensity as $I = I_{ri} + I_d$ where I_{ri} is the reduced (coherent) intensity and $I = I_d$ is the diffuse (incoherent) intensity. The reduced intensity is related to the single scattering and obeys $\mathbf{e}_\theta \cdot \nabla_r I_{ri} = -\rho\sigma_e I_{ri}$. So from RTE equation, the diffuse intensity obeys:

$$\mathbf{e}_\theta \cdot \nabla_r I_d = -\rho\sigma_e I_d + \rho\sigma_s \int d\theta' p(\theta, \theta') I_d + J, \quad J = \rho\sigma_s \int d\theta' p(\theta, \theta') I_{ri}. \tag{5.21}$$

Now, considering the diffusion approximation, we write: $I_d(\mathbf{r}, \theta) = U(\mathbf{r}) + \frac{1}{\pi}\mathbf{F}(\mathbf{r}) \cdot \mathbf{e}_\theta$.

This could be seen as a first order series in θ. We also note that the diffuse flux is: $\int I_d \mathbf{e}_\theta \, d\theta = \mathbf{F}$.

In order to obtain U and $\mathbf{F}$ we apply the operators $\int d\theta$ and $\int \mathbf{e}_\theta d\theta$ on Eq. (5.21). This leads to:

$$\begin{aligned} \nabla_r \cdot \mathbf{F} &= -2\pi\rho\sigma_a U + 2\pi\rho\sigma_s U_{ri}, \\ U_{ri}(\mathbf{r}) &= \frac{1}{2\pi}\int d\theta \; I_{ri}(\mathbf{r},\theta), \\ \nabla_r U &= -\frac{1}{\pi}\rho\sigma_{tr}\mathbf{F} + \frac{1}{\pi}\int d\theta \; J\hat{\mathbf{s}}, \end{aligned} \tag{5.22}$$

where $\sigma_{tr} = \sigma_e(1-p_1)$ and $\sigma_e p_1 = \int d\theta' p(\hat{\mathbf{s}},\hat{\mathbf{s}}')[\hat{\mathbf{s}}\cdot\hat{\mathbf{s}}']$, so that $p_1 = \sigma_s\mu/\sigma_e$ where μ is the average of the cosine of the scattering angle.

Equations (5.22) allow to solve for U and $\mathbf{F}$. Combining them, we obtain a diffusion equation for U:

$$\nabla^2 U - (\rho\sigma_d)^2 U = -2\rho^2\sigma_{tr}\sigma_s U_{ri} + \frac{1}{\pi}\nabla\cdot\int d\theta \; J\hat{\mathbf{s}} \tag{5.23}$$

Now we need to add appropriate boundary conditions. Supposing that we have a reflection coefficient R on the surface, this should be: $I_d(\mathbf{r},\theta) = R(\theta)I_d(\mathbf{r},\pi-\theta)$ for $\hat{\mathbf{s}}$ directed towards the inside of the medium. However, considering the assumed formula for I_d the condition cannot be satisfied exactly . A common approximate boundary condition is to verify the relation for the fluxes:

$$\int_{\hat{\mathbf{s}}\cdot\hat{\mathbf{n}}>0} I_d(\hat{\mathbf{s}}\cdot\hat{\mathbf{n}})d\theta = \int_{\hat{\mathbf{s}}\cdot\hat{\mathbf{n}}<0} R(\theta)I_d(\hat{\mathbf{s}}\cdot\hat{\mathbf{n}})d\theta \tag{5.24}$$

where $\hat{\mathbf{n}}$ is the normal to the surface directed inwards.

Using the formula for I_d we obtain:

$$2(1-r_1)U + \frac{(1+r_2)}{2}\mathbf{F}\cdot\hat{\mathbf{n}} = 0 \tag{5.25}$$

where $r_i = \int_{-\pi/2}^{\pi/2} R(\theta)\cos^i(\theta)d\theta / \int_{-\pi/2}^{\pi/2}\cos^i(\theta)d\theta$.

— **Asymmetry factor** — The asymmetry factor usually used in diffusion models is [62, 161] $\mu = \mu_1$, where in general $\mu_i = \int_{2\pi}\cos(i\theta)p(\theta)d\theta$ (where we take $p(\theta,\theta') = p(\theta-\theta')$). Since the diffusion result depends only on v_s, v_a and μ_1, it can be seen as approximating the differential scattering cross section by: $p(\theta-\theta') = \frac{1}{2\pi}[1+2\mu_1\cos(\theta-\theta')]$.

The Delta-Eddington approximation [10] allows to incorporate the second moment of p by including the forward scattering peak using a "delta function" term so that: $p(\theta,\theta') =$

$\mu_2\delta(\theta-\theta') + \frac{1-\mu_2}{2\pi}[1+2\mu\cos(\theta-\theta')]$ where $\mu = (\mu_1-\mu_2)/(1-\mu_2)$. This approximation matches the Fourier decomposition of p up to the second term. By incorporating this expression in RTE (Eq. 5.13), one recovers a *second* RTE with p replaced by $\frac{1}{2\pi}[1+2\mu\cos(\theta-\theta')]$ and σ_s replaced by $\sigma_s(1-\mu_2)$. So the diffusion approximation can be made more accurate by replacing μ by $(\mu_1-\mu_2)/(1-\mu_2)$ and σ_s by $\sigma_s(1-\mu_2)$. This is known as the Delta-Eddington approximation [10].

In a three-dimensional medium, $\mu_i = \int_{4\pi} P_i(\cos\theta)p(\cos\theta)d\Omega$ where P_i is the i^{th} Legendre polynomial.

Enhancement

By defining the cross sections per unit of length as $\upsilon_{s,a,e} = \rho d\sigma_{s,a,e}$, the previous diffusion model predicts an interaction factor q of:

$$q(\theta) = q_0(\theta)\left(\eta\left[D\frac{\xi(\upsilon_d)}{\xi(\upsilon_e\sec\theta)} + C\right] + 1\right) \tag{5.26}$$

where $\upsilon_d^2 = \gamma\upsilon_a(\upsilon_e - \upsilon_s\mu)$ is the diffusion coefficient [$\gamma = 2$ (resp. $=3$) in 2D (resp. 3D)], $\xi(x)$ is the function $(1-e^{-x})/x$, $C = \gamma[\upsilon_s(\upsilon_e+\mu\upsilon_a)]/[\upsilon_d^2 - (\upsilon_e\sec\theta)^2]$, D is given by the boundary conditions, $q_0(\theta)$ is the reduced factor and η is an additional correction term that we discuss later. $q_0(\theta)$ is given by:

$$q_0(\theta) = \frac{(1-\tilde{R}_1)(1+\tilde{R}_2Y)}{1-\tilde{R}_1\tilde{R}_2Y^2}\xi(\upsilon_e\sec\theta) \tag{5.27}$$

with $\tilde{R}_i = R_i(\theta)$, $Y = e^{-\upsilon_e\sec\theta}$ and R_1 refers to the boundary facing the incident wave.

D is given through boundary conditions by $D = \frac{A+B}{1+\tilde{R}_2Y}$, where:

$$\begin{aligned}\begin{bmatrix} \alpha_1 + \beta\frac{\upsilon_d}{\upsilon_{tr}} & (\alpha_1 - \beta\frac{\upsilon_d}{\upsilon_{tr}})e^{-\upsilon_d} \\ (\alpha_2 - \beta\frac{\upsilon_d}{\upsilon_{tr}})e^{-\upsilon_d} & (\alpha_2 + \beta\frac{\upsilon_d}{\upsilon_{tr}}) \end{bmatrix}\begin{bmatrix} A \\ B \end{bmatrix} = X = \\ -\begin{bmatrix} C(1+\tilde{R}_2Y^2)\alpha_1 + \beta\frac{\upsilon_e}{\upsilon_{tr}}(\frac{C}{\cos\theta} + \gamma p_1\cos\theta)(1-\tilde{R}_2Y^2) \\ [C(1+\tilde{R}_2)\alpha_2 - \beta\frac{\upsilon_e}{\upsilon_{tr}}(\frac{C}{\cos\theta} + \gamma p_1\cos\theta)(1-\tilde{R}_2)]Y \end{bmatrix}\end{aligned} \tag{5.28}$$

with $\upsilon_{tr} = \upsilon_e - \upsilon_s\mu$, $\alpha_i = (1-r_1^i)/(1+r_2^i)$ and $r_p^i = \int_{-\pi/2}^{\pi/2} R_i(\theta)\cos^p(\theta)\mathrm{d}\theta / \int_{-\pi/2}^{\pi/2}\cos^p(\theta)\mathrm{d}\theta$. We recall that ($\gamma = 2$, $\beta = \pi/4$) [resp. ($\gamma = 3$, $\beta = 1$)] in 2D [resp. 3D].

In the absence of reflecting walls ($R_i = 0$) previous experssions simplify to $q_0(\theta) =$

$\xi(\upsilon_e \sec\theta)$ and:

$$D = -\frac{C(1+e^{-\upsilon_e \sec\theta}) + \beta\frac{(C+\gamma p_1 \cos^2\theta)}{(1-p_1)\cos\theta}(1-e^{-\upsilon_e\sec\theta})}{(1+e^{-\upsilon_d}) + \beta\frac{\upsilon_d}{\upsilon_e(1-p_1)}(1-e^{-\upsilon_d})}, \tag{5.29}$$

where $p_1 = \sigma_s\mu/\sigma_e$ and $\beta = \pi/4$ (resp. $= 1$) in 2D (resp. 3D).

Corrected radiative-diffusion

Equation (5.26) with $\eta = 1$ is obtained from the standard diffusion model. However, it is also known that the diffusion solution is inaccurate for small thicknesses [180–182]. A major problem is that it does *not* guarantee $\langle q \rangle = 1$ for isotropic incidence and negligible absorption, even though we previously mentioned that this is the case for any solution of RTE. The reason behind this problem is that the term I_{ri} is not isotropic even for an isotropic incidence. For large thicknesses, however, the contribution of the term I_{ri} becomes negligible and the diffuse term I_d can ensure an isotropic solution. This simply means that the higher order terms in the expression of I_d cannot be neglected for small thicknesses. In order to keep the simplicity of the diffusion solution, we suppose that the effects of higher order terms can be incorporated by the introduction of a scalar term in the diffuse intensity ηI_d instead of I_d. η is then defined so as ensure the condition $\langle q \rangle = 1$ for isotropic incidence and zero absorption. This procedure is somewhat similar to the approach in Ref. 181 except that we use a constant factor η since we are interested in the total q and not the spatially resolved I. In order to define η, we study the limit of negligible absorption for which $\upsilon_d \to 0$, $C \to -2\cos^2\theta$ and $D \to \cos^2\theta(1-e^{-\upsilon_e\sec\theta}) + \frac{\pi}{4}\cos\theta(1-e^{-\upsilon_e\sec\theta})$. After simplification, the condition $\langle q \rangle = 1$ allows to define η as:

$$\eta = \frac{\pi - \sum_{i=1}^{2}\int_0^{\pi/2} q_0^{(i)}\,d\theta}{\sum_{i=1}^{2}\int_0^{\pi/2}\left[\frac{q_0^{(i)}D_0^{(i)}(\theta,\upsilon_e,\upsilon_{tr})}{\xi(\upsilon_e\sec\theta)} - \gamma\cos^2\theta q_0^{(i)}\right]d\theta} \tag{5.30}$$

with:

$$(1+\tilde{R}_2 Y)D_0(\theta,\upsilon_e,\upsilon_{tr}) = \frac{(\alpha_2 + \frac{2\beta}{\upsilon_{tr}})X_{0,1} + (\alpha_1 + \frac{2\beta}{\upsilon_{tr}})X_{0,2}}{\frac{2\beta}{\upsilon_{tr}}(\alpha_1+\alpha_2) + 2\alpha_1\alpha_2} \tag{5.31}$$

where:

$$X_0 = \begin{bmatrix} \gamma\cos^2\theta(1+\tilde{R}_2Y^2)\alpha_1 + 2\beta\cos\theta(1-\tilde{R}_2Y^2) \\ [\gamma\cos^2\theta(1+\tilde{R}_2)\alpha_2 - 2\beta\cos\theta(1-\tilde{R}_2)]Y \end{bmatrix} \tag{5.32}$$

Superscripts for $q_0^{(i)}$ and $D_0^{(i)}$ refer to the boundary that is facing the incident wave.

In absence of reflecting walls ($R_i = 0$), this simplifies to:

$$\eta = \frac{\frac{\pi}{2} - \frac{1}{\upsilon_e}[1 - e_1(\upsilon_e)]}{\beta + \frac{\pi}{8}\gamma - \frac{2\gamma}{3\upsilon_e} - \beta e_1(\upsilon_e) + \frac{\gamma}{2}e_2(\upsilon_e) + \frac{\gamma}{\upsilon_e}e_3(\upsilon_e)}. \tag{5.33}$$

We note that, as expected, $\eta \to 1$ for an absorber that is thick compared to the extinction length. From our discussion above, this corrected radiative-diffusion model can now be used to estimate the upper bound on the interaction factor even in regimes where the standard diffusion model is not expected to be accurate (optically thin or large absorption).

Scattering particles embedded in low-absorbing layer

As a first example, we consider scattering particles embedded in a layer of index n and negligible absorption in the presence of perfect back-reflector ($R_2 = 1$). In the limit of large scattering we obtain:

$$q(\theta) = 3\cos^2\theta + \frac{2}{\alpha_1}\cos\theta \tag{5.34}$$

where θ is the *refraction* angle ($< \theta_c = \operatorname{asin}\frac{1}{n}$) and $\alpha_1^{-1} = n^2\left[1 + \left(1 + \frac{1}{n^2}\right)^{\frac{3}{2}}\right]$.

For isotopic incidence ($f = \frac{n^2}{\pi}\delta(\theta < \theta_c)$), we have:

$$\langle q\rangle = \int_{4\pi} q(\theta)f(\theta)d\Omega = 2\pi\frac{n^2}{\pi}\int_0^{\theta_c} q(\theta)\sin\theta d\theta = 4n^2. \tag{5.35}$$

In the presence of bulk scattering, the Yablonovitch limit is indeed maintained for isotropic incidence but can be overcome at normal incidence.

5.5 Ocean-buoy arrays

5.5.1 Example

We now present a validation of the accuracy of Eq. (5.26) in a model of ocean-wave energy converter (WEC) consisting of a truncated cylinder in heave motion (Fig. 5-2). The isolated-buoy properties can be obtained analytically [183–185] and are depicted in Fig. 5-4: they are designed [8] to have an absorption resonance that matches the typical Bretschneider spectrum [9] of ocean waves. We choose the array density based on an earlier optimized periodic 3-row WEC arrangement [8]. For this density, we then compare the exact numerical scattering solution calculated for both random and optimized-periodic arrays (using the method from Ref. 8) to both the analytical radiation-diffusion q from Eq. (5.26), with and without the correction η, and the numerical solution of RTE model by a Monte Carlo method [186].

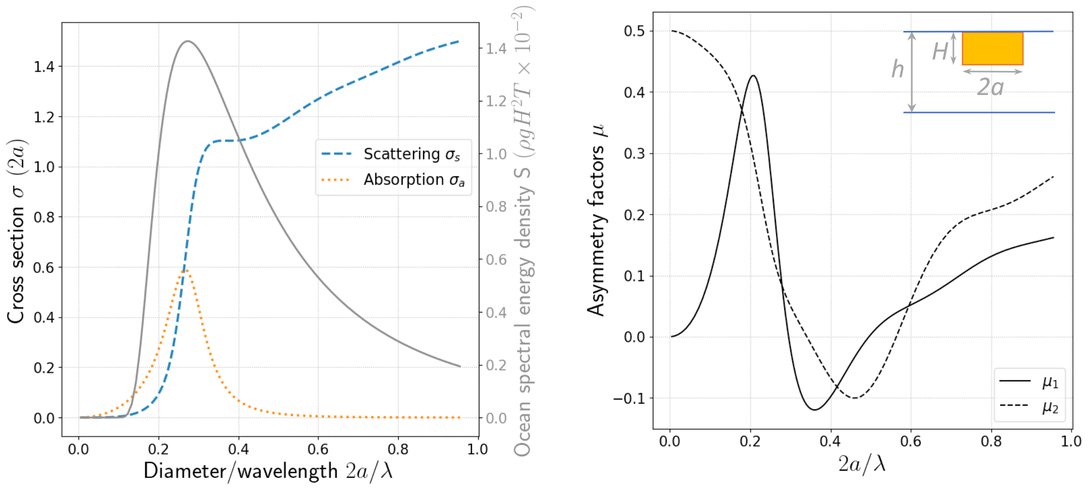

Figure 5-4: Properties of a single truncated-cylinder wave energy converter (WEC) in heave (vertical) motion, with radius $a = 0.3h$ and draft $H = 0.2h$ where h is the ocean depth. The WEC has an isotropic response with respect to the direction of the incident field. Left: Scattering and absorption cross sections of a single buoy normalized to the cylinder diameter ($\sigma/2a$). The ocean spectral energy density (energy per horizontal surface) is chosen as Bretschneider [9] with resonant frequency matching that of the body and is shown in units of $\rho g H^2 T$ (ρ is the water density, g the acceleration of gravity, T the mean wave period and H the significant wave height). Right: Asymmetry factors, defined as the average of $\cos\phi$ and $\cos 2\phi$ for the two-dimensional differential scattering cross section. These parameters enter into the diffusion equation as $\mu = (\mu_1 - \mu_2)/(1 - \mu_2)$ and with σ_s replaced by $\sigma_s(1 - \mu_2)$ [10].

In Fig. 5-5 (left), our corrected model agrees to $< 2\%$ accuracy with exact solutions for random arrays at $\theta < 80°$, as long as the results are frequency-averaged. The importance of frequency averaging is shown by the q frequency spectrum shown in the inset for $\theta = 0°$. For an ensemble of random structures, this spectrum exhibits a large standard deviation (gray shaded region), due to the many resonance peaks that are typical of absorption by randomized thin films [23, 25], but the *frequency average* mostly eliminates this variance and matches our predicted $q(\theta)$. Precisely such an average over many resonances is what allows the Yablonovitch model to accurately predict the performance of textured solar cells even though it cannot reproduce the detailed spectrum [7, 25].

At first glance, our model does *not* agree in Fig. 5-5 with the performance of the optimized periodic array from Ref. 8: the periodic array, which was optimized for waves

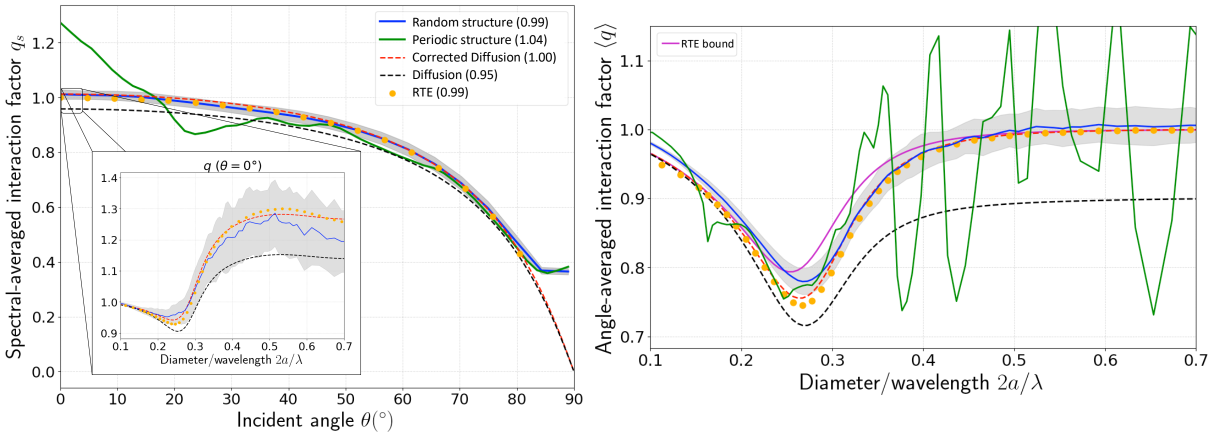

Figure 5-5: Left: Frequency-averaged interaction factor q_s vs incident angle θ for $N_x \times N_y = 3 \times 30$ arrays of buoys from exact solution [8] (solid lines), compared to standard-diffusion (black dashed lines), corrected-diffusion (red dashed lines) and radiative-transfer (RTE with Monte Carlo simulation, dots) models. ($q =$ array absorption / isolated-buoys absorption.) The average buoy spacings (randomly chosen via a Gamma distribution) are $d_x/h = 1.73$, $d_y/h = 3.63$, with $h =$ ocean depth (the density is $\rho = 1/d_y d_x$). Numbers in legend are q_s averaged over θ for a typical ocean-wave directional spectrum $\cos^{2s}\theta$ with $s = 4$ [11]. Inset: q vs. wavelength at $\theta = 0$, where shaded regions is one standard deviation from mean value (blue line) for 100 random structures. Right: $\langle q \rangle$ for over isotropic incidence. Results compared to limit in Eq. (5.17).

near normal incidence, is better at θ near 0° and worse elsewhere. However, when we *also* average over θ (from a typical ocean-wave directional spectrum [11]), the result (shown as a parenthesized number in the legend of Fig. 5-5) matches Eq. (5.26) within 5%. If we average over all angles assuming an *isotropic* distribution of incident waves, the results match within 1%. Similar results have been observed for thin-film solar cells, in which an optimized structure can easily exceed the $4n^2$ Yablonovitch limit for particular incident angles, but the Yablonovitch result is recovered upon angle-averaging [7, 25, 155, 158].

Finally, we note in Fig. 5-5 (right) that RTE results respect indeed the bound in Eq. (5.17) for isotropic incidence. In particular, we confirm that random arrays achieve $\langle q \rangle = 1$ for small absorption (i.e. small wavelength in our case). The periodic array, on the other hand, doesn't satisfy this relation unless it is frequency averaged. We also mention that the limit Eq. (5.17) is very loose for anisotropic incidence and cannot be reached without using external reflectors as discussed in Section IV-B below.

5.5.2 Larger interaction factor

Given this model, we can now explore ways to increase the interaction factor q. By examining the dependence of q in Eq. (5.26) on the parameters (Fig. 5-6), we find that for a fixed scattering-to-absorption ratio σ_s/σ_a, q reaches a maximum q_{max} for an intermediate value of scattering per unit length $\rho d\sigma_s$, whereas it increases monotonically with μ. A maximum μ is achieved by increasing μ_1 (forward scattering) and decreasing μ_2 (lateral scattering). The optimal value of $\rho d\sigma_s$ and q_{max} both increase with σ_s/σ_a; as the single particle absorbs more, the interaction factor decreases and the optimal configuration requires a larger spacing between the particles. The maximum q is then achieved in the limit of small absorption ($\rho d\sigma_a \ll 1$) and large scattering ($\rho d\sigma_s \gg 1$) for which we obtain a perfect isotropic diffuse intensity.

From Fig. 5-4, we see that we have $\sigma_a/\sigma_s \approx 1$ at the resonance of the WEC. In this case, the enhancement is expected to be smaller than 1 around the resonance and optimal structures will tend to have a large spacing d_y. (If the array were optimized for small wavelengths λ, where $\sigma_s \gg \sigma_a$, then a larger q could be obtained at those wavelengths, but q_s would be worse because the optimal spacing in this case is too small for good performance at the resonance.) Still, multiple scattering significantly improves the broadband performance of our array: our $\langle q\rangle \approx 0.99$ is larger than the $\langle q_0\rangle \approx 0.78$ that is obtained from RTE in absence of multiple scattering (reduced factor q_0). The performance is still lower than the 1.65 that would be obtained for $\sigma_s \gg \sigma_a$ in the ideal isotropic regime discussed below, essentially because σ_a/σ_s is too small and the structure is too thin (as for example quantified by the transport mean-free path $d/l_{tr} = \upsilon_s(1-\mu) \approx 0.5$ for $\frac{2a}{\lambda} \gtrsim 0.3$) to practically achieve an isotropic diffuse intensity.

Alternatively, we show that q can be enhanced by putting partially reflecting strips around the array. Similar to light-trapping by total internal reflection [22, 157], one possibility is to use a strip of a lower-“index” [177] medium (compared to the array’s ambient medium) on either side of the array. In the ocean-buoy problem, this can for example be achieved by either a depth change or the use of a tension/bending surface membrane which can lead to near-zero index [187, 188].

In Fig. 5-6, we show the effect of an increase in the scattering cross section and/or the index contrast for the same array studied before. By combining both effects, a large (> 3) spectral interaction factor can be achieved at normal incidence. At the same time, waves incident at large angles will be reflected out, so that the interaction factor integrated over isotropic incidence is still smaller than 1. For a given directional spectrum and scattering cross section of a single buoy, the optimal interaction factor is achieved for a specific value

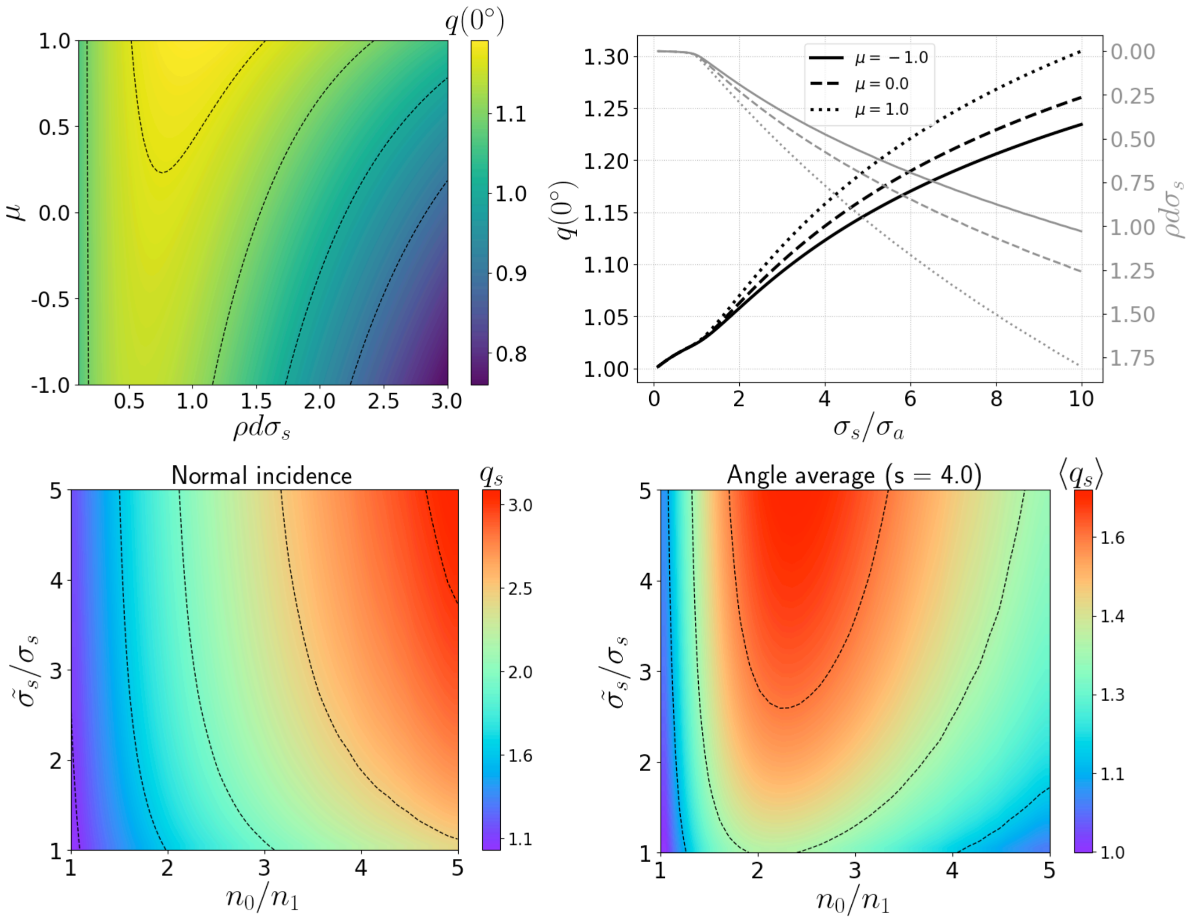

Figure 5-6: Upper: Dependence of $q(0^\circ)$ on parameters in absence of reflecting boundaries. In the left plot, we take $\sigma_s/\sigma_a = 5$. In the right plot, we show the optimal $\rho d\sigma_s$ and q_{max} for different values of σ_s/σ_a and μ. Lower: Effect of a change in the index contrast and scattering cross section on the bandwidth-averaged factor q_s for the same array in Fig. 5-5. We tune the index n_1 along a strip surrounding the array, with n_0 being the index of the array's ambient medium. We suppose that the WEC has new scattering cross section $\tilde{\sigma}_s$, but keep the same absorption cross section. Left: q_s at normal incidence. Right: q_s averaged over θ with a directional spectrum of $\cos^{2s}\theta$ and s = 4.

of the index contrast as can be seen in Fig. 5-6 (right).

Finally, it is instructive to look at the ideal case of small absorption and large scattering, for which Eq. (5.26) simplifies to:

$$q(\theta) = [1 - R_1(\theta)] \left(\frac{\pi}{4\alpha} + \cos\theta \right) \cos\theta \tag{5.36}$$

where R_1 is the reflection coefficient of the front-surface and $\alpha = (1-r_1)/(1+r_2)$ with $r_i = \int_{-\pi/2}^{\pi/2} R_1(\theta)\cos^i(\theta)\mathrm{d}\theta / \int_{-\pi/2}^{\pi/2} \cos^i(\theta)\mathrm{d}\theta$. Equation (5.36) still gives 1 when averaged over isotropic incidence, but the interaction factor is larger near normal incidence. Without reflectors ($R_1 = 0$), the maximum value of q at normal incidence is $1 + \frac{\pi}{4}$, and the previous directional spectrum gives $\langle q \rangle \approx 1.65$. This maximum value of $q(0)$ does not reach the arbitrarily large enhancement allowed by Eq. (5.17). However, $q(0)$ can still be made sufficiently large by including a reflector designed for transmission near normal incidence and reflection elsewhere (since $\alpha \to 0$).

5.5.3 Surface membrane

We now use a specific example to demonstrate a larger interaction factor q using surface membranes surrounding the WEC array. For large scale applications, such membranes could be designed to have the desired properties by connecting floating pontoons with elastic elements of appropriate stiffness.

A thin bending membrane on the water surface changes the "refractive index" ($\sim k/\omega$) through the following dispersion relation (e.g. Ref. 189):

$$\omega^2 = gk \tanh(kh) \frac{1 + C_b (kh)^4}{1 + m \cdot kh \tanh(kh)} \tag{5.37}$$

where ω is the frequency, g the acceleration of gravity, k the wavenumber, C_b is a dimensionless bending coefficient, m is the mass of the membrane relative to the mass of the water beneath it and h is the water depth. We simply assume $m = 0$ in the following.

At a fixed ω, the membrane decreases k (decreases the "index") compared to the surrounding medium. This change of index leads to a reflection off the membrane's edges. In particular, total internal reflection traps the water waves similarly to light trapping in solar cells, which increases the interaction factor q. The reflection coefficient, which depends on ω, C_b, the incident angle and the membrane's width w, can be computed by applying appropriate boundary conditions on either side of the membrane and using a transfer-matrix method as reviewed we show in the following. We note that evanescent modes need to be included because of the change in dispersion relations.

The index contrast increases with C_b (increasing stiffness), which increases the range of angles undergoing total internal reflection, making a more effective mirror. Since no waves are coming from the rear of the array, the optimal membrane behind the array should be a perfect reflector ($C_b \to \infty$, limited only by the attainable practical C_b).

Reflection coefficient with membranes

We consider a plane wave arriving from medium (1), that is a free-surface ocean with finite depth h, at angle θ with respect to the x-axis. We suppose that we have a thin membrane

(2) on the water surface extended from $x = 0$ to $x = w$. Change in the dispersion relation leads to different wavenumbers k_i^n verifying:

$$\omega^2 = gk_1^n h \tanh(k_1^n h) = gk_2^n h \tanh(k_2^n h)(1 + C_b(k_2^n h)^4) \tag{5.38}$$

where C_b is a bending coefficient of the membrane. k_i^0 corresponds to a (real) propagating wave while the other k_i^n correspond to (pure imaginary) evanescent waves.

We first compute the transfer-matrix between medium (1) and medium (2). We write the velocity potential in each medium i as:

$$\phi_i = \sum_{n=0}^{N} f_{n,i}(z) \left[\alpha_{n,i} e^{ik_{x,i}^n} + \beta_{n,i} e^{-ik_{x,i}^n}\right] e^{ik_y y} \tag{5.39}$$

where $(k_{x,i}^n)^2 + k_y^2 = (k_i^n)^2$ and $f_{n,i}(z) = N_{n,i} \cosh k_i^n(z + h)$ ($z = 0$ is the water's free surface). $N_{n,i} = 1/\sqrt{1 + \frac{\sinh(2k_i^n h)}{2k_i^n h}}$ is defined so as to ensure that $\langle f_{n,i}, f_{n,i}\rangle = \int_{-h}^{0} f_{n,i}^2 dz = 1$. We also note that $(f_{n,1})_n$ form an orthogonal basis while $(f_{n,2})_n$ are not orthogonal but still complete (in the limit of $N \to \infty$) [189]. Finally, for a propagating wave incident from medium (1) with angle θ, we have $k_y = k_1^0 \sin\theta$.

The boundary condition requires continuity of ϕ and $\partial_x \phi$ at $x = 0$. We write then:

$$\begin{aligned} \sum_n f_{n,1}(\alpha_{n,1} + \beta_{n,1}) &= \sum_n f_{n,2}(\alpha_{n,2} + \beta_{n,2}) \\ \sum_n f_{n,1}(\alpha_{n,1} - \beta_{n,1}) ik_{x,1}^n &= \sum_n f_{n,2}(\alpha_{n,2} - \beta_{n,2}) ik_{x,2}^n \end{aligned} \tag{5.40}$$

By projecting the previous equations on $f_{n,1}$, we can deduce:

$$\begin{aligned} 2ik_{x,1}^n \alpha_{n,1} &= \sum_m \left[i(k_{x,1}^n + k_{x,2}^m)\alpha_{m,2} + i(k_{x,1}^n - k_{x,2}^m)\beta_{m,2}\right] \langle f_{n,1}, f_{m,2}\rangle \\ 2ik_{x,1}^n \beta_{n,1} &= \sum_m \left[i(k_{x,1}^n - k_{x,2}^m)\alpha_{m,2} + i(k_{x,1}^n + k_{x,2}^m)\beta_{m,2}\right] \langle f_{n,1}, f_{m,2}\rangle. \end{aligned} \tag{5.41}$$

This allows us to define the transfer matrix as $X_1 = M_{12} X_2$ where $X_i = (\alpha_{0,i}, \alpha_{1,i}, ..., \beta_{0,i}, ...)$. M_{21} is subsequently defined as M_{12}^{-1}.

We finally write the global transfer matrix as $M = M_{12} M_p M_{21}$, where M_p is a diagonal matrix that propagates the modes along the membrane and that is defined as:

$$\begin{aligned} M_{p,(n,n)} &= e^{ik_{x,2}^n w}, \\ M_{p,(n+N+1,n+N+1)} &= e^{-ik_{x,2}^n w}, \quad 0 \le n \le N \end{aligned} \tag{5.42}$$

We can now write $X_{out} = MX_{in}$ where $X_{in} = (I, R) = (1, 0, ..., r, \beta_{1,1}...)$ and $X_{out} = (T, 0) = (t, \alpha_{1,1}, ..., 0, ...)$. By writing $M = \begin{bmatrix} M_1 & M_2 \\ M_3 & M_4 \end{bmatrix}$, we have:

$$T = M_1 I + M_2 R, \quad 0 = M_3 I + M_4 R \tag{5.43}$$

which allows us to compute the transmission and reflection coefficients as:

$$R = -M_4^{-1} M_3 I, \quad T = M_1 I + M_2 R. \tag{5.44}$$

We check of course that $|t|^2 + |r|^2 = 1$.

Enhancement

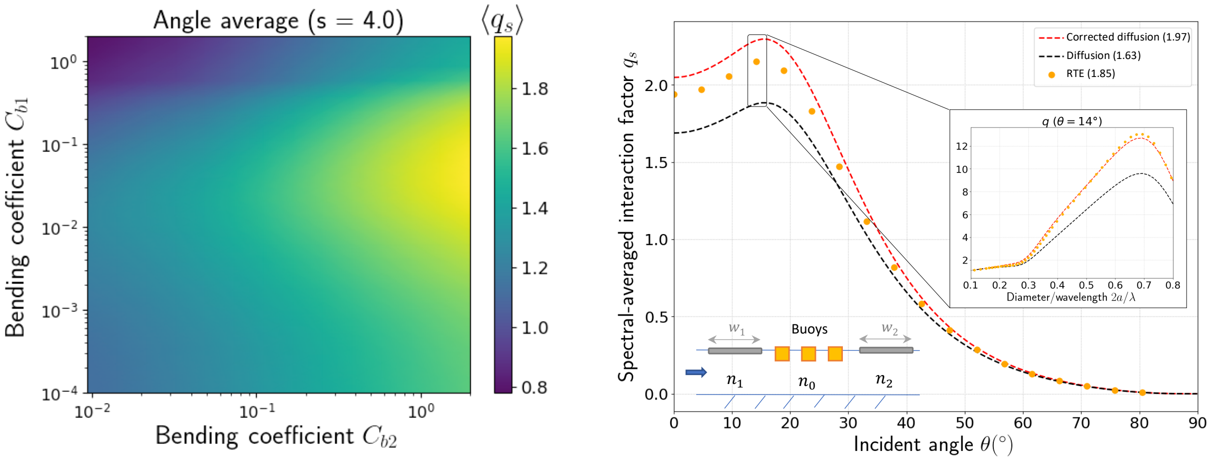

Figure 5-7: Left: $\langle q_s \rangle$ with a directional spectrum of $\cos^{2s}\theta$ and s = 4 for different values of C_{b1} and C_{b2} corresponding to the front and back membranes respectively. Each point is obtained after optimizing over the membranes' thicknesses. Right: Frequency-averaged interaction factor q_s vs incident angle θ for the previously studied array using additional membranes with parameters $(C_{b1}, C_{b2}) = (0.048, 2)$ and $w_1 = w_2 = 1.6h$.

We can now use our corrected diffusion model to predict the upper-bound for the previously studied array as we change C_b. For each value of C_{b1} and C_{b2} representing the front and rear membranes, respectively, we find the optimal membrane widths that maximize the radiative-diffusion bound. The resulting optimized $\langle q_s \rangle$ values are shown are shown in Fig. 5-7 (left). We first note that the frequency/angle-averaged interaction factor $\langle q_s \rangle$ increases significantly (> 1.8) compared to the $\langle q_s \rangle = 1.00$ without the membranes. We also confirm that $\langle q_s \rangle$ increases with C_{b2} (rear membrane) as expected. On the other hand, there is an optimal value for C_{b1} depending on the directional spectrum $f(\theta)$. For a *focused* incident field, only angles near normal incidence matter so that C_{b1} can be increased allowing more of the waves scattered by the WECs to be trapped. On the other hand, for a broad directional spectrum, a large value of C_{b1} prevents waves incident from wide angles from reaching the WECs.

For our array, supposing for example that the maximal attainable value of C_{b2} is equal to 2, the optimal value for C_{b1} is 0.048 with optimal widths equal to $1.6h$ for both the front and rear membranes. The frequency-averaged interaction factor q_s for the optimal parameters is shown in Fig. 5-7 (right). Our predicted bound (red dashed line = corrected diffusion) is indeed larger than the actual performance of the array as modeled by RTE (orange dots). That is mainly due to the relatively small scattering cross section compared to the absorption cross section. As illustrated in the inset of Fig. 5-7 at small wavelengths where σ_s is large (Fig. 5-4), we see that an increase in the scattering cross section leads to arrays with performance closer to the radiative-diffusion bound.

We finally mention that in the case of using a perfect back-reflector, $\langle q_s \rangle$ can reach a value of 2.26 for $C_{b1} = 0.06$ and $w_1 = 1.65h$.

5.6 Conclusion

We believe that the angle/frequency-averaged limits presented in this chapter provide guidelines for future designs to achieve a large q factor which may open the path for the realization of large arrays of buoys for efficient ocean energy harvesting. In particular, the use of external reflecting elements such as surface membranes seems a promising approach. The results are also applicable to other problems where multiple scattering effects are used to achieve enhancement, including scattering particles inside an absorbing layer. As we saw earlier, we can for example recover the standard Yablonovitch-$4n^2$ value in an appropriate limit, but the real power of our result is that it allows to study the effect of single-metaparticle properties, angle of incidence and reflecting boundaries.

THIS PAGE INTENTIONALLY LEFT BLANK

Chapter 6

Infinity of resonances: The periodic laser problem[1]

6.1 On resonances

In the previous chapters, we have seen examples of applications making use of resonances in numbers ranging from few to many. As a next step, we will consider a system with an "infinity" of resonances which can happen in the limit of an infinitely large system. For example, the modes of a box of size L are typically separated by a factor $\propto 1/L$ and thus become infinitely dense for large enough L. In particular, if we consider an arbitrary periodic structure, and as known in solid-state physics, Bloch theorem tells us that we have a *continuum* of modes described by a band diagram $\omega_n(\mathbf{k})$, which is parameterized by the band number n and the wavevector $\mathbf{k}$. The corresponding eigenfields are Bloch-periodic and can be written as $e^{i\mathbf{k}\cdot\mathbf{x}}\psi_{\mathbf{k},n}(\mathbf{x})$, where $\psi_{\mathbf{k},n}(\mathbf{x})$ is a periodic function [61]. If the structure is only periodic along certain directions (e.g. $\mathbf{x}$ and $\mathbf{y}$), as in a periodically perforated slab, the Bloch wavevector $\mathbf{k}$ is parallel to these directions (e.g. $\mathbf{k}\cdot(\mathbf{x}\times\mathbf{y}) = 0$). Assuming that the structure is surrounded by free space, the far field is proportional to a planewave term $\propto e^{i(\mathbf{k}+\mathbf{k}_\perp)\cdot\mathbf{x}}$, where $\mathbf{k}_\perp$ is perpendicular to $\mathbf{k}$. The wave equation then gives $\omega^2 = c^2(k^2 + k_\perp^2)$. For real ω, $k_\perp$ is real only when $\omega \geq ck$. This region is called the *light cone*, and $\omega = ck$ is called the light line. Modes below the light line have an imaginary $k_\perp$, meaning that the field is exponentially decaying outside the structure. These are called trapped, bound or guided modes. As a consequence, resonances that couple to incident planewaves can only be found inside the light cone. However, some trapped modes can still be found inside the light cone and are called bound-in-continuum

---

[1] Our work on this topic was published in Ref. 26.

(BiC) states [190].

A consequence from group representation theory is that $\mathbf{k}$ is conserved [61]. In particular, a Bloch-periodic incident wave has its parallel (along directions of periodicity) wavevector conserved inside the structure, and can then only excite modes with the same wavevector. For example, a normally-incident ($\mathbf{k} = \mathbf{0}$) planewave only excites the modes $\omega_n(\mathbf{k} = \mathbf{0})$. This was the case for the structures analyzed in Chapter 3 and Chapter 4 where we considered a fixed angle of incidence, and only a discrete number of modes were relevant. So, even though we mentioned that such periodic structures host a continuum of resonances, only a few discrete set is relevant for the scattering problem with an incident planewave.

However, if we consider a laser system, described semiclassically as an electromagnetic resonator coupled to oscillating dipoles [191–193], all the modes with different wavevectors can be excited, and the full continuum of resonances become relevant. This means that studies of periodic lasers should in general take into account effects stemming from the interactions between the different modes of the continuum bands. The fact that the equations describing the laser behaviour above threshold are nonlinear can make the problem intractable for large structures. As a consequence, practically all previous theoretical results are only based on single-unit-cell simulations with Bloch-periodic boundary conditions, only considering a single Bloch wavevector [194–199]. Such simulations, which do not take into account the continuum of modes, cannot be used to check the lasing stability (since modes that are not taken into account can lead to instabilities). In this chapter, we rigorously solve the stability problem of single-mode lasing in periodic structures and obtain a general numerical stability criterion in addition to simple analytical conditions. In the next section, we give a brief overview of the problem and describe the new results presented in this chapter.

6.2 Overview

Many lasers rely on resonances in periodic systems, ranging from band-edge modes of grated distributed-feedback (DFB) waveguides [200, 201] or photonic-crystal surface-emitting lasers (PCSELS) [202–208] to more exotic bound-in-continuum (BiC) states [209, 210]. In this chapter, we address a fundamental question for periodic lasers: does stable single-mode lasing exist in an infinite periodic structure, or does it inherently require the boundaries of a finite structure to stabilize? A number of theoretical works have studied lasing with periodic boundary conditions as in Fig. 6-1(left) and found lasing modes [194–199], but neglected a key concern: even if the structure and the lasing mode are periodic, stable lasing requires that arbitrary *aperiodic* electromagnetic perturbations [as in Fig. 6-1(right)] must decay rather than grow [211–213]. At first glance, such stability may seem unlikely: any resonance in a periodic system is part of a continuum of resonances at different Bloch wavevectors with arbitrarily close lasing thresholds, and this seems to violate typical assumptions for stable lasing [214–216]. A finite-size structure discretizes the resonance spectrum and hence may suppress this problem, but instabilities have been observed in large enough finite periodic lasers where the resonances become very closely spaced [217]. Analogous transverse instabilities are known to occur in translation-invariant (period → 0) lasers such as VCSELs [218], for which stability analysis has been performed with various assumptions [219, 220]. In fact, however, we show in subsection 6.3 that single-mode lasing *is* possible even in *infinite* periodic structures for range of powers above threshold, by applying a Bloch adaptation of linear-stability analysis to the full Maxwell–Bloch equations [212, 213]. (Instabilities can still arise if our criteria are violated, or from effects such as disorder not considered in this work.) In subsection 6.4, we use perturbation theory to obtain a simple condition for stability near threshold of low-loss resonances and confirm it numerically: the sign of the laser detuning from the gain frequency should match the sign of the band curvature at threshold. We then consider examples for both 1d DFB-like lasers (subsection 6.5) and 2d BiC-based lasing (subsection 6.6), and validate our result against brute-force time-domain simulations [221, 222]. Finally, in subsection 6.7, we perform numerical simulations to further confirm our perturbation theory.

6.3 Stability of steady state solution Maxwell-Bloch

We consider lasing systems described by the semi-classical Maxwell–Bloch equations (with the rotating-wave approximation), which fully include nonlinear mode-competitition effects (such as spatial hole-burning) [193]:

$$\begin{aligned} -\nabla\times\nabla\times\mathbf{E}^{+} &= \ddot{\mathbf{P}}^{+} + \epsilon_c\ddot{\mathbf{E}}^{+} + \sigma_c\dot{\mathbf{E}}^{+} \\ i\dot{\mathbf{P}}^{+} &= (\omega_a - i\gamma_\perp)\mathbf{P}^{+} + \gamma_\perp\mathbf{E}^{+}D \\ \dot{D}/\gamma_\parallel &= D_0 - D + \mathrm{Im}(\mathbf{E}^{+*}\cdot\mathbf{P}^{+}), \end{aligned} \tag{6.1}$$

where $\mathbf{E}^{+}$ is the positive-frequency component of the electric field (the physical field being given by $2\mathrm{Re}[\mathbf{E}^{+}]$), $\mathbf{P}^{+}$ is the positive-frequency polarization describing the transition between two atomic energy levels (with frequency ω_a and linewidth $\gamma_\perp$), D is the population

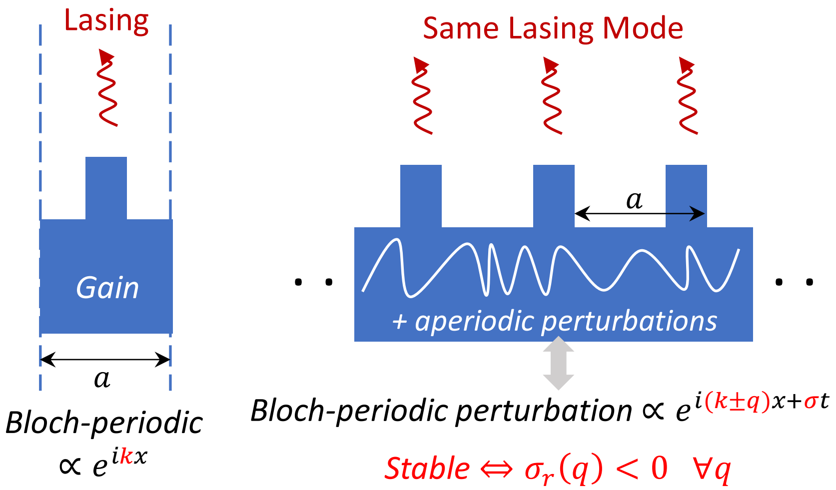

Figure 6-1: We study the stability of a single Bloch-periodic lasing mode under *aperiodic* perturbations. The stability eigenproblem can be solved using Bloch theorem by writing perturbations as a general Bloch wave. The lasing mode is stable when real parts of the eigenvalues $\sigma(q)$ are negative for all wavevectors q.

inversion (with relaxation rate $\gamma_{\parallel}$), D_0 is the pump strength, ϵ_c is the cold-cavity real permittivity, and σ_c is a cold-cavity conductivity loss. Here, we are assuming that the orientation of the atomic transition is parallel to the electric field, and have written all three fields in their natural units [212].

A steady-state solution of these equations can be obtained via steady-state ab-initio lasing theory (SALT), which is exact for single-mode lasing and approximate for multi-mode lasing with well-separated modes [214–216]. For a periodic system, we consider a Bloch-mode steady-state solution $\mathbf{E}^+ = \mathbf{E}_\mathbf{k} e^{i(\mathbf{k}\cdot\mathbf{x}-\omega t)}$ satisfying the stationary ($\dot{D} = 0$) SALT equation:

$$\Theta_\mathbf{k}\mathbf{E}_\mathbf{k} = \omega_\mathbf{k}^2 \left[\epsilon_c + i\frac{\sigma_c}{\omega_\mathbf{k}} + \Gamma(\omega_\mathbf{k})D_\mathbf{k}\right]\mathbf{E}_\mathbf{k}, \tag{6.2}$$

where $\Gamma(\omega) = \gamma_\perp/(\omega - \omega_a + i\gamma_\perp)$, $\mathbf{P}_\mathbf{k} = \Gamma(\omega_\mathbf{k})D_\mathbf{k}\mathbf{E}_\mathbf{k}$, $D_\mathbf{k} = D_0/(1 + |\Gamma(\omega_\mathbf{k})\mathbf{E}_\mathbf{k}|^2)$ and $\Theta_\mathbf{k} = e^{-i\mathbf{k}\cdot\mathbf{x}}\nabla\times\nabla\times e^{i\mathbf{k}\cdot\mathbf{x}}$ is a periodic operator.

Given this steady-state solution, one can then apply linear-stability analysis to the full Maxwell–Bloch equations, linearizing *arbitrary aperiodic* perturbations $X = X_\mathbf{k} + \delta X$, for $X \in \{\mathbf{E}, \mathbf{P}, D\}$, to determine whether perturbations δX exponentially grow (unstable) or shrink (stable) [211–213]. Here, our key point is that, because the linearized equations for the perturbations δX are periodic (for a Bloch-mode steady state), we can apply Bloch's theorem [223] to decompose the perturbations *themselves* into Bloch-wave modes $\delta\mathbf{E}_\mathbf{q}$, solving a separate linear-stability eigenproblem for each wavevector $\mathbf{q}$.

The well-known linear-stability analysis [212] of the Maxwell–Bloch equations (6.1) proceeds as follows. Linearization of (6.1) in δX gives:

$$\begin{aligned} \mathbf{0} &= \Theta_{\mathbf{k}}\delta\mathbf{E} + d_\omega^2(\epsilon_c\delta\mathbf{E} + \delta\mathbf{P}) + d_\omega\sigma_c\delta\mathbf{E} \\ i\delta\dot{\mathbf{P}} &= (\omega_a - \omega - i\gamma_\perp)\delta\mathbf{P} + \gamma_\perp(D_{\mathbf{k}}\delta\mathbf{E} + \mathbf{E}_{\mathbf{k}}\delta D) \\ \delta\dot{D}/\gamma_\parallel &= -\delta D + \mathrm{Im}(\mathbf{P}_{\mathbf{k}}\cdot\delta\mathbf{E}^* + \mathbf{E}_{\mathbf{k}}^*\cdot\delta\mathbf{P}), \end{aligned} \tag{6.3}$$

where $d_\omega = \left(\frac{d}{dt} - i\omega\right)$. Splitting complex variables into real and imaginary parts yields a set of linear equations $\left(C\frac{d^2}{dt^2} + B\frac{d}{dt} + A\right)u(\mathbf{x},t) = 0$ [212], where $u = (\mathrm{Re}(\delta\mathbf{E}), \mathrm{Im}(\delta\mathbf{E}), \mathrm{Re}(\delta\mathbf{P}), \mathrm{Im}(\delta\mathbf{P}), \delta D)$ and A, B and C are operator matrices readily obtained from (6.3). Stability analysis consists of looking for solutions of the form $u = \mathrm{Re}(Ue^{\sigma t})$, which leads to a quadratic eigenproblem:

$$\left(A + B\sigma + C\sigma^2\right)U = 0. \tag{6.4}$$

The sign of $\mathrm{Re}(\sigma)$ determines the stability of the single-mode solution [212].

Since the operators A, B and C are periodic in our case, however, we can use Bloch's theorem to further simplify the problem: the eigenfunctions can be chosen in the Bloch form $U = U_{\mathbf{q}}e^{i\mathbf{q}\cdot\mathbf{x}}$ where $U_{\mathbf{q}}$ is periodic. The eigenvalues $\sigma(\mathbf{q}, D_0)$ then determine the stability: If there exists a wavevector $\mathbf{q}$ so that $\mathrm{Re}[\sigma(\mathbf{q}, D_0)] > 0$, then the single-mode solution is unstable at the pump rate D_0, with exponential growth at the wavevector $\mathbf{k} \pm \mathbf{q}$. Since (A, B, C) are real, we also have $\sigma(\mathbf{q}, D_0) = \sigma(-\mathbf{q}, D_0)^*$, so we need only consider one side of $\mathbf{q}$ within the Brillouin zone.

6.4 Perturbation theory

The condition obtained in Sec. 6.3 can be used to numerically evaluate the single-mode lasing stability for an arbitrary value of the pump D_0. Here, we derive analytical results for the specific question of stability near lasing threshold. In particular, we use perturbation theory to compute the stability eigenvalues $\sigma(q = q_0 + \delta k, d)$ for small δk, where $D_0 = D_t(1 + d^2)$ with D_t being the pump at threshold, for points q_0 where $\sigma(q_0, 0) = 0$. Such perturbation theory is particularly subtle due to eigenvalue crossings that result in "critical lines" (similar to the so-called exceptional points) where σ changes form, and these are also reproduced in the numerical validation (Sec. 6.7). The final result is a formula that determines stability near threshold in terms of simple integrals of the threshold lasing mode. In the limit of low-loss resonances, this result further simplifies to a criterion relating band curvature to gain detuning as we show later [Eq. (6.24)].

In all systems, we have by definition $\sigma(0,0) = 0$. For reciprocal systems, the mode at $-k$ also reaches threshold at D_t so that $\sigma(\pm 2k, 0) = 0$ [213]. Note that this last case does not need to be considered when k and $-k$ are separated with lattice vectors, as for example when lasing at a band edge or at the center of the Brillouin zone. We first give a detailed derivation in the case $q_0 = 0$, and then present the results for $q_0 = \pm 2k$.

The stability eigenproblem is given by $\left(A_q + B\sigma + C\sigma^2\right) U_q = 0$, where:

$$A_q = \begin{pmatrix} \Delta^r_{k,q} & -\Delta^i_{k,q} & \omega^2 & 0 & 0 \\ \Delta^i_{k,q} & \Delta^r_{k,q} & 0 & \omega^2 & 0 \\ \gamma_\perp D & 0 & \omega_a - \omega & \gamma_\perp & \gamma_\perp \mathbf{E}^r \\ 0 & \gamma_\perp D & -\gamma_\perp & \omega_a - \omega & \gamma_\perp \mathbf{E}^i \\ -\gamma_\parallel \mathbf{P}^i & \gamma_\parallel \mathbf{P}^r & \gamma_\parallel \mathbf{E}^i & -\gamma_\parallel \mathbf{E}^r & \gamma_\parallel \end{pmatrix},$$

$$B = \begin{pmatrix} -\sigma_c & -2\epsilon_c\omega & 0 & -2\omega & 0 \\ 2\epsilon_c\omega & -\sigma_c & 2\omega & 0 & 0 \\ 0 & 0 & 0 & 1 & 0 \\ 0 & 0 & -1 & 0 & 0 \\ 0 & 0 & 0 & 0 & 1 \end{pmatrix}, C = \begin{pmatrix} -\epsilon_c & 0 & -1 & 0 & 0 \\ 0 & -\epsilon_c & 0 & -1 & 0 \\ 0 & 0 & 0 & 0 & 0 \\ 0 & 0 & 0 & 0 & 0 \\ 0 & 0 & 0 & 0 & 0 \end{pmatrix} \tag{6.5}$$

with $\Delta^r_{k,q} = -e^{-iqx}\mathrm{Re}(\Theta_k)e^{iqx} + \epsilon_c\omega^2$, $\Delta^i_{k,q} = -e^{-iqx}\mathrm{Im}(\Theta_k)e^{iqx} + \sigma_c\omega$, $\mathbf{E}^r = \mathrm{Re}(\mathbf{E})$ and $\mathbf{E}^i = \mathrm{Im}(\mathbf{E})$. For brevity of notation, we removed the subscript k from ω_k, $\mathbf{E}_k$, $\mathbf{P}_k$, D_k, but vectors still refer to the periodic part of Bloch terms. The SALT mode can be expanded in d, as for example done in Ref. 213. In particular, we have:

$$\omega \approx \omega_t + \omega_2 d^2,\ \mathbf{E} \approx d\frac{a\mathbf{E}_+}{\Gamma_t},\quad |a|^2 = \frac{G_D + \omega_2 H}{I},\ \omega_2 = -\mathrm{Im}\left(\frac{G_D}{I}\right)/\mathrm{Im}\left(\frac{H}{I}\right) \tag{6.6}$$

where $\mathbf{E}_+$ (resp. $\mathbf{E}_-$) is a solution to the linear SALT equation at threshold with Bloch vector k (resp. $-k$). G_D, I and H are given by:

$$\begin{gathered} G_C = \int d\mathbf{x}(\epsilon_c + i\sigma_c\omega_t)\,\mathbf{E}_- \cdot \mathbf{E}_+,\ G_D = \int d\mathbf{x} D_t\,\mathbf{E}_- \cdot \mathbf{E}_+, \\ I = \int d\mathbf{x} D_t|\mathbf{E}_+|^2\mathbf{E}_- \cdot \mathbf{E}_+,\quad H = \frac{1}{\omega_t^2\Gamma_t}\frac{\partial}{\partial\omega_t}\left[\omega_t^2\left(G_C + G_D\Gamma_t\right)\right]. \end{gathered} \tag{6.7}$$

Note that there is an arbitrary choice for the phase of a. To simplify some computations, we take $a\Gamma_t^*$ to be real.

Operators A_q, B and C can then be expanded in $(\delta k = q - q_0, d)$:

$$A_q \approx A_{00} + A_{01}d + A_{02}d^2 + A_{10}\delta k + A_{20}\delta k^2, \quad B \approx B_0 + B_2 d^2, \quad C = C_0. \tag{6.8}$$

As a result, eigenvalues and eigenvectors can be expanded in the same way:

$$U_q \approx \sum_{i,j\leq 2} U_{ij}\delta k^i d^j, \;\; \sigma \approx \sum_{i,j\leq 2} \sigma_{ij}\delta k^i d^j. \tag{6.9}$$

A crucial point that we confirm later, is that σ is *not* necessarily analytical at $(q_0, 0)$ since there is a degeneracy. So equation (6.9) is not valid inside a ball around $(\delta k, d) = (0, 0)$. Instead, we have different expansion coefficients depending on the path $(\delta k, d)$.

We first consider $q_0 = 0$. The zeroth-order stability problem is equivalent to the threshold SALT equation at k. Because real and imaginary parts of the field are split, we have two degenerate eigenvectors v_p corresponding to $\sigma_{00} = 0$, where:

$$v_p = \left(\mathrm{Re}\left(\mathbf{e}_p^+\right),\ \mathrm{Im}\left(\mathbf{e}_p^+\right),\ D_t\mathrm{Re}\left(\Gamma_t\mathbf{e}_p^+\right),\ D_t\mathrm{Im}\left(\Gamma_t\mathbf{e}_p^+\right),\ 0\right), \tag{6.10}$$

for $\mathbf{e}_{1,2}^+ = \mathbf{E}_+,\ i\mathbf{E}_+$. We also need solutions w_p to the transverse problem $w_p^t A_{00} = 0$ given by:

$$w_p = \left(\mathrm{Re}\left(\mathbf{e}_p^-\right),\ -\mathrm{Im}\left(\mathbf{e}_p^-\right),\ \frac{\omega_t^2}{\gamma_\perp}\mathrm{Re}\left(\Gamma_t\mathbf{e}_p^-\right),\ -\frac{\omega_t^2}{\gamma_\perp}\mathrm{Im}\left(\Gamma_t\mathbf{e}_p^-\right),\ 0\right), \tag{6.11}$$

where $\mathbf{e}_{1,2}^- = \mathbf{E}_-,\ i\mathbf{E}_-$.

We now have $U_{00} = b_1 v_1 + b_2 v_2$, where b_p are to be determined by degenerate perturbation theory. As we will see later, the coefficients b_p depend on the path $(\delta k, d)$. To simplify notations, we note $\bar{M} = \left[w_j^t M v_p\right]_{jp}$ for a given operator matrix M. The first order perturbation equations are given by:

$$\begin{aligned} (\delta k) \quad & (B_0\sigma_{10} + A_{10})U_{00} + A_{00}U_{10} = 0 \ \rightarrow\ \bar{A}_{10}b = -\sigma_{10}\bar{B}_0 b \\ (d) \quad & (B_0\sigma_{01} + A_{01})U_{00} + A_{00}U_{01} = 0 \ \rightarrow\ \bar{A}_{01}b = -\sigma_{01}\bar{B}_0 b. \end{aligned} \tag{6.12}$$

It is straightforward to show that $\bar{A}_{01} = 0$, $\bar{B}_0 = -\mathrm{Im}\left(\omega_t^2\Gamma_t H M\right)$ and $\bar{A}_{10} = i\mathrm{Im}\left(LM\right)$, where $M = \begin{pmatrix} 1 & i \\ i & -1 \end{pmatrix}$ and $L = -\int d\mathbf{x}\ \mathbf{E}_-\cdot\partial_q\Theta_{k+q}\mathbf{E}_+$ (in particular, $-\partial_q\Theta_{k+q} = 2i\ e^{-ikx}\nabla e^{ikx}$ for $\mathbf{E} = \mathrm{E}_z\mathbf{z}$ waves). We then have:

$$\sigma_{01} = 0, \quad \sigma_{10} = i\frac{L}{\omega_t^2\Gamma_t H} \text{ or } \sigma_{10} = i\left(\frac{L}{\omega_t^2\Gamma_t H}\right)^*. \tag{6.13}$$

Since 0 is a maximum of $\mathrm{Re}[\sigma(\delta k, 0)]$, σ_{01} is purely imaginary and the two eigenvalues are identical. So $\bar{A}_{10} + \sigma_{10}\bar{B}_0 = 0$ and b is not determined by first order equations. Note that $i\sigma_{10}$ is simply the slope of $\omega(k)$ at the lasing k. We can also see that:

$$U_{01} = -\sum b_p g_p + \sum c_l v_l, \quad U_{10} = -\sum b_p A_{00}^{-1}(\sigma_{10}B_0 + A_{10})v_p + \sum \tilde{c}_l v_l, \tag{6.14}$$

where $g_p^5 = 2D_t\mathrm{Re}\left(\Gamma_t a^* \mathbf{e}_p^+ \cdot \mathbf{E}_+^*\right)$ and the first fourth components of g_p are zero. c_l and $\tilde{c}_l$ are arbitrary complex coefficients that will not affect our results. Note also that the fifth component of U_{10} is equal to zero.

The second order perturbation equations are now given by:

$$\begin{aligned}
(\delta k d) \quad & \sigma_{11}B_0U_{00} + \left(A_{10} + \sigma_{10}B_0\right)U_{01} + A_{01}U_{10} + A_{00}U_{11} = 0 \\
(\delta k^2) \quad & \left(A_{20} + \sigma_{20}B_0 + \sigma_{10}^2 C\right)U_{00} + \left(A_{10} + \sigma_{10}B_0\right)U_{10} + A_{00}U_{20} = 0 \\
(d^2) \quad & \left(A_{02} + \sigma_{02}B_0\right)U_{00} + A_{01}U_{01} + A_{00}U_{02} = 0.
\end{aligned} \tag{6.15}$$

We start by solving the three equations independently. From results of first-order perturbation we can see that $w_j^t(A_{10} + \sigma_{10}B_0)U_{01} = 0$ and $w_j^t A_{01}U_{10} = 0$. The equation of order $\delta k d$ then gives $\sigma_{11} = 0$.

Multiplying the equation of order δk^2 by w_j^t we get:

$$-\sigma_{20}\bar{B}_0 b = \left(\bar{A}_{20} + \sigma_{10}^2\bar{C} + \bar{P}\right)b = \mathrm{Re}\left(XM\right)b, \quad \text{where } P = (\sigma_{10}B_0 + A_{10})A_{00}^{-1}(\sigma_{10}B_0 + A_{10}), \tag{6.16}$$

where eigenvalues are simply related to the curvature of $\omega(k)$ at the lasing k $(= i\sigma_{20})$:

$$\sigma_{20} = i\frac{X}{\omega_t^2\Gamma_t H} \ \text{ or } \ \sigma_{20} = -i\left(\frac{X}{\omega_t^2\Gamma_t H}\right)^*, \quad b = (1, \mp i). \tag{6.17}$$

The degeneracy is artificially due to the separation of the real and imaginary parts of the field, so X can be easily recovered from the non-degenerate perturbation theory of $\omega(k)$ in k. We obtain:

$$\begin{gathered}
X = \int d\mathbf{x}\, \mathbf{E}_- \cdot \Box \mathbf{E}_+, \\
\Box = \partial_q^2\Theta_{k+q} - \frac{\sigma_{10}^2}{2}\partial^2 G + (i\partial_q\Theta_{k+q} + \sigma_{10}\partial G)(-\Theta_k + G)^{-1}(i\partial_q\Theta_{k+q} + \sigma_{10}\partial G), \\
G(\omega_t) = \omega_t^2\left[\epsilon_c + i\frac{\sigma_c}{\omega_t} + D_t\Gamma(\omega_t)\right] \text{ and } \partial_q^2\Theta_{k+q} = -I \text{ for } \mathbf{E} = \mathrm{E}_z\mathbf{z} \text{ waves.}
\end{gathered} \tag{6.18}$$

Finally, multiplying the equation of order d^2 by w_j^t we get (using $a\Gamma_t^* = a^*\Gamma_t$):

$$-\sigma_{02}\bar{B}_0 b = \left(\bar{A}_{02} - \bar{Q}\right) b, \ \text{ with } \bar{Q} = \left[w_j^t A_{01} g_p\right]_{jp} = \mathrm{Re}\left[\omega_t^2 \Gamma_t |a|^2 I \left(M' + M\right)\right] \text{ and } \bar{A}_{02} = 0, \tag{6.19}$$

where $M' = \begin{pmatrix} 1 & -i \\ i & 1 \end{pmatrix}$. The eigenvalues are then given by:

$$\sigma_{02} = 0, \ b = (0,1) \ \text{ or } \ \sigma_{02} = 2|a|^2 \mathrm{Im}\left(\frac{I}{H}\right), \ b = (-\mathrm{Im}[I/H], \mathrm{Re}[I/H]). \tag{6.20}$$

We see that we obtain different eigenvectors in (6.17) and (6.20). This means that the expansion in (6.9) depends on the path $(\delta k, d)$. If $d = o(\delta k)$, the expansion is determined by (6.17); while it is determined by (6.20) if $\delta k = o(d)$. A critical behaviour is obtained along the linse $\delta k = \alpha d$ for which the second order term is given by $\sigma_2 d^2$ and the three equations in (6.15) have to be combined. In this case, the second order perturbation eigenproblem becomes:

$$-\sigma_2 \bar{B}_0 b = \left[\alpha^2 \mathrm{Re}\left(XM\right) - \bar{Q}\right] b, \tag{6.21}$$

and the eigenvalues are given by:

$$\sigma_2 = \mathrm{Im}\left(\alpha^2\theta + \eta_I\right) \pm \sqrt{|\eta_I|^2 - \left[\mathrm{Re}\left(\alpha^2\theta + \eta_I\right)\right]^2}, \ \ \theta = -\frac{X}{\omega_t^2 \Gamma_t H}, \ \eta_I = |a|^2 \frac{I}{H}. \tag{6.22}$$

Note that θ is simply the band curvature at threshold ($\omega(k) \approx \omega_t + i\sigma_{10}\delta k + \theta\delta k^2$).

The presence of the square root function clearly shows the non-analyticity of σ. In particular, the there is an eigenvalue crossing for $\alpha_c^2 = \left(-\mathrm{Re}\left(\eta_I\right) \pm |\eta_I|\right)/\mathrm{Re}\left(\theta\right)$. The stability condition ($\sigma_2 \leq 0$) can also be immediately retrieved:

$$\alpha_s^2 = -2\mathrm{Re}\left(\eta_I/\theta\right) \leq 0. \tag{6.23}$$

We can simplify the stability condition in the limit of small loss. In this case, $H \approx 2\omega_t \int \epsilon_c \mathbf{E}_- \cdot \mathbf{E}_+/\Gamma_t$, $\mathbf{E}_- \approx \mathbf{E}_+^*$ and $\mathrm{Im}\left(\theta\right) \approx 0$. The stability condition $\mathrm{Re}\left(\eta_I\right)\mathrm{Re}\left(\theta\right) + \mathrm{Im}\left(\eta_I\right)\mathrm{Im}\left(\theta\right) \geq 0$ becomes equivalent to:

$$\mathrm{Re}\left(\theta\right)\left(\omega_t - \omega_a\right) \gtrsim 0. \tag{6.24}$$

This means that the sign of the detuning $(\omega_t - \omega_a)$ should be the same as the sign of the band curvature ($\mathrm{Re}[\theta]$). For example, when lasing at a bandedge, this means that ω_a should be inside the bandgap.

As mentioned in the beginning of the section, in the case of degenerate lasing, the previous analysis should also be carried out at $q_0 = -2k$ (or eqivalently at $2k$). (Note that we are not considering the special case of a degeneracy that comes for a wavevector other than $-k$. However, this situation can be studied in a similar way by computing a perturbation expansion of σ around multiple adequate q_0s.) It is easy to see that the solutions of the zeroth order problem $A_{-2k}U_{00} = 0$ are related to solutions of SALT at $k \pm 2k$. Two separate cases should then be considered.

$\underline{ka = \pi/2:}$ In this case, the problems at $-k$ and $3k$ are equivalent (separated by a lattice vector) and the zeroth order problem is degenerate. The eigenvectors are given by:

$$v_p = e^{i\frac{\pi x}{a}} \left(\mathrm{Re}\left(e^{-i\frac{\pi x}{a}}\mathbf{e}_p^-\right), \mathrm{Im}\left(e^{-i\frac{\pi x}{a}}\mathbf{e}_p^-\right), D_t\mathrm{Re}\left(e^{-i\frac{\pi x}{a}}\Gamma_t\mathbf{e}_p^-\right), D_t\mathrm{Im}\left(e^{-i\frac{\pi x}{a}}\Gamma_t\mathbf{e}_p^-\right), 0\right), \tag{6.25}$$

while solutions of the transverse problem become:

$$w_p = e^{-i\frac{\pi x}{a}} \left(\mathrm{Re}\left(e^{i\frac{\pi x}{a}}\mathbf{e}_p^+\right), -\mathrm{Im}\left(e^{i\frac{\pi x}{a}}\mathbf{e}_p^+\right), \frac{\omega_t^2}{\gamma_\perp}\mathrm{Re}\left(e^{i\frac{\pi x}{a}}\Gamma_t\mathbf{e}_p^+\right), \frac{-\omega_t^2}{\gamma_\perp}\mathrm{Im}\left(e^{i\frac{\pi x}{a}}\Gamma_t\mathbf{e}_p^+\right), 0\right). \tag{6.26}$$

We now have $g_p^5 = 2D_t e^{i\pi x/a}\mathrm{Re}\left(\Gamma_t a^* e^{-i\pi x/a}\mathbf{e}_p^- \cdot \mathbf{E}_+^*\right)$ and $\bar{Q} = \mathrm{Re}\left[\omega_t^2\Gamma_t|a|^2(KM' + JM)\right]$, where:

$$J = \int d\mathbf{x}\; D_t(\mathbf{E}_+^* \cdot \mathbf{E}_-)(\mathbf{E}_+ \cdot \mathbf{E}_+) \text{ and } K = \int d\mathbf{x}\; e^{2i\pi x/a} D_t(\mathbf{E}_-^* \cdot \mathbf{E}_+)(\mathbf{E}_+ \cdot \mathbf{E}_+). \tag{6.27}$$

We can then obtain the eigenvalues of the problem (6.21) for $\delta k = q + 2k = \alpha d$:

$$\sigma_2 = \mathrm{Im}\left(\alpha^2\theta + \eta_J\right) \pm \sqrt{|\eta_K|^2 - \left[\mathrm{Re}\left(\alpha^2\theta + \eta_J\right)\right]^2}, \;\; \eta_J = |a|^2\frac{J}{H}, \; \eta_K = |a|^2\frac{K}{H}. \tag{6.28}$$

The stability condition is now equivalent to:

$$\alpha_s^2 = -\mathrm{Re}\left(\frac{\eta_J}{\theta}\right) + \sqrt{\left|\frac{\eta_K}{\theta}\right|^2 - \left|\frac{\eta_J}{\theta}\right|^2 + \mathrm{Re}\left(\frac{\eta_J}{\theta}\right)^2} \text{ non-real or real negative.} \tag{6.29}$$

$\underline{ka \neq \pi/2:}$ In this case, the problems at $-k$ and $3k$ are different, and only $-k$ has a solution. The zeroth order problem for $q_0 = -2k$ is now *not* degenerate and eigenvectors are given by:

$$v = (1,\; -i,\; D_t\Gamma_t,\; -iD_t\Gamma_t,\; 0)\,\mathbf{E}_-,\; w = \left(1,\; i,\; \frac{\omega_t^2\Gamma_t}{\gamma_\perp},\; i\frac{\omega_t^2\Gamma_t}{\gamma_\perp},\; 0\right)\mathbf{E}_+. \tag{6.30}$$

The dimension of our problem is now one and we have $g^5 = 2D_t\Gamma_t a^* \mathbf{E}_+^* \cdot \mathbf{E}_-$, $\bar{B}_0 = 2i\omega_t^2\Gamma_t H$, $A_{20} = 2X$ and $\bar{Q} = 2\omega_t^2\Gamma_t|a|^2 J$. The unique eigenvalue of (6.21) is now equal to:

$$\sigma_2 = -i(\theta\alpha^2 + \eta_J). \tag{6.31}$$

This simply means that there is no eigenvalue crossing and that the expansion of σ does not depend on the path $(\delta k, d)$. Note that σ_2^* is also an eigenvalue around $q_0 = 2k$ (which is is simply due to the facts that our operators A, B and C are real as indicated in the main text). The stability condition is immediately given by:

$$\mathrm{Im}\,(\eta_J) \leq 0, \tag{6.32}$$

since we already have $\mathrm{Im}\,(\theta) \leq 0$ ($\mathrm{Im}[\omega(k)]$ has a maximum at k). Note that this stability condition is equivalent to having a stable lasing close to threshold for the *single* unit-cell problem.

Finally, some useful points to mention:

- We have $\eta_I = G_D/H + \omega_2$. It is also straightforward to use perturbation theory to show that $\omega_2^l = -G_D/H$ where ω_2^l is the slope (in $D_0/D_t - 1$) of the eigenfrequency of the linear problem at the threshold *without* gain saturation ($\omega^l \approx \omega_t + \omega_2^l(D_0/D_t - 1)$). By definition, threshold should be reached from below the real axis, so $\mathrm{Im}\left(\omega_2^l\right) \geq 0$. Since ω_2 is real, we conclude that $\mathrm{Im}\,(\eta_I) = -\mathrm{Im}\left(\omega_2^l\right) \leq 0$. This means that $\sigma_{02} \leq 0$ and that the single unit-cell lasing problem is always stable near threshold in absence of degeneracy.

- For TM waves ($\mathbf{E} = \mathrm{E}_z\mathbf{z}$), we have $I = J$. This means that $\mathrm{Im}\,(\eta_J) \leq 0$ and that the single unit-cell lasing problem is also stable in the degenerate case when $k \neq \pi/2$. This is an analytical proof for part of the stability result conjectured in Ref. 213. Note that $k = \pi/2$ is equivalent to the condition $n = 4\ell$ in Ref. 213.

- For TM waves and $k \neq \pi/2$, we conclude that $\sigma_2 \leq 0$ when expanding around $-2k$. So the stability is only determined by the expansion around 0 ($-\mathrm{Re}\,(\eta_I/\theta) \leq 0$.)

6.5 DFB laser: 1d example

We can now use our stability criteria to study a simplified model for a DFB laser formed by a 1D photonic crystal with alternating layers of equal thickness and dielectric constants equal to 1 and 3 (Figure 6-2). We assume a uniform conductivity loss $\sigma_c = 0.001\omega_a$ and a two-level gain medium with $\omega_a a/2\pi c = 0.31$ and $\gamma_\perp a/2\pi c = 0.008$. Figure 6-2 shows part of the band diagram, with ω_a chosen near the first band edge. For every wavevector k of the first band, we compute the pump threshold D_t, defined as the lowest pump rate D_0 that compensates the loss and leads to a *real* eigenfrequency ω_k in (6.2). As expected, the smallest D_t is obtained at the band edge $k = \pi/a$ of the first band, which we therefore take to be the first lasing mode. However, as discussed earlier, D_t varies continuously with k and other modes are expected to reach threshold for arbitrary close values of the pump in the *linear* model.

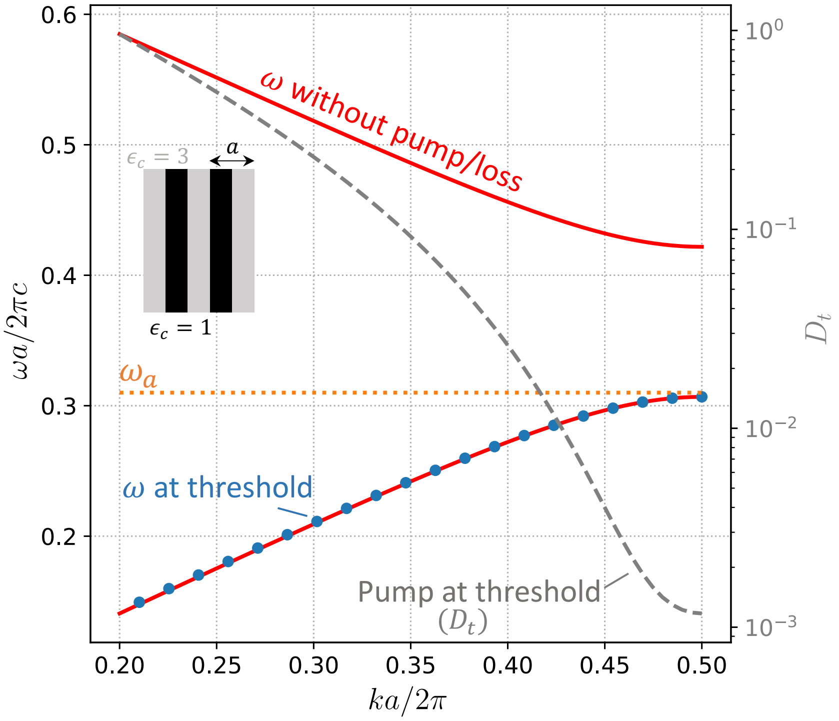

Figure 6-2: The cold cavity is 1D photonic crystal with uniform conductivity loss $\sigma_c = 0.001\omega_a$. The two-level gain medium is characterized by $\omega_a a/2\pi c = 0.31$ and $\gamma_\perp a/2\pi c = 0.008$. The frequency (dots) and pump (dashed lines) at the lasing threshold are computed for modes of the first band. The minimum pump at threshold is obtained at the band edge $ka = \pi$. In absence of gain, the decay rate for the band-edge mode is equal to $\kappa \approx 5.8 \times 10^{-5}(2\pi c/a)$.

In order to study the stability of the lasing band-edge mode, we first solve the steady-state nonlinear equation (6.2) at higher pump values with a Newton-Raphson solver as described in Ref. 216. We then use the obtained steady-state solution to solve the stability eigenproblem (6.4) for different pump values. Results are summarized in Fig. 6-3 and Fig. 6-4. First, note that the single mode solution is *stable* close to threshold, unlike a linear model (Fig. 6-2). This can be attributed to the nonlinear gain saturation, which prevents arbitrary close modes from reaching threshold. In general, the stability of the laser depends on the relationship between the decay rates of the three fields, $\gamma_\perp$ for $\mathbf{P}$, $\gamma_\parallel$ for D, and κ for $\mathbf{E}$, the decay rate of the cavity in the absence of gain [224]. When two (or more) of these decay rates become similar, we notice a sharp reduction of D_0 for the onset of instability (in this case, $\gamma_\parallel \sim \kappa$).

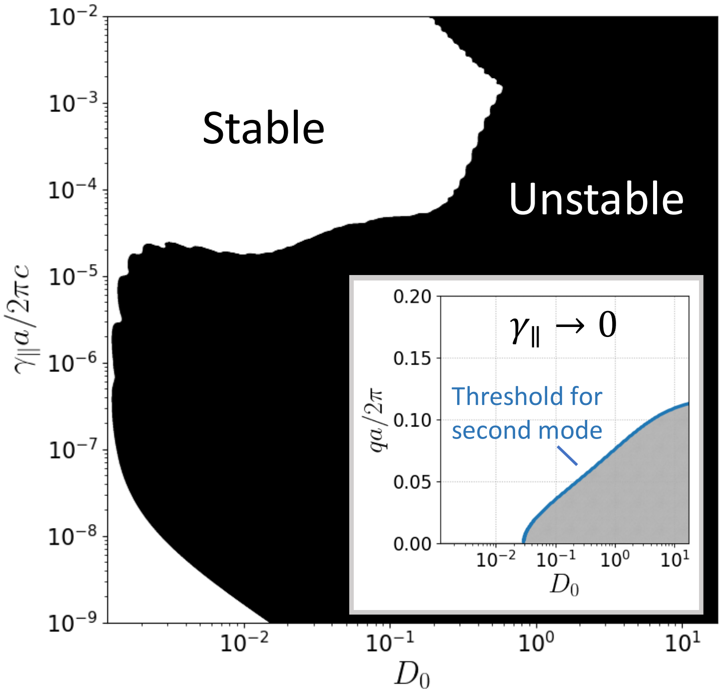

Figure 6-3: Detailed stability map for $\gamma_\parallel a/2\pi c = 10^{-4}$ as a function of q. We compare results to FDTD simulations using a finite supercell with periodic boundary conditions (unstable in shaded regions), initialized with the SALT solution plus $\sim 1\%$ noise and checking stability after $\sim 10^5$ optical periods. Stars show the allowed q due to the finite supercell ($2\pi\ell/aN_{\text{cells}}$). (b) Modal intensity of lasing modes with FDTD ($N_{\text{cells}} = 50$) and multimode SALT (assuming second lasing mode at $q = 4\pi/50a$).

Stability can also be studied using a multimode SALT by including the first lasing mode in the gain saturation and computing the pump threshold for a second lasing mode as a function of k (inset of Fig. 6-3). In particular, this coincides with the results from the stability eigenproblem in the limit $\gamma_\parallel \rightarrow 0$. Solving (6.3) for $\gamma_\parallel \rightarrow 0$ is indeed equivalent to having $\delta D \rightarrow 0$ and δX being a solution to SALT equation. As can be seen in the inset of Fig. 6-3, the nonlinear gain saturation pushes the threshold of the arbitrary close modes ($q \rightarrow 0$) to a higher pump value compared to what is expected from a linear model. However, this multimode SALT predicts a second lasing mode that is arbitrary close to the first lasing mode, which is outside the domain of validity of SALT. Furthermore, the instability onset depends rather strongly on $\gamma_\parallel$, emphasizing the need for a full Maxwell–Bloch stability analysis.

From the results of our perturbation theory (Sec. 6.4), we remind that in the case of small loss, a simple approximate condition for stability near threshold is: the band curvature $\mathrm{Re}\left(\frac{d^2\omega}{dk^2}\right)$ and the laser detuning $(\omega_t - \omega_a)$ should have the *same sign* at threshold. When lasing at the band edge, as in this example, this is equivalent to requiring ω_a to lie inside the band gap.

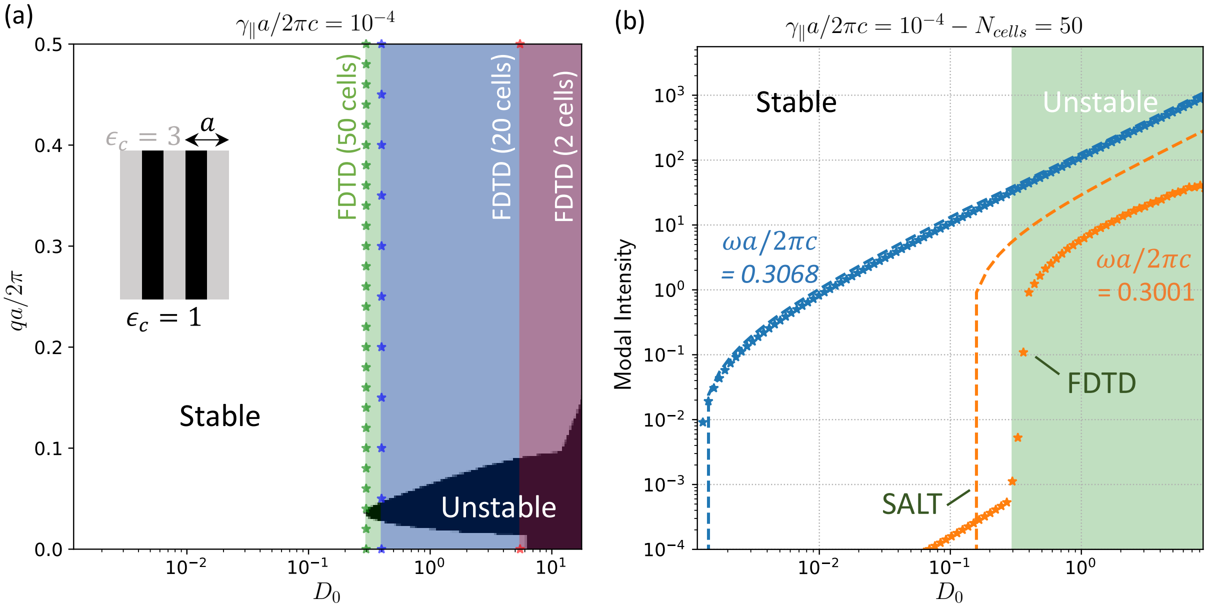

Figure 6-4: (a) Detailed stability map for $\gamma_\parallel a/2\pi c = 10^{-4}$ as a function of q. We compare results to FDTD simulations using a finite supercell with periodic boundary conditions (unstable in shaded regions), initialized with the SALT solution plus $\sim 1\%$ noise and checking stability after $\sim 10^5$ optical periods. Stars show the allowed q due to the finite supercell ($2\pi\ell/aN_{\text{cells}}$). (b) Modal intensity of lasing modes with FDTD ($N_{\text{cells}} = 50$) and multimode SALT (assuming second lasing mode at $q = 4\pi/50a$).

We now validate the results of stability analysis against FDTD simulations [221, 222] with a finite supercell and periodic boundary conditions. We initialize the simulation fields with the SALT solution plus additional noise, and analyze whether the system remains in the same steady-state at later times. Note that for a supercell with N_{cells} periods, only a finite set of values for q is allowed ($= 2\pi\ell/aN_{\text{cells}}$ for $\ell = 0, \ldots, N_{\text{cells}} - 1$). Figure 6-4(a) shows a perfect match between the two computations. In particular, the instability onset for the FDTD simulations corresponds to the value of the pump D_0 for which at least one *allowed* q reaches the instability region obtained from the stability eigenproblem (6.4). Once instability is reached, a second lasing mode starts. This second lasing mode corresponds to the first q that hits the instability region. However, the new lasing solution is not accurately described by two-mode SALT (Figure 6-4(b)) because the small frequency difference violates the SALT assumptions (exact in the limit $\gamma_{\parallel} \to 0$). In particular, the inset of Fig. 6-3 shows that the threshold of the multimode SALT (for $q = 4\pi/50a$) does not match the actual threshold for the stability eigenproblem. As N_{cells} increases, the second lasing frequency becomes arbitrary close to the first mode, requiring an ever-smaller $\gamma_{\parallel}$ for the multimode SALT approach to be viable. On the other hand, for a fixed N_{cells}, the multimode SALT approach becomes increasingly accurate for smaller $\gamma_{\parallel}$. The two-mode regime here also exhibits a chaotic behaviour, typical in certain classes of lasers [224].

6.6 BiC lasing: 2d example

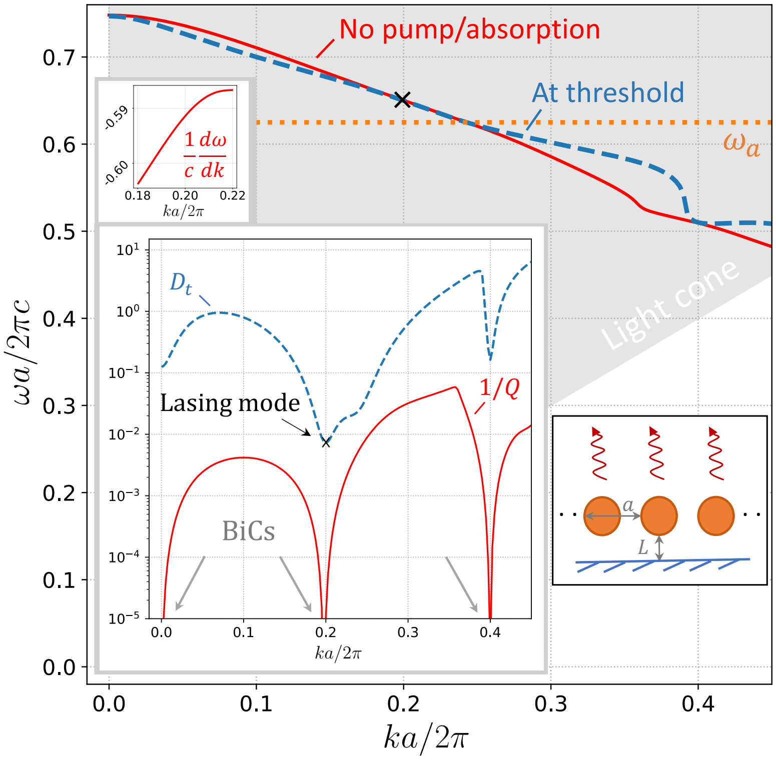

Figure 6-5: Inset shows a 2d array of cylindrical rods with diameter $= 0.7a$, $\epsilon_c = 2.58$, $\sigma_c = 0.001\omega_a$ and a separation $L = 1.078a$ to a perfect mirror. Gain inside the rods is characterized by $\omega_a a/2\pi c = 0.625$ and $\gamma_{\perp} a/2\pi c = 0.01$. Three BiCs are shown at $ka = 0, 0.4\pi, 0.8\pi$. The minimum pump at threshold D_t is obtained at $ka = 0.4\pi$ which is the first lasing mode. In absence of gain, the decay rate for this mode is equal to $\kappa \approx 8 \times 10^{-5}(2\pi c/a)$. Top inset shows a positive band curvature at threshold.

We next consider a 2d (E_z-polarized) example to study the stability of a BiC lasing mode. The structure is a periodic line of surface rods placed at a distance L from a perfect-metal boundary (Figure 6-5 inset), which is known to have multiple BiCs [190]. BiCs are characterized by a quality factor $Q \to \infty$ in absence of external pump and absorption loss, as seen in the inset. As in the previous 1d example, we compute the pump threshold D_t at different wavevectors k and find the lasing mode corresponding to the smallest D_t. In this example, the first lasing mode corresponds to the BiC at $ka = 0.4\pi$, with $D_t \approx 7 \times 10^{-3}$ and a lasing frequency $\omega_t a/2\pi c \approx 0.65$.

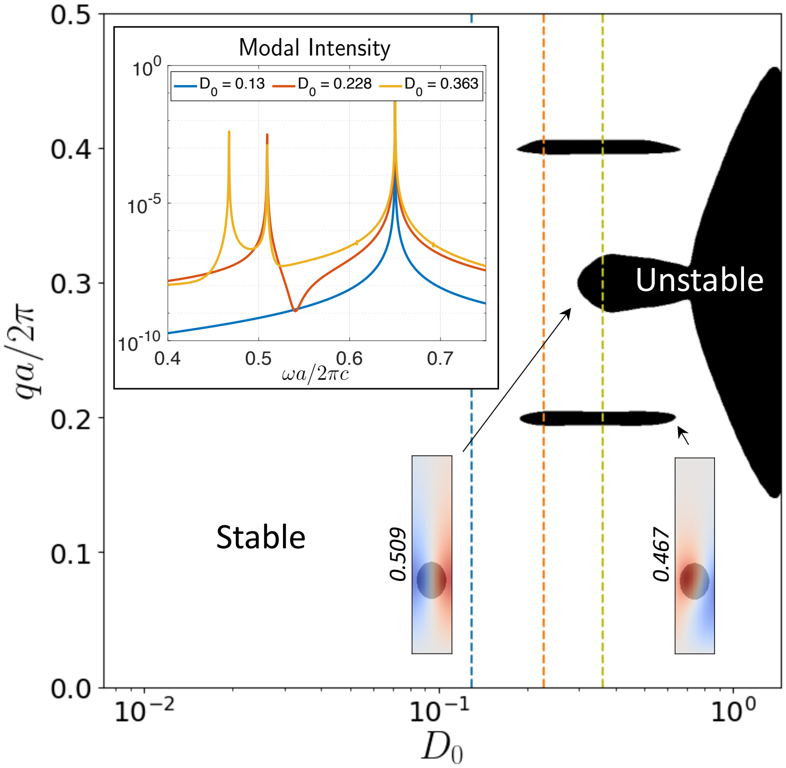

Figure 6-6: Result from stability eigenproblem. Shaded region indicates instability. Inset shows FDTD results using a supercell with 20 unit cells and periodic boundary conditions. Plots show the Fourier transform of the electric field at a point near a rod. Small insets show the eigenvectors obtained from (6.4) along with their frequencies $\omega a/2\pi c$. They do match modes obtained in the linear regime (below threshold) at $ka = 0.8\pi$ and $ka = \pi$.

The results of the stability analysis are shown in Fig. 6-6 for $\gamma_{\parallel} a/2\pi c = 5 \times 10^{-3}$. We first note that the lasing mode is stable near threshold and that instability occurs at a higher pump value D_0 [Fig. 6-7(left)]. This matches our condition for stability near threshold (positive band curvature and laser detuning). As clear from the corresponding q and eigenfrequencies, instabilities at higher pump correspond to modes that become active at $ka = 0.8\pi$ (BiC) and $ka = \pi$ (guided mode). A comparison between our stability results and FDTD simulations is shown in Fig. 6-6(inset), where we plot the Fourier transform of the electric field at a given point outside a rod for different pump values. The number and frequencies of lasing modes match our stability computations.

Finally, in order to confirm our simple analytical stability condition [Eq. (6.24)], we study the same system with a larger ω_a corresponding to a negative laser detuning. As shown in Fig. 6-7(right), the lasing system is indeed *not* stable for any value of pump above threshold. Such instabilities may arise in very large systems (small q).

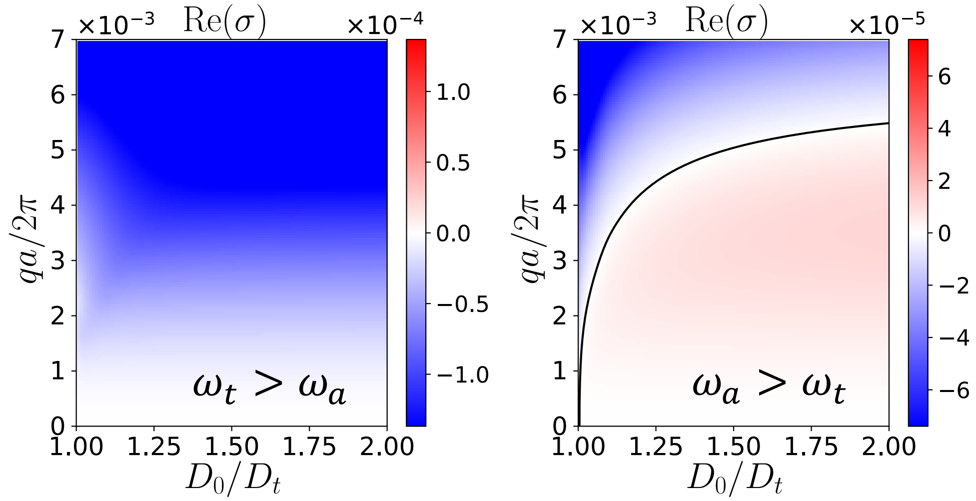

Figure 6-7: $\mathrm{Re}(\sigma)$ as a function of q and D_0/D_t for different transition frequencies $\omega_a a/2\pi c$ $(= 0.625, 0.675)$. The threshold lasing frequency $\omega_t a/2\pi c$ is maintained at ≈ 0.65. The system is unstable near threshold when the laser detuning $(\omega_t - \omega_a)$ has opposite sign to the band curvature. Black solid line corresponds to $\mathrm{Re}\,(\sigma) = 0$.

6.7 Numerical validation of perturbation theory

Before concluding this chapter, we present further numerical validation for the analytical perturbation-theory results discussed in Sec. 6.4.

Figure 6-8 shows results for the 1d structure studied in Sec. 6.5. Figures 6-9 and 6-10 are for the same structure, but with ω_a lying below the lasing band edge, outside the bandgap, leading to instability near threshold as predicted by our simplified stability condition [Eq. (6.24)]. In both cases, the numerical simulations show near-perfect agreement with the analytical results.

Figures 6-12 and 6-11 show results for the 2d structures presented in Sec. 6.6 with a positive and negative laser detuning, respectively. Again, numerical simulations are in agreement with the analytical results.

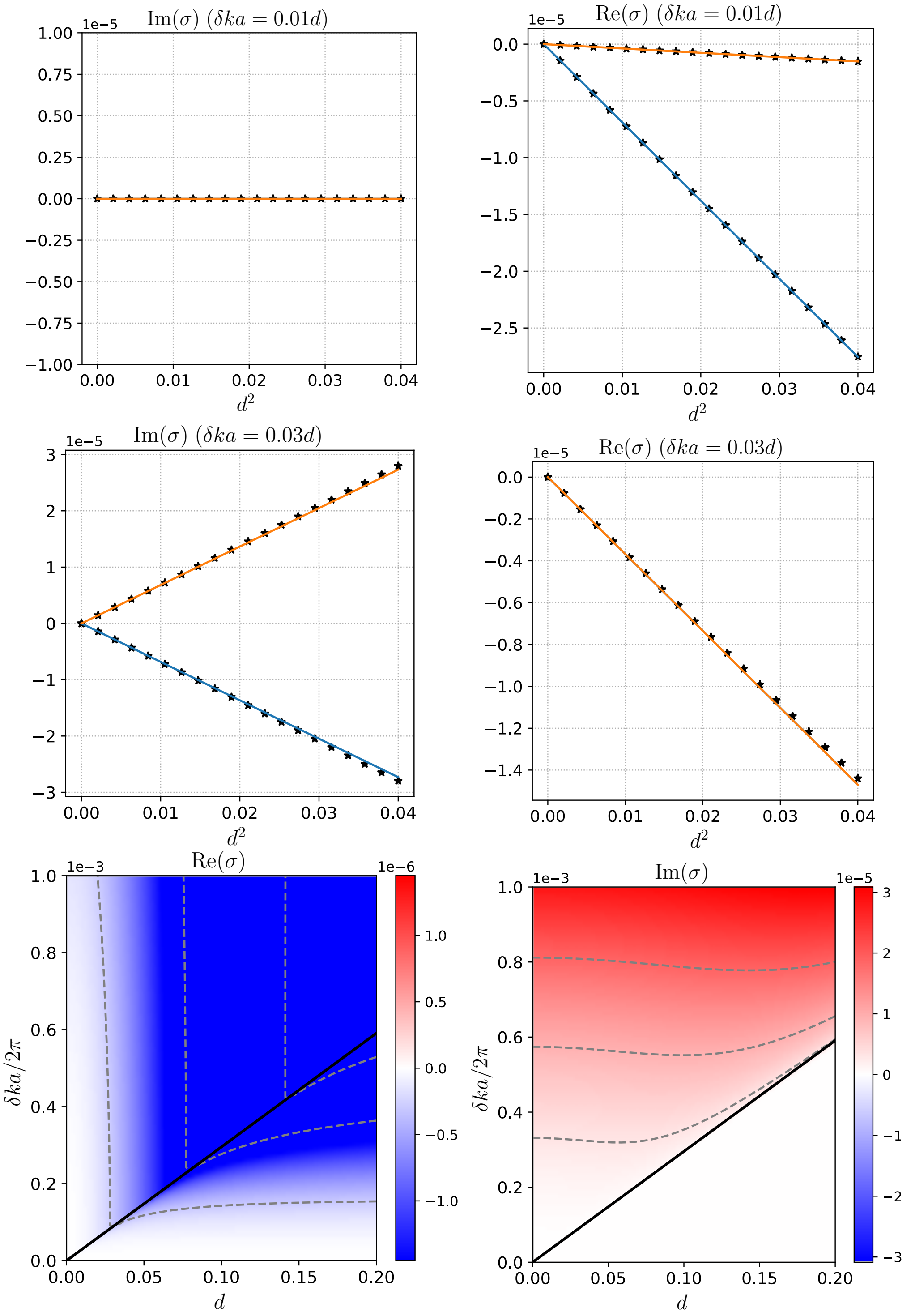

Figure 6-8: Same 1d structure in Sec. 6.5. Numerical simulation (stars and dashed contour lines) are in agreement with analytical results (solid lines). Since the lasing mode is at a bandedge, we have $\sigma_{10} = 0$. Black line corresponds to $\delta ka = \alpha_c d$ and represents the line of eigenvalue crossing (transition from two real to two complex conjugate eigenvalues). $\alpha_c \approx 0.018$ and $\alpha_s^2 \approx -4.2 \times 10^{-4}$.

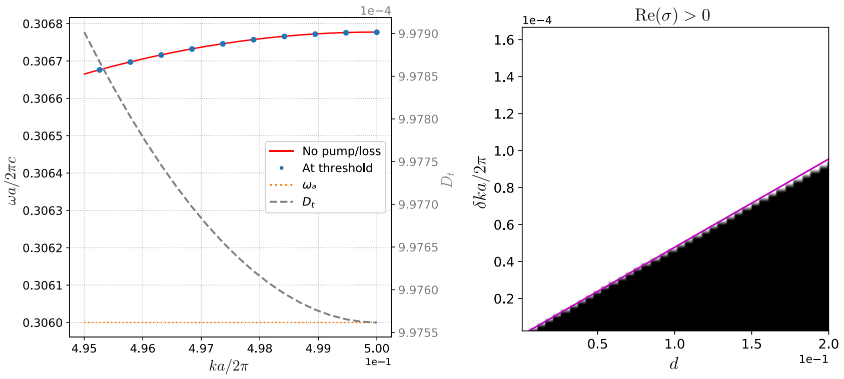

Figure 6-9: Same 1d structure in Sec. 6.5 but with $\omega_a a/2\pi c = 0.306$ and $\gamma_\perp/2\pi c = 0.08$. The lasing mode is still at the band edge but the laser detuning $(\omega_t - \omega_a)$ is now positive.

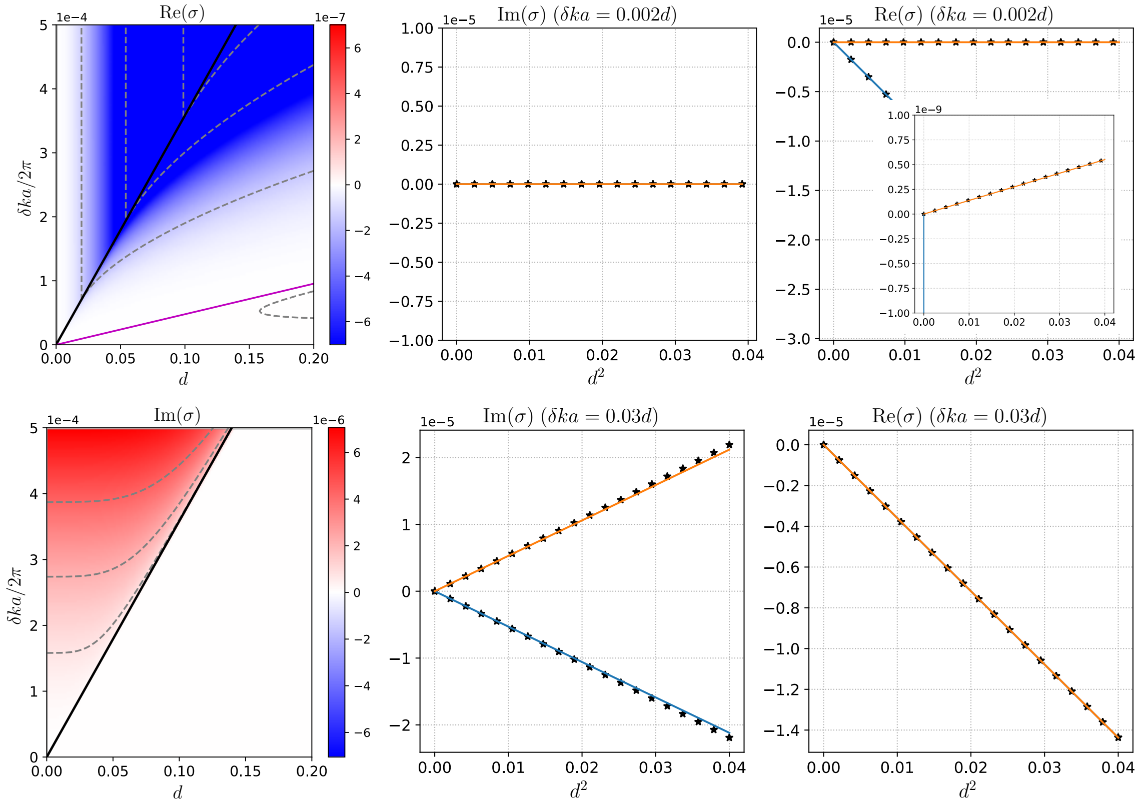

Figure 6-10: Same 1d structure studied in Sec. 6.5 but with $\omega_a a/2\pi c = 0.306$ and $\gamma_\perp/2\pi c = 0.08$. Numerical simulation (stars and dashed contour lines) are in agreement with analytical results (solid lines). Black line corresponds to $\delta ka = \alpha_c d$ and represents the line of eigenvalue crossing (transition from two real to two complex conjugate eigenvalues). Magenta solid line corresponds to $\delta k = \alpha_s d$ from analytical perturbation results and matches $\mathrm{Re}\,(\sigma) = 0$ from numerical simulation. $\alpha_c \approx 0.022$ and $\alpha_s \approx 3 \times 10^{-3}$.

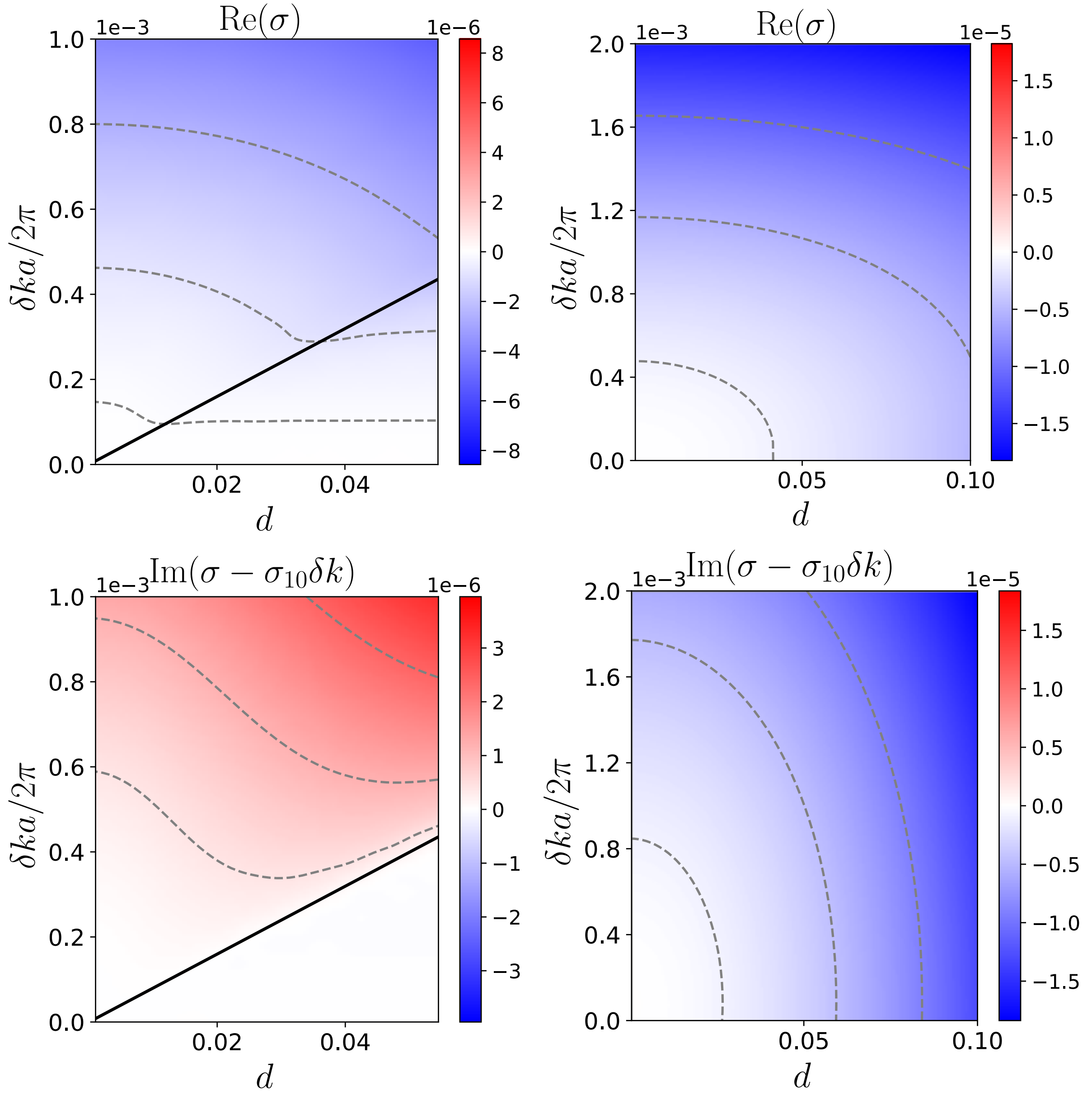

Figure 6-11: Same 2d structure in Sec. 6.6 with $\omega_a a/2\pi c = 0.625$ and $\omega_t a/2\pi c \approx 0.65$. Left: $q_0 = 0$. Right: $q_0 = -2k$. Contour lines (dashed) are from numerical simulation. Black solid line corresponds to $\delta k = \alpha_c d$ from analytical perturbation results and represents the line of eigenvalue crossing (transition of $\sigma - \sigma_{10}\delta k$ from two real to two complex conjugate eigenvalues) when expanding around $q_0 = 0$. The analytical line matches results of numerical simulation. Expansion around $-2k$ does not show a critical line in agreement with perturbation theory (case $ka \neq \pi/2$). We have $\alpha_c \approx 0.05$, $\alpha_s^2 \approx -0.018$ and $\sigma_{10} \approx 0.59i$ when expanding around $q_0 = 0$ (opposite sign for $i\sigma_{10}$ when expanding around $q_0 = -2k$).

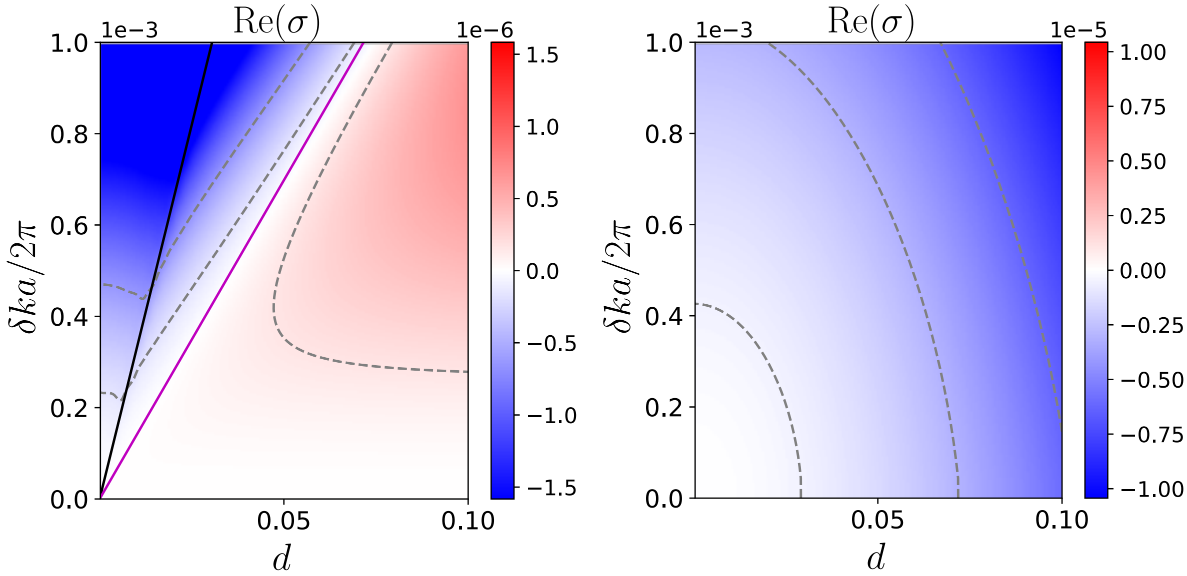

Figure 6-12: Same 2d structure in Sec. 6.6 with $\omega_a a/2\pi c = 0.675$. Left: $q_0 = 0$. Right: $q_0 = -2k$. The lasing mode is slightly shifted to $ka/2\pi \approx 0.1944$ but still with $\omega_t a/2\pi c \approx 0.65$. Contour lines (dashed) are from numerical simulation. Black solid line corresponds to $\delta k = \alpha_c d$ and magenta solid line corresponds to $\delta k = \alpha_s d$ from analytical perturbation results when expanding around $q_0 = 0$. Majenta line (analytical) matches $\mathrm{Re}\,(\sigma) = 0$ from numerical simulation. Expansion around $-2k$ does not show a critical line in agreement with perturbation theory (case $ka \neq \pi/2$). We have $\alpha_c \approx 0.21$, $\alpha_s \approx 0.088$ and $\sigma_{10} \approx 0.59i$ when expanding around $q_0 = 0$ (opposite sign for $i\sigma_{10}$ when expanding around $q_0 = -2k$).

6.8 Conclusion

The method presented in this chapter gives a rigorous answer to the fundamental question of stable lasing in infinite periodic systems and provides practical guidance in the form of theoretical criterion for stability. If these criteria are satisfied, the main theoretical challenges for future work are to analyze the effects of boundaries (which we expect are negligible for sufficiently large systems) and manufacturing disorder (which must eventually limit single-mode lasing).

THIS PAGE INTENTIONALLY LEFT BLANK

Chapter 7

Concluding remarks

In this thesis, we explored various applications where the resonances of the system play an important role and allow for a general and simple understanding of the problem.

We first quantified the limitations imposed by absorption losses on enhancement effects in electromagnetic systems and obtained fundamental limits on the surface-enhanced Raman scattering (SERS) in terms of the material susceptibility. While these limits are proven to be tight only in the quasistatic regime, they are still an important tool for guiding the optimization of arbitrary-shaped nanostructures to obtain larger enhancements. We also investigated design methods for high-order filters, especially in strongly coupled resonant systems, where individual resonators cannot be designed independently. In particular, we developed a quasinormal mode theory (QNMT) to compute the scattering matrix directly from the resonant modes of the system, making sure to enforce all physical constraints of energy conservation and reciprocity, even for finite truncated expansions. While this QNMT is a great numerical tool for computing the spectral response, especially in the presence of sharp features that are difficult to resolve using a frequency-domain simulation, it also offers better physical insight and can be seen as an effective reduced-order model (reducing the complexity of the system from a spatially-dependent geometrical profile to a few parameters associated with each resonance). This model allowed us to obtain analytical design criteria for the realization of standard filers based on the sole knowledge of the system resonances, which we applied to design various microwave metasurfaces. We then studied limitations on absorption enhancement in metaparticle arrays for problems with large spectral and angular bandwidth, where a large number of resonances is in play and coherent effects tend to average out. We found approximate limits in the radiative transfer regime, and, highlighting the similarity between light trapping in solar cells and multiple scattering enhancement in ocean buoy arrays (two seemingly different renewable-energy problems), we suggested new ways to further increase the total absorption in the ocean buoy system, in particular using external membranes that act as partial reflectors, as in solar-cells' light trapping. Finally, we explored foundations of single-mode lasing in periodic structures, where a continuum of modes need to be taken into account. Using Bloch theorem for the stability analysis of the nonlinear Maxwell-Bloch equations, we obtained numerical and analytical criteria for single-mode lasing. We showed that, under the right conditions, single-mode lasing is possible in an infinite periodic structure, with practical limitations potentially stemming from boundary effects and manufacturing disorder. These results are particularly relevant for novel (e.g., BiC-based) lasers.

Multiple directions are worth exploring in the future. The methods for fundamental bounds have been extended in multiple ways since our work, including the possibility of frequency-averaged bounds as well as tighter single-frequency bounds using additional constraints (albeit the increased complexity). It would be interesting to apply these new techniques to the nonlinear Raman problem. Additionally, our work on quasinormal modes can trigger new research directions such as: new QNMT enforcing *other* symmetry constraints, rigorous treatment of absorption loss, QNMT for finite-sized scatterers with spherical or cylindrical ports, or necessary symmetries of QNMs (in terms of QNM-to-ports coupling coefficients) assuming certain symmetries of S (e.g., unitarity and/or symmetry). Other applications of our theory can also be explored such as the design of metalenses (especially those with multi-wavelength constraints) or thermal emitters (requiring a more rigorous treatment of absorption/emission channels). Looking further ahead, our work can be seen as part of a larger effort to obtain simplified models for complex systems. One of the interesting directions to explore is the possibility of a more general and systematic framework to obtain such simplified models, potentially combined with more recent data-driven approaches, but making sure that any model satisfies the necessary physical constraints. Furthermore, our work on single-mode stability in periodic structures can be extended to include effects of boundaries and manufacturing disorder to attempt experimental investigations. Finally, while we have presented a variety of scenarios where resonances are involved in different ways, there are still many situations that we have not looked at. One such case corresponds to the collapse of two (or more) resonances (i.e., eigenfrequencies and eigenfields become identical) making the operator defective (not diagonalizable). These are called exceptional points (EPs). While in reality, they may not be as exceptional as they are claimed to be, they still present a peculiar state worth investigating as new effects may emerge. In particular, our QNMT and the laser stability conditions can be used to investigate, respectively, the spectral response as well as the nonlinear lasing behaviour in the presence of such exceptional points.

THIS PAGE INTENTIONALLY LEFT BLANK

Chapter 8

Bibliography

[1] M. Agustoni, H. P. Beck, A. Cervelli, A. Ereditato, V. Gallo, S. Haug, T. Kruker, L. Marti, F. Meloni, B. Schneider, *et al.*, "Measurement of the Higgs boson mass from the $H \to \gamma\gamma$ and $H \to ZZ^* \to 4\ell$ collisions at center-of-mass energies of 7 and 8 tev with the atlas detector," *Physical Review D*, vol. 90, no. 5, p. 052004, 2014.

[2] B. Lassagne, Y. Tarakanov, J. Kinaret, D. Garcia-Sanchez, and A. Bachtold, "Coupling mechanics to charge transport in carbon nanotube mechanical resonators," *Science*, vol. 325, no. 5944, pp. 1107–1110, 2009.

[3] A. Bienfait, J. Pla, Y. Kubo, M. Stern, X. Zhou, C. Lo, C. Weis, T. Schenkel, M. Thewalt, D. Vion, *et al.*, "Reaching the quantum limit of sensitivity in electron spin resonance," *Nature Nanotechnology*, vol. 11, no. 3, pp. 253–257, 2016.

[4] E. D. Palik, *Handbook of optical constants of solids.* Academic Press, 1998.

[5] O. D. Miller, A. G. Polimeridis, M. T. H. Reid, C. W. Hsu, B. G. DeLacy, J. D. Joannopoulos, M. Soljačić, and S. G. Johnson, "Fundamental limits to optical response in absorptive systems," *Optics Express*, vol. 24, pp. 3329–3364, feb 2016.

[6] F. Alpeggiani, N. Parappurath, E. Verhagen, and L. Kuipers, "Quasinormal-mode expansion of the scattering matrix," *Physical Review X*, vol. 7, no. 2, p. 021035, 2017.

[7] Z. Yu, A. Raman, and S. Fan, "Fundamental limit of light trapping in grating structures," *Optics Express*, vol. 18, no. 103, pp. A366–A380, 2010.

[8] G. Tokic, *Optimal Configuration of Large Arrays of Floating Bodies for Ocean Wave Energy Extraction.* PhD thesis, MIT, 2016. `http://hdl.handle.net/1721.1/104198`.

[9] C. L. Bretschneider, "Wave variability and wave spectra for wind-generated gravity waves," Tech. Rep. 118, US Beach Erosion Board, Washington D.C., 1959.

[10] J. H. Joseph, W. Wiscombe, and J. Weinman, "The delta-eddington approximation for radiative flux transfer," *Journal of the Atmospheric Sciences*, vol. 33, no. 12, pp. 2452–2459, 1976.

[11] H. Mitsuyasu, F. Tasai, T. Suhara, S. Mizuno, M. Ohkusu, T. Honda, and K. Rikiishi, "Observations of the directional spectrum of ocean waves using a cloverleaf buoy," *Journal of Physical Oceanography*, vol. 5, no. 4, pp. 750–760, 1975.

[12] P. D. Hislop and I. M. Sigal, *Introduction to Spectral Theory: With Applications to Schrödinger Operators*, vol. 113. Springer Science & Business Media, 2012.

[13] S. Dyatlov and M. Zworski, *Mathematical Theory of Scattering Resonances*, vol. 200. American Mathematical Soc., 2019.

[14] J. Michon, M. Benzaouia, W. Yao, O. D. Miller, and S. G. Johnson, "Limits to surface-enhanced raman scattering near arbitrary-shape scatterers," *Optics express*, vol. 27, no. 24, pp. 35189–35202, 2019.

[15] R. E. Christiansen, J. Michon, M. Benzaouia, O. Sigmund, and S. G. Johnson, "Inverse design of nanoparticles for enhanced raman scattering," *Optics Express*, vol. 28, no. 4, pp. 4444–4462, 2020.

[16] H. G. Dimopoulos, *Analog Electronic Filters: Theory, Design and Synthesis*. Springer Science & Business Media, 2011.

[17] W. Suh, Z. Wang, and S. Fan, "Temporal coupled-mode theory and the presence of non-orthogonal modes in lossless multimode cavities," *IEEE Journal of Quantum Electronics*, vol. 40, no. 10, pp. 1511–1518, 2004.

[18] M. Benzaouia, J. D. Joannopoulos, S. G. Johnson, and A. Karalis, "Quasi-normal mode theory of the scattering matrix, enforcing fundamental constraints for truncated expansions," *Physical Review Research*, vol. 3, no. 3, p. 033228, 2021.

[19] M. Benzaouia, J. D. Joannopoulos, S. G. Johnson, and A. Karalis, "Analytical design criteria for realizing ideal standard filters in strongly coupled resonant systems, with application to microwave metasurfaces," *arXiv:2103.08866*, 2021.

[20] B. A. Munk, *Frequency Selective Surfaces: Theory and Design*. John Wiley & Sons, 2005.

[21] G. Tokić and D. K. Yue, "Hydrodynamics of periodic wave energy converter arrays," *Journal of Fluid Mechanics*, vol. 862, pp. 34–74, 2019.

[22] E. Yablonovitch, "Statistical ray optics," *JOSA*, vol. 72, no. 7, pp. 899–907, 1982.

[23] Z. Yu, A. Raman, and S. Fan, "Fundamental limit of nanophotonic light trapping in solar cells," *Proceedings of the National Academy of Sciences*, vol. 107, no. 41, pp. 17491–17496, 2010.

[24] H. Wolgamot, P. Taylor, and R. E. Taylor, "The interaction factor and directionality in wave energy arrays," *Ocean Engineering*, vol. 47, pp. 65–73, 2012.

[25] X. Sheng, S. G. Johnson, J. Michel, and L. C. Kimerling, "Optimization-based design of surface textures for thin-film si solar cells," *Optics Express*, vol. 19, no. 104, pp. A841–A850, 2011.

[26] M. Benzaouia, A. Cerjan, and S. G. Johnson, "Is single-mode lasing possible in an infinite periodic system?," *Applied Physics Letters*, vol. 117, no. 5, p. 051102, 2020.

[27] M. Benzaouia, J. Michon, R. E. Christiansen, W. Yao, O. D. Miller, O. Sigmund, and S. G. Johnson, "Limits to surface-enhanced raman scattering near arbitrary-shape scatterers," in *Plasmonics: Design, Materials, Fabrication, Characterization, and Applications XVIII*, vol. 11462, p. 114621R, International Society for Optics and Photonics, 2020.

[28] J. D. Joannopoulos, S. G. Johnson, J. N. Winn, and R. D. Meade, *Photonic Crystals: Molding the Flow of Light.* Princeton University Press, second ed., 2008.

[29] O. D. Miller, S. G. Johnson, and A. W. Rodriguez, "Shape-independent limits to near-field radiative heat transfer," *Physical Review Letters*, vol. 115, no. 20, p. 204302, 2015.

[30] H. Shim, L. Fan, S. G. Johnson, and O. D. Miller, "Fundamental limits to near-field optical response, over any bandwidth," *Physical Review X*, vol. 9, p. 011043, mar 2018.

[31] I. M. Vellekoop and A. P. Mosk, "Focusing coherent light through opaque strongly scattering media," *Optics Letters*, vol. 32, pp. 2309–2311, aug 2007.

[32] A. P. Mosk, A. Lagendijk, G. Lerosey, and M. Fink, "Controlling waves in space and time for imaging and focusing in complex media," *Nature Photonics*, vol. 6, pp. 283–292, may 2012.

[33] S. Dodson, M. Haggui, R. Bachelot, J. Plain, S. Li, and Q. Xiong, "Optimizing electromagnetic hotspots in plasmonic bowtie nanoantennae," *Journal of Physical Chemistry Letters*, vol. 4, pp. 496–501, feb 2013.

[34] P. Kühler, M. Weber, and T. Lohmüller, "Plasmonic Nanoantenna Arrays for Surface-Enhanced Raman Spectroscopy of Lipid Molecules Embedded in a Bilayer Membrane," *ACS Applied Materials & Interfaces*, vol. 6, pp. 8947–8952, jun 2014.

[35] J. Zhang, M. Irannejad, and B. Cui, "Bowtie Nanoantenna with Single-Digit Nanometer Gap for Surface-Enhanced Raman Scattering (SERS)," *Plasmonics*, vol. 10, pp. 831–837, aug 2015.

[36] D. A. Long, *Raman spectroscopy.* McGraw-Hill, 1977.

[37] M. Moskovits, "Surface-enhanced spectroscopy," *Reviews of Modern Physics*, vol. 57, pp. 783–826, jul 1985.

[38] G. Turrell and J. Corset, *Raman Microscopy: Developments and Applications*. Academic Press, 1996.

[39] K. Kneipp, Y. Wang, H. Kneipp, L. T. Perelman, I. Itzkan, R. R. Dasari, and M. S. Feld, "Single molecule detection using surface-enhanced raman scattering (SERS)," *Physical Review Letters*, vol. 78, pp. 1667–1670, mar 1997.

[40] S. Nie and S. R. Emory, "Probing Single Molecules and Single Nanoparticles by Surface-Enhanced Raman Scattering," *Science*, vol. 275, pp. 1102–1106, feb 1997.

[41] C. L. Haynes, A. D. McFarland, and R. P. Van Duyne, "Surface-Enhanced Raman Spectroscopy," *Analytical Chemistry*, vol. 77, pp. 338–346, sep 2005.

[42] P. L. Stiles, J. A. Dieringer, N. C. Shah, and R. P. Van Duyne, "Surface-Enhanced Raman Spectroscopy," *Annual Review of Analytical Chemistry*, vol. 1, pp. 601–626, jul 2008.

[43] K. Kneipp, M. Moskovits, and H. Kneipp, eds., *Surface-Enhanced Raman Scattering*. Springer, 2006.

[44] A. Campion and P. Kambhampati, "Surface-enhanced Raman scattering," *Chemical Society Reviews*, vol. 27, pp. 241–250, jan 1998.

[45] L. Jensen, C. M. Aikens, and G. C. Schatz, "Electronic structure methods for studying surface-enhanced Raman scattering," *Chemical Society Reviews*, vol. 37, pp. 1061–1073, apr 2008.

[46] D. P. Fromm, A. Sundaramurthy, A. Kinkhabwala, P. J. Schuck, G. S. Kino, and W. E. Moerner, "Exploring the chemical enhancement for surface-enhanced Raman scattering with Au bowtie nanoantennas," *Journal of Chemical Physics*, vol. 124, p. 061101, feb 2006.

[47] J. P. Camden, J. A. Dieringer, Y. Wang, D. J. Masiello, L. D. Marks, G. C. Schatz, and R. P. Van Duyne, "Probing the structure of single-molecule surface-enhanced Raman scattering hot spots," *Journal of the American Chemical Society*, vol. 130, pp. 12616–12617, sep 2008.

[48] E. C. Le Ru, E. Blackie, M. Meyer, and P. G. Etchegoint, "Surface enhanced raman scattering enhancement factors: A comprehensive study," *Journal of Physical Chemistry C*, vol. 111, no. 37, pp. 13794–13803, 2007.

[49] E. Hao and G. C. Schatz, "Electromagnetic fields around silver nanoparticles and dimers," *Journal of Chemical Physics*, vol. 120, pp. 357–366, jan 2004.

[50] D. A. Genov, A. K. Sarychev, V. M. Shalaev, and A. Wei, "Resonant Field Enhancements from Metal Nanoparticle Arrays," *Nano Letters*, vol. 4, no. 1, pp. 153–158, 2004.

[51] A. Sundaramurthy, K. B. Crozier, G. S. Kino, D. P. Fromm, P. J. Schuck, and W. E. Moerner, "Field enhancement and gap-dependent resonance in a system of two opposing tip-to-tip Au nanotriangles," *Physical Review B - Condensed Matter and Materials Physics*, vol. 72, p. 165409, oct 2005.

[52] Y. Deng, Z. Liu, C. Song, P. Hao, Y. Wu, Y. Liu, and J. G. Korvink, "Topology optimization of metal nanostructures for localized surface plasmon resonances," *Structural and Multidisciplinary Optimization*, vol. 53, pp. 967–972, may 2016.

[53] R. E. Christiansen, J. Vester-Petersen, S. P. Madsen, and O. Sigmund, "A non-linear material interpolation for design of metallic nano-particles using topology optimization," *Computer Methods in Applied Mechanics and Engineering*, vol. 343, pp. 23–39, jan 2019.

[54] E. Le Ru and P. Etchegoin, *Principles of Surface-Enhanced Raman Spectroscopy: and Related Plasmonic Effects*. Elsevier, 2008.

[55] K. Joulain, J.-P. Mulet, F. Marquier, R. Carminati, and J.-J. Greffet, "Surface electromagnetic waves thermally excited: Radiative heat transfer, coherence properties and Casimir forces revisited in the near field," *Surface Science Reports*, vol. 57, pp. 59–112, may 2005.

[56] L. Novotny and B. Hecht, *Principles of nano-optics*. Cambridge University, 2006.

[57] P. Lancaster and M. Tismenetsky, *The Theory of Matrices: with Applications*. Elsevier, 1985.

[58] W. C. Chew, *Waves and Fields in Inhomogeneous Media*. IEEE press, 1995.

[59] K. Kreutz-Delgado, "The complex gradient operator and the cr-calculus," *arXiv preprint arXiv:0906.4835*, 2009.

[60] J. Nocedal and S. J. Wright, *Numerical Optimization*. Springer, 2nd ed., 2006.

[61] J. D. Joannopoulos, S. G. Johnson, J. N. Winn, and R. D. Meade, *Photonic Crystals: Molding the Flow of Light*. Princeton University, 2nd ed., 2008.

[62] L. Tsang, J. A. Kong, and K.-H. Ding, *Scattering of Electromagnetic Waves, Theories and Applications*. John Wiley and Sons, New York, 2000.

[63] M. T. H. Reid and S. G. Johnson, "Efficient Computation of Power, Force, and Torque in BEM Scattering Calculations," *IEEE Transactions on Antennas and Propagation*, vol. 63, pp. 3588–3598, aug 2015.

[64] `http://github.com/homerreid/scuff-EM`.

[65] M. Kaniber, K. Schraml, A. Regler, J. Bartl, G. Glashagen, F. Flassig, J. Wierzbowski, and J. J. Finley, "Surface plasmon resonance spectroscopy of single bowtie nano-antennas using a differential reflectivity method," *Scientific Reports*, vol. 6, p. 23203, mar 2016.

[66] S. G. Johnson, "Notes on perfectly matched layers (PMLs)." `https://math.mit.edu/~stevenj/18.369/pml.pdf`, 2010.

[67] A. Taflove and S. C. Hagness, *Computational Electrodynamics: The Finite-Difference Time-Domain Method.* Artech house, 2005.

[68] M. Reed, B. Simon, B. Simon, and B. Simon, *Methods of modern mathematical physics*, vol. 1. Elsevier, 1972.

[69] E. Ching, P. Leung, A. M. van den Brink, W. Suen, S. Tong, and K. Young, "Quasinormal-mode expansion for waves in open systems," *Reviews of Modern Physics*, vol. 70, no. 4, p. 1545, 1998.

[70] B. Vial, F. Zolla, A. Nicolet, and M. Commandré, "Quasimodal expansion of electromagnetic fields in open two-dimensional structures," *Physical Review A*, vol. 89, no. 2, p. 023829, 2014.

[71] H. A. Haus, *Waves and Fields in Optoelectronics.* Prentice-Hall,, 1984.

[72] W. L. Brogan, *Modern Control Theory.* Pearson education India, 1991.

[73] H. M. Nussenzveig, *Causality and Dispersion Relations.* Academic Press, 1972.

[74] J. T. Cushing, "The importance of heisenberg's s-matrix program for the theoretical high-energy physics of the 1950's," *Centaurus*, vol. 29, no. 2, pp. 110–149, 1986.

[75] X. Shan and J. Connor, "Angular scattering using parameterized s matrix elements for the h+ d 2 (vi= 0, ji= 0)→ hd (vf= 3, jf= 0)+ d reaction: an example of heisenberg's s matrix programme," *Physical Chemistry Chemical Physics*, vol. 13, no. 18, pp. 8392–8406, 2011.

[76] V. Grigoriev, A. Tahri, S. Varault, B. Rolly, B. Stout, J. Wenger, and N. Bonod, "Optimization of resonant effects in nanostructures via weierstrass factorization," *Physical Review A*, vol. 88, no. 1, p. 011803, 2013.

[77] L. O. Krainov, P. A. Batishchev, and O. I. Tolstikhin, "Siegert pseudostate formulation of scattering theory: General three-dimensional case," *Physical Review A*, vol. 93, no. 4, p. 042706, 2016.

[78] T. Weiss and E. A. Muljarov, "How to calculate the pole expansion of the optical scattering matrix from the resonant states," *Phys. Rev. B*, vol. 98, p. 085433, Aug 2018.

[79] H. Zhang and O. D. Miller, "Quasinormal coupled mode theory," *arXiv preprint arXiv:2010.08650*, 2020.

[80] M. F. Limonov, M. V. Rybin, A. N. Poddubny, and Y. S. Kivshar, "Fano resonances in photonics," *Nature Photonics*, vol. 11, no. 9, p. 543, 2017.

[81] C. W. Hsu, B. Zhen, J. Lee, S.-L. Chua, S. G. Johnson, J. D. Joannopoulos, and M. Soljačić, "Observation of trapped light within the radiation continuum," *Nature*, vol. 499, no. 7457, pp. 188–191, 2013.

[82] P. Lalanne, W. Yan, K. Vynck, C. Sauvan, and J.-P. Hugonin, "Light interaction with photonic and plasmonic resonances," *Laser & Photonics Reviews*, vol. 12, no. 5, p. 1700113, 2018.

[83] P. T. Kristensen, K. Herrmann, F. Intravaia, and K. Busch, "Modeling electromagnetic resonators using quasinormal modes," *Advances in Optics and Photonics*, vol. 12, no. 3, pp. 612–708, 2020.

[84] S. Franke, M. Richter, J. Ren, A. Knorr, and S. Hughes, "Quantized quasinormal-mode description of nonlinear cavity-QED effects from coupled resonators with a fano-like resonance," *Physical Review Research*, vol. 2, no. 3, p. 033456, 2020.

[85] W. R. Sweeney, C. W. Hsu, and A. D. Stone, "Theory of reflectionless scattering modes," *Physical Review A*, vol. 102, no. 6, p. 063511, 2020.

[86] P. T. Kristensen, R.-C. Ge, and S. Hughes, "Normalization of quasinormal modes in leaky optical cavities and plasmonic resonators," *Physical Review A*, vol. 92, no. 5, p. 053810, 2015.

[87] A. Gras, W. Yan, and P. Lalanne, "Quasinormal-mode analysis of grating spectra at fixed incidence angles," *Optics Letters*, vol. 44, pp. 3494–3497, Jul 2019.

[88] A. V. Oppenheim, A. S. Willsky, and S. H. Nawab, *Signals and systems.* Prentice Hall, 2nd ed., 1983.

[89] W. Yan, R. Faggiani, and P. Lalanne, "Rigorous modal analysis of plasmonic nanoresonators," *Physical Review B*, vol. 97, no. 20, p. 205422, 2018.

[90] A. I. Markushevich, *Theory of Functions of a Complex Variable.* American Mathematical Soc., 2013.

[91] A. R. Conn, N. I. Gould, and P. Toint, "A globally convergent augmented lagrangian algorithm for optimization with general constraints and simple bounds," *SIAM Journal on Numerical Analysis*, vol. 28, no. 2, pp. 545–572, 1991.

[92] J. Revels, M. Lubin, and T. Papamarkou, "Forward-mode automatic differentiation in Julia," *arXiv:1607.07892 [cs.MS]*, 2016.

[93] M. Åbom, "Measurement of the scattering-matrix of acoustical two-ports," *Mechanical Systems and Signal Processing*, vol. 5, no. 2, pp. 89–104, 1991.

[94] S. Sack, M. Abom, and G. Efraimsson, "On acoustic multi-port characterisation including higher order modes," *Acta Acustica united with Acustica*, vol. 102, no. 5, pp. 834–850, 2016.

[95] Y. Tong and J. Pan, "Modal analysis of the scattering coefficients of an open cavity in a waveguide," *Wave Motion*, vol. 68, pp. 242–252, 2017.

[96] S. Datta, *Electronic transport in mesoscopic systems.* Cambridge university press, 1997.

[97] *Comsol Multiphysics® v5.1, www.comsol.com, COMSOL AB, Stockholm, Sweden.*

[98] S. Kim and J. Pasciak, "The computation of resonances in open systems using a perfectly matched layer," *Mathematics of Computation*, vol. 78, no. 267, pp. 1375–1398, 2009.

[99] L. Nannen and M. Wess, "Spurious modes of the complex scaled helmholtz equation," *ASC Report, TU Wien*, vol. 15, 2016.

[100] M. Mojahedi, K. J. Malloy, G. V. Eleftheriades, J. Woodley, and R. Y. Chiao, "Abnormal wave propagation in passive media," *IEEE J. Selected Topics in Quantum Electronics*, vol. 9, no. 1, pp. 30–39, 2003.

[101] E. L. Bolda, R. Y. Chiao, and J. C. Garrison, "Two theorems for the group velocity in dispersive media," *Phys. Rev. A*, vol. 48, pp. 3890–3894, Nov 1993.

[102] B. Ravelo, ed., *Negative Group Delay Devices: From Concepts to Applications.* Institution of Engineering and Technology, 2018.

[103] J. Peatross, S. Glasgow, and M. Ware, "Average energy flow of optical pulses in dispersive media," *Physical Review letters*, vol. 84, no. 11, p. 2370, 2000.

[104] P. Bienstman, "CAMFR: CAvity Modeling FRamework." http://camfr.sf.net.

[105] K. B. Dossou, L. C. Botten, A. A. Asatryan, B. C. P. Sturmberg, M. A. Byrne, C. G. Poulton, R. C. McPhedran, and C. M. de Sterke, "Modal formulation for diffraction by absorbing photonic crystal slabs," *J. Opt. Soc. Am. A*, vol. 29, no. 5, pp. 817–831, 2012.

[106] T. Paul, C. Menzel, W. Śmigaj, C. Rockstuhl, P. Lalanne, and F. Lederer, "Reflection and transmission of light at periodic layered metamaterial films," *Phys. Rev. B*, vol. 84, no. 11, p. 115142, 2011.

[107] B. E. Little, S. T. Chu, H. A. Haus, J. Foresi, and J.-P. Laine, "Microring resonator channel dropping filters," *Journal of Lightwave Technology*, vol. 15, no. 6, pp. 998–1005, 1997.

[108] S. Fan, P. R. Villeneuve, J. D. Joannopoulos, and H. A. Haus, "Channel drop filters in photonic crystals," *Optics Express*, vol. 3, no. 1, pp. 4–11, 1998.

[109] C. Manolatou, M. Khan, S. Fan, P. R. Villeneuve, H. Haus, and J. Joannopoulos, "Coupling of modes analysis of resonant channel add-drop filters," *IEEE Journal of Quantum Electronics*, vol. 35, no. 9, pp. 1322–1331, 1999.

[110] M. A. Popovic, T. Barwicz, M. R. Watts, P. T. Rakich, L. Socci, E. P. Ippen, F. X. Kärtner, and H. I. Smith, "Multistage high-order microring-resonator add-drop filters," *Optics Letters*, vol. 31, no. 17, pp. 2571–2573, 2006.

[111] S. Xiao, M. H. Khan, H. Shen, and M. Qi, "A highly compact third-order silicon microring add-drop filter with a very large free spectral range, a flat passband and a low delay dispersion," *Optics Express*, vol. 15, no. 22, pp. 14765–14771, 2007.

[112] H.-C. Liu and A. Yariv, "Synthesis of high-order bandpass filters based on coupled-resonator optical waveguides (crows)," *Optics Express*, vol. 19, no. 18, pp. 17653–17668, 2011.

[113] Z. Dai, J. Wang, and Y. Heng, "Circuit-based method for synthesizing of coupled-resonators bandpass photonic crystal filters," *Optics Express*, vol. 19, no. 4, pp. 3667–3676, 2011.

[114] W. Bogaerts, P. De Heyn, T. Van Vaerenbergh, K. De Vos, S. Kumar Selvaraja, T. Claes, P. Dumon, P. Bienstman, D. Van Thourhout, and R. Baets, "Silicon microring resonators," *Laser & Photonics Reviews*, vol. 6, no. 1, pp. 47–73, 2012.

[115] T.-K. Wu, *Frequency Selective Surface and Grid Array*, vol. 40. Wiley-Interscience, 1995.

[116] J. C. Vardaxoglou, *Frequency Selective Surfaces: Analysis and Design.* Research Studies Press, 1997.

[117] D. Morgan, *Surface Acoustic Wave Filters: With applications to Electronic Communications and Signal Processing.* Academic Press, 2010.

[118] A. Colombi, D. Colquitt, P. Roux, S. Guenneau, and R. V. Craster, "A seismic metamaterial: The resonant metawedge," *Scientific Reports*, vol. 6, no. 1, pp. 1–6, 2016.

[119] B. Rostami-Dogolsara, M. K. Moravvej-Farshi, and F. Nazari, "Acoustic add-drop filters based on phononic crystal ring resonators," *Physical Review B*, vol. 93, no. 1, p. 014304, 2016.

[120] L. D'Alessandro, E. Belloni, R. Ardito, F. Braghin, and A. Corigliano, "Mechanical low-frequency filter via modes separation in 3d periodic structures," *Applied Physics Letters*, vol. 111, no. 23, p. 231902, 2017.

[121] D. Colquitt, A. Colombi, R. Craster, P. Roux, and S. Guenneau, "Seismic metasurfaces: Sub-wavelength resonators and rayleigh wave interaction," *Journal of the Mechanics and Physics of Solids*, vol. 99, pp. 379–393, 2017.

[122] G. Manara, A. Monorchio, and R. Mittra, "Frequency selective surface design based on genetic algorithm," *Electronics Letters*, vol. 35, no. 17, pp. 1400–1401, 1999.

[123] D. J. Kern, D. H. Werner, A. Monorchio, L. Lanuzza, and M. J. Wilhelm, "The design synthesis of multiband artificial magnetic conductors using high impedance frequency selective surfaces," *IEEE Transactions on Antennas and Propagation*, vol. 53, no. 1, pp. 8–17, 2005.

[124] J. A. Bossard, D. H. Werner, T. S. Mayer, J. A. Smith, Y. U. Tang, R. P. Drupp, and L. Li, "The design and fabrication of planar multiband metallodielectric frequency selective surfaces for infrared applications," *IEEE Transactions on Antennas and Propagation*, vol. 54, no. 4, pp. 1265–1276, 2006.

[125] Z. H. Jiang, S. Yun, L. Lin, J. A. Bossard, D. H. Werner, and T. S. Mayer, "Tailoring dispersion for broadband low-loss optical metamaterials using deep-subwavelength inclusions," *Scientific Reports*, vol. 3, no. 1, pp. 1–9, 2013.

[126] G. Q. Luo, W. Hong, Q. H. Lai, K. Wu, and L. L. Sun, "Design and experimental verification of compact frequency-selective surface with quasi-elliptic bandpass response," *IEEE Transactions on Microwave Theory and Techniques*, vol. 55, no. 12, pp. 2481–2487, 2007.

[127] B. Li and Z. Shen, "Synthesis of quasi-elliptic bandpass frequency-selective surface using cascaded loop arrays," *IEEE Transactions on Antennas and Propagation*, vol. 61, no. 6, pp. 3053–3059, 2013.

[128] Q. Lv, C. Jin, B. Zhang, and R. Mittra, "Wide-passband dual-polarized elliptic frequency selective surface," *IEEE Access*, vol. 7, pp. 55833–55840, 2019.

[129] R.-X. Liao, S.-W. Wong, Y. Li, J.-Y. Lin, B.-Y. Liu, F.-C. Chen, and Z. Quan, "Quasi-elliptic bandpass frequency selective surface based on coupled stubs-loaded ring resonators," *IEEE Access*, vol. 8, pp. 113675–113682, 2020.

[130] K. Sarabandi and N. Behdad, "A frequency selective surface with miniaturized elements," *IEEE Transactions on Antennas and Propagation*, vol. 55, no. 5, pp. 1239–1245, 2007.

[131] F. Bayatpur and K. Sarabandi, "Single-layer high-order miniaturized-element frequency-selective surfaces," *IEEE Transactions on Microwave Theory and Techniques*, vol. 56, no. 4, pp. 774–781, 2008.

[132] O. Luukkonen, C. Simovski, G. Granet, G. Goussetis, D. Lioubtchenko, A. V. Raisanen, and S. A. Tretyakov, "Simple and accurate analytical model of planar grids and high-impedance surfaces comprising metal strips or patches," *IEEE Transactions on Antennas and Propagation*, vol. 56, no. 6, pp. 1624–1632, 2008.

[133] F. Bayatpur, *Metamaterial-Inspired Frequency-Selective Surfaces.* PhD thesis, 2009.

[134] F. Mesa, R. Rodriguez-Berral, M. Garcia-Vigueras, F. Medina, and J. R. Mosig, "Simplified modal expansion to analyze frequency-selective surfaces: An equivalent circuit approach," *IEEE Transactions on Antennas and Propagation*, vol. 64, no. 3, pp. 1106–1111, 2015.

[135] C. Molero, R. Rodriguez-Berral, F. Mesa, and F. Medina, "Wideband analytical equivalent circuit for coupled asymmetrical nonaligned slit arrays," *Physical Review E*, vol. 95, no. 2, p. 023303, 2017.

[136] S. Fan and J. D. Joannopoulos, "Analysis of guided resonances in photonic crystal slabs," *Physical Review B*, vol. 65, no. 23, p. 235112, 2002.

[137] L. Maloratsky, *Passive RF and Microwave Integrated Circuits*. Elsevier, 2003.

[138] Q. Li, T. Wang, Y. Su, M. Yan, and M. Qiu, "Coupled mode theory analysis of mode-splitting in coupled cavity system," *Optics Express*, vol. 18, no. 8, pp. 8367–8382, 2010.

[139] C. W. Hsu, B. G. DeLacy, S. G. Johnson, J. D. Joannopoulos, and M. Soljacic, "Theoretical criteria for scattering dark states in nanostructured particles," *Nano Letters*, vol. 14, no. 5, pp. 2783–2788, 2014.

[140] J. S. Jensen and O. Sigmund, "Topology optimization for nano-photonics," *Laser & Photonics Reviews*, vol. 5, no. 2, pp. 308–321, 2011.

[141] S. Molesky, Z. Lin, A. Y. Piggott, W. Jin, J. Vucković, and A. W. Rodriguez, "Inverse design in nanophotonics," *Nature Photonics*, vol. 12, pp. 659–670, Oct. 2018.

[142] N. Aage and V. Egede Johansen, "Topology optimization of microwave waveguide filters," *International Journal for Numerical Methods in Engineering*, vol. 112, no. 3, pp. 283–300, 2017.

[143] M. A. Popović, C. Manolatou, and M. R. Watts, "Coupling-induced resonance frequency shifts in coupled dielectric multi-cavity filters," *Optics Express*, vol. 14, no. 3, pp. 1208–1222, 2006.

[144] M. A. Al-Joumayly and N. Behdad, "Wideband planar microwave lenses using sub-wavelength spatial phase shifters," *IEEE Transactions on Antennas and Propagation*, vol. 59, no. 12, pp. 4542–4552, 2011.

[145] M. Li, M. A. Al-Joumayly, and N. Behdad, "Broadband true-time-delay microwave lenses based on miniaturized element frequency selective surfaces," *IEEE transactions on antennas and propagation*, vol. 61, no. 3, pp. 1166–1179, 2012.

[146] S. B. Glybovski, S. A. Tretyakov, P. A. Belov, Y. S. Kivshar, and C. R. Simovski, "Metasurfaces: From microwaves to visible," *Physics Reports*, vol. 634, pp. 1–72, 2016.

[147] L. Maleki, A. Matsko, A. Savchenkov, and V. Ilchenko, "Tunable delay line with interacting whispering-gallery-mode resonators," *Optics Letters*, vol. 29, no. 6, pp. 626–628, 2004.

[148] É. Chéron, S. Félix, and V. Pagneux, "Broadband-enhanced transmission through symmetric diffusive slabs," *Physical Review Letters*, vol. 122, no. 12, p. 125501, 2019.

[149] See Supplemental Material.

[150] A. Ahmed, I. A. Goldthorpe, and A. K. Khandani, "Electrically tunable materials for microwave applications," *Appl. Phys. Rev.*, vol. 2, no. 1, p. 011302, 2015.

[151] O. Tsilipakos, T. Koschny, and C. M. Soukoulis, "Antimatched electromagnetic metasurfaces for broadband arbitrary phase manipulation in reflection," *ACS Photonics*, vol. 5, pp. 1101–1107, 2018.

[152] W. T. Chen, A. Y. Zhu, and F. Capasso, "Flat optics with dispersion-engineered metasurfaces," *Nat. Rev. Mat.*, vol. 5, pp. 604–620, 2020.

[153] M. Benzaouia, G. Tokić, O. D. Miller, D. K. Yue, and S. G. Johnson, "From Solar Cells to Ocean Buoys: Wide-Bandwidth Limits to Absorption by Metaparticle Arrays," *Physical Review Applied*, vol. 11, p. 034033, mar 2019.

[154] D. M. Callahan, J. N. Munday, and H. A. Atwater, "Solar cell light trapping beyond the ray optic limit," *Nano Letters*, vol. 12, no. 1, pp. 214–218, 2012.

[155] V. Ganapati, O. D. Miller, and E. Yablonovitch, "Light trapping textures designed by electromagnetic optimization for subwavelength thick solar cells," *IEEE Journal of Photovoltaics*, vol. 4, no. 1, pp. 175–182, 2014.

[156] J. Falnes, "A review of wave-energy extraction," *Marine Structures*, vol. 20, no. 4, pp. 185–201, 2007.

[157] M. A. Green, "Lambertian light trapping in textured solar cells and light-emitting diodes: analytical solutions," *Progress in Photovoltaics: Research and Applications*, vol. 10, no. 4, pp. 235–241, 2002.

[158] Z. Yu and S. Fan, "Angular constraint on light-trapping absorption enhancement in solar cells," *Applied Physics Letters*, vol. 98, no. 1, p. 011106, 2011.

[159] K. X. Wang, Z. Yu, V. Liu, Y. Cui, and S. Fan, "Absorption enhancement in ultrathin crystalline silicon solar cells with antireflection and light-trapping nanocone gratings," *Nano Letters*, vol. 12, no. 3, pp. 1616–1619, 2012.

[160] S. Buddhiraju and S. Fan, "Theory of solar cell light trapping through a nonequilibrium green's function formulation of maxwell's equations," *Physical Review B*, vol. 96, no. 3, p. 035304, 2017.

[161] A. Ishimaru, *Wave Propagation and Scattering in Random Media.* Academic press New York, 1978.

[162] J. R. Nagel and M. A. Scarpulla, "Enhanced absorption in optically thin solar cells by scattering from embedded dielectric nanoparticles," *Optics Express*, vol. 18, no. 102, pp. A139–A146, 2010.

[163] J.-Y. Wang, F.-J. Tsai, J.-J. Huang, C.-Y. Chen, N. Li, Y.-W. Kiang, and C. Yang, "Enhancing ingan-based solar cell efficiency through localized surface plasmon interaction by embedding ag nanoparticles in the absorbing layer," *Optics Express*, vol. 18, no. 3, pp. 2682–2694, 2010.

[164] G. Rothenberger, P. Comte, and M. Grätzel, "A contribution to the optical design of dye-sensitized nanocrystalline solar cells," *Solar Energy Materials and Solar Cells*, vol. 58, no. 3, pp. 321–336, 1999.

[165] F. E. Gálvez, P. R. Barnes, J. Halme, and H. Míguez, "Dye sensitized solar cells as optically random photovoltaic media," *Energy & Environmental Science*, vol. 7, no. 2, pp. 689–697, 2014.

[166] R. Mupparapu, K. Vynck, T. Svensson, M. Burresi, and D. S. Wiersma, "Path length enhancement in disordered media for increased absorption," *Optics Express*, vol. 23, no. 24, pp. A1472–A1484, 2015.

[167] J. Tollefson, "Blue energy," *Nature*, vol. 508, no. 7496, p. 302, 2014.

[168] V. Stratigaki, P. Troch, T. Stallard, D. Forehand, J. P. Kofoed, M. Folley, M. Benoit, A. Babarit, and J. Kirkegaard, "Wave basin experiments with large wave energy converter arrays to study interactions between the converters and effects on other users in the sea and the coastal area," *Energies*, vol. 7, no. 2, pp. 701–734, 2014.

[169] I. Penesis, R. Manasseh, J.-R. Nader, S. De Chowdhury, A. Fleming, G. Macfarlane, and M. K. Hasan, "Performance of ocean wave-energy arrays in australia," in *3rd Asian Wave and Tidal Energy Conference (AWTEC 2016)*, vol. 1, pp. 246–253, 2016.

[170] J. Cruz, R. Sykes, P. Siddorn, and R. E. Taylor, "Wave farm design: preliminary studies on the influences of wave climate, array layout and farm control," in *Proceedings of the 8th European Wave and Tidal Energy Conference*, pp. 736–745, 2009.

[171] B. Child and V. Venugopal, "Optimal configurations of wave energy device arrays," *Ocean Engineering*, vol. 37, no. 16, pp. 1402–1417, 2010.

[172] T. C. Choy, *Effective Medium Theory: Principles and Applications*, vol. 165. Oxford University Press, Oxford, 2015.

[173] D. R. Smith, S. Schultz, P. Markoš, and C. M. Soukoulis, "Determination of effective permittivity and permeability of metamaterials from reflection and transmission coefficients," *Physical Review B*, vol. 65, no. 19, p. 195104, 2002.

[174] J. Falnes, "Radiation impedance matrix and optimum power absorption for interacting oscillators in surface waves," *Applied Ocean Research*, vol. 2, no. 2, pp. 75–80, 1980.

[175] D. Evans, "Power from water waves," *Annual review of Fluid mechanics*, vol. 13, no. 1, pp. 157–187, 1981.

[176] J. Choi, "The method of stationary phase," 2011. `http://www.math.uchicago.edu/~may/VIGRE/VIGRE2011/REUPapers/Choi.pdf`.

[177] C. M. Chiang, M. Stiassnie, and D. K. Yue, *Theory and Applications of Ocean Surface Waves.* World Scientific, Singapore, 2005.

[178] K. M. Case and P. F. Zweifel, *Linear Transport Theory.* Addison-Wesley, Reading, Mass., 1967.

[179] R. Aronson, "A theorem concerning reflection and transmission from a nonabsorbing slab," *Nuclear Science and Engineering*, vol. 44, no. 3, pp. 449–450, 1971.

[180] A. D. Kim, "Correcting the diffusion approximation at the boundary," *JOSA A*, vol. 28, no. 6, pp. 1007–1015, 2011.

[181] C. Chen, Z. Du, and L. Pan, "Extending the diffusion approximation to the boundary using an integrated diffusion model," *AIP Advances*, vol. 5, no. 6, p. 067115, 2015.

[182] U. Tricoli, C. M. Macdonald, A. Da Silva, and V. A. Markel, "Optimized diffusion approximation," *JOSA A*, vol. 35, no. 2, pp. 356–369, 2018.

[183] C. Garrett, "Wave forces on a circular dock," *Journal of Fluid Mechanics*, vol. 46, no. 1, pp. 129–139, 1971.

[184] R. W. Yeung, "Added mass and damping of a vertical cylinder in finite-depth waters," *Applied Ocean Research*, vol. 3, no. 3, pp. 119–133, 1981.

[185] D. Bhatta and M. Rahman, "On scattering and radiation problem for a cylinder in water of finite depth," *International Journal of Engineering Science*, vol. 41, no. 9, pp. 931–967, 2003.

[186] G. I. Marchuk, G. A. Mikhailov, M. Nazareliev, R. A. Darbinjan, B. A. Kargin, and B. S. Elepov, *The Monte Carlo Methods in Atmospheric Optics*, vol. 12. Springer, Berlin, 2013.

[187] C. Zhang, C.-T. Chan, and X. Hu, "Broadband focusing and collimation of water waves by zero refractive index," *Scientific Reports*, vol. 4, p. 6979, 2014.

[188] T. Bobinski, A. Eddi, P. Petitjeans, A. Maurel, and V. Pagneux, "Experimental demonstration of epsilon-near-zero water waves focusing," *Applied Physics Letters*, vol. 107, no. 1, p. 014101, 2015.

[189] C. Fox and V. A. Squire, "On the oblique reflexion and transmission of ocean waves at shore fast sea ice," *Phil. Trans. R. Soc. Lond. A*, vol. 347, no. 1682, pp. 185–218, 1994.

[190] C. W. Hsu, B. Zhen, S.-L. Chua, S. G. Johnson, J. D. Joannopoulos, and M. Soljačić, "Bloch surface eigenstates within the radiation continuum," *Light: Science & Applications*, vol. 2, no. 7, pp. e84–e84, 2013.

[191] G. J. d. Valcárcel, E. Roldán, and F. Prati, “Semiclassical theory of amplification and lasing,” *Revista mexicana de física E*, vol. 52, no. 2, pp. 198–214, 2006.

[192] A. Cerjan and A. D. Stone, “Why the laser linewidth is so narrow: a modern perspective,” *Physica Scripta*, vol. 91, no. 1, p. 013003, 2015.

[193] H. Haken, “Laser Light Dynamics, Vol. 2,” 1986.

[194] S.-L. Chua, Y. Chong, A. D. Stone, M. Soljačić, and J. Bravo-Abad, “Low-threshold lasing action in photonic crystal slabs enabled by Fano resonances,” *Optics Express*, vol. 19, no. 2, pp. 1539–1562, 2011.

[195] S. Wuestner, A. Pusch, K. L. Tsakmakidis, J. M. Hamm, and O. Hess, “Overcoming losses with gain in a negative refractive index metamaterial,” *Physical Review Letters*, vol. 105, no. 12, p. 127401, 2010.

[196] R. Marani, A. D’Orazio, V. Petruzzelli, S. G. Rodrigo, L. Martín-Moreno, F. J. García-Vidal, and J. Bravo-Abad, “Gain-assisted extraordinary optical transmission through periodic arrays of subwavelength apertures,” *New Journal of Physics*, vol. 14, no. 1, p. 013020, 2012.

[197] M. Dridi and G. C. Schatz, “Model for describing plasmon-enhanced lasers that combines rate equations with finite-difference time-domain,” *JOSA B*, vol. 30, no. 11, pp. 2791–2797, 2013.

[198] J. Cuerda, F. Rüting, F. García-Vidal, and J. Bravo-Abad, “Theory of lasing action in plasmonic crystals,” *Physical Review B*, vol. 91, no. 4, p. 041118, 2015.

[199] S. Droulias, A. Jain, T. Koschny, and C. M. Soukoulis, “Novel lasers based on resonant dark states,” *Physical Review Letters*, vol. 118, no. 7, p. 073901, 2017.

[200] H. Kogelnik and C. Shank, “Stimulated emission in a periodic structure,” *Applied Physics Letters*, vol. 18, no. 4, pp. 152–154, 1971.

[201] J. E. Carroll, J. Whiteaway, D. Plumb, and R. Plumb, *Distributed Feedback Semiconductor Lasers*, vol. 10. IET, 1998.

[202] M. Imada, S. Noda, A. Chutinan, T. Tokuda, M. Murata, and G. Sasaki, “Coherent two-dimensional lasing action in surface-emitting laser with triangular-lattice photonic crystal structure,” *Applied Physics Letters*, vol. 75, no. 3, pp. 316–318, 1999.

[203] M. Meier, A. Mekis, A. Dodabalapur, A. Timko, R. Slusher, J. Joannopoulos, and O. Nalamasu, “Laser action from two-dimensional distributed feedback in photonic crystals,” *Applied Physics Letters*, vol. 74, no. 1, pp. 7–9, 1999.

[204] S. Noda, M. Yokoyama, M. Imada, A. Chutinan, and M. Mochizuki, “Polarization mode control of two-dimensional photonic crystal laser by unit cell structure design,” *Science*, vol. 293, no. 5532, pp. 1123–1125, 2001.

[205] Y. Kurosaka, S. Iwahashi, Y. Liang, K. Sakai, E. Miyai, W. Kunishi, D. Ohnishi, and S. Noda, "On-chip beam-steering photonic-crystal lasers," *Nature Photonics*, vol. 4, no. 7, p. 447, 2010.

[206] W. Zhou, M. Dridi, J. Y. Suh, C. H. Kim, D. T. Co, M. R. Wasielewski, G. C. Schatz, T. W. Odom, *et al.*, "Lasing action in strongly coupled plasmonic nanocavity arrays," *Nature Nanotechnology*, vol. 8, no. 7, p. 506, 2013.

[207] K. Hirose, Y. Liang, Y. Kurosaka, A. Watanabe, T. Sugiyama, and S. Noda, "Watt-class high-power, high-beam-quality photonic-crystal lasers," *Nature Photonics*, vol. 8, no. 5, pp. 406–411, 2014.

[208] D. Zhao, S. Liu, H. Yang, Z. Ma, C. Reuterskiöld-Hedlund, M. Hammar, and W. Zhou, "Printed large-area single-mode photonic crystal bandedge surface-emitting lasers on silicon," *Scientific Reports*, vol. 6, p. 18860, 2016.

[209] A. Kodigala, T. Lepetit, Q. Gu, B. Bahari, Y. Fainman, and B. Kanté, "Lasing action from photonic bound states in continuum," *Nature*, vol. 541, no. 7636, p. 196, 2017.

[210] S. T. Ha, Y. H. Fu, N. K. Emani, Z. Pan, R. M. Bakker, R. Paniagua-Domínguez, and A. I. Kuznetsov, "Directional lasing in resonant semiconductor nanoantenna arrays," *Nature Nanotechnology*, vol. 13, no. 11, pp. 1042–1047, 2018.

[211] P. Glendinning, *Stability, Instability and chaos: An Introduction to the Theory of Nonlinear Differential Equations*, vol. 11. Cambridge University Press, 1994.

[212] S. Burkhardt, M. Liertzer, D. O. Krimer, and S. Rotter, "Steady-state ab initio laser theory for fully or nearly degenerate cavity modes," *Physical Review A*, vol. 92, no. 1, p. 013847, 2015.

[213] D. Liu, B. Zhen, L. Ge, F. Hernandez, A. Pick, S. Burkhardt, M. Liertzer, S. Rotter, and S. G. Johnson, "Symmetry, stability, and computation of degenerate lasing modes," *Physical Review A*, vol. 95, no. 2, p. 023835, 2017.

[214] H. E. Türeci, A. D. Stone, and B. Collier, "Self-consistent multimode lasing theory for complex or random lasing media," *Physical Review A*, vol. 74, no. 4, p. 043822, 2006.

[215] L. Ge, R. J. Tandy, A. D. Stone, and H. E. Türeci, "Quantitative verification of ab initio self-consistent laser theory," *Optics Express*, vol. 16, no. 21, pp. 16895–16902, 2008.

[216] S. Esterhazy, D. Liu, M. Liertzer, A. Cerjan, L. Ge, K. Makris, A. Stone, J. Melenk, S. Johnson, and S. Rotter, "Scalable numerical approach for the steady-state ab initio laser theory," *Physical Review A*, vol. 90, no. 2, p. 023816, 2014.

[217] Y. Liang, T. Okino, K. Kitamura, C. Peng, K. Ishizaki, and S. Noda, "Mode stability in photonic-crystal surface-emitting lasers with large $\kappa_{1\mathrm{D}}L$," *Applied Physics Letters*, vol. 104, no. 2, p. 021102, 2014.

[218] K. Iga and H. Li, *Vertical-Cavity Surface-Emitting Laser Devices*. Springer, 2003.

[219] M. San Miguel, Q. Feng, and J. V. Moloney, "Light-polarization dynamics in surface-emitting semiconductor lasers," *Physical Review A*, vol. 52, no. 2, p. 1728, 1995.

[220] P. Mandel and M. Tlidi, "Transverse dynamics in cavity nonlinear optics (2000–2003)," *Journal of Optics B: Quantum and Semiclassical Optics*, vol. 6, no. 9, p. R60, 2004.

[221] A. F. Oskooi, D. Roundy, M. Ibanescu, P. Bermel, J. D. Joannopoulos, and S. G. Johnson, "MEEP: A flexible free-software package for electromagnetic simulations by the FDTD method," *Computer Physics Communications*, vol. 181, pp. 687–702, January 2010.

[222] A. Cerjan, A. Oskooi, S.-L. Chua, and S. G. Johnson, "Modeling lasers and saturable absorbers via multilevel atomic media in the *Meep* fdtd software: Theory and implementation," *arXiv: 2007.09329*, July 2020.

[223] M. Tinkham, *Group Theory and Quantum Mechanics*. Courier Corporation, 2003.

[224] J. Ohtsubo, *Semiconductor Lasers: Stability, Instability and Chaos*, vol. 111. Springer, 2012.

[225] E. M. Purcell, "Spontaneous emission probabilities at radio frequencies," *Physical Review*, vol. 69, p. 681, 1946.

[226] K. Joulain, R. Carminati, J.-P. Mulet, and J.-J. Greffet, "Definition and measurement of the local density of electromagnetic states close to an interface," *Physical Review B*, vol. 68, no. 24, p. 245405, 2003.

THIS PAGE INTENTIONALLY LEFT BLANK

Appendix A

Elementary concepts

In this appendix, we describe important scattering problems and some physical quantities associated with them.

A.1 Planewave scattering

We consider a planewave incident upon a finite-sized structure [defined by a permittivity $\epsilon_s(\mathbf{r})$] embedded in a homogeneous background with permittivity ϵ and permeability μ. Using the $e^{-i\omega t}$ harmonic time-dependence convention, the electric field of the incident wave is given by $\mathbf{E_{inc}} = E_0 \hat{\mathbf{e}}_i e^{i\mathbf{k}\cdot\mathbf{x}}$, where $\mathbf{k}$ is the incident wavevector, E_0 is the amplitude and $\hat{\mathbf{e}}_i$ is a unit vector defining the incident polarization.

For a three-dimensional structure, the far-field scattered field is a spherical wave[1]. Along a direction $\hat{\mathbf{k}}_s$, the scattered field can be written as:

$$\mathbf{E_s} = E_0 \hat{\mathbf{e}}_s f(\hat{\mathbf{k}}_s, \hat{\mathbf{k}}) \frac{e^{ikr}}{r}, \tag{A.1}$$

where $\hat{\mathbf{e}}_s$ is perpendicular to $\hat{\mathbf{k}}_s$ and $f(\hat{\mathbf{k}}_s, \hat{\mathbf{k}})$ is the scattering amplitude from $\hat{\mathbf{k}}$ to $\hat{\mathbf{k}}_s$.

The power flow per unit area is given by the Poynting vector. For the incident wave, this is equal to:

$$\mathbf{\Pi_{inc}} = \frac{1}{2}\mathrm{Re}\left(\mathbf{E_{inc}} \times \mathbf{H_{inc}}^*\right) = \frac{|E_0|^2}{2\eta}\hat{\mathbf{k}}, \tag{A.2}$$

where $\eta = \sqrt{\mu/\epsilon}$ is the background impedance. Similarly for the scattered wave, $\mathbf{\Pi_s} = |\mathbf{E_s}|^2 \hat{\mathbf{k}}_s / 2\eta$.

The differential scattered power dP_s through an elementary surface $dA = r^2 d\Omega$ asso-

---

[1] Similar results can be defined in a two-dimensional space using cylindrical waves.

ciated with solid angle $d\Omega$ in the direction $\hat{\mathbf{k}}_s$ is given by $|\mathbf{\Pi_s}|dA$. It is then convenient to define a differential scattering cross section as:

$$\sigma_s^d(\hat{\mathbf{k}}_s, \hat{\mathbf{k}}) = \frac{dP_s}{|\mathbf{\Pi_{inc}}|d\Omega} = |f(\hat{\mathbf{k}}_s, \hat{\mathbf{k}})|^2. \tag{A.3}$$

Note that σ_s^d has the unit of a surface area (per solid angle). The total scattering cross section is defined as:

$$\sigma_s = \int |f(\hat{\mathbf{k}}_s, \hat{\mathbf{k}})|^2 d\Omega = \frac{P_s}{|\mathbf{\Pi_{inc}}|}, \tag{A.4}$$

where P_s is the total scattered power.

We can also define an absorption cross section associated with the absorbed power. The latter is given by:

$$P_a = \frac{1}{2}\omega \int \mathrm{Im}\left(\epsilon_s\right) |\mathbf{E}|^2 d\mathbf{r}, \tag{A.5}$$

where $\mathbf{E}$ is the total field inside the structure. The absorption cross section is then defined as $\sigma_a = P_a/|\mathbf{\Pi_{inc}}|$.

Finally, we can define the extinction (total) cross section as $\sigma_e = \sigma_s + \sigma_a$, which quantifies the total interaction (scattering and absorption) between the incident planewave and the scatterer.

A.2 Dipolar emission

A dipolar emitter is one of the simplest and common sources of electromagnetic radiation. A dipole at $\mathbf{r}_0$ behaves as a current source with density $\mathbf{j} = -i\omega\delta(\mathbf{r}-\mathbf{r}_0)\mathbf{p}$. The associated dipolar emission is related to important concepts such as the rate of spontaneous emission and the local density of states.

Spontaneous emission is a quantum process resulting from the decay of an electron from an excited to a lower state, typically accompanied by a photon emission (radiative) or heat (non radiative). In 1946, Purcell showed that the spontaneous emission rate is not an intrinsic property of atoms and molecules, and that it can be enhanced, for example, in the presence of a resonant device [225]. While spontaneous emission is fundamentally a quantum effect, the enhancement of its rate (Purcell factor) can still be estimated classically.

The decay rate Γ can be computed using Fermi's rule and decomposing the electric into the cavity modes [56]. This gives:

$$\Gamma = \frac{2\pi\omega}{\hbar\epsilon}|\mathbf{p_q}|^2\rho^E_{\mathbf{p_q}}, \quad \rho^E_{\mathbf{p}} = \frac{\epsilon}{\epsilon_0}\frac{1}{\pi\omega}\left[\hat{\mathbf{p}}^\dagger \, \mathrm{Im}\mathbf{G} \, \hat{\mathbf{p}}\right], \tag{A.6}$$

where $\mathbf{p_q}$ refers to the dipole moment of the transition between two quantum states, $\rho^E_{\mathbf{p}}$ is the partial (or polarized) electric local density of states (which describes the overlap of the cavity modes with the dipole), and $\mathbf{G}$ is the dyadic Green's function[2] (at the emitter's position). The average power radiated is then given by $\Gamma\hbar\omega = 2\omega\left[\mathbf{p_q}^\dagger \, \mathrm{Im}\mathbf{G} \, \mathbf{p_q}\right]/\epsilon_0$.

We can compare the previous result with the total power lost by a *classical* dipole $\mathbf{p}$ which is given by:

$$P_{\mathbf{p}} = \frac{\omega}{2\epsilon_0}\left[\mathbf{p}^\dagger \, \mathrm{Im}\mathbf{G} \, \mathbf{p}\right]. \tag{A.7}$$

We see that the classical model matches the quantum model for $\mathbf{p} = 2\mathbf{p_q}$ [56]. However, this constant factor is not of much importance, since we are usually interested in computing the power/rate *enhancement* in the presence of a nearby scatterer (resonator) compared to the background. The enhancement (Purcell) factor Γ/Γ_b (with Γ_b the spontaneous emission in a homogeneous background medium) can still be computed from the classical dipole model.

From the two previous equations, we note that the partial electric local density of states can be computed based on the power emitted by a classical dipole:

$$\rho^E_{\mathbf{p}} = \frac{2\epsilon}{\pi\omega^2}P_{\mathbf{p}}. \tag{A.8}$$

The fact that the power emitted by a dipole depends on the environment is simply due to the fact that a fixed dipole amplitude requires a fixed current density. The power required to maintain this current is then dependent on the environment (equivalent to changing the load impedance). This power can be decomposed into two contributions: absorptive (lost as heat inside the scatterer/resonator in the presence of absorption loss) and radiative (emitted to the far-field). Similarly, we can talk about radiation and absorption LDOS (local density of states).

The LDOS is also an important quantity to compute the thermal emission of an object. In this case, both the electric and magnetic LDOS need to be taken into account [226]. The total LDOS can be estimated by summing over three orthogonal polarization directions. In a homogeneous medium with refractive index n_b, both contributions are equal and

---

[2] $\mathbf{G}$ is defined here so that $\mathbf{E} = \mu_r/\epsilon_0\mathbf{G}\mathbf{p}$.

$\rho_{\mathbf{p}}^{E} = \rho_{\mathbf{p}}^{H} = n_b^3\omega^2/6\pi^2c^3$. The total LDOS is then equal to:

$$\rho = \sum_{\mathbf{p}} \rho_{\mathbf{p}}^{E} + \sum_{\mathbf{p}} \rho_{\mathbf{p}}^{H} = \frac{n_b^3\omega^2}{\pi^2c^3}. \tag{A.9}$$

Appendix B

QNM parameters for structures in Chapter 3 and Chapter 4

Here, we provide all the QNMs computed via finite-element simulations. The computed QNM-to-CPM ratios are indicated by σ^c, while the ones fine-tuned by Eq. 3.16 of the main text are denoted by σ. The modes used to calculate the background C matrix are marked in bold.

B.1 Structures of Chapter 3

For simplicity, Ω and Γ in the tables denote the dimensionless frequency values as defined in the corresponding figures.

- Normal incidence on microwave metasurface of Fig. 3-2:

Ω	**0**	0.2020	0.2929	**0.3510**	**0.5099**
Γ	**0.0699**	0.0136	0.0218	**0.0625**	**0.0905**
σ^c	**0.98**	-1.01+0.09i	0.14+0.01i	**1.23+4.29i**	**-0.27+0.11i**
σ	**1.00**	-1.04+0.07i	0.14+0.02i	**1.14+4.50i**	**-0.28+0.09i**
$\tilde{\Omega}$	**0**	0.2018	0.2925	**0.3503**	**0.5091**
$\tilde{\Gamma}$	**0.0699**	0.0147	0.0234	**0.0641**	**0.0926**

Ω	0.6207	0.6431	0.6539	0.6932	**0.7395**
Γ	0.0029	0.0145	0.0048	0.0048	**0.0363**
σ^c	-0.81+0.18i	-0.07+0.19i	-0.26-1.70i	-0.93-0.36i	**0.89+0.2i**
σ	-0.78+0.12i	-0.09+0.20i	-0.05-1.67i	-0.94-0.61i	**0.75+0.3i**
$\tilde{\Omega}$	0.6206	0.6428	0.6538	0.6931	**0.7388**
$\tilde{\Gamma}$	0.0056	0.0171	0.0077	0.0081	**0.0397**

- 4-port metasurface via coupled polarizations of Fig. 3-3:

Ω_n	0.3826	0.4093	0.5288	0.5753	0.5948	0.6753
Γ_n	0.0011	0.0007	0.0095	0.0029	0.0011	0.0064
$\sigma^c_{1,2n}$	-1.44-0.36i	-0.07+0.01i	2.00+0.62i	0.57+0.23i	-17.60-5.09i	1.68+1.69i
$\sigma_{1,2n}$	-1.50-0.13i	-0.06+0.03i	2.24-0.21i	0.59-0.06i	-14.57+3.13i	3.17-0.01i
$\sigma^c_{1,3n}$	0.71+0.00i	0.15+0.03i	1.01-0.02i	0.66-0.03i	-3.62+2.09i	-0.71-0.03i
$\sigma_{1,3n}$	0.72+0.00i	0.13+0.03i	1.01-0.03i	0.70-0.02i	-2.40+1.190i	-0.72-0.03i
$\sigma^c_{1,4n}$	-2.32-0.60i	1.20+0.25i	2.83+0.79i	0.43+0.00i	9.97+4.22i	-1.37-1.40i
$\sigma_{1,4n}$	-2.37-0.23i	1.18+0.01i	3.11-0.36i	0.41-0.17i	8.90-1.07i	-2.60+0.00i

- Oblique incidence on 2d photonic metasurface of Fig. 3-4:

Ω	**0**	**0.187**	0.3157	**0.362**	0.427
Γ	**0.0402**	**0.0377**	0.0026	**0.0265**	0.0012
σ^c	**0.953**	**-0.679+0.03i**	0.345+0.274i	**0.992-0.051i**	1.08-0.181i
σ	**0.973**	**-0.689-0.019i**	0.289+0.329i	**1.11+0.088i**	1.21+0.032i
$\tilde{\Omega}$	**0**	**0.184**	0.3152	**0.359**	0.4264
$\tilde{\Gamma}$	**0.0402**	**0.0440**	0.0121	**0.0391**	0.0180

Ω	**0.444**	**0.499**	**0.5219**	0.5716
Γ	**0.0107**	**0.0106**	**0.0122**	0.00024
σ^c	**-0.841+0.062i**	**-1.71+1.19i**	**-0.078+0.24i**	-0.051+0.137i
σ	**-0.787-0.073i**	**-1.99+0.865i**	**-0.125+0.221i**	-0.081+0.120i
$\tilde{\Omega}$	**0.443**	**0.498**	**0.5195**	0.5708
$\tilde{\Gamma}$	**0.0237**	**0.0274**	**0.0278**	0.0175

Ω	0.6044	**0.6514**	0.6737	0.7231
Γ	0.0011	**0.016**	0.0065	0.0052
σ^c	-3.09-0.498i	**0.409+0.012i**	1.39+3.76i	0.246-0.008i
σ	-2.96-1.43i	**0.369+0.155i**	0.769+5.40i	0.266-0.024i
$\tilde{\Omega}$	0.6032	**0.6499**	0.6702	0.7218
$\tilde{\Gamma}$	0.0221	**0.0373**	0.0311	0.0279

B.2 Structures of Chapter 4

Ω and Γ in the tables are in units of $\omega_c = 2\pi \times 10$ GHz.

We remind that good approximate solutions with complex $\gamma = e^{i\varphi}$ can be found, so we allow a common phase $\sqrt{\gamma}$ for the ratios σ during optimization. Deviations of the final computed $\sigma/\sqrt{\gamma}$ from the ideal ± 1 or $\pm i$ shown below lead to only small errors in the ISF designs. For symmetric structures, all computed σ are equal to ± 1 anyway. (Note that, after the design optimization process is completed, we do not care to fine-tune σ for QNMT modeling, since in Figs. 4,5 we only show the exact transmission spectra from direct frequency-domain simulations anyway.)

- Third-order bandpass filters of Fig. 4-4:

Type	Butterworth ($\varphi = 0$)			Chebyshev ($\varphi = 0$)		
Ω	0.9774	1.0010	1.0210	0.9788	1.0009	1.0223
Γ	0.0127	0.0251	0.0123	0.0079	0.0154	0.0075
$\sigma/\sqrt{\gamma}$	1	-1	1	1	-1	1

Type	Inverse Chebyshev ($\varphi = -0.07\pi$)			Elliptic 2% ($\varphi = -0.066\pi$)		
Ω	0.9885	0.9995	1.0101	0.9728	0.9975	1.0254
Γ	0.0032	0.0086	0.0028	0.0119	0.0341	0.0128
$\sigma/\sqrt{\gamma}$	-1.04-0.14i	1.16+0.03i	-1.10+0.17i	-0.94+0.00i	1.05+0.02i	-0.98+0.03i

Type	Elliptic 6% ($\varphi = -0.059\pi$)			Elliptic 10% ($\varphi = -0.075\pi$)		
Ω	0.9718	0.9987	1.0274	0.9516	0.9972	1.0504
Γ	0.0076	0.0218	0.0078	0.0124	0.0392	0.0145
$\sigma/\sqrt{\gamma}$	-1.04+0.03i	0.91-0.01i	-1.01-0.04i	-1.04-0.15i	1.19+0.00i	-1.03+0.15i

- Third-order bandstop filter of Fig. 4-5(a): ($\varphi = -0.16\pi$)

Ω	0.949	1.004	1.065
Γ	0.0156	0.0809	0.0158
$\sigma/\sqrt{\gamma}$	0.95+0.04i	-0.97+0.00i	0.97-0.04i

- Second-order bandpass filter of Fig. 4-5(b):

Ω	**0.738**	**0.751**	0.996	1.004	**1.186**	**1.191**	**1.289**	**1.362**
Γ	**0.297**	**0.301**	0.0031	0.0031	**0.0012**	**0.011**	**0.0084**	**0.0007**
σ	**1**	**-1**	-1	1	**-1**	**1**	**-1**	**1**

The modes marked in bold lead to $|C_{21}(\omega_c)| = -24.9$ dB and $\beta = C_{11}C_{21}^{*}/|C_{11}C_{21}| = -i$.

- Second-order bandstop filter of Fig. 4-5(c):

Ω	**0**	0.954	1.042	**1.109**	**1.459**	**1.481**	**1.892**
Γ	**0.851**	0.0313	0.0343	**0.993**	**0.0156**	**0.0024**	**0.945**
σ	**1**	-1	1	**-1**	**1**	**-1**	**1**

Note that the "Fabry-Perot" modes in this final table have such a large Γ that higher-order such modes will still have an effect at frequencies around $\omega \sim \omega_c$. However, they lie deep inside the diffraction zone, so they are hard to identify from spurious modes. Therefore, as explained in Chapter 4, we calculated more accurately $C(\omega_c) = \bar{S}^{-1}(\omega_c)S(\omega_c)$, with $\bar{S}$ and S obtained at ω_c from QNMT on the two high-Q modes and a direct computation respectively. The optimized result is then indeed $|C_{21}(\omega_c)| = -0.25$ dB and $\beta = i$.